Hierarchical and Synergistic Assembly of Amphiphilic DNA Nanostructures

By

Pongphak Chidchob

A thesis submitted to McGill University in partial fulfillment of the requirements of the degree of Doctor of Philosophy

Department of Chemistry, McGill University

Montreal, Quebec, Canada

December 2017

I dedicate this thesis to my mother Nataya, my father Chaiyasit, my brother Pattawee, and many members of my extended family for their love, support and encouragement.

Abstract

DNA assembly offers a powerful molecular tool to create arbitrary structures with excellent size and shape control through selective assembly, sequence programmability and well-defined, rigid structure of DNA. As designer scaffolds, DNA materials have a tremendous potential for precise organization of molecules into any pattern. In most DNA-based constructions, Watson-Crick base-pairing serves as the only instruction rule. However, their efficiency can reach a limit when the design complexity increases. As a unique approach, supramolecular DNA assembly has emerged from the deliberate blend between the toolbox of supramolecular chemistry and DNA programmability to address this complexity-efficiency issue and to generate new structures and functions. The aim of this thesis is to integrate hydrophobic interactions as orthogonal instruction rules in the design and assembly of amphiphilic DNA nanostructures, through the use of small molecule- and polymer-DNA conjugates. Firstly, polymer-DNA conjugates are anisotropically organized on DNA cages. The polymer association modes are directed by their decoration geometry on DNA cages. A library of well-defined, hierarchical amphiphilic DNA nanostructures can be generated by polymer's sequence regulation. Secondly, to demonstrate the versatility of DNA cages in the structure-function design, multiple cholesterol units are site-specifically organized on DNA cubes to allow their binding to lipid vesicles. The membrane interactions of these nanostructures are dependent on the decoration geometry as well as structural flexibility. Finally, to further improve the stability of hydrophobic interactions, three chemical approaches are developed to crosslink the hydrophobic micellar cores of amphiphilic DNA nanostructures. Overall, the work presented herein demonstrate that there is a synergy between DNA base-pairing and hydrophobic interactions that lead to new or even unprecedented structural and functional modes of amphiphilic DNA nanostructures. The opportunity from this work could not only contribute to a better fundamental understanding of self-assembly, but also provide guidelines to rationally design target structures, which could facilitate the development of advanced materials for applications in materials science and biomedicine.

Résumé

La nanotechnologie de l'ADN est un outil puissant permettant la création de structures arbitraires de forme et de taille contrôlées via l'assemblage sélectif de l'ADN, sa séquence programmable ainsi que sa structure rigide et bien définie. En termes de design et d'architecture, les matériaux à base d'ADN possèdent un énorme potentiel pour l'organisation précise de molécules ou de matériaux selon des motifs prédéterminés. Dans la plupart des constructions à base d'ADN, l'appariement des bases (A-T et C-G) tel qu'édicté par Watson et Crick sert comme seule règle d'assemblage. Cependant, l'efficacité de cette approche peut atteindre une limite lorsque la complexité du design augmente. En tant qu'approche innovatrice, l'assemblage supramoléculaire de l'ADN, issue du mélange délibéré entre le savoir-faire de la chimie supramoléculaire et la programmabilité de l'ADN, permet d'adresser ce problème de complexité-efficacité et de générer de nouveaux modes d'assemblage structurels et fonctionnels. L'objectif de cette thèse est d'examiner l'incorporation d'interactions hydrophobes en tant que règles d'instruction orthogonales dans le design et l'assemblage de nanostructures amphiphiles en ADN, à travers l'utilisation de petites molécules et de polymères conjugués à l'ADN. En premier lieu, des conjugués ADN-polymères sont organisés de façon anisotrope sur des cages d'ADN tridimensionnelles. Les modes d'assemblage des polymères sont dirigés par la géométrie de leurs points d'attachements sur les cages d'ADN. Une librairie de nanostructures d'ADN amphiphiles hiérarchiques et bien définies peut être générée en contrôlant la séquence des polymères. En deuxième lieu, afin de démontrer la polyvalence des cages d'ADN tridimensionnelles dans le design structure-fonction, plusieurs unités de cholestérol sont placées à des endroits spécifiques sur des cubes d'ADN afin de permettre l'association de ces cubes d'ADN avec des vésicules à membrane lipidique. Les interactions et les modes d'association de ces nanostructures amphiphiles avec les membranes lipidiques dépendent de l'arrangement géométrique de leurs points d'attachement et de leur flexibilité structurelle. En dernier lieu, afin d'améliorer davantage la stabilité des interactions hydrophobes, trois approches chimiques sont développées afin de réticuler les noyaux micellaires hydrophobes de nanostructures d'ADN amphiphiles. Dans l'ensemble, le travail présenté ici démontre qu'il existe un effet synergique entre l'appariement des bases de l'ADN et les interactions hydrophobes qui mènent vers de nouveaux modes d'assemblage structurel et fonctionnel inédits de nanostructures d'ADN amphiphiles. Le potentiel de ces travaux ne se résume pas qu'à l'amélioration de la compréhension fondamentale de l'auto-

assemblage, mais fournit aussi des lignes directrices permettant le design rationnel de structures cibles qui pourraient être utiles dans le développement de matériaux avancés pour des applications en science des matériaux et en biomédecine.

Translated by Katherine Bujold

Acknowledgments

To many people who have helped me along the way, thank you for making my life in Montreal and my study at McGill Chemistry full of memorable moments and joys. Firstly, I would like to thank my supervisor, Professor Hanadi Sleiman, for her guidance and support throughout my research, even before I arrived in Montreal. Thank you for giving me a wonderful opportunity to be a part of this fascinating world of DNA and supramolecular chemistry. Her strong motivation, hard-work and unlimited creativity have always inspired and encouraged me. Hanadi is also an excellent teacher. Her Supramolecular class is one of my favorite courses ever!

I would like to thank Professor Dima Perepichka and Professor Janine Mauzeroll for actively being the great committee members in the past four years. I would like to thank Professor Gonzalo Cosa for his guidance and invaluable insight into single-molecule TIRF microscopy. I also would like to acknowledge our collaborator at University College London, Professor Stefan Howorka and Daniel Offenbartl-Stiegert, for their expertise with nanopore and lipid membrane, which are greatly helpful for my research.

I am grateful to all people who have trained me since day 1 at McGill. Janane Rahbani, the greatest mentor I have ever met, for his devoted training on essential lab and research skills and fruitful discussions and advice for my research. Christopher Serpell for teaching me synthesis skills and his great guidance for the work in Chapter 2. Thomas Edwardson for teaching me many lab techniques and his invaluable insight into DNA amphiphiles. Amani Hariri for giving me great advice and hands-on experience on TIRF. Mohini Ramkaran, Béatrice Lego and Julia Del Re for AFM. Kaustuv Basu, Kelly Sears and David Liu for TEM. Erika Wee for CLSM. Nadim Saadeh and Alexander Wahba for MS. Frederick Morin and Robin Stein for NMR.

I am thankful for all people with whom I have collaborated and worked. Janane Rahbani for DNA origami and nanotubes. Tuan Trinh for many possible chemical reactions with DNA. Xin Luo for DNA origami and gold nanoparticles. Danny Bousmail for DNA origami. Daniel Saliba for aptamers. Johans Fakhoury and Empar Vengut Climent for cellular uptake of DNA nanostructures. Mohammad Askari for metal coordination. Yasser Gidi for TIRF issue and analysis. Violeta Toader for phosphoramidite synthesis.

I am grateful to all Sleiman members for being amazing colleagues and friends- Adrienne Gallant Lanctôt, Alan Blayney, Albert Daubry, Alexa Carla Bobica, Alexander Prinzen, Alexander Rousina-Webb, Amani Hariri, Amine Garci, Andrea Greschner, Aurélie Lacroix, Casey Platnich, Christophe Lachance-Brais, Christopher Serpell, Danny Bousmail, Daniel Saliba, Donatien de Rochambeau, Empar Vengut Climent, Farhad Khan, Graham Hamblin, Hammond Sun, Hassan Fakih, Janane Rahbani, Janet McMillan, Johans Fakhoury, John Hsu, Justin Conway, Kai Lin Lau, Kamila Mustafina, Karina Carneiro, Katherine Bujold, Katherine Castor, Keith Husted, Kimberly Metera, Kitty Chen, Klaudia Englert, Maciej Barlog, Michael Dore, Mohammad Askari, Sally Xiao, Sanchit Gupta, Simon Arsène, Sonia Romero, Thomas Edwardson, Tolulope Ifabiyi, Tuan Trinh, Violeta Toader and Xin Luo (alphabetical, first name). It has truly been a pleasure working with you all and best of luck, everyone!

I would like to thank many people in the department for keeping good company. I am also grateful to all faculty and staff in McGill Chemistry, especially for those who gave me help and advice, and Chantal Marotte for her remarkable help and support with all paperwork starting from the moment I decided to apply for McGill Chemistry. I would like to thank Department of Chemistry, McGill University and CREATE training program in Bionanomachines for all financial support I have received over the years.

To many people outside research, I am thankful for many Thai friends and family in Montreal for their support and making my life in Montreal never become boring. Many friends from MWIT, KAIST, and MU who constantly give me support and advice- I also thank them all.

Finally, it would have been impossible to survive the PhD journey without the unwavering support, understanding, and encouragement from my parents, my brother and many members of my extended family, who are always there with me no matter what. Moreover, to my passed-away grandparents, they, unfortunately, won’t be able to witness my achievement, but I have made it!

Table of Contents

List of figures

List of tables

List of abbreviations

1D	One dimensional
2D	Two dimensional
3D	Three dimensional
A	Adenine
AFM	Atomic force microscopy
AGE	Agarose gel electrophoresis
Ant	Anthracene
AuNP	Gold nanoparticle
bp	Base-pair
C	Cytosine
CLSM	Confocal laser scanning microscopy
CMC	Critical micelle concentration
Cy3	Cyanine 3
DDAB	Didodecyldimethylammonium bromide
DLS	Dynamic light scattering
DMT	Dimethoxytrityl
DNA	Deoxyribonucleic acid
DOPC	1,2-dioleoyl-*sn*-glycero-3-phosphocholine
DPhPC	1,2-diphytanoyl-*sn*-glycero-3-phosphocholine
DX	Double crossover
FWHM	Full width at half-maximum
G	Guanine
GUV	Giant unilamellar vesicle
HE	Hexaethylene
HEG	Hexaethylene glycol
LC-ESI-MS	Liquid chromatography-electrospray ionization mass spectroscopy
NMR	Nuclear magnetic resonance
OD	Optical density
PAGE	Polyacrylamide gel electrophoresis
PBS	Phosphate buffered saline
PEG	Polyethylene glycol
R_h	Hydrodynamic radius
RP-HPLC	Reversed-phase high-performance liquid chromatography
RT	Room temperature
sm-TIRF	Single-molecule total internal reflection fluorescence microscopy
T	Thymine
TAMg	Tris/acetate/magnesium
TBE	Tris/borate/EDTA
TEAA	Triethylammonium acetate
TEM	Transmission electron microscopy
T_m	Melting temperature
Tris	Tris(hydroxymethyl)aminomethane

Contribution of authors

Hanadi F. Sleiman provided funding, research objectives, experimental design and intellectual guidance for all the projects described in this thesis.

Chapter 2 **Christopher J. Serpell** contributed to the project design and synthesized clip strands. **Thomas. G. W. Edwardson** synthesized polymer-DNA conjugates and clip strands, and provided the protocol and materials for gold-labeling experiment. **Amani A. Hariri** and **Gonzalo Cosa** contributed to the experimental design and helped with the single-molecule photobleaching.

Chapter 3 **Stefan Howorka** contributed to the project design and data analysis. **Daniel Offenbartl-Stiegert** designed and performed nanopore experiments in Section 3.3.5.

Chapter 4 **Tuan Trinh** contributed to the project design in Section 4.3.1, synthesis and characterization of amino-modified polymer-DNA amphiphiles.

Appendix **Janane F. Rahbani** contributed to the project design and synthesis of DNA amphiphiles, and performed AFM characterization in Section A.3.2.

| 1 |

Introduction

This chapter is composed of the work published as "Supramolecular Chemistry with DNA" by Pongphak Chidchob and Hanadi F. Sleiman as a book chapter in *Macrocyclic and Supramolecular Chemistry: How Izatt-Christensen Award Winners Shaped the Field (ed. R. M. Izatt)*, **2016**, John Wiley & Sons, Ltd, Chichester, UK.

1.1 Construction at the nanoscale

Structure-function relationships are key concepts shared by all structures with length scales covering from the molecular to the macroscopic levels. As such, it is essential to accurately build structures to avoid functional failures. Biological systems have relied on many elegant strategies to build structures with varying complexity. For example, protein folding is a highly programmed process guided by various information inputs, and three lessons can be learned. i) The sequence information encoded in polypeptides allows them to fold properly into subunits. This is facilitated by a combination of twenty natural amino acids, which have diverse physical and chemical properties. ii) The precise 3D positioning of functional groups allows the subunits to efficiently form hierarchical structures or to interact selectively with environments. iii) There are multiple orthogonal molecular interactions working together to organize the subunits into their final form.

Many approaches have been explored to build synthetic structures across length scales. At the molecular level, synthetic chemistry provides a foundation for the limitless creation of any molecule with excellent control of its structure. A fundamental framework offered by supramolecular chemistry brings these molecular building blocks into a dynamic and functional system through non-covalent interactions. At another end of the length scale, the microscale construction with accurate size and component control can be achieved by microfabrication technology. However, the nanoscale construction has yet to be perfectly manipulated compared to other length scales. It is worth noting that the nanoscale regime is important not only in biological systems where numerous biological machines perform their tasks, but also in artificial systems where new properties can emerge.

Nanotechnology aims to construct and manipulate materials in the size range of 1-100 nm. Many types of materials have been used as building blocks, giving rise to complexity. New unique properties have been noted in inorganic materials and polymeric assembly, but there is a limited

scope of nanostructures that one can make. Inspired by nature, an assembly of polypeptide-based materials should, in principle, enable easy access to structural diversity. As protein folding is not fully understood, an in-depth understanding of assembly mechanism and structural prediction will be necessary to use polypeptides as designer materials at their full capability. Nevertheless, a significant progress towards nanoscale construction with polypeptides has been made such as 3D protein cages.[1-2] As another type of programmable materials, DNA has emerged as a powerful guiding molecule to achieve supramolecular organization.[3] Our current understanding of DNA properties permits the finely tunable construction of arbitrary structures as well as their use as addressable scaffolds for organizing other materials.

1.2 Structural DNA assembly

The fundamental features of DNA include highly selective assembly, programmable sequence design, and a well-defined, rigid structure. These properties make DNA one of the most programmable building blocks for nanoscale constructions, which is currently unparalleled by other types of materials. This section will survey designs and developments of DNA motifs and their hierarchical assembly towards the construction of DNA objects.

1.2.1 DNA as a building block

DNA is a biopolymer of four nucleoside monomers. It consists of nitrogen-containing bases (nucleobases) attached to five-membered deoxyribose units, which are connected by phosphodiester bonds (Figure 1.1a). Adenine (A) and guanine (G) belong to one type of nucleobases called purines and can form specific hydrogen bonds to thymine (T) and cytosine (C), respectively, which are pyrimidine bases (Figure 1.1b). These A:T and G:C hydrogen-bond motifs are called Watson-Crick base-pairs. Two DNA single strands that have complementary sequences can selectively bind to each other into a double helix (or DNA duplex). The two strands in this duplex are antiparallel, meaning that the 3'- sugar end of one strand is on the same side of the 5'-end of another strand. DNA hybridization is highly cooperative and can be driven by a combination of π- π stacking of nucleobases and hydrogen bonds.[4] The most common duplex structure is B-

DNA. This right-handed duplex has a diameter of 2 nm and ~10.5 bases per helical turn, with a pitch length of 3.4 nm (Figure 1.1c). It behaves like a rigid polymer with the persistence length of about 50 nm. The well-defined 3D structure of B-DNA constitutes the fundamental design element for DNA materials.

The development of solid-phase DNA synthesis has significantly advanced the progress in synthetic DNA assembly. Among many available approaches, routine DNA synthesis is currently based on phosphoramidite chemistry.[5-9] The DNA synthesis cycle is illustrated in Figure 1.1d and contains four steps, which can be carried out in an automated synthesizer: i) deprotection of the dimethoxytrityl group on the 5'-end, ii) coupling with a nucleoside phosphoramidite unit, iii) capping the strands that failed to undergo coupling and iv) oxidation of phosphorus (III) to phosphorus (V). Pure DNA strands can be obtained after base-mediated deprotection and cleavage from solid support followed by purifications. Consequently, DNA strands can now be easily generated, theoretically in a nearly infinite number of sequences. Moreover, the solid-phase approach has enabled the synthesis of DNA conjugates, where functional molecules are appended to DNA strands to introduce new functions in DNA materials. Thus, unlike many supramolecular building blocks, DNA is a highly programmable molecule that has the potential to assemble into symmetric, as well as asymmetric and anisotropic structures.

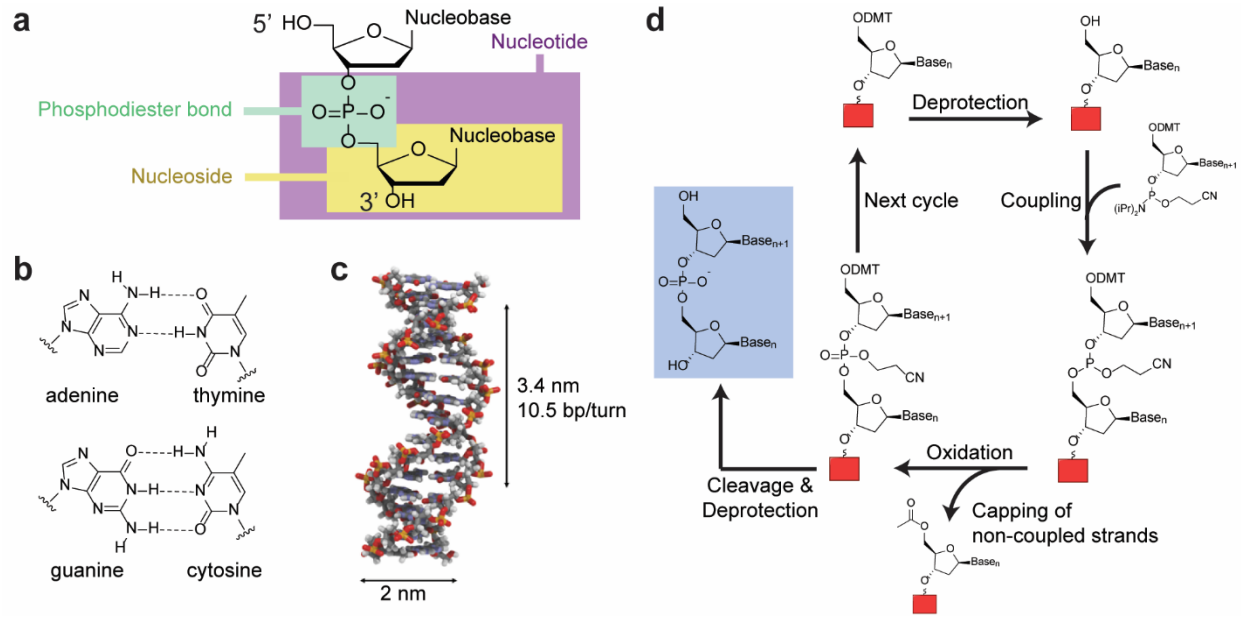

Figure 1.1 | DNA as a building block. a) Chemical structure of DNA, consisting of nucleotides as monomeric units. b) Watson-Crick hydrogen-bond motifs of A:T and G:C. c) Well-defined B-form of DNA duplex. d) DNA synthesis cycle based on phosphoramidite approach.

1.2.2 Branched DNA motifs

The linear connection of multiple DNA duplexes can mainly generate 1D polymers that have length-dependent stiffness. To build more complex structures, it is necessary to go beyond linearity. The simplest strategy is to introduce branched motifs that allow 1D and 2D extensions. First proposed by Nadrian Seeman in 1982, the DNA crossover junction was the first branched DNA motif, whose design was based on the Holliday junction found in DNA recombination. In the crossover motif, a strand starts from one DNA helix and switches over to the next, connecting two DNA helices (Figure 1.2a).[10] Initially, the four-way junction (4WJ) consisting of four DNA strands was used.[11] The goal was to build a well-defined, hierarchical network that can serve as a template for protein crystallography. Unfortunately, such purpose was not realized with 4WJ due to its flexibility. Yet, 4WJ could be applied to generate disordered gel networks.[12] Indeed, it was shown that there were unpaired bases at the branched point in the fully-complementary three-way junction (3WJ), which created a nanoscale cavity and increased structural flexibility.[13] With a similar strategy, DNA junctions of higher branching degree were then reported, including five-, six-, eight- and twelve-way junctions.[14-15]

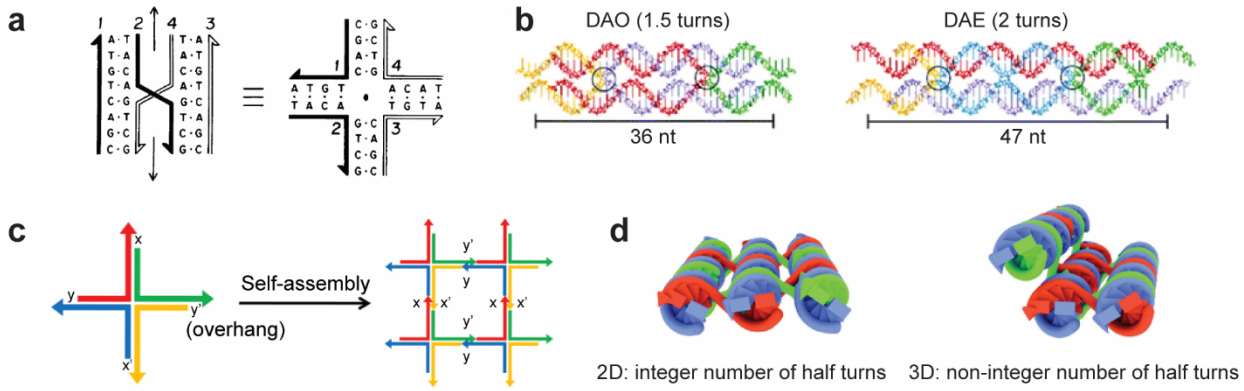

Figure 1.2 | DNA junctions as basic structural motifs. a) Flexible 4WJ composed of four DNA strands. Adapted with permission from reference 10 (Elsevier, 1982). b) Double-crossover motifs from two connected duplexes via two crossovers. Adapted with permission from reference 25 (NPG, 1998). c) Sticky-end cohesion for hierarchical assembly of DNA motifs. d) Controllable angle between two connected DNA duplexes by changing the number of DNA bases between two crossovers. Adapted with permission from reference 24 (RSC, 2011).

To improve rigidity, it was important to increase the number of branched points (or crossovers) in the motifs to allow stiffer connections between helices. DNA double-crossover (DX) junction

was reported in 1993 as the first design with a stiffness as twice as that of a linear duplex.[16-17] The most stable coplanar forms contained two anti-parallel double helices connected to each other twice through crossovers, which were separated by integral numbers of helical half-turns (a full turn contains 10.5 base pairs, Figure 1.2b). Following the lead of DX design, other rigid DNA motifs have been developed.[18-23] Their hierarchical assembly will be covered in Section 1.2.3.

The next step towards fabricating DNA materials is to organize and connect the motifs into the desired pattern. Several design concepts have been implemented to obtain a successful construction. i) The sticky-end cohesion allows a connection between two duplexes: If a duplex has a short single-stranded component at its end (sticky-end or overhang), it can come together with another duplex having the complementary overhang via base-pairings (Figure 1.2c). This interaction allows DNA motifs to selectively connect into structures. ii) The rotation of DNA bases along the duplex provides a controllable alignment of the overhang protruding from the duplex, allowing the connection between two motifs at a specific angle (Figure 1.2d).[24] The angle of ~34° can be obtained when shifting from n to n+1 bases. iii) The stability of DNA structures is also a requirement to maintain their structural integrity. Longer DNA duplexes generally have higher thermal stability. Duplexes are more stable when the GC content of their sequences is increased.

1.2.3 Discrete DNA assembly

Discrete DNA objects constitute one of the major classes of DNA structures. Their assembly can be controlled in most cases to generate well-defined sizes and shapes. Wireframe structures have their edges represented by DNA duplexes connected via branched DNA junctions at the vertices. They are usually DNA-minimal design and have a porous structure. Another category are dense structures, whose entire structures are typically composed of dense DNA layers. In the case of 3D design, the interior of the structure could be empty or filled with DNA layers.

1.2.3.1 Wireframe DNA structures

In 1991, a DNA cube reported by the Seeman group was the first example of discrete DNA objects.[26] It was constructed by repetitive ligation and hybridization of ten DNA strands. Each face

of the cube was composed of a cyclic DNA strand, which was hybridized to four neighboring faces. This resulted in 20-bp double-stranded edges, joined together via 3WJs at the vertices (Figure 1.3a). The same group then showed the assembly of a truncated octahedron.[27] However, the major drawbacks of these assemblies are multistep preparations and low yields.

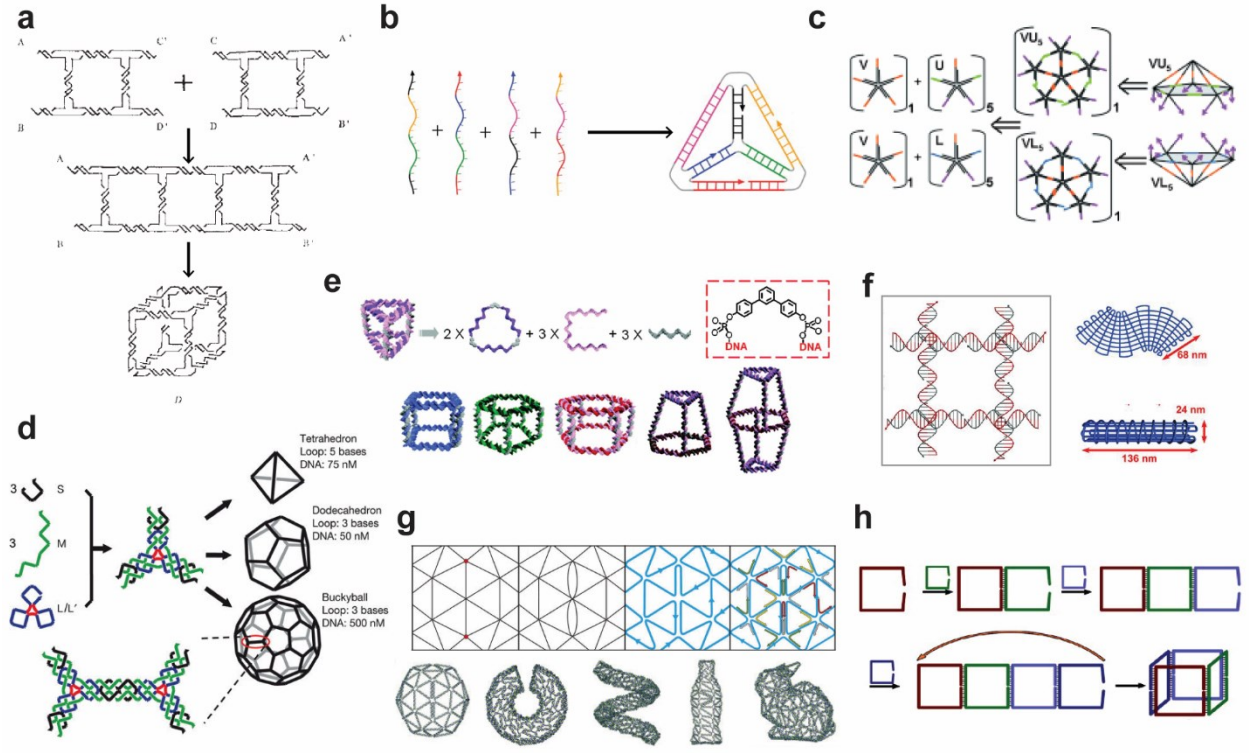

Figure 1.3 | Wireframe DNA structures. a) DNA cube prepared from repetitive hybridization and ligation. Adapted with permission from reference 26 (NPG, 1991). b) Single-step assembly of DNA tetrahedron. Adapted with permission from reference 29 (AAAS, 2005). c) Modular assembly of icosahedral cage in two steps. Adapted with permission from reference 30 (Wiley-VCH, 2009). d) Hierarchical assembly of DNA polyhedron from 3PS motifs. Reproduced with permission from reference 32 (NPG, 2008). e) DNA prism assembly from hierarchical linking of DNA polygons with organic junctions. Adapted with permission from reference 35 (ACS, 2007). f) DNA gridiron nanostructures based on flexible 4WJs. Adapted with permission from reference 37 (AAAS, 2013). g) Scaffold-based 3D assembly based on polyhedral-mesh strategy. Adapted with permission from reference 38 (NPG, 2015). h) 'Clip-by-clip' assembly of DNA cage. Adapted with permission from reference 40 (ACS, 2012).

Without the need of ligation, the single-step folding of four DNA strands into a tetrahedral cage with 3WJs at the vertices was reported by the Turberfield group (Figure 1.3b).[28-29] A key was to incorporate unhybridized-thymine hinges to increase flexibility and relieve structural strain

arising from the bending of DNA duplexes at the vertices. With a modular approach, the Krishnan group carried out two-step assembly of DNA icosahedron from three distinct 5WJs (Figure 1.3c).[30] Additionally, a scaffolding approach was adopted by Shih and Joyce to fold a 1.7-kilobase DNA strand with five short DNA strands into an octahedron with six 4WJs connecting its twelve edges.[31]

To create more geometrical variations, the Mao group presented a three-point star (3PS) motif, where seven DNA strands were connected by three 4WJs. They were able to selectively assemble polyhedra including tetrahedron, dodecahedron, and buckyball by altering the flexibility and concentration of 3PS motifs (Figure 1.3d).[32] The higher the concentration and the stiffness of the building blocks, the larger the structures that one can obtain. Similarly, an octahedron was assembled from four-point star motifs[33], while the assembly of five-point star motifs generated icosahedra and larger cages[34]. These polyhedra were fully symmetrical. To introduce asymmetry, Sleiman and co-workers used DNA polygon as a modular component to access a DNA polyhedron of predefined geometry.[35] The polygon was prepared by templated ligation of single-stranded DNA strands, which contained rigid triphenylene linkers as the corner units to separate single-stranded arms of different sequences. The alignment and connection of two polygons by linking strands can generate DNA prisms of various geometries (Figure 1.3e).

The invention of a scaffolding approach called 'DNA origami' has revolutionized the fields by enabling access to arbitrary shape and size (see Section 1.2.3.2).[36] As an example, flexible 4WJs were linked together to form a two-layer square frame, where one continuous layer was made entirely of a long DNA scaffold strand (Figure 1.3f).[37] Multilayer stacking of these frames using different locations and distances between connection points led to 3D structures with controlled curvatures. Additionally, inspired by graph theory, a design pattern of complex objects such as a Stanford bunny could be converted into a polyhedral triangulated mesh.[38] In this design, a long DNA scaffold was routed on the 3D mesh, and the edges of polygons were replaced by DNA helices. The folding of the scaffold strand was then guided by multiple short, unique single-stranded DNA strands (Figure 1.3g).

One of the challenges in DNA assembly is that as structures become more complicated, more unique DNA strands are required. This can increase the assembly errors, which subsequently lower the yield of target products. Yan and co-workers simplified DNA tetrahedron design that required only a 286-mer DNA strand.[39] However, this could pose a limitation when a longer strand is needed

for a more complicated structure. To avoid such problem, a DNA-minimal 'clip-by-clip' approach was demonstrated by the Sleiman group to build DNA prisms.[40] Each DNA clip was designed so that its two ends can be brought together by hybridization with the back edge of the next clip. To form a cube, the two ends of the fourth clip were designed to be complementary to the back edge of the first clip (Figure 1.3h). Importantly, all single-stranded segments on the prisms can have unique sequences, which are useful for anisotropic functionalization.

1.2.3.2 Dense DNA structures

Inspired by the scaffolding strategy[31, 41], Rothemund reported an elegant concept called DNA origami, which significantly increased the complexity of DNA nanostructures.[36] The folding of a 7-kilobase single-stranded DNA strand was guided by hundreds of unique staples, which were short DNA single strands, into a variety of 2D objects such as rectangles, stars, and smiley faces (Figure 1.4a).[36] Importantly, a large excess of unpurified staples can be tolerated by this technique, which eliminates the need of purified DNA strands and perfect stoichiometric concentrations. Patterning on DNA origami object can be easily done as staple sequences are all unique. In addition, hollow 3D objects such as DNA tetrahedron[42] and DNA box[43] were created by folding flat DNA origami sheets.

Shih, Yan and others have extended DNA origami into 3D.[44] Multilayer DNA origami design is based on layering a sheet of continuous helices into honeycomb[45], square[46] and hexagonal[47] lattices, which allow the crossover connections of one DNA helix to its 3, 4 and 5 neighboring helices (Figure 1.4b). Higher connection symmetry led to higher helical packing density and stronger resistance to mechanical forces. Twist and curvature in DNA origami could be introduced by an insertion/deletion of base pairs, which altered the distances between crossovers points (Figure 1.4c).[48] Another strategy to create highly curved, hollow 3D objects such as a nanoflask involves an alteration of positions and patterns of crossover points between layers of concentric rings (Figure 1.4d).[49]

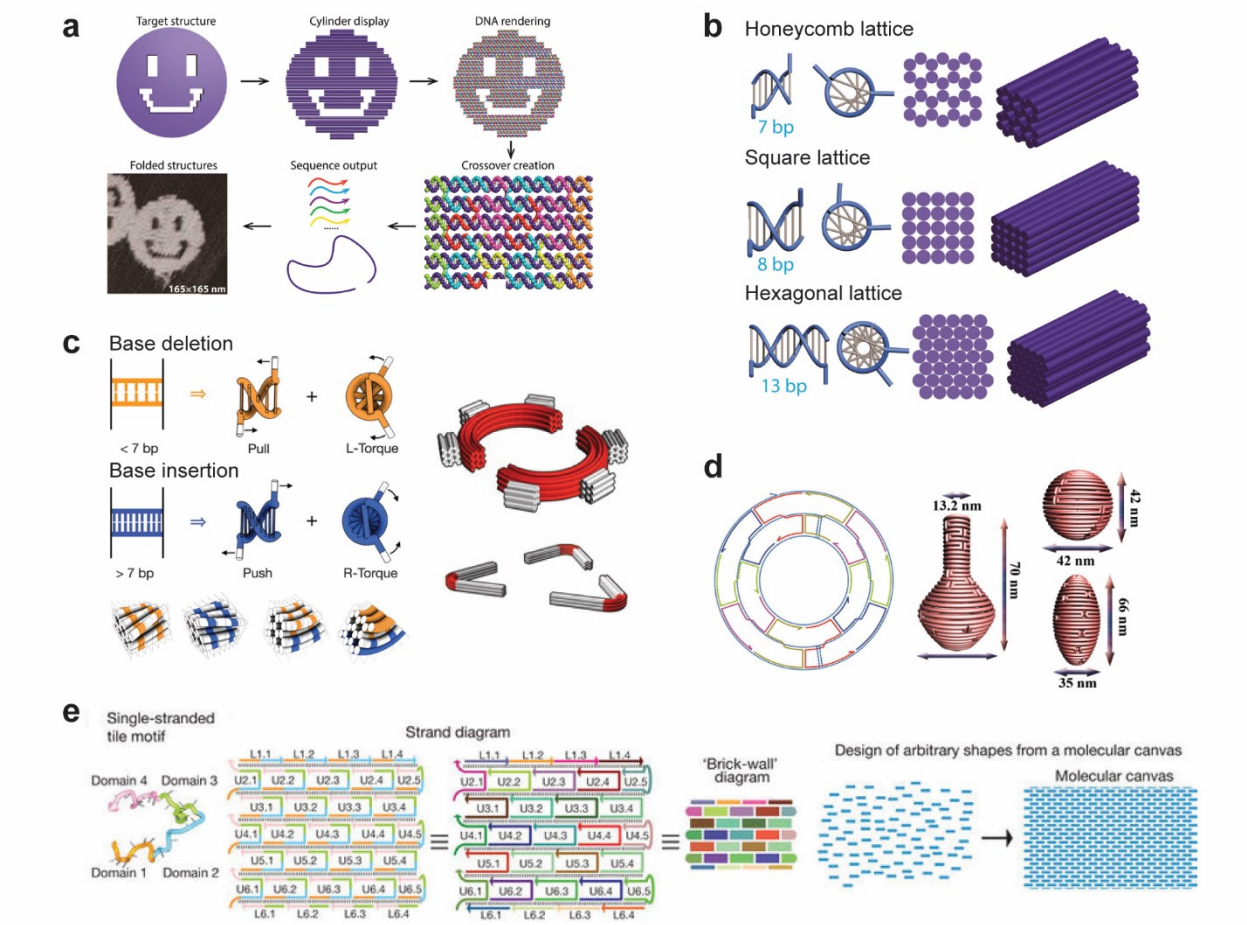

Figure 1.4 | Dense DNA structures. a) Folding of a long scaffold with hundreds of short staples into an arbitrary shape. b) Helical-packing strategies for multilayer DNA origami. Adapted with permission from reference 44 (ACS, 2017). c) Twist and curvature introduction by base deletion/insertion strategy. Adapted with permission from reference 48 (AAAS, 2009). d) Concentric-ring strategy for highly-curved objects. Adapted with permission from reference 49 (AAAS, 2011). e) Scaffold-free single-stranded tiles for an arbitrary shape design. Adapted with permission from reference 50 (NPG, 2012).

As a complementary approach to DNA origami, the Yin's group introduced the concept of single-stranded DNA tiles, which created objects with similar complexity to DNA origami without the need for a scaffold.[50] The basic motifs were DNA single strands containing four modular domains. It can form interconnected staggered duplexes with one another, resulting in DNA lattices. As sequences were all unique, these 3x7 nm motifs can be used as a molecular canvas where one can make any arbitrary shape by selecting a set of strands which defines the structure (Figure 1.4e). This approach was later extended into 3D, analogous to Lego bricks.[51]

DNA origami has become the state-of-the-art approach in DNA nanotechnology owing to its versatility.[52] The computer-aided design process is also user-friendly and highly automated.[53-54] Still, there are some challenges before translating DNA origami into practical and scalable use. In many cases, most strand components serve purely for a structural purpose, and only some are used for functionality. Niekamp and Douglas addressed this by redesigning a scaffold strand that could be folded with the repetitive binding of as few as 10 unique staple sequences, which significantly simplified the design and reduced synthesis cost.[55] In addition, the assembly of more complex structures typically requires high Mg^{2+} concentrations and extremely long folding times (up to a week). As such, several application-friendly conditions were examined such as an assembly in Na^{+}-based solution[56] and a rapid isothermal assembly either optimized from hybridization kinetics[57] or in the presence of chemical additives[58-59] and deep-eutectic solvent[60].

1.2.4 Extended DNA Assembly

Another major class of DNA nanostructures is extended periodic and aperiodic DNA arrays. Their formation typically involves hierarchical assembly of DNA motifs through sticky-end cohesion. Although their growth is mostly uncontrollable, extended DNA arrays up to microscopic size can serve as addressable scaffolds with a large surface area for material periodic organization.

The double crossover DX structure was the first motif to be successfully generated into 2D periodic lattices. This was mediated by the cohesion of complementary sticky ends extended from different DX units (Figure 1.5a).[25] Since then, several groups have developed new motifs with different morphologies and complexities to gain better control of the final assembly such as cross-shaped tiles[20], tensegrity triangles[21], six-helix bundles[23], and to name a few. As a step towards DNA networks for protein crystallography, the first macroscopic DNA crystal was shown by Seeman and co-workers.[61] Rhombohedral 3D DNA crystals with the dimension of more than 250 μm were assembled from tensegrity triangles (Figure 1.5b). A sticky-end extension from the motifs also allowed dynamic incorporation of fluorescent dyes in the crystals.[62] It is of note that the DNA sequences in these motifs are all unique, enabling a simple but powerful access to site-specific functionalization on these networks.

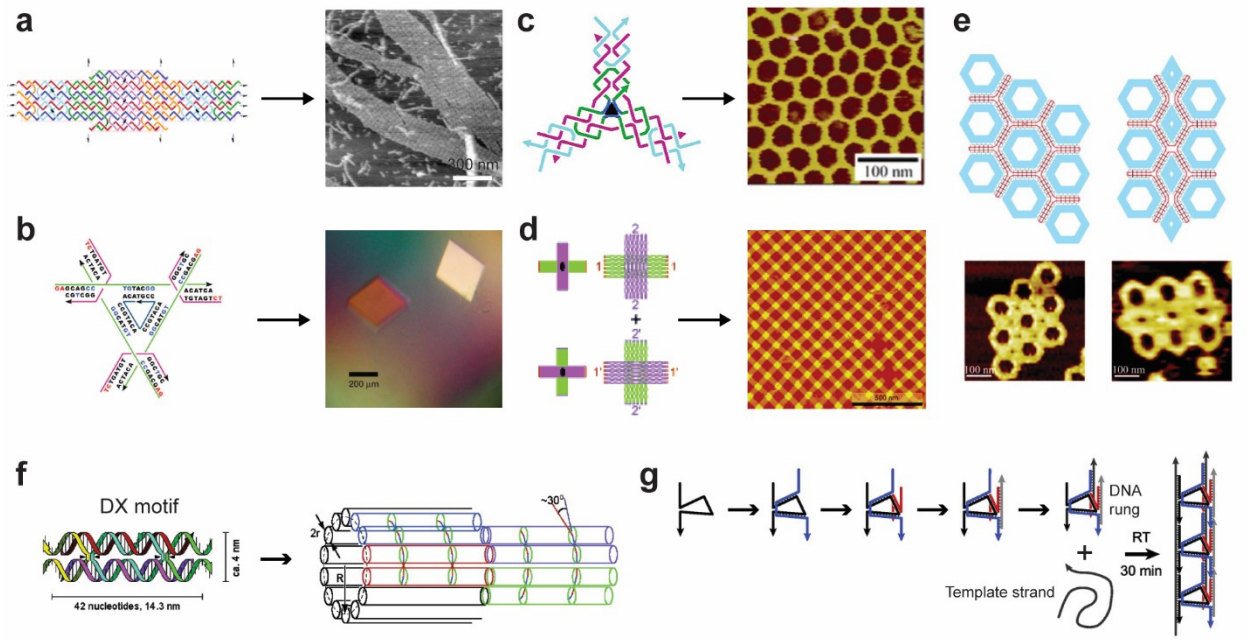

Figure 1.5 | DNA lattices and DNA nanotubes. a) 2D periodic lattices from the hierarchical assembly of DX motifs. Adapted with permission from reference 25 (NPG, 1998). b) Macroscopic DNA crystals constructed from tensegrity triangles. Adapted with permission from reference 61 (NPG, 2009). c) 2D hexagonal arrays from the hierarchical assembly of 3PS motifs. Adapted with permission from reference 22 (ACS, 2005). d) 2D crystalline arrays from the hierarchal assembly of cross-shaped DNA tiles. Adapted with permission from reference 70 (Wiley-VCH, 2010). e) 'Origami of origami' strategy for sized-defined, complex 2D arrays. Adapted with permission from reference 72 (ACS, 2011). f) DNA nanotubes generated from the intrinsic curvature of DX motifs. Adapted with permission from reference 76 (ACS, 2004). g) Modular nanotube construction by attaching DNA rungs on a template strand. Adapted with permission from reference 81 (ACS, 2013).

As the DNA motifs become more complicated, more unique DNA sequences will be required. However, sequence asymmetry (i. e., the use of DNA strands of different sequences) in the motifs is not always necessary. A design strategy that can reduce the number of different sequences but can retain the desired geometry would be highly useful. To address this, the Mao group applied a sequence symmetry approach in the array design. For example, the three-point star (3PS) motif containing seven strands of three different sequences can assemble into hexagonal porous 2D arrays (Figure 1.5c).[22] Similarly, four-point star motifs of nine strands formed square lattices[63], while six-point star motifs from thirteen strands led to crystalline arrays with triangular and hexagonal pores.[64] They also found that the motif flexibility can affect the assembly behavior, where too stiff and too flexible motifs yielded structures of lower quality.[65]

Other challenges in the hierarchical assembly from DNA motifs include the need to reduce numbers of DNA strand components, the construction of aperiodic lattices, and the sized-defined growth. Firstly, to approach the number limit, the Mao group showed that one symmetric DNA strand can generate extended arrays through T junctions.[66] Secondly, to introduce aperiodicity, Rothemund and Winfree applied an algorithmic assembly to construct Sierpinski triangles from DX motifs by modulating their binding affinity through sticky-end sequences, selective motif association through cooperative binding events, and controlled nucleation guided by a template DNA strand.[67] Another example used templating approach to create 'barcode' ribbon lattices from two types of DX motifs.[41] Finally, to control the size of arrays, a straightforward strategy was to redesign all sequences of sticky ends to be completely unique.[68] Sequence number could also be reduced through the hierarchical assembly where the formation of multiple substructures could share a set of sequences.[68-69]

Apart from small-motif units, DNA origami has been assembled into hierarchical structures. Small DX motifs were replaced with cross-shaped origami tiles to produce crystalline grid-like arrays (Figure 1.5d).[70] To further control the growth and complexity of DNA origami arrays, the group of Yan and Liu replaced conventional staples with more complex structures. Serving as a sized-defined frame, the scaffold strand was able to bring multiple tiles to form 5x5 and 7x8 arrays.[71] DNA origami themselves can also be folded into predefined framework to organize smaller DNA origami, thus creating 'origami of origami' superstructures (Figure 1.5e).[72]

Nanotubes, a class of 1D nanostructures, have received great interest due to their high aspect ratio and continuous cavity that are suitable for templating, material organization and molecular encapsulation.[73] Several strategies based on rolling of 2D DNA arrays into nanotubes were reported.[74-75] As an example, Rothemund and Winfree showed that DNA nanotubes could be constructed by employing the intrinsic curvature of DX motifs (Figure 1.5f).[76] To reduce the number of strands, nanotube assembly from DX-like motifs consisting of two identical DNA single strands was demonstrated by Liu and co-workers.[77] Additionally, it is of note that many efforts have been made to control geometrical parameters of DNA nanotubes. DNA helix bundles[23]and single-stranded tiles[78] were shown to generate nanotubes with defined diameters. A templating approach was adopted by the Sleiman group to control the nanotube growth by binding multiple

DNA rungs on a size-controlled DNA single strand containing repeating rung-binding regions (Figure 1.5g).[79-82]

1.2.5 Templated assembly for material organization

The unique feature of DNA nanostructures is their high templating potential from small molecules to nanoparticles and proteins.[44, 83-84]As representative examples, several groups have organized individual gold nanoparticles into predefined patterns. Alivisatos and co-workers reported 1D discrete structures, where predetermined numbers of gold clusters were organized on a single-stranded DNA template.[85] They later designed 3D chiral tetrahedral structures containing four gold nanoparticles (Figure 1.6a).[86] As well, more complex patterning of nanoparticles to obtain novel optical properties can be achieved with DNA origami.[87-88] More recently, DNA patterns were transferred onto a gold nanoparticle's surface by using DNA 'nanostamps'. These open an exciting avenue to create highly asymmetric nanoparticles with molecular recognition properties (Figure 1.6b).[89-90]

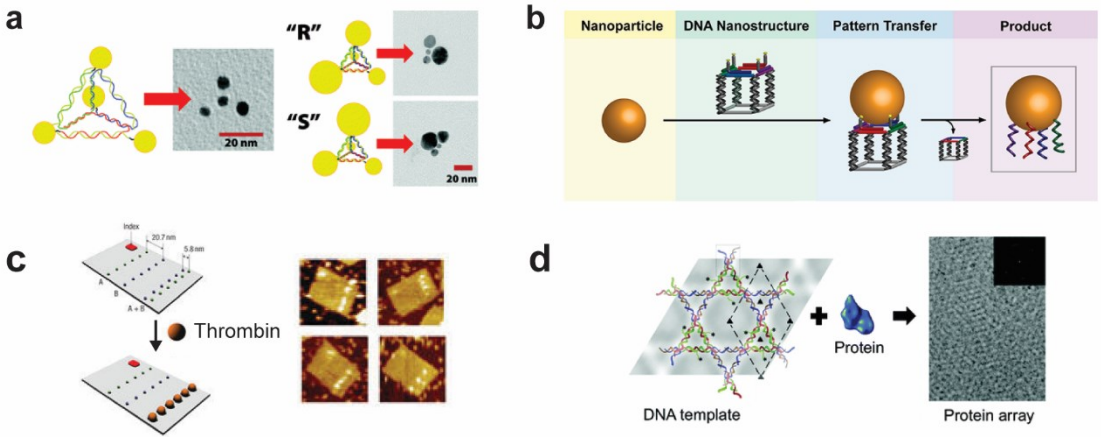

Figure 1.6 | Material organization on DNA structures. a) Chiral DNA/gold-nanoparticle tetrahedron constructed from four DNA strands monoconjugated with gold nanoparticles.[86] Reproduced with permission from reference 86 (ACS, 2009). b) 2D DNA pattern transfer from DNA cube to gold nanoparticle. Adapted with permission from reference 89 (NPG, 2016). c) Distance-dependent biding of thrombin on DNA tiles functionalized with two types of thrombin-binding aptamers. Adapted with permission from reference 93 (NPG, 2008). d) Protein templating on ordered DNA arrays for molecular imaging with cryo-electron microscopy. Reproduced with permission from reference 96 (ACS, 2011).

Protein organization has attracted a great deal of attention due to its substantial role in biological systems. 2D multiprotein arrays with precise spatial resolution can be easily created by incorporating protein-binding ligands at specific positions on DNA nanostructures.[91-92] This high structural control can lead to a systematic study of protein interactions. The Yan group, for example, investigated the multivalent binding of thrombin to two types of aptamers on DNA tiles.[93] The inter-aptamer distance could be precisely controlled by attaching aptamers at different positions on the tiles (Figure 1.6c). The distance-dependent activity of an enzyme pair could be studied in a similar way.[94] Additionally, structural characterizations of proteins can be aided by DNA assembly.[95-96] To increase the protein density, Turberfield and co-workers templated membrane proteins on 2D trigonal arrays and were able to improve the imaging efficiency on cryo-electron microscopy (Figure 1.6d).[96]

1.3 Dynamic DNA assembly

The dynamic character of DNA can be highly advantageous in functional systems that perform precise tasks in response to stimuli. Within this context, strand displacement has been widely applied to program dynamic motion in DNA nanostructures, leading to many stimuli-responsive DNA systems, DNA machines, and DNA computing tools.[97] The mechanism of strand displacement is shown in Figure 1.7a. If a DNA strand **a-b** is hybridized to a shorter complementary strand **a'**, then a duplex will form with single-stranded 'overhangs' or 'toeholds' **b**. When a fully complementary 'input' strand **b'-a'** is added, 'output' strand **a'** is displaced to yield a fully complementary, longer duplex. This process occurs rapidly and in quantitative yields with overhangs above 6 bases.[98]

The groups of Turberfield and Yurke demonstrated the first use of strand displacement to operate a conformational change of molecular DNA tweezer.[99] This tweezer was closed by addition of input strand, $\boldsymbol{F}$**,** which bound to its two arms. Addition of another input strand, $\overline{\boldsymbol{F}}$**,** removed the first input strand and opened the tweezer (Figure 1.7b). Yan and Seeman then extended this concept to perform a larger-scale mechanical motion on rotatable DNA device, where DNA structures on 1D arrays could be reversibly rotated up and down by using input strands.[100] As an example in 3D structures, the Sleiman group designed a triangular prism that

could switch between three predetermined sizes merely by controlling the length of linking regions (Figure 1.7c). Since then, even more complex motion of DNA machines has been reported, such as a DNA walker that can move and collect cargo[101] or perform a series of organic syntheses[102] along the track.

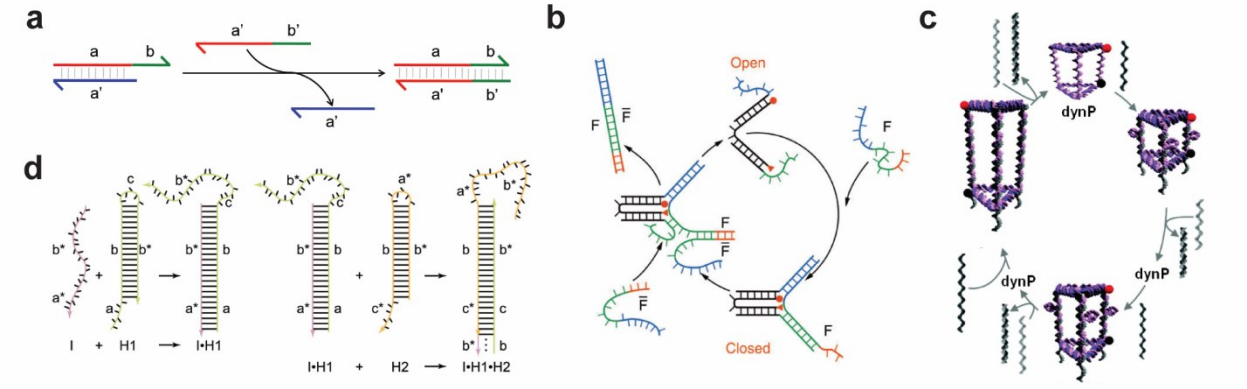

Figure 1.7 | Dynamic DNA assembly. a) Strand displacement strategy where **b'-a'** input strand binds to duplex **a'**:**a-b** and removes **a'**, to form new duplex **b'-a'**:**a-b**. b) Stimuli-responsive molecular DNA tweezer that operated via strand displacement mechanism. Reproduced with permission from reference 99 (NPG, 2000) c) Reversible size-switching of triangular prism. Adapted with permission from reference 35 (ACS, 2007). d) Hybridization chain reaction from the repeated triggered opening of hairpin DNA. Adapted with permission from reference 104 (NAS, 2004).

DNA stimuli can be manipulated in an analogous way for logic-gate signal processing by dynamic DNA assembly.[103] The hybridization chain reaction was developed for signal amplification, where the transducer contained two species of hairpin DNA (**H1** and **H2**) and could repeatedly assemble with the trigger from input strand, **I** (Figure 1.7d).[104] As well, dynamic assembly can be applied to release cargo molecules from DNA nanostructures. The Sleiman group demonstrated this concept through the stimuli-responsive release of gold nanoparticles from DNA nanotubes[105] and the conditional unzipping of DNA cube that can recognize a cancer-specific gene product[106].

Therefore, DNA nanotechnology has presented a great opportunity to efficiently create designer structures that fulfill both structural and dynamic requirements, leading to their exploration as programmable materials in many research fields such as nanoelectronics, biophysics, biomedical engineering and DNA computing.[107] Very importantly, DNA assembly has

fruitfully adopted two construction concepts from biological systems discussed in Section 1.1: i) the sequence programmability allows selective association of DNA strands into target structures and ii) the rigidity and addressability of DNA frameworks provide 3D positioning of functional units that can be organized into hierarchical structures or template other materials into predesigned patterns. Some challenges in this field include the cost of DNA synthesis, which makes scaling-up of this technology difficult, and the complexity/error issue.

1.4 Supramolecular DNA assembly

Biological systems rely on many interactions to achieve order and build their functional structures. Over the last 50 years, supramolecular chemistry has taken advantage of these multiple non-covalent interactions to assemble materials with exquisite control over geometry and function. While DNA assembly follows the sequences of DNA components, Watson-Crick base-pairing is the only driving force. Thus, an incorporation of supramolecular interactions which are orthogonal to DNA base-pairing is an attractive approach to expand assembly languages of DNA, and one might expect new assembly modes which would not be solely possible from a single type of interactions.

1.4.1 Non-Watson-Crick interactions in hierarchical DNA assembly

The interaction toolbox of DNA assembly using unmodified DNA strands is not only limited to Watson-Crick base-pairing. It is only recently that the blunt-end stacking by π–π stacking of the terminal base-pairs between two structures has become one of the simplest yet powerful tools for selective assembly of DNA nanostructures. The Sugiyama's group applied this concept, together with Watson-Crick base-pairing and shape complementarity, to program a selective 'lock-and-key' arrangement of 'DNA jigsaw pieces' made of DNA origami into 1D and 2D arrays (Figure 1.8a).[108-109] 3D hierarchical assembly mediated by shape complementarity through blunt-end stacking was demonstrated by Dietz and co-workers.[110] This dynamic conformational switching could be selectively shifted by merely altering cation concentration and temperature (Figure 1.8b). A systematic engineering of blunt-end stacking was investigated by Woo and

Rothemund, showing that the stacking bond was sequence- and number-dependent, and showed stacking polarity, a similar concept to the polarity of DNA strands.[111]

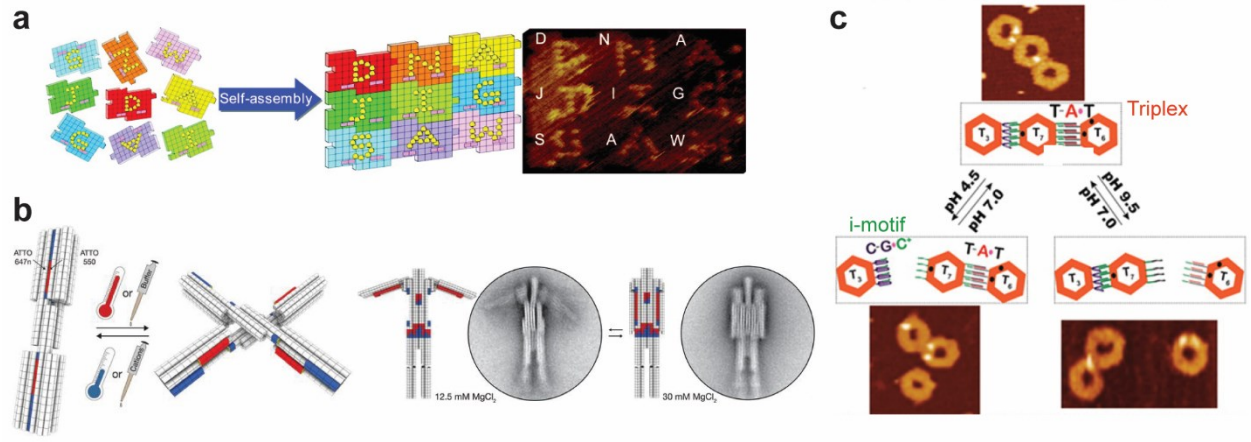

Figure 1.8 | Non-Watson-Crick interactions in hierarchical DNA assembly. a) 'Lock-and-key' assembly of DNA Jigsaws mediated by blunt-end and base-pairing interactions. Reproduced with permission from reference 109 (ACS, 2010). b) Dynamic motions of 3D shape-complementary DNA nanostructures by blunt-end stacking. Adapted with permission from reference 110 (AAAS, 2015). c) The pH-dependent oligomerization of DNA hexagons incorporated with i-motif and triplex-forming domains. Adapted with permission from reference 115 (ACS, 2016).

In the context of noncanonical B-DNA base-pairing, some hydrogen-bond motifs between nucleobases have been incorporated into DNA nanostructure designs. An i-motif, which is a tetraplex of interdigitated C·CH$^+$ pairs, can occur in C-rich sequences under acidic pH.[112] Liu *et al.* prepared a pH-responsive hydrogel from the i-motif-bearing 3WJs.[113] Another interesting conformation is a DNA triplex, consisting of a homopurine/homopyrimidine duplex that is able to form Hoogsteen base-pairing with another single-stranded DNA.[114] Wu and Willner applied triplex formation to control reversible, pH-dependent dimer- and trimer-formation of DNA hexagons (Figure 1.8c).[115]

1.4.2 Synthetic insertion for DNA assembly and stability

Supramolecular chemistry uses branched units to construct discrete self-assembled structures. The guiding information in these structures, including defined angles and branching degree, are usually provided by rigid synthetic building blocks.[116] Inspired by this concept, many synthetic

molecules have been inserted into DNA by several research groups to direct DNA assembly and improve the structural stability.

1.4.2.1 Organic vertices

Using rigid organic molecules to provide directional control was demonstrated by Shi and Bergstrom.[117] Two self-complementary DNA strands were attached to a tetrahedral carbon center with rigid arms. These branched DNA can self-assemble into a set of discrete macrocycles ranging from dimer to heptamer (Figure 1.9a). The Sleiman group applied this concept to assemble discrete 2D and 3D structures by using a rigid triaryl vertex. In one work, six DNA strands containing the linker in the middle were used to generate a DNA hexagon, which could be used to template individual gold nanoparticles into discrete assembly (Figure 1.9b).[118] This strategy has been extended to construct 2D DNA polygons as precursors for 3D assembly.[35, 80, 105, 119] Interestingly as well, inserting organic vertices could increase the duplex stability and direct the assembled product distribution.[120] Dimer formation from two complementary strands was favored by flexible linkers, while rigid linkers resulted in oligomerization. In this case, the assembly selectivity could be contributed by linker structures and linker-to-DNA connectivity. It was also found that there was a higher melting cooperativity when organic vertices were inserted in DNA duplexes.[120-122]

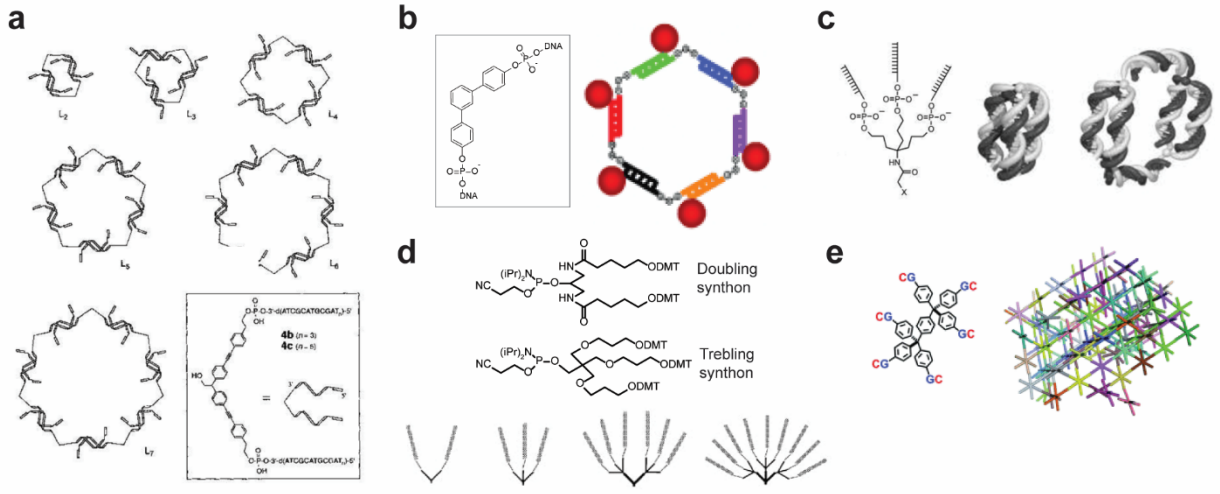

Figure 1.9 | Insertion of organic vertices. a) Discrete macrocycles created from the assembly of self-complementary branched DNA motifs. Reproduced with permission from reference 117 (Wiley-VCH, 1997). b) Templated gold-nanoparticle assembly on DNA hexagon. Adapted with permission from reference 118 (Wiley-VCH, 2006). c) Wireframe cages constructed from DNA

3WJs using alkyl tris-linker as the core. Adapted with permission from reference 123 (Wiley-VCH, 1999). d) Organic branched molecules for synthesizing dendritic DNA structures. Adapted with permission from reference 130 (OUP, 1999). e) Network formation of branched units containing multiple copies of GC dinucleotides. Adapted with permission from reference 132 (Wiley-VCH, 2011).

A variety of branched DNA motifs has been designed by incorporating branched organic linkers to DNA strands. The von Kiedrowski group synthesized 3WJs by attaching identical DNA strands to alkyl tris-linkers, and were able to create a wireframe cage from two complementary junctions (Figure 1.9c).[123] Since then, many tris-linker designs have been shown to change core flexibility, to control DNA sequences and to modulate the assembly behavior of the resulting 3WJs.[124-128] As an attempt to construct a single and well-defined nanostructure, Zimmermann *et al.* reported the assembly of DNA dodecahedron by using 20 different 3WJs.[129]

Higher branching degree typically results in ill-defined yet highly stable networked structures through multivalent interactions. Shchepinov *et al*. attached multiple DNA strands (from 2 to 27) to an organic dendron core (Figure 1.9d).[130] The assembly of these dendrimers showed higher thermal stability compared to same-length linear duplexes. Interestingly, the Richert group was able to increase the association strength of extremely short GC dinucleotides by attaching them on rigid linkers with 4-8 arms, creating a solid formation that was stable at high temperature (Figure 1.9e).[131-133] Finally, to control the network formation, Hong and Nguyen synthesized size-tunable nanoparticles from the assembly of two complementary 4WJs. Their size control was dependent on concentration and assembly time.[134]

1.4.2.2 Metal-coordination complexes

Another important research area in synthetic DNA insertions focuses on metal incorporation with an aim to bring many intrinsic properties of metal ions into DNA assembly. The duplex stability can be enhanced even in unmodified DNA with the selective binding of Ag(I) or Hg(II) to mismatched pyrimidine base pairs.[135] Importantly, the metal-coordination complex is highly directional with a range of coordination geometries, and different choices of metals can impart novel functions such as catalytic, electronic and magnetic properties into DNA structures.

Two main approaches have been developed to site-specifically incorporate metal ions into DNA. The first approach involves a modification of DNA bases with metal-binding ligands. The Shionoya group replaced natural nucleobases with hydroxypyridone nucleobase.[136] In the presence of Cu^{2+}, DNA duplexes containing 1-5 modified nucleobases can form a stable square-planar complex with Cu^{2+}. Different metal ions could also be stacked on top of one another inside the duplexes by various types of modifications on nucleobases (Figure 1.10a).[137] A great variety of modifications was also demonstrated with this approach[138-141] The second approach is to covalently attach metal-binding units directly to a DNA backbone. Several groups have designed ligands and tethered them to DNA strands.[142-145] Inspired by the design of supramolecular catenane complexes,[146] the Sleiman group showed the DNA-templated creation of three different ligand environments, each selective for a specific transition metal ion, from a combination of phenanthroline and terpyridine (Figure 1.10b).[145] Furthermore, metal binding has been shown to profoundly stabilize DNA duplexes[140, 145] as well as branched DNA motifs[144, 147].

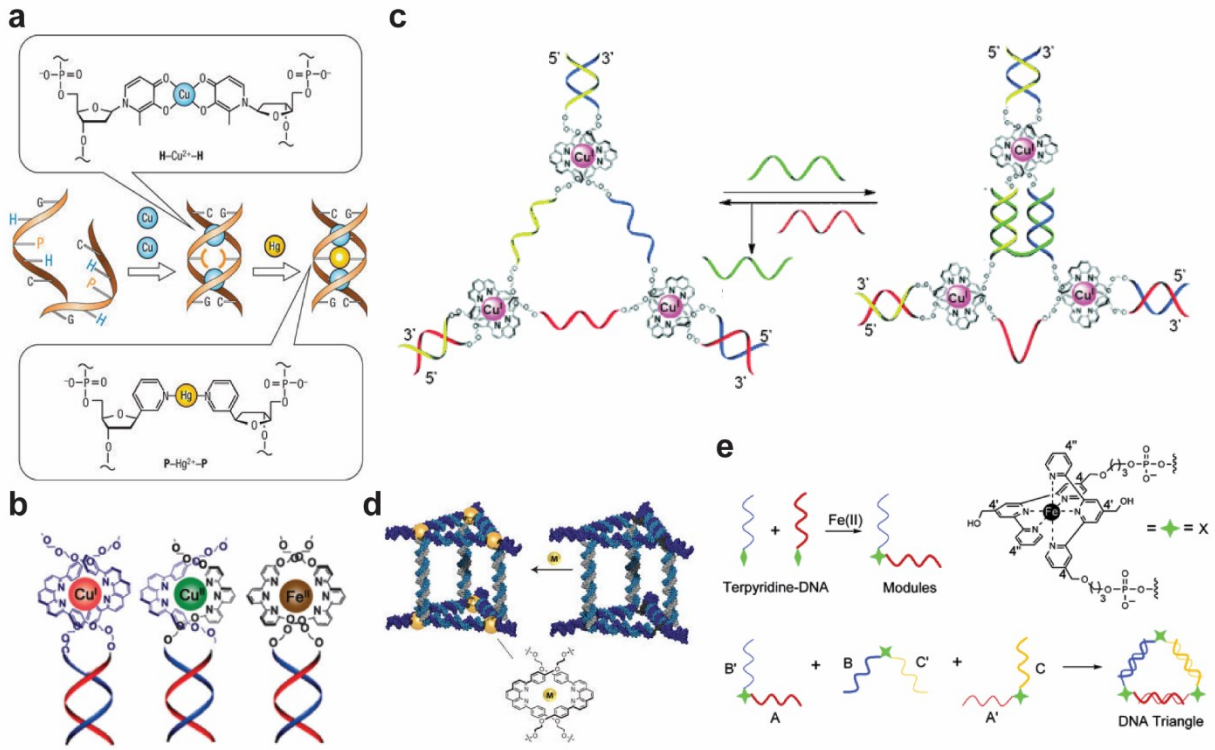

Figure 1.10 | Metal-coordination complexes. a) Multimetal array in artificial DNA duplex. Reproduced with permission from reference 137 (NPG, 2006). b) DNA-templated creation of three ligand environments to incorporate three different reactive transition metals. Adapted with permission from reference 145 (Wiley-VCH, 2009). c) Dynamic metallic DNA nanostructures

containing three Cu(I) complexes at the corners. Adapted with permission from reference 144 (Wiley-VCH, 2008). d) Metal-nucleic acid cage with the site-specific incorporation of transition metals in the vertices. Adapted with permission from reference 152 (NPG, 2009). e) Assembly of DNA triangle from metal-coordination-driven branched DNA motifs. Reproduced with permission from reference 153 (ACS, 2004).

There are two main approaches that create metal-DNA components for hierarchical DNA assembly. A more popular approach uses DNA hybridization to guide a connection of multiple metal-DNA branched motifs and to preorganize organic ligands into a suitable coordination environment for metal binding. As an early example, ruthenium complexes were tethered in the middle of DNA strands that could assemble into 1D polymers[148] and discrete cyclic structures.[149] DNA-templated formation of metal-salen complexes has been shown to generate covalently-linked linear and branched DNA oligomers.[126] The McLaughlin group demonstrated the formation of larger DNA networks from branched junctions with four[150] and six[151] DNA arms connected to the metal-complex cores. With the goal to introduce a dynamic behavior in metal/DNA nanostructures, Yang and Sleiman prepared a DNA triangle containing three Cu(I) coordination sites at its corner. The distance between two metal centers can be reversibly controlled by adding specific DNA strands (Figure 1.10c).[144] They further expanded this strategy to build a 3D metal-DNA cage with the site-specific incorporation of transition metals in its vertices (Figure 1.10d).[152] On the other hand, the second approach uses metal coordination to build hierarchical DNA structures from individual strand functionalized with the ligands. Choi and co-workers appended terpyridine units to the 3'-end of two complementary DNA strands that can create 2WJ motifs in the presence of Fe(II). Discrete DNA triangles can be assembled from these motifs by programming their sequences in a quantitative yield (Figure 1.10e).[153] This approach is still unexplored, and there have been only a few examples reported since the work of Choi.[154-156]

The design of DNA nanostructures with symmetrical or repeating sequences is challenging as this can lead to assembly errors, particularly in complex structures. As an alternative approach to address such problems, the synthetic incorporation can profoundly impact DNA stability and self-assembly by introducing new structural requirements and orthogonal interactions to change the outcome and selectivity of DNA self-assembly. In addition, there are other small molecules that can potentially endow dynamic, stimuli-responsive properties to DNA nanostructures, which is beyond the scope of this section.[157]

1.4.3 Supramolecular organization of amphiphilic DNA materials

Amphiphiles are molecules that contain hydrophilic and hydrophobic components within the same structure. In aqueous solution, there is a strong aggregation tendency of hydrophobic components, forming hydrophobic/hydrophilic core/shell structures. Their morphologies such as spherical micelles, cylindrical micelles, and vesicles, could be dictated by the packing parameter, which is defined as the core volume of hydrophobic component divided by the length of hydrophobic component and the cross-sectional area occupied by hydrophilic corona component.[158-159] Thus, DNA modification with hydrophobic moieties is an attractive approach to bring amphiphilic properties into DNA assembly, providing an alternative way to combine the hierarchical and long-range organization mediated by hydrophobic interactions with the programmability and anisotropy provided by DNA.

1.4.3.1 DNA-lipid and dendron conjugates

A variety of DNA-lipid conjugates, such as long-chain fatty acids, diacylglycerol, cholesterol, and tocopherol has been explored primarily for their potential use in delivering nucleic acid therapeutics.[160] Many of these materials self-assemble into spherical micelles with DNA strands as their corona. The Tan group prepared phospholipid-like amphiphiles containing DNA and two C18 alkyl tails.[161-162] Homogenous size of the micelles could be tuned by changing DNA strand's length, and these micelles were efficiently taken up by cells. Regarding the stability, Bergstrom and co-workers showed that there was a significant increase in the melting temperatures of self-complementary DNA duplexes terminally modified with C12 alkyl chains.[163] Depending on their position and number, the alkyl chains could stabilize DNA duplexes by a combination of CH-π stacking interactions, hydrophobic interactions between alkyl chains and shielding of hydrogen bonds on terminal base pairs. Other morphological self-assemblies of DNA-lipid conjugates have also been reported such as vesicles and three-dimensional networks.[164-166] Interestingly, manipulating DNA corona provides a reversible switching mechanism between vesicles and micelles.[167] Vesicle formation is favorable when short DNA strands were attached to two C18 alkyl chains. The hybridization with complementary, longer DNA strands could induce shape-shifting to smaller micelles (Figure 1.11a), which could be converted back by strand displacement.

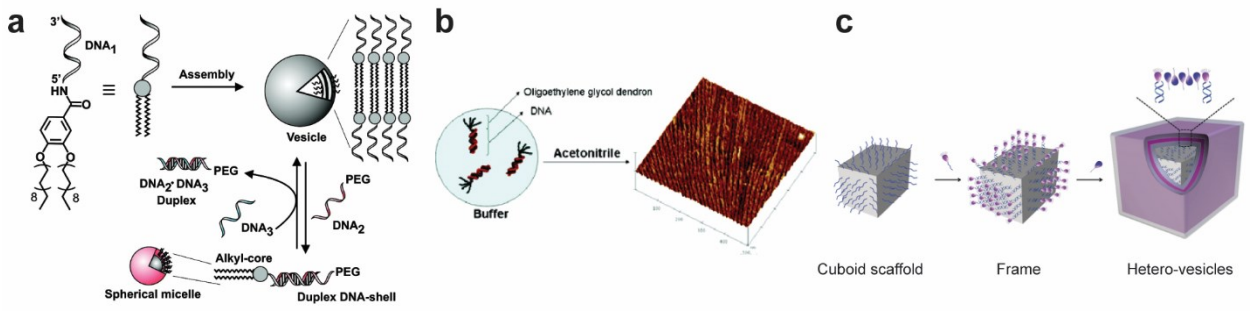

Figure 1.11 | Self-assembly and dynamic behaviors of DNA-small molecule conjugates. a) Reversible switching between vesicles and micelles by manipulating their hydrophobic corona. Adapted with permission from reference 167 (ACS, 2010). b) Long-range assembly into fibers and 2D networks from DNA duplexes with dendritic oligo(ethylene glycol). Adapted with permission from reference 168 (ACS, 2009). c) Templated heterovesicle formation of DNA-dendron conjugates on frame materials. Adapted with permission from reference 172 (Wiley-VCH, 2017).

Another interesting structure of low-molecular-weight DNA modifications is a dendrimer, due to its high density of surface functional group. Sleiman and co-workers attached dendritic hydrophobic oligo(ethylene glycol) units on short DNA duplexes, which dramatically changed their long-range self-assembly. These hybrid duplexes assembled end-to-end, forming long fibers and 2D networks in selective solvents (Figure 1.11b).[168] The Liu group reported the assembly of DNA functionalized with hydrophobic poly(benzyl ether) dendron into nanofibers[169], which could reversibly transform into spherical micelles by tuning assembly conditions[170]. They later prepared heterovesicles by frame-guided assembly strategy using gold nanoparticles[171] and DNA origami[172]. The DNA-dendron conjugates were hybridized to the complementary DNA strands on the frames, resulting in hydrophobically-driven precipitation. An addition of non-complementary DNA-dendron conjugates or other amphiphilic molecules could re-disperse the precipitates and generate asymmetric vesicles along the frame (Figure 1.11c).

1.4.3.2 DNA-polymer conjugates

Block copolymers are an interesting class of polymers in which two or more different polymer chains are attached to one another end to end. These molecules show a range of self-assembled structures, ranging from spheres, cylinders to bilayers and vesicles.[159] As a result, there is a considerable attention to combine DNA with synthetic polymers. Jeong and Park reported an early

example of DNA-polymer assembly.[173] Hydrophobic poly(D,L-lactic-co-glycolic acid) was conjugated to a DNA strand and could self-assemble in aqueous solution into spherical micelles. Due to the biodegradability of PLGA, this micelle exhibited sustained release of DNA strands over time which is a useful delivery platform. Additionally, other copolymer structures have been conjugated to DNA as well. Mirkin and co-workers synthesized comb DNA-polymer conjugates by grafting multiple DNA strands to the polymer chains, which formed extended, aggregated networks upon the hybridization of complementary conjugates.[174] The Li group prepared an alternating copolymer of perylene tetracarboxylic diimide and DNA segments.[175-176] When heated, this polymer exhibited an unusual folding by stacking π-conjugated rings together (Figure 1.12a). The π–π stacking of pyrene units was applied by Häner and co-workers to generate DNA-grafted supramolecular polymers.[177-178]

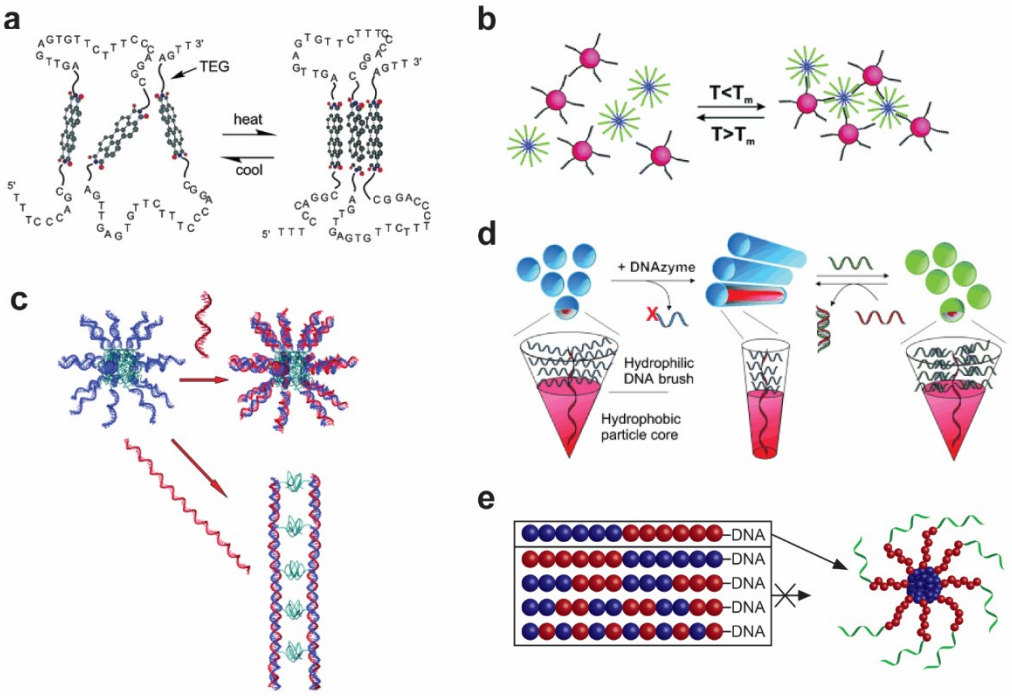

Figure 1.12 | Self-assembly and dynamic behaviors of DNA-polymer conjugates. a) Temperature-dependent folding of DNA/perylene alternating polymers. Adapted with permission from reference 176 (ACS, 2003). b) Temperature-dependent association of DNA-polystyrene micelles. Adapted with permission from reference 179 (ACS, 2004). c) Morphological change of DNA-poly(propylene oxide) micelles in response to DNA stimuli. Adapted with permission from reference 183 (Wiley-VCH, 2007). d) Programmable morphological transition of DNA-brush polymer micelles by using two stimuli. Adapted with permission from reference 184 (Wiley-VCH, 2010). e) Sequence-dependent assembly of sequence-controlled DNA-polymer conjugates containing hydrophobic (blue) and hydrophilic (red) monomers. Adapted with permission from reference 190 (Wiley-VCH, 2014).

Reversible control of micelle aggregation has been demonstrated by Li and Mirkin.[179] Addition of linking DNA strands that were complementary to DNA strands on DNA-polystyrene micelles could bring together individual micelles into the aggregated state. This transition was temperature-dependent, where heating up higher than duplex melting temperature disrupted the aggregation (Figure 1.12b). A similar strategy was applied to reversibly control the aggregation of star polymers containing complementary DNA sequences, and the disaggregation was induced by strand displacement.[180] Within the context of structural stability, the Nguyen group observed an enhanced thermal stability with a sharp melting transition when assembling two DNA-grafted polymers of complementary sequences.[181] In contrast, such behavior was not present when hybridizing with unmodified DNA strands. Subsequent systematic study suggested that the melting cooperativity originated from neighboring-duplex interactions where nearby DNA duplexes shared a condensed cation cloud, while the enhanced stabilization stemmed from a combination of neighboring-duplex interactions, phase separation behavior and multivalency.[182]

Another interesting aspect of DNA-polymer conjugates is their ability to undergo stimuli-responsive morphological conversion. Herrmann and co-workers showed that spherical micelles of DNA-b-poly(propylene oxide) could switch to rod-like micelles when binding them on a long DNA template encoding multiple copies of complementary sequence (Figure 1.12c).[183] The Gianneschi group used two stimuli to control the morphological conversion of DNA-brush copolymer conjugates.[184] Upon DNAzyme addition, the micelles transformed into cylinders. Hybridizing complementary DNA strands to the shortened DNA strands on the cylinders could induce the cylinder-to-micelle transition. This was reversible by adding another DNA strands that were fully complementary to the previously added strands (Figure 1.12d). Other stimuli such as pH and temperature were also reported.[185-186]

All examples above attach polymer chains to DNA through different chemistries such as phosphoramidite chemistry, amide coupling, disulfide formation, Michael addition and Click reaction.[187-188] A recent strategy functionalized a DNA strand with an initiator group, which was then used as a macroinitiator in the polymerization process to generate DNA-polymer conjugates.[189] Another elegant strategy demonstrated by the Sleiman group was to use stepwise solid-phase synthesis to prepare monodisperse, sequence-defined DNA-polymer conjugates.[190]

The chemical nature, number and sequence order of monomer units were important parameters to determine their self-assembly behavior in solution (Figure 1.12e)

1.4.3.3 Hierarchical assembly with 3D DNA scaffolds

Using DNA scaffolds to arrange lipid/polymer chains into an arbitrarily chosen 3D pattern is interesting in the sense that it can direct the association of the non-directional hydrophobic molecules, and at the same time offer a greater control on the hierarchical assembly to achieve the next level of complexity. Cholesterol modification of highly flexible DNA 4WJs was able to force their assembly into 3D crystals, which otherwise usually require stiff and directional unmodified DNA motifs (Figure 1.13a).[191] The Sleiman group demonstrated an entirely new mode of protein-inspired interactions by decorating dendritic alkyl-DNA conjugates on different positions of DNA cube (Figure 1.13b).[192] When four conjugates were organized on one face of the cube, they engaged in an intermolecular association across two cubes, resulting exclusively in a cube dimer. Interestingly, when eight conjugates were organized on the top and bottom faces of the cube, an intramolecular association of these chains occurred inside the cube, forming a monodisperse micelle within a DNA cube that could encapsulate small hydrophobic molecules and release them with added DNA strands.

Stimuli-responsive system has been introduced to generate dynamic hybrid DNA/polymer nanostructures. Spherical aggregates of PEG-DNA can be regularly decorated on DNA nanotubes, creating a striped structure, and can be displaced from the nanotube by adding DNA strands complementary to PEG-DNA conjugates (Figure 1.13c).[193] The O'Reilly group attached poly(*N*-isopropylacrylamide) to DNA tetrahedron, giving the ability to switch between individual tetrahedrons and their aggregated state in response to a temperature change (Figure 1.13d).[194] Simmel and co-workers showed that an intramolecular folding of DNA origami sheet could be achieved by decorating the sheets with cholesterol-DNA conjugates. External stimuli such as surfactant and lipid membrane could unfold the sheets (Figure 1.13e).[195] The selectivity between self-folding and sandwich-like dimerization could be encouraged through adjusting the number and position of hydrophobic units on the surface. Similarly, Zhou and Liu showed the folding of DNA sheets by using DNA-dendron conjugates.[196]

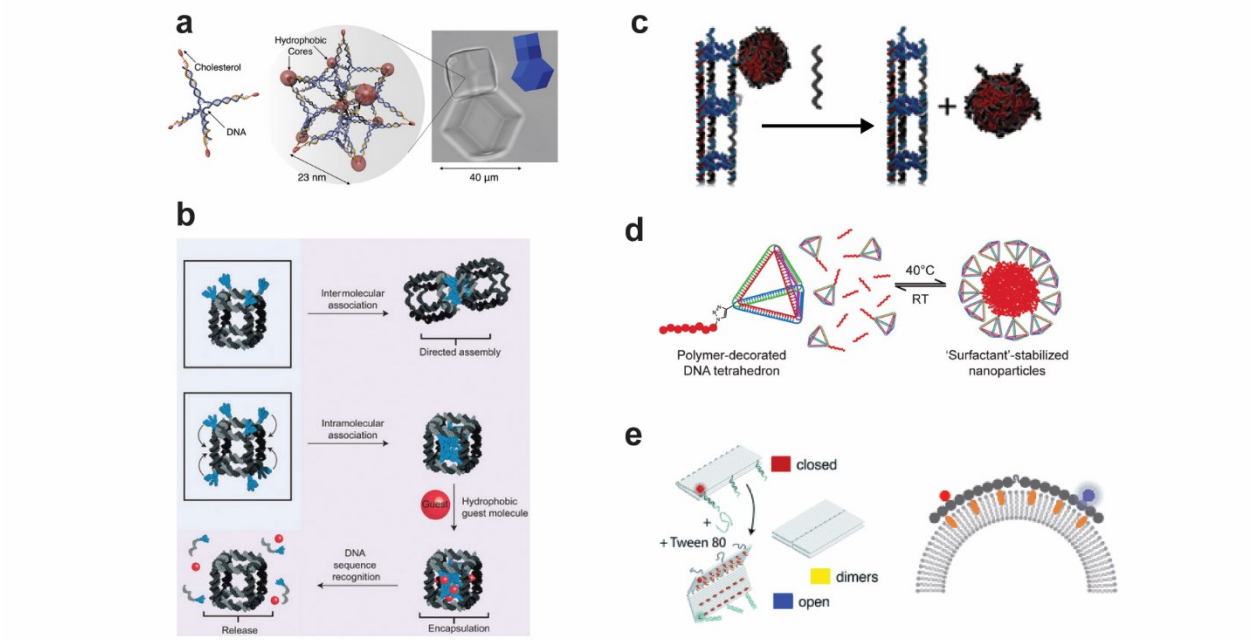

Figure 1.13 | Hierarchical assembly of DNA-polymer conjugates and 3D DNA scaffolds. a) Crystallization of cholesterol-modified DNA 4WJS. Adapted with permission from reference 191 (ACS, 2017). b) Inter- and intramolecular association of dendritic alkyl-DNA conjugates on DNA cubes. Adapted with permission from reference 192 (NPG, 2013). c) Periodic decoration of DNA-PEG micelles on DNA nanotubes. Adapted with permission from reference 193 (RSC, 2012). d) Temperature-responsive aggregation of DNA tetrahedron functionalized with poly(N-isopropylacrylamide). Adapted with permission from reference 194 (ACS, 2013). e) Stimuli-responsive unfolding of self-folded cholesterol-modified DNA origami sheets. Adapted with permission from reference 195 (Wiley VCH, 2014).

DNA assembly is well-known for its capability for precise construction and structural organization, whereas hydrophobic interactions can bring new structures and functions which are far more challenging when using DNA alone. The marriage of the two worlds gives an opportunity to generate hybrid structures that inherit many advantages from the two materials. Although the incorporation of hydrophobic molecules in the design of 3D DNA nanostructures is still in its early stages, many exciting applications have begun to emerge from these hybrid materials, which will be detailed in the next section. Consequently, more design varieties and boarder application scope of DNA hybrid materials can be envisaged in the future.

1.4.4 Amphiphilic DNA nanostructures at work

Given a spectrum of functional and dynamic properties endowed by synthetic modifications discussed earlier, tremendous potential uses of supramolecular DNA hybrid materials can be anticipated in many research fields, from materials sciences to biological sciences and biomedicine. A full discussion of these applications is beyond the scope of this thesis; therefore, this section will be dedicated to the hydrophobically modified DNA nanostructures and their potential biophysical and biomedical applications.

Lipid attachment as described in Section 1.4.3.1 originally aimed to enhance interactions with cells. Interestingly as well, synthetic modifications can improve biological properties of DNA, which is of significance when nucleic acid therapeutics are to be implemented in the clinic. The Sleiman group showed that simple end-modifications such as hexa(ethylene glycol) and 1,6-hexanediol insertions could significantly increase the stability of DNA cages in serum from less than 20 minutes, for simple DNA, to multiple days.[197] More recently, the engineering of DNA cube decorated with dendritic alkyl chains generated a strong binder for albumin, which is an abundant protein that has been used to deliver small-molecule drugs.[198]

Membrane proteins are the important components in cell membranes because of their major roles in cell communication and cargo transport. As such, it is foreseeable that amphiphilic DNA nanostructures will find their ways towards protein-membrane mimicry.[199] To regulate ion or cargo transport, synthetic DNA nanopores have been designed, typically by enclosing parallelly aligned duplexes to form a protected channel.[200-201] The group of Dietz and Simmel created a DNA origami that could attach to one side of the membranes by using multiple cholesterol units and had a stem that can penetrate the bilayers. They observed ion transport across the membranes, and the threading of DNA single strands into the channel can block the ion flux.[200] The Howorka group simplified the nanopore design by using six DNA strands to build six-helix bundles through interconnected crossovers and by modifying the pores with a variety of chemical modifications.[202-203] They later reported an even simpler design of six concatenated DNA strands with a ‘lock’ DNA strand functioning as a gate. Adding the key strand will release the lock strand, thus opening the pore and allowing small-molecule diffusion (Figure 1.14a).[204]

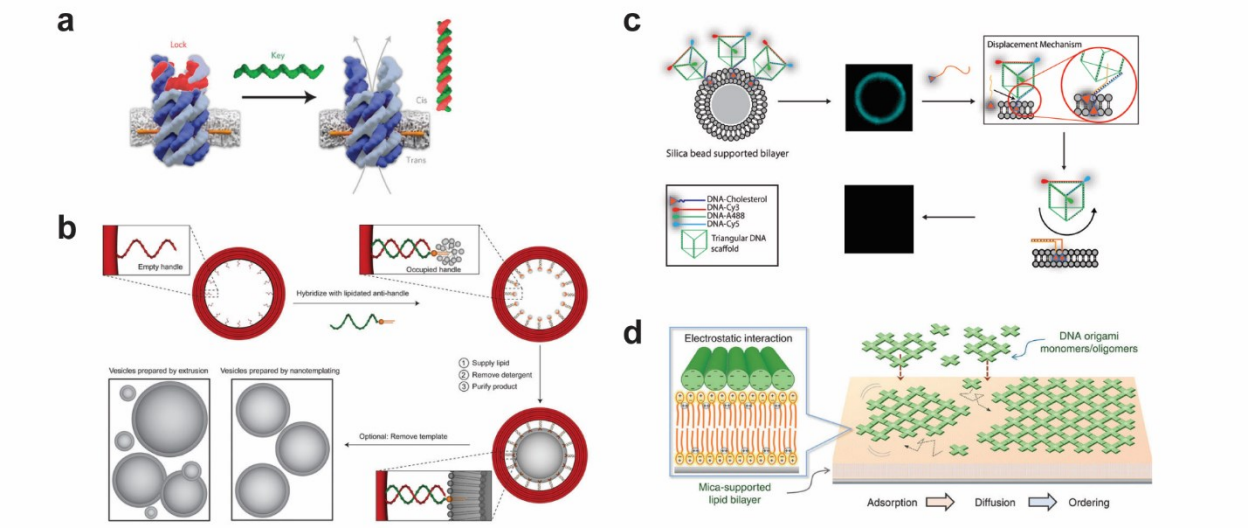

Figure 1.14 | Biophysical and biomedical applications of amphiphilic DNA materials. a) Synthetic DNA nanopore for controlled transport of charged molecules. Adapted with permission from reference 204 (NPG, 2016). b) Templated liposome formation by sized-controlled DNA nanorings. Adapted with permission from reference 205 (NPG, 2016). c) Dynamic interactions of cholesterol-modified DNA cages with the supported lipid bilayer. Adapted with permission from reference 214 (ACS, 2014). d) 2D assembly of DNA origami on supported lipid bilayer. Adapted with permission from reference 216 (NPG, 2015).

The membrane physical properties can be modulated by coating with DNA nanostructures. As a recent example, highly monodisperse and size-defined liposomes can be generated by DNA templating.[205] This involved the binding of DNA-lipid conjugates to rigid DNA rings, serving as nucleation sites. The templated vesicle formation was then initiated by lipid addition (Figure 1.14b). This strategy was later applied to engineer the shapes and dynamics of liposomes by hierarchical assembly of DNA-cage templates.[206] Membrane deformation can also be induced by an oligomerization of rigid DNA monoliths anchored on the lipid vesicle's surface.[207] Additionally, vesicle fusion[208-209] and reversible vesicle aggregation[210-211] mediated by DNA hybridization were also reported. All these examples demonstrate that various roles of membrane proteins can be efficiently mimicked by designer DNA nanostructures.

In bilayer/cell surface engineering, surface-diffusing DNA nanostructures have a great potential as an addressable interfacial platform between solution and membrane surface.[212-213] The Sleiman group examined the dynamic interactions of cholesterol-functionalized DNA cages with supported bilayers.[214] These cages could land on then be lifted off from the bilayers with strand

displacement (Figure 1.14c). Importantly, the free face of the cage can be functionalized with multiple fluorescent dyes, demonstrating its capability to serve as a module for material organization on bilayers. A recent work by Song and Castro's group showed programmable cell-cell adhesion which was mediated by hierarchical assembly of DNA origami anchored on the cell surface.[215] Finally, long-range organization of DNA nanostructures has been demonstrated on supported lipid bilayers (Figure 1.15d).[216-218] It was found that the lipid bilayer increases the order and results in long-range DNA assemblies over microns, which could be useful for surface patterning and material organization on bilayers.

1.5 Context and scope of this thesis

DNA nanotechnology has revolutionized many research areas by offering powerful tools to create objects with arbitrary control of size and shape. The unique sequences of DNA strands within a nanostructure also provide a precise address to position molecules or materials into any geometry. Importantly, these structures use Watson-Crick base-pairing as the primary interaction for programmability and selectivity. However, the efficiency and accuracy of these assembly instructions could reach a limit when the complexity of DNA nanostructure increases. A large number of unique DNA sequences are required to build large, DNA-dense anisotropic structures. Because DNA assembly code consists of only four bases, the possibility of misassembled structures and kinetically trapped products also increases.

In the Sleiman group, minimalistic design has been pursued as an alternative strategy to overcome such complexity–error issue. A minimum number of DNA strands is used to build nanostructures, where only the essential structural and functional roles are retained. Another major approach is to bring the toolbox of supramolecular chemistry into DNA nanotechnology. The introduction of hydrophobic interactions in DNA nanostructures has led to completely new structures and functions while reducing the number of required DNA sequences. As such, the research body presented in this thesis aims to synergistically combine the two approaches to design amphiphilic DNA nanostructures. Fundamentally, three keys concepts will be presented: i) the geometry-dependent assembly of molecules on 3D DNA scaffolds, ii) the precise modulation of

hydrophobic interactions by using monodisperse, sequence-defined polymers and iii) the structural stability of amphiphilic DNA nanostructures.

Chapter 2 describes the decoration of sequence-defined amphiphilic polymers on 3D DNA cages to generate a library of hierarchical DNA nanostructures with unprecedented morphologies and increased stability. Inspired by the preliminary work of Edwardson *et al.*[190, 192], we explore a combinatorial library of design parameters and their effects on the assembly outcomes. DNA cages can be created in three sizes, each presenting different numbers and orientations of polymer-binding sites. On the polymer end, we systematically change its molecular structures such as lengths, sequences, and amphiphilicity. We demonstrate that DNA base-pairings and hydrophobic interactions can work together to introduce new directional assembly modes, generating a range of unique self-assembled amphiphilic DNA nanostructures.

Chapter 3 focuses on the extension of geometry-dependent assembly introduced in Chapter 2 to generate cholesterol-modified DNA cubes. Preliminary work by Conway *et al.* shows that a cholesterol-modified DNA trigonal prism can dynamically interact with supported bilayers.[214] To further challenge the structure-function relationship, this work seeks to address the fundamental design question: can we organize cholesterol units on 3D DNA scaffolds in different patterns to modulate their binding modes on lipid bilayers? Three structural parameters including the number, geometry and flexibility of cholesterol units on the cube will be examined. The solution self-assembly of several cholesterol-modified cubes and their binding behavior in terms of surface mobility, clustering and bilayer-embedding degree on giant unilamellar vesicles are presented.

One of the limitations of DNA amphiphiles is their instability in dilute conditions. In Chapter 4, three chemical cross-linking approaches are described to increase the stability of amphiphilic DNA nanostructures. The amide-based cross-linking method will be demonstrated with DNA amphiphiles bearing amino groups and bifunctional alkyl crosslinkers. The second approach will focus on the crosslinking of phosphorothioated DNA amphiphiles by using the intrinsic nucleophilicity of sulfur atom on phosphorothioate linker. The third approach involves the photo-crosslinking of DNA amphiphiles functionalized with anthracene units, which are well-known for their reversible photodimerization behavior. In the final part of this chapter, the site-specific hydrophobic modifications of phosphorothioated DNA using an *S*-alkylation strategy will be presented.

In the Appendix, we explore the generality of one of the two concepts in Chapter 2, where the interaction strength of sequenced-defined hydrophobic polymers can significantly dictate the assembly outcomes. We apply this concept to a rectangular DNA origami structure, which is widely used in numerous applications. As an alternative strategy in building hierarchical structures, the conventional DNA base-pairing through sticky-end cohesion between the rectangles is replaced with hydrophobic interactions. This is achieved by decorating the rectangles with sequence-defined hydrophobic polymer-DNA conjugates. A combination of multiple supramolecular interactions including DNA base-pairings, blunt-end stacking, hydrophobic interactions and electrostatic interactions results in less-ordered aggregates. Interestingly, we observe instead the site-specific attachment of polymer micelles on the origami rectangles.

1.6 References

1. Gradisar, H.; Bozic, S.; Doles, T.; Vengust, D.; Hafner-Bratkovic, I.; Mertelj, A.; Webb, B.; Sali, A.; Klavzar, S.; Jerala, R. *Nat. Chem. Biol.* 2013**,** 9, 362-366.
2. Lai, Y. T.; Reading, E.; Hura, G. L.; Tsai, K. L.; Laganowsky, A.; Asturias, F. J.; Tainer, J. A.; Robinson, C. V.; Yeates, T. O. *Nat. Chem.* 2014**,** 6, 1065-1071.
3. Aldaye, F. A.; Palmer, A. L.; Sleiman, H. F. *Science* 2008**,** 321, 1795-1799.
4. Yakovchuk, P.; Protozanova, E.; Frank-Kamenetskii, M. D. *Nucleic Acids Res.* 2006**,** 34, 564-574.
5. Khorana, H. G.; Razzell, W. E.; Gilham, P. T.; Tener, G. M.; Pol, E. H. *J. Am. Chem. Soc.* 1957**,** 79, 1002-1003.
6. Letsinger, R. L.; Ogilvie, K. K. *J. Am. Chem. Soc.* 1969**,** 91, 3350-3355.
7. Letsinger, R. L.; Finnan, J. L.; Heavner, G. A.; Lunsford, W. B. *J. Am. Chem. Soc.* 1975**,** 97, 3278-3279.
8. Beaucage, S. L.; Caruthers, M. H. *Tetrahedron Lett.* 1981**,** 22, 1859-1862.
9. Caruthers, M. H.; Barone, A. D.; Beaucage, S. L.; Dodds, D. R.; Fisher, E. F.; McBride, L. J.; Matteucci, M.; Stabinsky, Z.; Tang, J. Y. *Methods Enzymol.* 1987**,** 154, 287-313.
10. Seeman, N. C. *J. Theor. Biol.* 1982**,** 99, 237-247.
11. Kallenbach, N. R.; Ma, R.-I.; Seeman, N. C. *Nature* 1983**,** 305, 829-831.
12. Um, S. H.; Lee, J. B.; Park, N.; Kwon, S. Y.; Umbach, C. C.; Luo, D. *Nat. Mater.* 2006**,** 5, 797-801.
13. Sabir, T.; Toulmin, A.; Ma, L.; Jones, A. C.; McGlynn, P.; Schroder, G. F.; Magennis, S. W. *J. Am. Chem. Soc.* 2012**,** 134, 6280-6285.
14. Wang, Y.; Mueller, J. E.; Kemper, B.; Seeman, N. C. *Biochem.* 1991**,** 30, 5667-5674.
15. Wang, X.; Seeman, N. C. *J. Am. Chem. Soc.* 2007**,** 129, 8169-8176.
16. Fu, T. J.; Seeman, N. C. *Biochem.* 1993**,** 32, 3211-3220.
17. Sa-Ardyen, P.; Vologodskii, A. V.; Seeman, N. C. *Biophys. J.* 2003**,** 84, 3829-3837.

18. LaBean, T. H.; Yan, H.; Kopatsch, J.; Liu, F.; Winfree, E.; Reif, J. H.; Seeman, N. C. *J. Am. Chem. Soc.* 2000**,** 122, 1848-1860.
19. Seeman, N. C. *Nano Lett.* 2001**,** 1, 22-26.
20. Yan, H.; Park, S. H.; Finkelstein, G.; Reif, J. H.; LaBean, T. H. *Science* 2003**,** 301, 1882-1884.
21. Liu, D.; Wang, M.; Deng, Z.; Walulu, R.; Mao, C. *J. Am. Chem. Soc.* 2004**,** 126, 2324-2325.
22. He, Y.; Chen, Y.; Liu, H.; Ribbe, A. E.; Mao, C. *J. Am. Chem. Soc.* 2005**,** 127, 12202-12203.
23. Mathieu, F.; Liao, S.; Kopatsch, J.; Wang, T.; Mao, C.; Seeman, N. C. *Nano Lett.* 2005**,** 5, 661-665.
24. Torring, T.; Voigt, N. V.; Nangreave, J.; Yan, H.; Gothelf, K. V. *Chem. Soc. Rev.* 2011**,** 40, 5636-5646.
25. Winfree, E.; Liu, F.; Wenzler, L. A.; Seeman, N. C. *Nature* 1998**,** 394, 539-544.
26. Chen, J. H.; Seeman, N. C. *Nature* 1991**,** 350, 631-633.
27. Zhang, Y.; Seeman, N. C. *J. Am. Chem. Soc.* 1994**,** 116, 1661-1669.
28. Goodman, R. P.; Berry, R. M.; Turberfield, A. J. *Chem. Commun.* 2004, 1372-1373.
29. Goodman, R. P.; Schaap, I. A.; Tardin, C. F.; Erben, C. M.; Berry, R. M.; Schmidt, C. F.; Turberfield, A. J. *Science* 2005**,** 310, 1661-1665.
30. Bhatia, D.; Mehtab, S.; Krishnan, R.; Indi, S. S.; Basu, A.; Krishnan, Y. *Angew. Chem. Int. Ed.* 2009**,** 48, 4134-4137.
31. Shih, W. M.; Quispe, J. D.; Joyce, G. F. *Nature* 2004**,** 427, 618-621.
32. He, Y.; Ye, T.; Su, M.; Zhang, C.; Ribbe, A. E.; Jiang, W.; Mao, C. *Nature* 2008**,** 452, 198-201.
33. He, Y.; Su, M.; Fang, P.-a.; Zhang, C.; Ribbe, A. E.; Jiang, W.; Mao, C. *Angew. Chem. Int. Ed.* 2010**,** 49, 748-751.
34. Zhang, C.; Su, M.; He, Y.; Zhao, X.; Fang, P. A.; Ribbe, A. E.; Jiang, W.; Mao, C. *Proc. Natl. Acad. Sci. U.S.A.* 2008**,** 105, 10665-10669.
35. Aldaye, F. A.; Sleiman, H. F. *J. Am. Chem. Soc.* 2007**,** 129, 13376-13377.
36. Rothemund, P. W. *Nature* 2006**,** 440, 297-302.
37. Han, D.; Pal, S.; Yang, Y.; Jiang, S.; Nangreave, J.; Liu, Y.; Yan, H. *Science* 2013**,** 339, 1412-1415.
38. Benson, E.; Mohammed, A.; Gardell, J.; Masich, S.; Czeizler, E.; Orponen, P.; Hogberg, B. *Nature* 2015**,** 523, 441-444.
39. Li, Z.; Wei, B.; Nangreave, J.; Lin, C.; Liu, Y.; Mi, Y.; Yan, H. *J. Am. Chem. Soc.* 2009**,** 131, 13093-13098.
40. McLaughlin, C. K.; Hamblin, G. D.; Hanni, K. D.; Conway, J. W.; Nayak, M. K.; Carneiro, K. M.; Bazzi, H. S.; Sleiman, H. F. *J. Am. Chem. Soc.* 2012**,** 134, 4280-4286.
41. Yan, H.; LaBean, T. H.; Feng, L.; Reif, J. H. *Proc. Natl. Acad. Sci. U.S.A.* 2003**,** 100, 8103-8108.
42. Ke, Y.; Sharma, J.; Liu, M.; Jahn, K.; Liu, Y.; Yan, H. *Nano Lett.* 2009**,** 9, 2445-2447.
43. Andersen, E. S.; Dong, M.; Nielsen, M. M.; Jahn, K.; Subramani, R.; Mamdouh, W.; Golas, M. M.; Sander, B.; Stark, H.; Oliveira, C. L.; Pedersen, J. S.; Birkedal, V.; Besenbacher, F.; Gothelf, K. V.; Kjems, J. *Nature* 2009**,** 459, 73-76.
44. Hong, F.; Zhang, F.; Liu, Y.; Yan, H. *Chem. Rev.* 2017**,** 117, 12584-12640.

45. Douglas, S. M.; Dietz, H.; Liedl, T.; Hogberg, B.; Graf, F.; Shih, W. M. *Nature* 2009**,** 459, 414-418.
46. Ke, Y.; Douglas, S. M.; Liu, M.; Sharma, J.; Cheng, A.; Leung, A.; Liu, Y.; Shih, W. M.; Yan, H. *J. Am. Chem. Soc.* 2009**,** 131, 15903-15908.
47. Ke, Y.; Voigt, N. V.; Gothelf, K. V.; Shih, W. M. *J. Am. Chem. Soc.* 2012**,** 134, 1770-1774.
48. Dietz, H.; Douglas, S. M.; Shih, W. M. *Science* 2009**,** 325, 725-730.
49. Han, D.; Pal, S.; Nangreave, J.; Deng, Z.; Liu, Y.; Yan, H. *Science* 2011**,** 332, 342-346.
50. Wei, B.; Dai, M.; Yin, P. *Nature* 2012**,** 485, 623-626.
51. Ke, Y.; Ong, L. L.; Shih, W. M.; Yin, P. *Science* 2012**,** 338, 1177-1183.
52. Wagenbauer, K. F.; Engelhardt, F. A. S.; Stahl, E.; Hechtl, V. K.; Stommer, P.; Seebacher, F.; Meregalli, L.; Ketterer, P.; Gerling, T.; Dietz, H. *ChemBioChem* 2017**,** 18, 1873-1885.
53. Douglas, S. M.; Marblestone, A. H.; Teerapittayanon, S.; Vazquez, A.; Church, G. M.; Shih, W. M. *Nucleic Acids Res.* 2009**,** 37, 5001-5006.
54. Castro, C. E.; Kilchherr, F.; Kim, D. N.; Shiao, E. L.; Wauer, T.; Wortmann, P.; Bathe, M.; Dietz, H. *Nat. Methods* 2011**,** 8, 221-229.
55. Niekamp, S.; Blumer, K.; Nafisi, P. M.; Tsui, K.; Garbutt, J.; Douglas, S. M. *Nucleic Acids Res.* 2016**,** 44, e102.
56. Martin, T. G.; Dietz, H. *Nat. Commun.* 2012**,** 3, 1103.
57. Sobczak, J. P.; Martin, T. G.; Gerling, T.; Dietz, H. *Science* 2012**,** 338, 1458-1461.
58. Jungmann, R.; Liedl, T.; Sobey, T. L.; Shih, W.; Simmel, F. C. *J. Am. Chem. Soc.* 2008**,** 130, 10062-10063.
59. Kopielski, A.; Schneider, A.; Csaki, A.; Fritzsche, W. *Nanoscale* 2015**,** 7, 2102-2106.
60. Gallego, I.; Grover, M. A.; Hud, N. V. *Angew. Chem. Int. Ed.* 2015**,** 54, 6765-6769.
61. Zheng, J.; Birktoft, J. J.; Chen, Y.; Wang, T.; Sha, R.; Constantinou, P. E.; Ginell, S. L.; Mao, C.; Seeman, N. C. *Nature* 2009**,** 461, 74-77.
62. Hao, Y.; Kristiansen, M.; Sha, R.; Birktoft, J. J.; Hernandez, C.; Mao, C.; Seeman, N. C. *Nat. Chem.* 2017**,** 9, 824-827.
63. He, Y.; Tian, Y.; Chen, Y.; Deng, Z.; Ribbe, A. E.; Mao, C. *Angew. Chem. Int. Ed.* 2005**,** 44, 6694-6696.
64. He, Y.; Tian, Y.; Ribbe, A. E.; Mao, C. *J. Am. Chem. Soc.* 2006**,** 128, 15978-15979.
65. He, Y.; Mao, C. *Chem. Commun.* 2006, 968-969.
66. Tian, C.; Zhang, C.; Li, X.; Hao, C.; Ye, S.; Mao, C. *Langmuir* 2014**,** 30, 5859-5862.
67. Rothemund, P. W.; Papadakis, N.; Winfree, E. *PLoS Biol.* 2004**,** 2, e424.
68. Park, S. H.; Pistol, C.; Ahn, S. J.; Reif, J. H.; Lebeck, A. R.; Dwyer, C.; LaBean, T. H. *Angew. Chem. Int. Ed.* 2006**,** 45, 735-739.
69. Liu, Y.; Ke, Y.; Yan, H. *J. Am. Chem. Soc.* 2005**,** 127, 17140-17141.
70. Liu, W.; Zhong, H.; Wang, R.; Seeman, N. C. *Angew. Chem. Int. Ed.* 2011**,** 50, 264-267.
71. Zhao, Z.; Yan, H.; Liu, Y. *Angew. Chem. Int. Ed.* 2010**,** 49, 1414-1417.
72. Zhao, Z.; Liu, Y.; Yan, H. *Nano Lett.* 2011**,** 11, 2997-3002.
73. Lo, P. K.; Metera, K. L.; Sleiman, H. F. *Curr. Opin. Chem. Biol.* 2010**,** 14, 597-607.
74. Liu, D.; Park, S. H.; Reif, J. H.; LaBean, T. H. *Proc. Natl. Acad. Sci. U.S.A.* 2004**,** 101, 717-722.
75. Mitchell, J. C.; Harris, J. R.; Malo, J.; Bath, J.; Turberfield, A. J. *J. Am. Chem. Soc.* 2004**,** 126, 16342-16343.
76. Rothemund, P. W.; Ekani-Nkodo, A.; Papadakis, N.; Kumar, A.; Fygenson, D. K.; Winfree, E. *J. Am. Chem. Soc.* 2004**,** 126, 16344-16352.

77. Liu, H.; Chen, Y.; He, Y.; Ribbe, A. E.; Mao, C. *Angew. Chem. Int. Ed.* 2006**,** 45, 1942-1945.
78. Yin, P.; Hariadi, R. F.; Sahu, S.; Choi, H. M.; Park, S. H.; Labean, T. H.; Reif, J. H. *Science* 2008**,** 321, 824-826.
79. Lo, P. K.; Altvater, F.; Sleiman, H. F. *J. Am. Chem. Soc.* 2010**,** 132, 10212-10214.
80. Hamblin, G. D.; Carneiro, K. M.; Fakhoury, J. F.; Bujold, K. E.; Sleiman, H. F. *J. Am. Chem. Soc.* 2012**,** 134, 2888-2891.
81. Hamblin, G. D.; Hariri, A. A.; Carneiro, K. M.; Lau, K. L.; Cosa, G.; Sleiman, H. F. *ACS Nano* 2013**,** 7, 3022-3028.
82. Hamblin, G. D.; Rahbani, J. F.; Sleiman, H. F. *Nat. Commun.* 2015**,** 6, 7065.
83. Li, X.; Liu, D. R. *Angew. Chem. Int. Ed.* 2004**,** 43, 4848-4870.
84. Cecconello, A.; Besteiro, L. V.; Govorov, A. O.; Willner, I. *Nat. Rev. Mater.* 2017**,** 2.
85. Alivisatos, A. P.; Johnsson, K. P.; Peng, X. G.; Wilson, T. E.; Loweth, C. J.; Bruchez, M. P.; Schultz, P. G. *Nature* 1996**,** 382, 609-611.
86. Mastroianni, A. J.; Claridge, S. A.; Alivisatos, A. P. *J. Am. Chem. Soc.* 2009**,** 131, 8455-8459.
87. Ding, B.; Deng, Z.; Yan, H.; Cabrini, S.; Zuckermann, R. N.; Bokor, J. *J. Am. Chem. Soc.* 2010**,** 132, 3248-3249.
88. Pal, S.; Deng, Z.; Ding, B.; Yan, H.; Liu, Y. *Angew. Chem. Int. Ed.* 2010**,** 49, 2700-2704.
89. Edwardson, T. G.; Lau, K. L.; Bousmail, D.; Serpell, C. J.; Sleiman, H. F. *Nat. Chem.* 2016**,** 8, 162-170.
90. Zhang, Y.; Chao, J.; Liu, H.; Wang, F.; Su, S.; Liu, B.; Zhang, L.; Shi, J.; Wang, L.; Huang, W.; Wang, L.; Fan, C. *Angew. Chem. Int. Ed.* 2016**,** 55, 8036-8040.
91. Chhabra, R.; Sharma, J.; Ke, Y.; Liu, Y.; Rinker, S.; Lindsay, S.; Yan, H. *J. Am. Chem. Soc.* 2007**,** 129, 10304-10305.
92. Sacca, B.; Meyer, R.; Erkelenz, M.; Kiko, K.; Arndt, A.; Schroeder, H.; Rabe, K. S.; Niemeyer, C. M. *Angew. Chem. Int. Ed.* 2010**,** 49, 9378-9383.
93. Rinker, S.; Ke, Y.; Liu, Y.; Chhabra, R.; Yan, H. *Nat. Nanotechnol.* 2008**,** 3, 418-422.
94. Fu, J.; Liu, M.; Liu, Y.; Woodbury, N. W.; Yan, H. *J. Am. Chem. Soc.* 2012**,** 134, 5516-5519.
95. Douglas, S. M.; Chou, J. J.; Shih, W. M. *Proc. Natl. Acad. Sci. U.S.A.* 2007**,** 104, 6644-6648.
96. Selmi, D. N.; Adamson, R. J.; Attrill, H.; Goddard, A. D.; Gilbert, R. J.; Watts, A.; Turberfield, A. J. *Nano Lett.* 2011**,** 11, 657-660.
97. Zhang, D. Y.; Seelig, G. *Nat. Chem.* 2011**,** 3, 103-113.
98. Zhang, D. Y.; Winfree, E. *J. Am. Chem. Soc.* 2009**,** 131, 17303-17314.
99. Yurke, B.; Turberfield, A. J.; Mills, A. P., Jr.; Simmel, F. C.; Neumann, J. L. *Nature* 2000**,** 406, 605-608.
100. Yan, H.; Zhang, X.; Shen, Z.; Seeman, N. C. *Nature* 2002**,** 415, 62-65.
101. Gu, H.; Chao, J.; Xiao, S. J.; Seeman, N. C. *Nature* 2010**,** 465, 202-205.
102. He, Y.; Liu, D. R. *Nat. Nanotechnol.* 2010**,** 5, 778-782.
103. Seelig, G.; Soloveichik, D.; Zhang, D. Y.; Winfree, E. *Science* 2006**,** 314, 1585-1588.
104. Dirks, R. M.; Pierce, N. A. *Proc. Natl. Acad. Sci. U.S.A.* 2004**,** 101, 15275-15278.
105. Lo, P. K.; Karam, P.; Aldaye, F. A.; McLaughlin, C. K.; Hamblin, G. D.; Cosa, G.; Sleiman, H. F. *Nat. Chem.* 2010**,** 2, 319-328.

106. Bujold, K. E.; Fakhoury, J.; Edwardson, T. G. W.; Carneiro, K. M. M.; Briard, J. N.; Godin, A. G.; Amrein, L.; Hamblin, G. D.; Panasci, L. C.; Wiseman, P. W.; Sleiman, H. F. *Chem. Sci.* 2014**,** 5, 2449-2455.
107. Zhang, F.; Nangreave, J.; Liu, Y.; Yan, H. *J. Am. Chem. Soc.* 2014**,** 136, 11198-11211.
108. Endo, M.; Sugita, T.; Katsuda, Y.; Hidaka, K.; Sugiyama, H. *Chem. Eur. J.* 2010**,** 16, 5362-5368.
109. Rajendran, A.; Endo, M.; Katsuda, Y.; Hidaka, K.; Sugiyama, H. *ACS Nano* 2011**,** 5, 665-671.
110. Gerling, T.; Wagenbauer, K. F.; Neuner, A. M.; Dietz, H. *Science* 2015**,** 347, 1446-1452.
111. Woo, S.; Rothemund, P. W. *Nat. Chem.* 2011**,** 3, 620-627.
112. Dong, Y.; Yang, Z.; Liu, D. *Acc. Chem. Res.* 2014**,** 47, 1853-1860.
113. Cheng, E.; Xing, Y.; Chen, P.; Yang, Y.; Sun, Y.; Zhou, D.; Xu, L.; Fan, Q.; Liu, D. *Angew. Chem. Int. Ed.* 2009**,** 48, 7660-7663.
114. Hu, Y.; Cecconello, A.; Idili, A.; Ricci, F.; Willner, I. *Angew. Chem. Int. Ed.* 2017, 56, 15210-15233.
115. Wu, N.; Willner, I. *Nano Lett.* 2016**,** 16, 6650-6655.
116. Cook, T. R.; Zheng, Y. R.; Stang, P. J. *Chem. Rev.* 2013**,** 113, 734-777.
117. Shi, J.; Bergstrom, D. E. *Angew. Chem. Int. Ed.* 1997**,** 36, 111-113.
118. Aldaye, F. A.; Sleiman, H. F. *Angew. Chem. Int. Ed.* 2006**,** 45, 2204-2209.
119. Aldaye, F. A.; Lo, P. K.; Karam, P.; McLaughlin, C. K.; Cosa, G.; Sleiman, H. F. *Nat. Nanotechnol.* 2009**,** 4, 349-352.
120. Greschner, A. A.; Toader, V.; Sleiman, H. F. *J. Am. Chem. Soc.* 2012**,** 134, 14382-14389.
121. Eryazici, I.; Prytkova, T. R.; Schatz, G. C.; Nguyen, S. T. *J. Am. Chem. Soc.* 2010**,** 132, 17068-17070.
122. Yildirim, I.; Eryazici, I.; Nguyen, S. T.; Schatz, G. C. *J. Phys. Chem. B* 2014**,** 118, 2366-2376.
123. Scheffler, M.; Dorenbeck, A.; Jordan, S.; Wustefeld, M.; von Kiedrowski, G. *Angew. Chem. Int. Ed.* 1999**,** 38, 3311-3315.
124. Kuroda, T.; Sakurai, Y.; Suzuki, Y.; Nakamura, A. O.; Kuwahara, M.; Ozaki, H.; Sawai, H. *Chem. Asian J.* 2006**,** 1, 575-580.
125. Eckardt, L. H.; Naumann, K.; Pankau, W. M.; Rein, M.; Schweitzer, M.; Windhab, N.; von Kiedrowski, G. *Nature* 2002**,** 420, 286.
126. Gothelf, K. V.; Thomsen, A.; Nielsen, M.; Clo, E.; Brown, R. S. *J. Am. Chem. Soc.* 2004**,** 126, 1044-1046.
127. Eryazici, I.; Yildirim, I.; Schatz, G. C.; Nguyen, S. T. *J. Am. Chem. Soc.* 2012**,** 134, 7450-7458.
128. Hong, B. J.; Cho, V. Y.; Bleher, R.; Schatz, G. C.; Nguyen, S. T. *J. Am. Chem. Soc.* 2015**,** 137, 13381-13388.
129. Zimmermann, J.; Cebulla, M. P. J.; Mönninghoff, S.; von Kiedrowski, G. *Angew. Chem. Int. Ed.* 2008**,** 47, 3626-3630.
130. Shchepinov, M. S.; Mir, K. U.; Elder, J. K.; Frank-Kamenetskii, M. D.; Southern, E. M. *Nucleic Acids Res.* 1999**,** 27, 3035-3041.
131. Meng, M.; Ahlborn, C.; Bauer, M.; Plietzsch, O.; Soomro, S. A.; Singh, A.; Muller, T.; Wenzel, W.; Brase, S.; Richert, C. *ChemBioChem* 2009**,** 10, 1335-1339.
132. Singh, A.; Tolev, M.; Meng, M.; Klenin, K.; Plietzsch, O.; Schilling, C. I.; Muller, T.; Nieger, M.; Bräse, S.; Wenzel, W.; Richert, C. *Angew. Chem. Int. Ed.* 2011**,** 50, 3227-3231.

133. Schwenger, A.; Gerlach, C.; Griesser, H.; Richert, C. *J. Org. Chem.* 2014**,** 79, 11558-11566.
134. Hong, B. J.; Eryazici, I.; Bleher, R.; Thaner, R. V.; Mirkin, C. A.; Nguyen, S. T. *J. Am. Chem. Soc.* 2015**,** 137, 8184-8191.
135. Ono, A.; Torigoe, H.; Tanaka, Y.; Okamoto, I. *Chem. Soc. Rev.* 2011**,** 40, 5855-5866.
136. Tanaka, K.; Tengeiji, A.; Kato, T.; Toyama, N.; Shionoya, M. *Science* 2003**,** 299, 1212-1213.
137. Tanaka, K.; Clever, G. H.; Takezawa, Y.; Yamada, Y.; Kaul, C.; Shionoya, M.; Carell, T. *Nat. Nanotechnol.* 2006**,** 1, 190-194.
138. Weizman, H.; Tor, Y. *J. Am. Chem. Soc.* 2001**,** 123, 3375-3376.
139. Meggers, E.; Holland, P. L.; Tolman, W. B.; Romesberg, F. E.; Schultz, P. G. *J. Am. Chem. Soc.* 2000**,** 122, 10714-10715.
140. Clever, G. H.; Polborn, K.; Carell, T. *Angew. Chem. Int. Ed.* 2005**,** 44, 7204-7208.
141. Takezawa, Y.; Shionoya, M. *Acc. Chem. Res.* 2012**,** 45, 2066-2076.
142. Czlapinski, J. L.; Sheppard, T. L. *J. Am. Chem. Soc.* 2001**,** 123, 8618-8619.
143. Vargas-Baca, I.; Mitra, D.; Zulyniak, H. J.; Banerjee, J.; Sleiman, H. F. *Angew. Chem. Int. Ed.* 2001**,** 40, 4629-4632.
144. Yang, H.; Sleiman, H. F. *Angew. Chem. Int. Ed.* 2008**,** 47, 2443-2446.
145. Yang, H.; Rys, A. Z.; McLaughlin, C. K.; Sleiman, H. F. *Angew. Chem. Int. Ed.* 2009**,** 48, 9919-9923.
146. Cesario, M.; Dietrich-Buchecker, C. O.; Guilhem, J.; Pascard, C.; Sauvage, J. P. *J. Chem. Soc., Chem. Commun.* 1985, 244-247.
147. Duprey, J. L.; Takezawa, Y.; Shionoya, M. *Angew. Chem. Int. Ed.* 2013**,** 52, 1212-1216.
148. Stewart, K. M.; McLaughlin, L. W. *Chem. Commun.* 2003, 2934-2935.
149. Mitra, D.; Di Cesare, N.; Sleiman, H. F. *Angew. Chem. Int. Ed.* 2004**,** 43, 5804-5808.
150. Stewart, K. M.; McLaughlin, L. W. *J. Am. Chem. Soc.* 2004**,** 126, 2050-2057.
151. Stewart, K. M.; Rojo, J.; McLaughlin, L. W. *Angew. Chem. Int. Ed.* 2004**,** 43, 5808-5811.
152. Yang, H.; McLaughlin, C. K.; Aldaye, F. A.; Hamblin, G. D.; Rys, A. Z.; Rouiller, I.; Sleiman, H. F. *Nat. Chem.* 2009**,** 1, 390-396.
153. Choi, J. S.; Kang, C. W.; Jung, K.; Yang, J. W.; Kim, Y. G.; Han, H. *J. Am. Chem. Soc.* 2004**,** 126, 8606-8607.
154. Miyoshi, D.; Karimata, H.; Wang, Z. M.; Koumoto, K.; Sugimoto, N. *J. Am. Chem. Soc.* 2007**,** 129, 5919-5925.
155. Megger, N.; Welte, L.; Zamora, F.; Muller, J. *Dalton Trans* 2011**,** 40, 1802-1807.
156. Ensslen, P.; Wagenknecht, H.-A. *Dalton Trans* 2015**,** 44, 6715-6718.
157. Yang, Y.; Endo, M.; Hidaka, K.; Sugiyama, H. *J. Am. Chem. Soc.* 2012**,** 134, 20645-20653.
158. Nagarajan, R. *Langmuir* 2002**,** 18, 31-38.
159. Mai, Y.; Eisenberg, A. *Chem. Soc. Rev.* 2012**,** 41, 5969-5985.
160. Raouane, M.; Desmaele, D.; Urbinati, G.; Massaad-Massade, L.; Couvreur, P. *Bioconjugate Chem.* 2012**,** 23, 1091-1104.
161. Liu, H.; Zhu, Z.; Kang, H.; Wu, Y.; Sefan, K.; Tan, W. *Chem. Eur. J.* 2010**,** 16, 3791-3797.
162. Wu, Y.; Sefah, K.; Liu, H.; Wang, R.; Tan, W. *Proc. Natl. Acad. Sci. U.S.A.* 2010**,** 107, 5-10.
163. Laing, B. M.; Barrow-Laing, L.; Harrington, M.; Long, E. C.; Bergstrom, D. E. *Bioconjugate Chem.* 2010**,** 21, 1537-1544.
164. Dentinger, P. M.; Simmons, B. A.; Cruz, E.; Sprague, M. *Langmuir* 2006**,** 22, 2935-2937.

165. Takahashi, K.; Matsuo, M.; Banno, T.; Toyota, T. *Soft Matter* 2015**,** 11, 7053-7058.
166. Albert, S. K.; Golla, M.; Thelu, H. V. P.; Krishnan, N.; Varghese, R. *Chem. Eur. J.* 2017**,** 23, 8348-8352.
167. Thompson, M. P.; Chien, M.-P.; Ku, T.-H.; Rush, A. M.; Gianneschi, N. C. *Nano Lett.* 2010**,** 10, 2690-2693.
168. Carneiro, K. M. M.; Aldaye, F. A.; Sleiman, H. F. *J. Am. Chem. Soc.* 2010**,** 132, 679-685.
169. Wang, L.; Feng, Y.; Sun, Y.; Li, Z.; Yang, Z.; He, Y.-M.; Fan, Q.-H.; Liu, D. *Soft Matter* 2011**,** 7, 7187.
170. Wang, L.; Feng, Y.; Yang, Z.; He, Y. M.; Fan, Q. H.; Liu, D. *Chem. Commun.* 2012**,** 48, 3715-3717.
171. Dong, Y.; Sun, Y.; Wang, L.; Wang, D.; Zhou, T.; Yang, Z.; Chen, Z.; Wang, Q.; Fan, Q.; Liu, D. *Angew. Chem.* 2014**,** 126, 2645-2648.
172. Dong, Y.; Yang, Y. R.; Zhang, Y.; Wang, D.; Wei, X.; Banerjee, S.; Liu, Y.; Yang, Z.; Yan, H.; Liu, D. *Angew. Chem. Int. Ed.* 2017**,** 56, 1586-1589.
173. Jeong, J. H.; Park, T. G. *Bioconjugate Chem.* 2001**,** 12, 917-923.
174. Watson, K. J.; Park, S.-J.; Im, J.-H.; Mirkin, C. A. *J. Am. Chem. Soc.* 2001**,** 123, 5592-5593.
175. Wang, W.; Li, L. S.; Helms, G.; Zhou, H. H.; Li, A. D. *J. Am. Chem. Soc.* 2003**,** 125, 1120-1121.
176. Wang, W.; Wan, W.; Zhou, H. H.; Niu, S.; Li, A. D. *J. Am. Chem. Soc.* 2003**,** 125, 5248-5249.
177. Vyborna, Y.; Vybornyi, M.; Haner, R. *J. Am. Chem. Soc.* 2015**,** 137, 14051-14054.
178. Vyborna, Y.; Vybornyi, M.; Rudnev, A. V.; Haner, R. *Angew. Chem. Int. Ed.* 2015**,** 54, 7934-7938.
179. Li, Z.; Zhang, Y.; Fullhart, P.; Mirkin, C. A. *Nano Lett.* 2004**,** 4, 1055-1058.
180. Averick, S.; Paredes, E.; Li, W.; Matyjaszewski, K.; Das, S. R. *Bioconjugate Chem.* 2011**,** 22, 2030-2037.
181. Gibbs, J. M.; Park, S.-J.; Anderson, D. R.; Watson, K. J.; Mirkin, C. A.; Nguyen, S. T. *J. Am. Chem. Soc.* 2005**,** 127, 1170-1178.
182. Gibbs-Davis, J. M.; Schatz, G. C.; Nguyen, S. T. *J. Am. Chem. Soc.* 2007**,** 129, 15535-15540.
183. Ding, K.; Alemdaroglu, F. E.; Börsch, M.; Berger, R.; Herrmann, A. *Angew. Chem. Int. Ed.* 2007**,** 46, 1172-1175.
184. Chien, M. P.; Rush, A. M.; Thompson, M. P.; Gianneschi, N. C. *Angew. Chem. Int. Ed.* 2010**,** 49, 5076-5080.
185. Zhao, Z.; Wang, L.; Liu, Y.; Yang, Z.; He, Y.-M.; Li, Z.; Fan, Q.-H.; Liu, D. *Chem. Commun.* 2012**,** 48, 9753-9755.
186. Kim, C.-J.; Hu, X.; Park, S.-J. *J. Am. Chem. Soc.* 2016**,** 138, 14941-14947.
187. Kwak, M.; Herrmann, A. *Angew. Chem. Int. Ed.* 2010**,** 49, 8574-8587.
188. Schnitzler, T.; Herrmann, A. *Acc. Chem. Res.* 2012**,** 45, 1419-1430.
189. Averick, S. E.; Dey, S. K.; Grahacharya, D.; Matyjaszewski, K.; Das, S. R. *Angew. Chem. Int. Ed.* 2014**,** 53, 2739-2744.
190. Edwardson, T. G.; Carneiro, K. M.; Serpell, C. J.; Sleiman, H. F. *Angew. Chem. Int. Ed.* 2014**,** 53, 4567-4571.
191. Brady, R. A.; Brooks, N. J.; Cicuta, P.; Di Michele, L. *Nano Lett.* 2017**,** 17, 3276-3281.

192. Edwardson, T. G.; Carneiro, K. M.; McLaughlin, C. K.; Serpell, C. J.; Sleiman, H. F. *Nat. Chem.* 2013**,** 5, 868-875.
193. Carneiro, K. M. M.; Hamblin, G. D.; Hänni, K. D.; Fakhoury, J.; Nayak, M. K.; Rizis, G.; McLaughlin, C. K.; Bazzi, H. S.; Sleiman, H. F. *Chem. Sci.* 2012**,** 3, 1980.
194. Wilks, T. R.; Bath, J.; de Vries, J. W.; Raymond, J. E.; Herrmann, A.; Turberfield, A. J.; O'Reilly, R. K. *ACS Nano* 2013**,** 7, 8561-8572.
195. List, J.; Weber, M.; Simmel, F. C. *Angew. Chem. Int. Ed.* 2014**,** 53, 4236-4239.
196. Zhou, C.; Wang, D.; Dong, Y.; Xin, L.; Sun, Y.; Yang, Z.; Liu, D. *Small* 2015**,** 11, 1161-1164.
197. Conway, J. W.; McLaughlin, C. K.; Castor, K. J.; Sleiman, H. *Chem. Commun.* 2013**,** 49, 1172-1174.
198. Lacroix, A.; Edwardson, T. G. W.; Hancock, M. A.; Dore, M. D.; Sleiman, H. F. *J. Am. Chem. Soc.* 2017**,** 139, 7355-7362.
199. Howorka, S. *Science* 2016**,** 352, 890-891.
200. Langecker, M.; Arnaut, V.; Martin, T. G.; List, J.; Renner, S.; Mayer, M.; Dietz, H.; Simmel, F. C. *Science* 2012**,** 338, 932-936.
201. Howorka, S. *Nat. Nanotechnol.* 2017**,** 12, 619-630.
202. Burns, J. R.; Gopfrich, K.; Wood, J. W.; Thacker, V. V.; Stulz, E.; Keyser, U. F.; Howorka, S. *Angew. Chem. Int. Ed.* 2013**,** 52, 12069-12072.
203. Burns, J. R.; Al-Juffali, N.; Janes, S. M.; Howorka, S. *Angew. Chem. Int. Ed.* 2014**,** 53, 12466-12470.
204. Burns, J. R.; Seifert, A.; Fertig, N.; Howorka, S. *Nat. Nanotechnol.* 2016**,** 11, 152-156.
205. Yang, Y.; Wang, J.; Shigematsu, H.; Xu, W.; Shih, W. M.; Rothman, J. E.; Lin, C. *Nat. Chem.* 2016**,** 8, 476-483.
206. Zhang, Z.; Yang, Y.; Pincet, F.; M, C. L.; Lin, C. *Nat. Chem.* 2017**,** 9, 653-659.
207. Czogalla, A.; Kauert, D. J.; Franquelim, H. G.; Uzunova, V.; Zhang, Y.; Seidel, R.; Schwille, P. *Angew. Chem. Int. Ed.* 2015**,** 54, 6501-6505.
208. Loffler, P. M. G.; Ries, O.; Rabe, A.; Okholm, A. H.; Thomsen, R. P.; Kjems, J.; Vogel, S. *Angew. Chem. Int. Ed.* 2017**,** 56, 13228-13231.
209. Chan, Y. H.; van Lengerich, B.; Boxer, S. G. *Proc. Natl. Acad. Sci. U.S.A.* 2009**,** 106, 979-984.
210. Dave, N.; Liu, J. *ACS Nano* 2011**,** 5, 1304-1312.
211. Hernandez-Ainsa, S.; Ricci, M.; Hilton, L.; Avino, A.; Eritja, R.; Keyser, U. F. *Nano Lett.* 2016**,** 16, 4462-4466.
212. Borjesson, K.; Lundberg, E. P.; Woller, J. G.; Norden, B.; Albinsson, B. *Angew. Chem. Int. Ed.* 2011**,** 50, 8312-8315.
213. Johnson-Buck, A.; Jiang, S. X.; Yan, H.; Walter, N. G. *ACS Nano* 2014**,** 8, 5641-5649.
214. Conway, J. W.; Madwar, C.; Edwardson, T. G.; McLaughlin, C. K.; Fahkoury, J.; Lennox, R. B.; Sleiman, H. F. *J. Am. Chem. Soc.* 2014**,** 136, 12987-12997.
215. Akbari, E.; Mollica, M. Y.; Lucas, C. R.; Bushman, S. M.; Patton, R. A.; Shahhosseini, M.; Song, J. W.; Castro, C. E. *Adv. Mater.* 2017**,** 29, 1703632.
216. Suzuki, Y.; Endo, M.; Sugiyama, H. *Nat. Commun.* 2015**,** 6, 8052.
217. Kocabey, S.; Kempter, S.; List, J.; Xing, Y.; Bae, W.; Schiffels, D.; Shih, W. M.; Simmel, F. C.; Liedl, T. *ACS Nano* 2015**,** 9, 3530-3539.
218. Avakyan, N.; Conway, J. W.; Sleiman, H. F. *J. Am. Chem. Soc.* 2017**,** 139, 12027-12034.

| 2 |

Self-assembly of sequence-defined polymers on DNA cages

This chapter is composed mainly of the work published as "Synergy of Two Assembly Languages in DNA Nanostructures: Self-Assembly of Sequence-Defined Polymers on DNA Cages" by Pongphak Chidchob, Thomas G. W. Edwardson, Christopher J. Serpell and Hanadi F. Sleiman in *Journal of American Chemical Society*, **2016**, 138(13), 4416-4425. Parts of this chapter are adapted from "Precision Polymers and 3D DNA Nanostructures: Emergent Assemblies from New Parameter Space" by Christopher J. Serpell, Thomas G. W. Edwardson, Pongphak Chidchob, Karina M. M. Carneiro and Hanadi F. Sleiman in *Journal of American Chemical Society*, **2014**, 136(44), 15767-15774.

2.1 Preface

DNA base-pairing is the central interaction in DNA assembly. However, this simple four-letter (A-T and G-C) language makes it difficult to create complex structures without using a large number of DNA strands of different sequences. Inspired by the folding of coiled-coil motifs in proteins, this chapter aims to introduce hydrophobic interactions to expand the assembly language of DNA nanotechnology. To achieve this, DNA cages of different geometries were combined with sequence-defined polymers containing long alkyl and oligoethylene glycol repeat units. New structural and functional modes in DNA nanostructures such as quantized cage assembly, DNA-micelle cage, and doughnut-shaped cage-ring structures can emerge from the synergy of two interactions, where hydrophobic interactions can contribute to increased structural stability and assembly cooperativity in some cases. This provides an attractive approach to develop protein-inspired assembly modules in DNA nanotechnology.

2.2 Introduction

Sequence-controlled polymers, such as oligonucleotides and polypeptides, are remarkable macromolecules in which the order of the building blocks along the polymer chain provides all necessary instructions for efficient structural control, molecular recognition, and catalysis.[1] In particular, polypeptide chains are programmed to fold themselves into final predetermined structures with very high accuracy to construct important biological nanomachines. Although such

a level of structural and functional complexity has not been fully realized synthetically,[1] the field of DNA nanotechnology offers a powerful tool to create finely designed 2D and 3D architectures and devices by using DNA as the building block.[2-11] However, a large number of DNA strands of unique sequences are generally required for the assembly of more complex structures. This decreases scalability and can theoretically increase assembly errors, due to the limited four-letter A-T and G-C 'language' in DNA assembly.

The incorporation of multiple molecular interactions within the same building block is an efficient strategy to achieve complex and hierarchical assembly in biological systems. Of these, hydrophobic interactions are the underlying mechanism for many structural elements in biology such as phospholipid bilayers, vesicles, and many proteins. They are also a fundamental driving force for the self-assembly of synthetic block copolymers into various morphologies such as spherical micelles, cylindrical micelles, and vesicles.[12] The integration of hydrophobic interactions with DNA base-pairing is a promising approach not only to overcome the complexity-scalability-error issues but also to introduce new assembly modes and functions in DNA assembly.[13-14]

To our knowledge, the implementation of hydrophobic interactions in the design of DNA nanostructures is still considerably unexplored. Some examples that integrate hydrophobic interactions with DNA nanostructures include self-folding of DNA rectangles mediated by cholesterol[15] and hydrophobic dendritic molecules,[16] and DNA tetrahedra functionalized with a thermoresponsive polymer that can transition between a discrete tetrahedron and giant-surfactant aggregates.[17] Recent work by the Sleiman group has demonstrated the significant role of hydrophobic interactions in directing the association mode of alkyl chains on 3D DNA scaffolds. The number and position of the chains on DNA cubes can dramatically alter their assembly behavior.[14, 18]

Inspired by protein folding, we would like to create assembly modules, like protein coiled-coil motifs, as elementary repeats in DNA nanotechnology. Thus we need to understand the rules governing the interplay between the two languages in the assembly. However, one of the problems is the difficulty in the synthesis of DNA conjugated with hydrophobic molecules and polymers. Our group has recently developed an automated solid-phase synthesis to prepare monodisperse polymer-DNA conjugates based on phosphoramidite chemistry.[19] This approach is not only

convenient, rapid and high yielding but also allows one to place functional monomers in a sequence-controlled manner on the polymer backbone.

In this chapter, we report an in-depth study of the self-assembly of sequence-defined amphiphilic polymers on DNA cages. Our system allows the systematic change of cage structure, size, and orientation of individual polymer chains on the DNA scaffold. On the polymer end, the polymers are monodisperse and sequence controlled in such a way that we can precisely change the molecular structure of the polymers. We found that polymer decoration on the cages leads to new DNA higher-order structures through hierarchical assembly, such as quantized DNA cage assemblies, doughnut-shaped DNA-cage ring, and DNA-micelle cages, via DNA base-pairing and hydrophobic interactions. We propose a mechanism for the hydrophobically-driven quantized self-assembly that is dependent on the polymer length and investigated the dynamic behavior of the quantized DNA cage assemblies. Thus, sequence-defined amphiphilic polymers can be efficiently employed to create orthogonal assembly modes, which synergistically combine hydrophobic and base-pairing interactions in the assembly of DNA nanostructures.

2.3 Results and Discussion

2.3.1 Design of DNA cages and sequence-defined polymer-DNA conjugates

DNA cages were chosen as scaffolds for 3D positioning of polymer-DNA conjugates and were assembled via a 'clip-by-clip' approach.[14, 18] The clips are 80-mer DNA strands composed of four single-stranded segments separated by a hexaethylene glycol (HEG) spacer. The 20-mer segment in the middle of the clip can hybridize to two outer 10-mer segments of the next clip. Cube (C) can be constructed from four clips where the fourth clip folds back and hybridizes to the first clip, cyclizing the cubic assembly (Figure 2.1). This structure presents eight 20-mer segments that are single-stranded and provide binding sites for polymer-DNA conjugates. In a similar approach, a trigonal prism (TP) and a pentagonal prism (PP) can be generated from three and five clips, respectively, and structures were generated in near-quantitative yields.

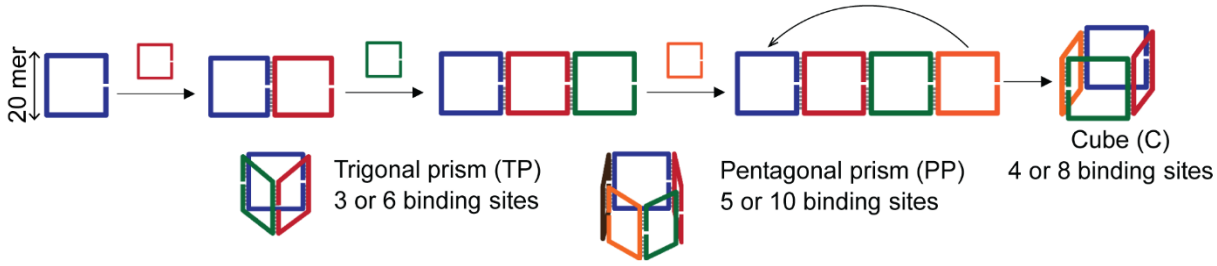

Figure 2.1 | Design of DNA cages. A cube can be constructed by a 'clip-by-clip' approach using four different 80-mer DNA clips. There is a maximum of 8 binding sites on the cube (C). Similarly, a trigonal prism (TP) and a pentagonal prism (PP) can be generated from three and five DNA clips.

To prepare sequence-defined DNA-polymer conjugates, hexaethylene (HE) and HEG were chosen as hydrophobic and hydrophilic monomers (Figure 2.2). These monomers were attached to a 19-mer DNA by an automated solid-phase synthesis using phosphoramidite chemistry.[19] The DNA segment, named A14, contains a five-thymidine (5T) spacer and 14-mer complementary sequence to the single-stranded segments on the cages. A series of HE homopolymer-DNA conjugates and HE/HEG copolymer-DNA conjugates was prepared to systematically investigate the design parameters of polymer-DNA conjugates for their assembly behavior on DNA cages (Figure 2.2).

We examined the purity of polymer-DNA conjugates by denaturing polyacrylamide gel electrophoresis (PAGE). The electrophoretic mobility of the homopolymers (HE-DNA) was inversely proportional to the number of HE repeats (Figure 2.2, left gel). In the case of copolymers (HE/HEG-DNA), the substitution of HE repeats with HEG repeats led to a higher degree of mobility change compared to HE-DNA conjugates (Figure 2.2, right gel). Interestingly, for the strands containing a constant number of 6 HE and 6 HEG repeats per chain, their electrophoretic mobility increased with the increasing number of adjacent HE repeats (for example, $(HE\text{-}HEG)_6$-A14 and $(HE_3\text{-}HEG_3)_2$-A14 in the right gel). These suggest that the HE chains extend in solution to a lesser extent than the HEG chains or, in other words, the HE chains could have a certain degree of chain folding. The difference in molecular behavior will translate into different assembly modes when organizing these polymer-DNA conjugates on the cages.

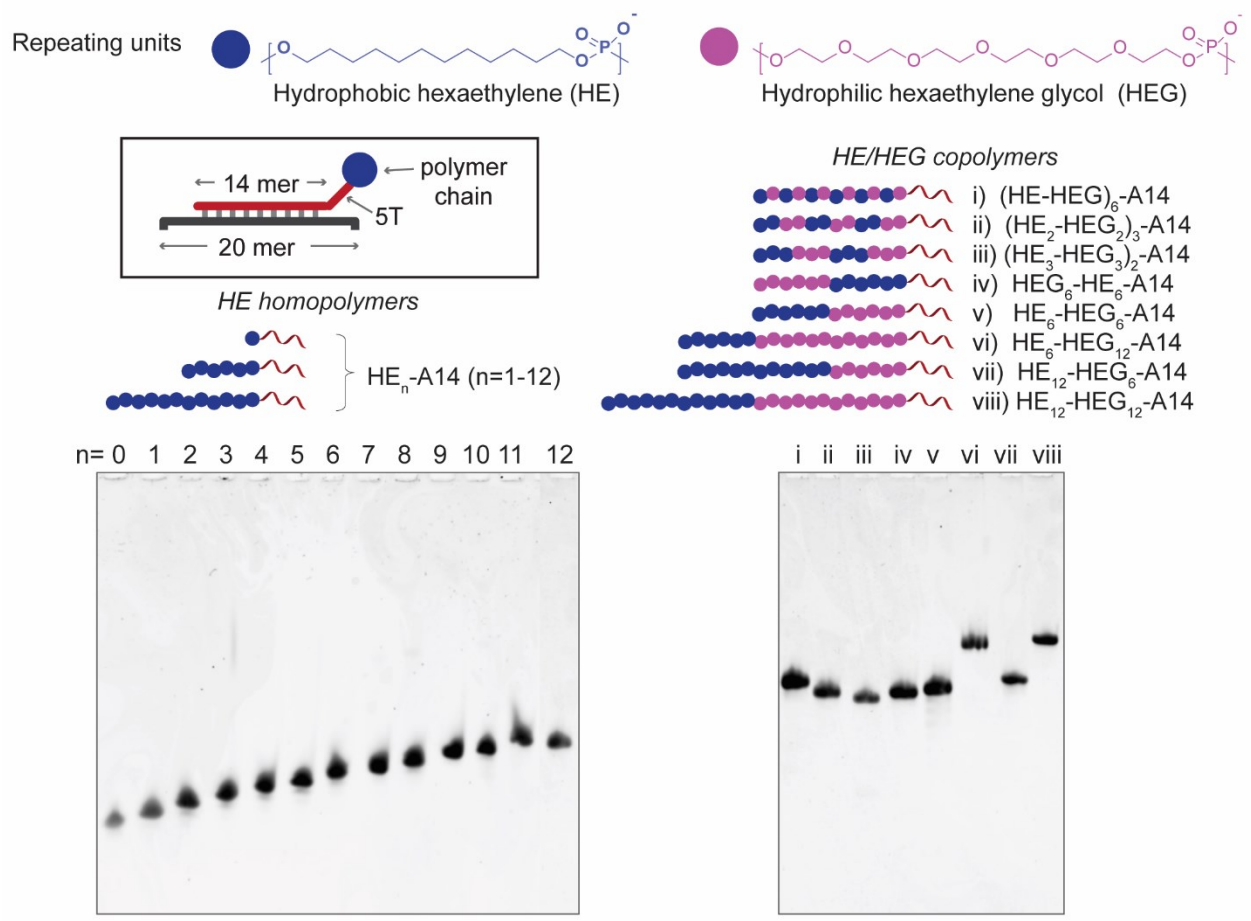

Figure 2.2 | Design of sequence-defined polymer-DNA conjugates. Hydrophilic hexaethylene glycol (HEG) and hydrophobic hexaethylene (HE) monomers were used to prepare the library of polymer-DNA conjugates. The 14-mer single-stranded segments on the 3' termini (colored in red) of polymer-DNA conjugates can hybridize to the single-stranded segments (colored in dark grey) on the cages. Denaturing PAGE (15%) shows good purity of monodisperse polymer-DNA conjugates.

2.3.2 Number of hydrophobic repeats on HE-DNA conjugates

2.3.2.1 Assembly of quantized cage structures

First, we introduced hydrophobic polymers HE_n-A14 on one face of a DNA cube and examined the effect of the chain length on their assembly with DNA cubes (Figure 2.3a). Cube C_4 has four identical single-stranded stretches on one of its faces, each complementary to the DNA strand of the DNA-polymer conjugates. The decoration of C_4 with four HE_n-A14 was achieved by mixing all components in the tris/acetate/magnesium (TAMg) buffer then thermally annealing from 95°C

to 4ºC over 4 hours. The formation of DNA nanostructures was followed by non-denaturing PAGE (Figure 2.3b).

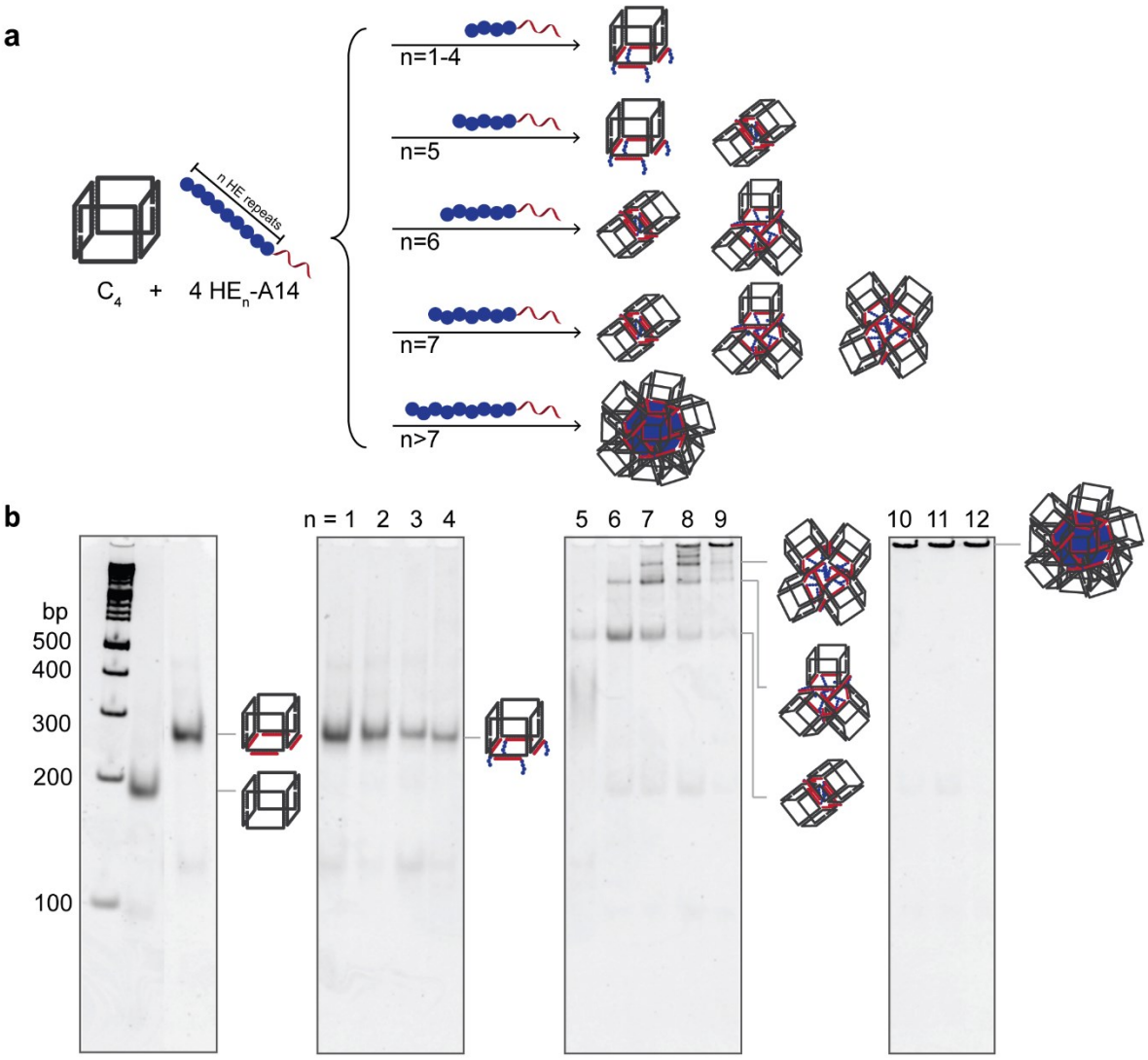

Figure 2.3 | Decoration of C_4 with HE-DNA conjugates. a) The assembly of C_4 with HE_n-A14 (n=1-12) generated quantized cube assembly. b) Non-denaturing PAGE (5%) shows the assembly of C_4, C_4/A14, and C_4/HE_n-A14. Finite cube aggregation number (cube dimer, trimer and tetramer) that scaled with the number of hydrophobic repeats was observed. Longer polymer chains led to the formation of cube micelles.

Addition of four complementary unmodified DNA strands (A14) to C_4 yielded a single band of lower electrophoretic mobility. Addition of strands with short hydrophobic chains to one face of C_4, from HE_1-A14 to HE_4-A14, resulted in single bands of similar electrophoretic mobility

compared to C_4/A14, consistent with a monomeric cube. The lack of difference in electrophoretic mobility for these cubes as the number of hydrophobic repeats in HE_n-A14 increases (n=1-4) is possibly consistent with some chain folding or interactions of these chains across one face of the cube in a way that does not impede the movement of the assemblies on the gel. Thus, when polymer-DNA conjugates with 1-4 hydrophobic repeats were added to one face of the cube, monomeric structures decorated with hydrophobic groups are formed.

When longer hydrophobic chains from HE_5-A14 to HE_{12}-A14 were added to C_4, the monomeric cube was no longer observed as a major product. Instead, we observed the combination of cubes into discrete aggregates, which we termed 'quantized cube assemblies'. This is likely due to the increased hydrophobicity of the polymer chains functionalized on the cubes, promoting interscaffold association of monomeric cubes to hide these hydrophobic chains in the hydrophobic core. Interestingly, their aggregation number correlated with the number of HE repeats. As the number of HE repeats increased, increasingly large higher-order structures formed. To our knowledge, this quantized assembly has not been previously observed for block copolymer assembly. It is possibly the result of the monodispersity of both the cubes and polymer-DNA conjugates. With a very long alkyl component in HE_{12}-A14 on one face of the cube, we observed the formation of a spherical micelle with a hydrophobic core and DNA cubes on its exterior, that we termed 'cube micelles'.

2.3.2.2 Structural characterization of quantized cube assemblies

We performed multiple characterization techniques to understand the molecular structures of C_4/HE_6-A14. First, the morphology of C_4/HE_6-A14 was elucidated by atomic force microscopy (AFM). Figure 2.4a reveals elongated structures of two spheres, which accounted for 76% of the population (cube dimers), and triangular structures with the edge length of ~30 nm (cube trimers). Some disaggregation of the higher-order structures into individual cubes (radius of ~8-9 nm) was also noted on the mica surface and can be attributed to strong electrostatic interactions between DNA and mica, which compete with the hydrophobic interactions holding together the DNA nanostructures.[15] The hydrodynamic size measured by dynamic light scattering (DLS, Figure 2.4b) shows that C_4/HE_6-A14 had a radius of ~7.5 nm, which was larger than C_4/AT (~6 nm). With low resolution, this technique was not able to differentiate between the two populations of higher-order

structures. We believe that the size discrepancy between the two techniques could be attributed to i) the adhesion of DNA to the mica surface and the drying effect, which are very likely to flatten the assemblies on the surface as implied by the AFM height of ~2 nm, and ii) the mathematical modeling in DLS measurement that bases on a hard sphere, which may not accurately reflect the actual size of the assembly.

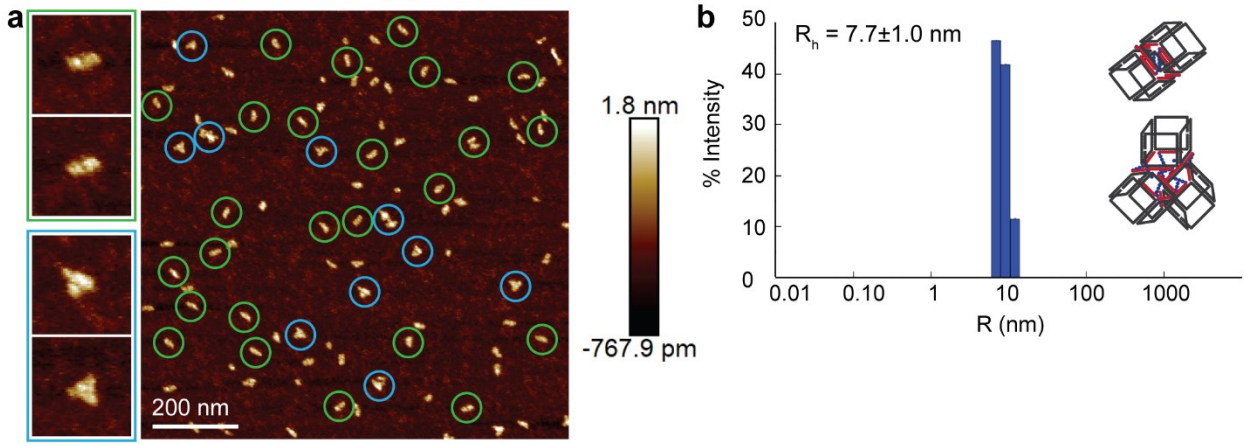

Figure 2.4 | Structural characterization of C_4/HE_6-A14. a) AFM image shows cube dimers (green circles) and cube trimers (blue circles) as the major products. b) Hydrodynamic radius (R_h) of C_4/HE_6-A14 measured by DLS was 7.7±1 nm.

To further study the cube aggregation number of C_4/HE_6-A14, we tagged each cube with a gold nanoparticle and preliminarily characterized them by transmission electron microscopy (TEM). The preparation of gold/cube constructs was performed according to the protocol developed by Edwardson *et al.*[20] as shown in Figure 2.5a (see Section 2.5.7 for experimental details). One side of the cubes was functionalized with DNA conjugates bearing cyclic disulfide moieties, where 10-nm gold nanoparticles were then attached through Au-S bonds.[20] This gold/cube construct was used to assemble with HE_6-A14 (Figure 2.5a). The cube aggregation number can be inferred from the number of AuNP observed in proximity. Figure 2.5b shows a population of the clusters containing 2 (13%) and 3 (6%) AuNPs in proximity. This technique was complicated by the instability of gold/cube constructs during sample handling, which led to significant amount of detached gold nanoparticles, and sample-surface (hydrophobic carbon-coated grids) interactions, which sometimes resulted in populations of higher-order aggregates. Nevertheless, the results of this method were consistent with those of AFM on the formation of dimers and trimers.

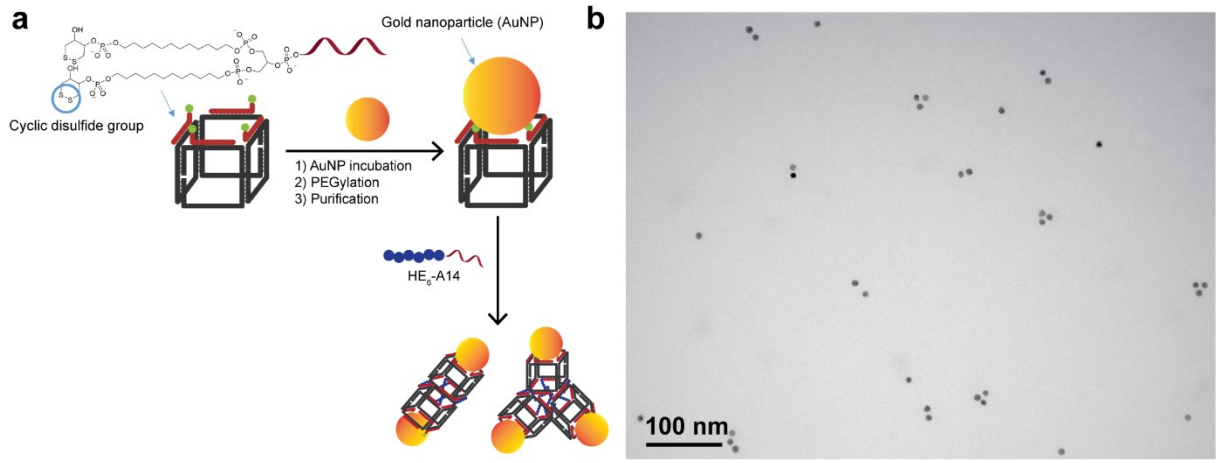

Figure 2.5 | Gold-nanoparticle labeling of C_4/HE_6-A14. a) Gold/cube constructs can be prepared by functionalizing one side of the cubes with cyclic disulfide moieties, which can form Au-S bonds with 10-nm gold nanoparticles. The constructs were then assembled with HE_6-A14. b) TEM image shows clusters of 2-4 AuNPs in proximity.

We also preliminarily attempted to count the cube aggregation number by single-molecule total internal reflection fluorescence microscopy (sm-TIRF, see Section 2.5.9 for experimental details). Each cube was monolabeled with a Cy3 fluorophore. To immobilize the assembly on the surface, Cy_3-C_4/HE_6-A14 was functionalized with biotin and deposited on a PEGylated glass coverslip which was pre-treated with streptavidin (Figure 2.6a). Upon prolonged exposure to the excitation light, the fluorophores bleach (Figure 2.6b) and the number of steps which correspond to sudden drops in fluorescence intensity over time can provide the number of Cy3 molecules presented in the assemblies (Figure 2.6c). We observed populations of monomer, dimer and trimer, again consistent with the previous two methods (Figure 2.6d). It is possible here that the sample-surface interactions can affect the structural integrity of the assembly, resulting in a large monomer proportion than observed by AFM. To prevent these undesired interactions, greater stability of the assembly is a requirement, and the possible strategies to increase the stability of DNA nanostructures will be discussed in Chapter 4.

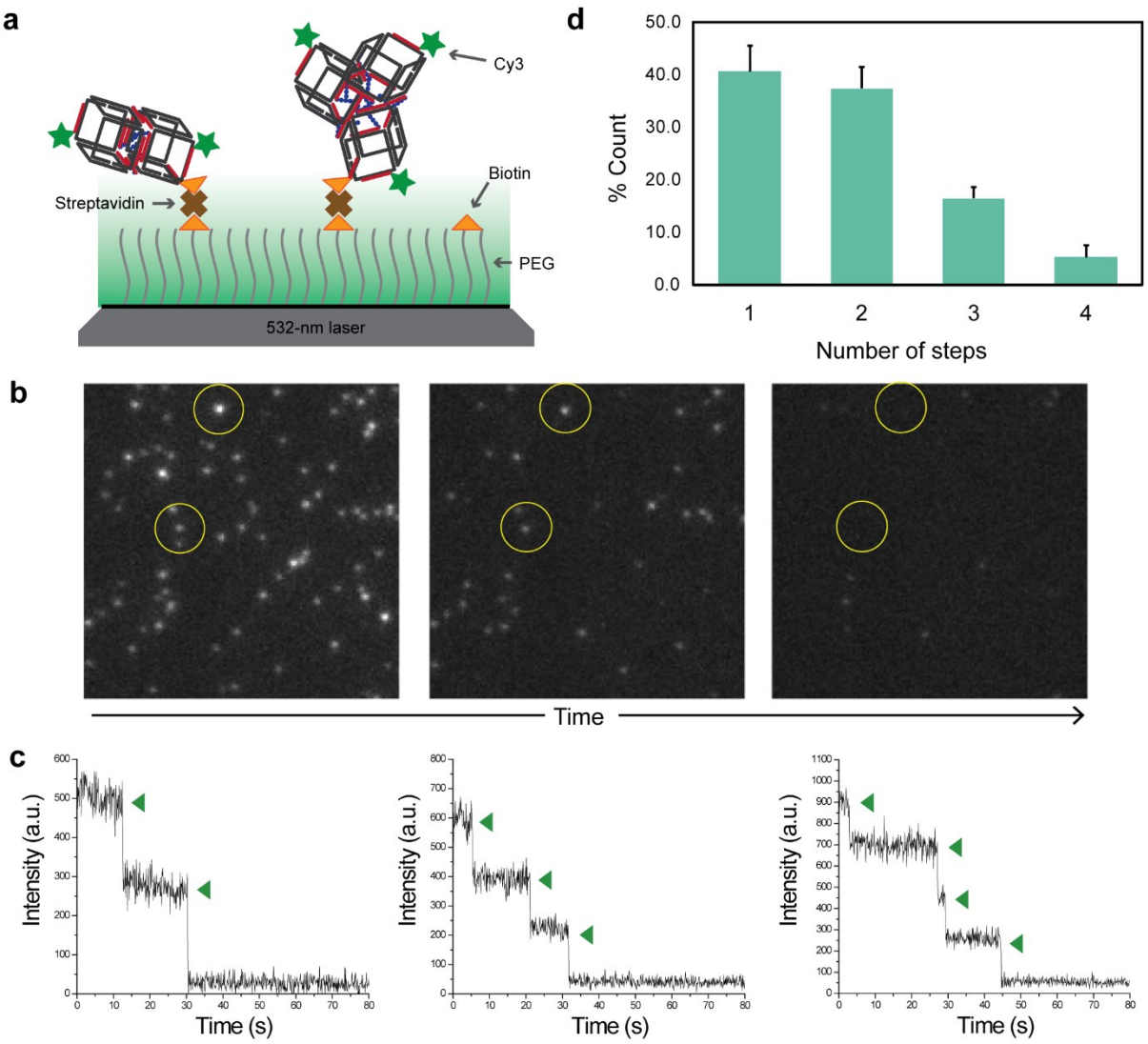

Figure 2.6 | Stepwise photobleaching of Cy3-labeled C_4/HE_6-A14. a) Stepwise photobleaching on sm-TIRF was performed by immobilizing Cy3-monolabeled C_4/HE_6-A14 on the PEGylated surface. The 532-nm laser was then used to bleach Cy3 dyes. b) There was a reduction in fluorescence intensity of individual particles over time. c) Examples of fluorescence intensity-time trajectories showing 2, 3 and 4 steps indicate that the particles have at least 2, 3 and 4 Cy3 dyes. d) The analysis shows a prevalence of monomeric and dimeric structures.

Altogether, these observations point towards dimeric and trimeric structures as the identity of the higher-order structures for C_4/HE_6-A14. We will provide further evidence of the cage aggregation number by gel electrophoresis in Section 2.3.5.3.

2.3.3 Sequences and block lengths of HE/HEG-DNA conjugates

The monomer sequence along polymer chains can significantly influence polymer's physical properties. To investigate this effect on DNA cages, we assembled cube C_4 with a series of copolymers of different sequences, all containing a constant number of 6 hydrophobic HE and 6 hydrophilic HEG repeats per chain. This includes alternating chains of single monomers (HE-HEG)$_6$-A14, two monomers (HE_2-HEG_2)$_3$-A14, three monomers (HE_3-HEG_3)$_2$-A14 and six monomers (Figure 2.7a). The latter polymer has two sequences; HEG_6-HE_6-A14, in which the hydrophobic portion is in between the DNA and HEG chains, and HE_6-HEG_6-A14, in which the hydrophobic portion is at the chain-end. Only the latter structure of this copolymer series was previously shown to assemble into micellar aggregates, whereas the other structures remain as unimers in solution.[19]

The decoration of HE/HEG-A14 on C_4 yielded monomeric structures (Figure 2.7a, with one exception, see below). In Figure 2.7b, the electrophoretic mobility of these structures on non-denaturing PAGE increased with HE block length, consistent with higher structure compaction. In this case, the local hydrophobicity of individual HE segments is most likely to increase with HE block length, which can potentially enable more efficient folding of the hydrophobic chains and make the structures increasingly compact, thus increasing their electrophoretic mobility (Figure 2.7c). Interestingly, these polymers did not result in cube aggregation, despite their relatively high hydrophobic content. It is of note that this behavior is a direct result of sequence control of the polymers, where regular block copolymers would not be able to generate this property.

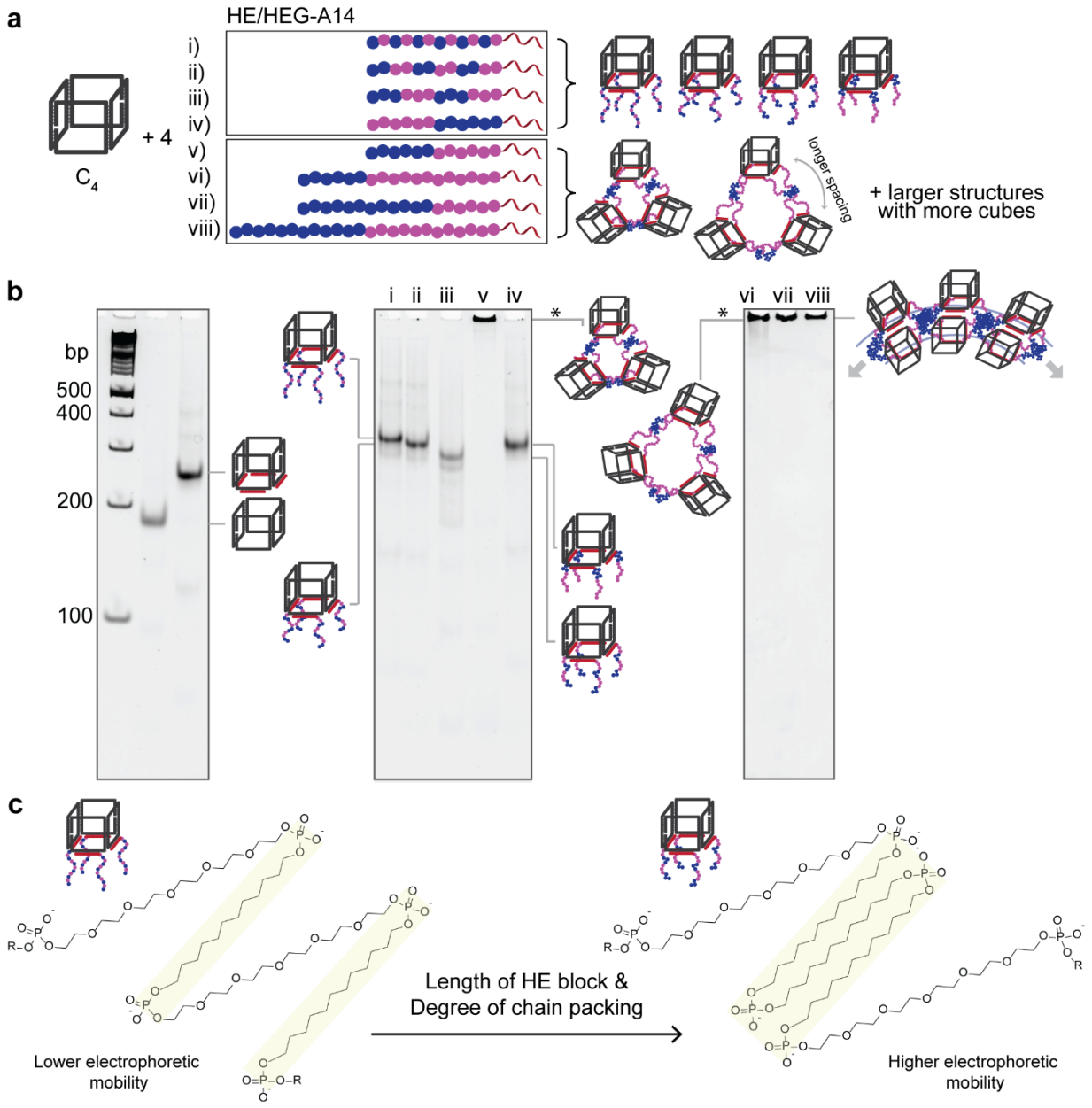

Figure 2.7 | Decoration of C_4 with HE/HEG-DNA. a) The polymer sequences of HE/HEG-A14 can dictate whether their assembly with C_4 generates a monomeric cube or form higher-order structures. b) Non-denaturing PAGE (5%) shows the assembly of C_4, C_4/A14, and C_4 with HE/HEG-A14. We note that only the schematic of 3-vertice ring is shown here, but rings of other sizes were also the assembly products of C_4/HE_6-HEG_6-A14 and C_4/HE_6-HEG_{12}-A14. c) Possible modes of HE-chain packing were highlighted in light yellow. The degree of HE-chain packing most likely increases with HE block length.

The exception to this monomeric assembly was C_4/HE_6-HEG_6-A14, which gave higher-order structures that appeared as a non-penetrating band on the gel (Figure 2.7b). Its AFM image (Figure 2.8a, top left) reveals polygonal rings containing 3-5 vertices with the edge length of ~30 nm. The size of the structures was also supported by DLS measurements (R_h~14 nm). We believe that the flexible HEG block can serve as a spacer between hydrophobic HE domains and the cubes. The HE blocks of HE_6-HEG_6-A14 can form hydrophobic domains by interacting with the chains on the other cubes side-to-side, resulting in polygonal rings.

As the HEG block might be a crucial parameter for the diameter of the ring-like structures, we hypothesized that a longer HEG block could create structures with larger spacing between the cubes. The hydrodynamic radius of C_4/HE_6-HEG_{12}-A14 (~18 nm) was indeed significantly larger than that of C_4/HE_6-HEG_6-A14. However, in this case, we also observed disassembly of some of the structures on the mica surface by AFM, which is likely due to the larger hydrophilic-to-hydrophobic content of this polymer (Figure 2.8a, bottom left). Still, the presence of clusters of the ~12 nm spheres in the proximity suggests that the morphology of C_4/HE_6-HEG_{12}-A14 should be similar to C_4/HE_6-HEG_6-A14.

To further increase the stability of this hydrophobic interscaffold association, we assembled C_4/HE_{12}-HEG_6-A14, which has a longer hydrophobic HE block than C_4/HE_6-HEG_6-A14. This molecule generated a high yield of well-defined doughnut-shaped structures with hollow features in the middle as observed by AFM (Figure 2.8a, top right). Further increasing the length of HEG block (C_4/HE_{12}-HEG_{12}-A14) also showed the efficient formation of ring structures (Figure 2.8a, bottom right). The radii of both structures were comparable (~20 nm/~27 nm (DLS/AFM) for C_4/HE_{12}-HEG_6-A14; ~21/~24 nm (DLS/AFM) for C_4/HE_{12}-HEG_{12}-A14). TEM characterization also confirmed the presence of relatively homogeneous spherical structures (radius ~12 nm for C_4/HE_{12}-HEG_6-A14 and ~15 nm for C_4/HE_{12}-HEG_{12}-A14, Figure 2.8b). It should be noted that the sizes obtained from AFM and DLS were similar to one another, and were significantly larger than those obtained by TEM, suggesting that the structures may be ring-like in solution. The possible explanation for the smaller sizes measured by TEM is a collapse of the structures on the hydrophobic carbon-coated grids and the drying of DNA structures under high vacuum.[21]

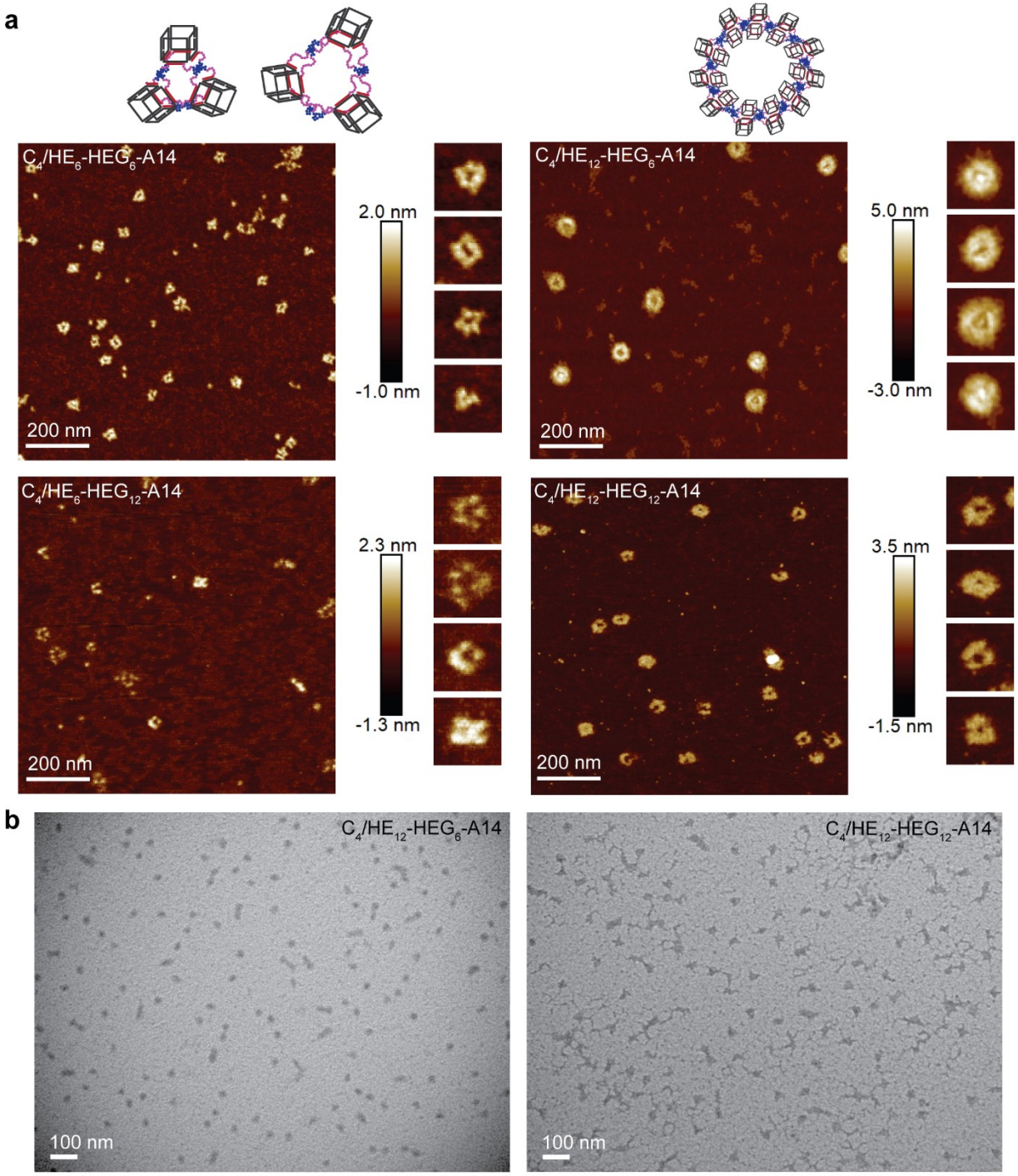

Figure 2.8 | Structural characterization of C_4 decorated with HE/HEG-DNA. a) AFM images of C_4 assembled with HE_n-HEG_m-A14 (n=6,12 and m=6,12) show polygonal rings and doughnut-shaped DNA-cage rings as the assembly products for short (n=6) and long (n=12) HE blocks. HEG block (n=12) can also increase the spacing between the cubes. b) TEM images show spherical structures for C_4/HE_{12}-HEG_6-A14 but irregular aggregates for C_4/HE_{12}-HEG_{12}-A14.

The estimated yields of the ring structures obtained by the analysis of AFM images were high in all cases, except for the sequence in which the HE block is short (6 repeats) as compared to the HEG block (12 repeats). Thus, we can conclude that the addition of HEG repeats provides a spacer between DNA scaffolds and yields ring structures. To our knowledge, the assembly of DNA cages into doughnut-shaped DNA-cage rings is unprecedented. It is interesting that, despite the flexibility of both HE and HEG chains, we observed discrete cube assemblies here, rather than linear or randomly branched oligomers.

2.3.4 Orientation of polymer chains on DNA cages

2.3.4.1 Assembly with HE-DNA conjugates

We previously reported that 8 dendritic HE chains attached on both faces of a DNA cube result in an intrascaffold association, with the ability to encapsulate molecules in the internal hydrophobic environment.[14] We were interested in probing the dependence of this phenomenon on polymer architecture and chain length. Cube C_8 was designed to allow the decoration of 8 polymer chains on both faces (Figure 2.9a). In Figure 2.9b, short HE chains generated monomeric structures with a sharp band on non-denaturing PAGE. Interestingly, as the number of hydrophobic repeats increased, the electrophoretic mobility of this band increased (rather than decreased) and then remained constant at HE_4-A14 until HE_6-A14. The structure of C_8/HE_6-A14 was characterized by AFM, which revealed mostly single spherical structures with a diameter comparable to C_8. DLS measurements (Figure 2.9c) showed that C_8/HE_6-A14 (R_h=6.4±0.3 nm) was smaller than C_8/A14 (R_h=7.1±0.6 nm). A likely assembly mode here is that HE chains (HE_4-HE_6) collapse and create a hydrophobic core inside the cube, resulting in a more compact structure similar to that of dendritic HE chains.[14] The formation of hydrophobic core in C_8/HE_6-A14 was further supported by the encapsulation of hydrophobic Nile Red fluorescent dye.[22] Compared to a cube decorated with unmodified DNA, there was a significantly higher fluorescence signal of Nile Red in C_8/HE_6-A14 (Figure 2.9d).

HE_7-A14 started to form a cube dimer, and longer hydrophobic chains generated higher-order structures as the major products. Both AFM and DLS measurements suggest that extended structures were formed in the cases of C_8/HE_8-A14 and C_8/HE_{12}-A14 (see Section 2.5.6 and 2.5.7

for AFM and DLS). Thus, up to 6 HE repeats per polymer chain can be accommodated in the core of DNA cube, beyond which the interscaffold assembly sets in.

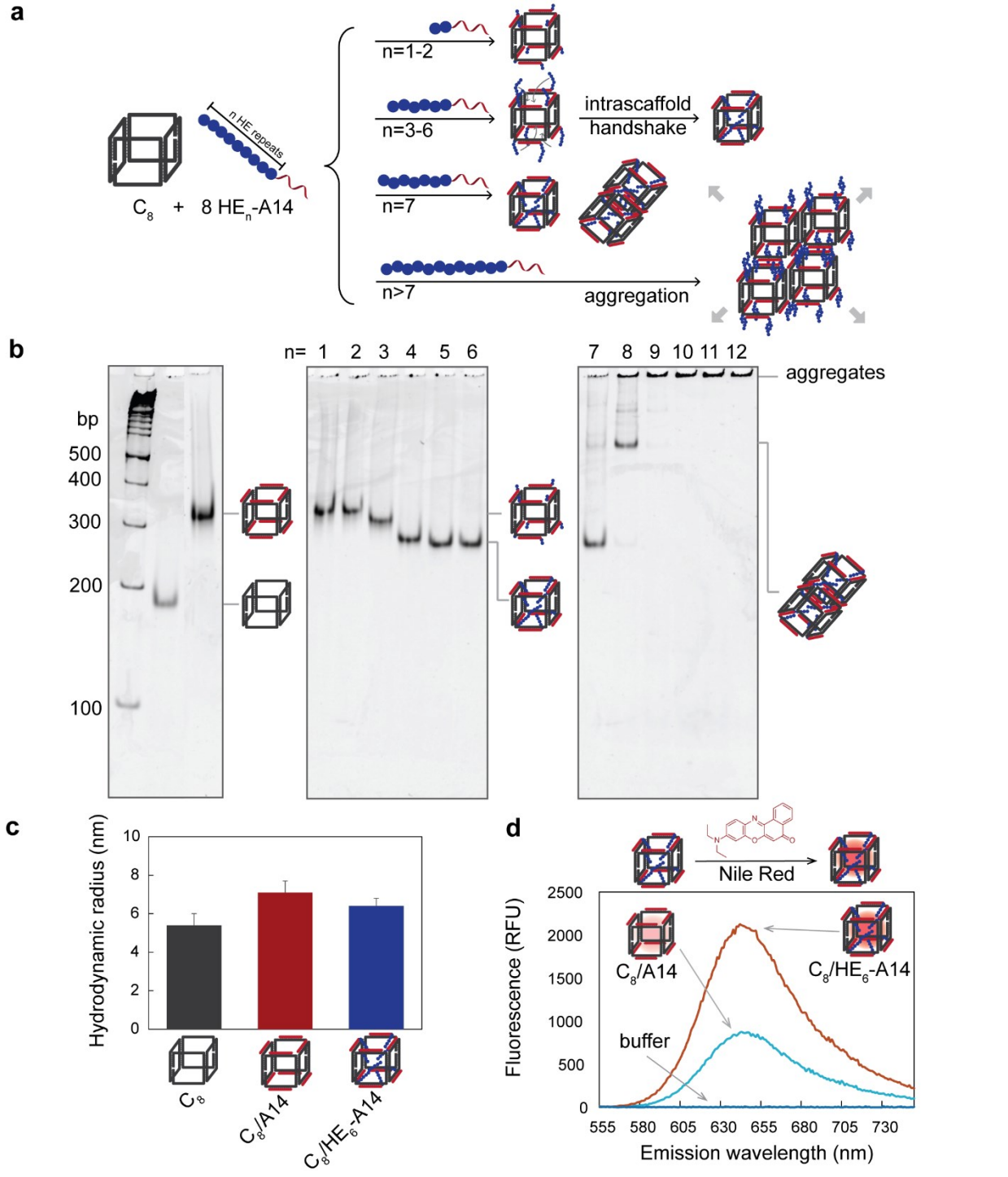

Figure 2.9 | Decoration of C8 with HE-DNA. a) Short to intermediate HE chain lengths of HE_n-A14 (n=3-6) preferred an intrascaffold association and created a hydrophobic core inside the cube.

Longer HE chain lengths generated cube aggregates. b) Non-denaturing PAGE (5%) shows the assembly products of C_8, C_8/A14, and C_8/HE_n-A14. c) Hydrodynamic radius of C_8/HE_6-A14 was smaller than C_8/A14. d) There was a higher fluorescence intensity of Nile Red encapsulated inside the hydrophobic core of C_8/HE_6-A14 than in an empty cavity of C_8/A14.

2.3.4.2 Assembly with HE/HEG-DNA conjugates

We then carried out the assembly of C_8 with HE/HEG-A14 and HE_n-HEG_m-A14 (Figure 2.10a). In general, the assembly behaved in a similar trend to the assembly with C_4. Monomeric cubes were generated as the only products for C_8/HE/HEG-A14, except for C_8/HE_6-HEG_6-A14, which gave non-penetrating materials (Figure 2.8b). The HE/HEG chains are less likely to interact with one another within the cube's cavity, as indicated by lower electrophoretic mobility of C_8/HE/HEG-A14 when compared to C_8/A14.

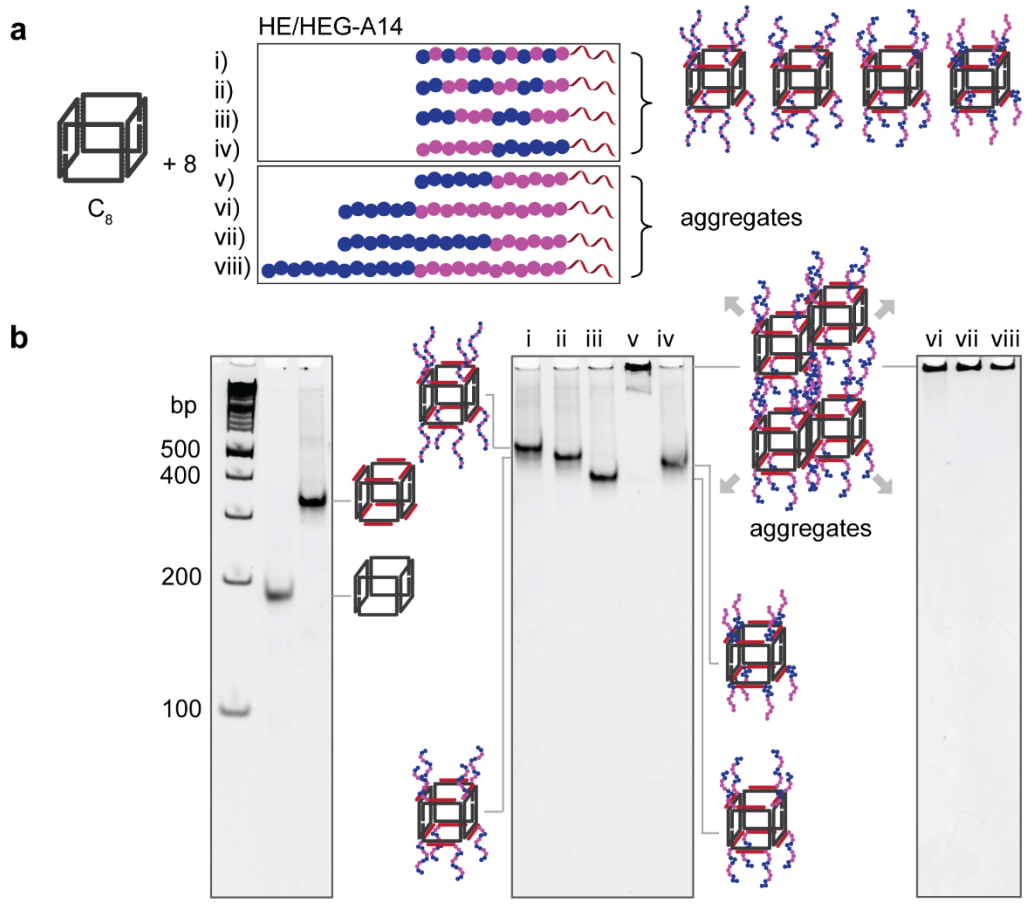

Figure 2.10 | Decoration of C_8 with HE/HEG-DNA. a) C_8 assembly with HE/HEG-A14 generated monomeric cubes or aggregates, similar to C_4 assembly with HE/HEG-A14. b) Non-denaturing PAGE (5%) shows the assembly of C_8, C_8/A14, and C_8 with HE/HEG-A14.

We expected the formation of large aggregates from C_8/HE_n-HEG_m-A14 because of two-face assembly and the spacing provided by HEG blocks. Unexpectedly, AFM images in Figure 2.11a show that all generated relatively well-defined spherical structures with the size (radii ~13 nm for C_8/HE_6-HEG_6-A14 and ~23-25 nm for other structures) being in a comparable range to those of C_4/HE_n-HEG_m-A14. In contrast, DLS measurements indicated that the hydrodynamic radii of these structures were more than 90 nm, except for C_8/HE_6-HEG_6-A14. TEM images of C_8/HE_{12}-HEG_m-A14 (Figure 2.11b) show considerably large aggregates with the radii of ~50-70 nm as well as small spherical structures. The size discrepancy of AFM is most likely due to low binding affinity of large hydrophobic cube aggregates on the hydrophilic mica surface, leading to smaller size than expected and low particle density. We can conclude that C_8/HE_n-HEG_m-A14 forms cube aggregates. An improvement in the stability of these nanostructures can be helpful for further structural characterization.

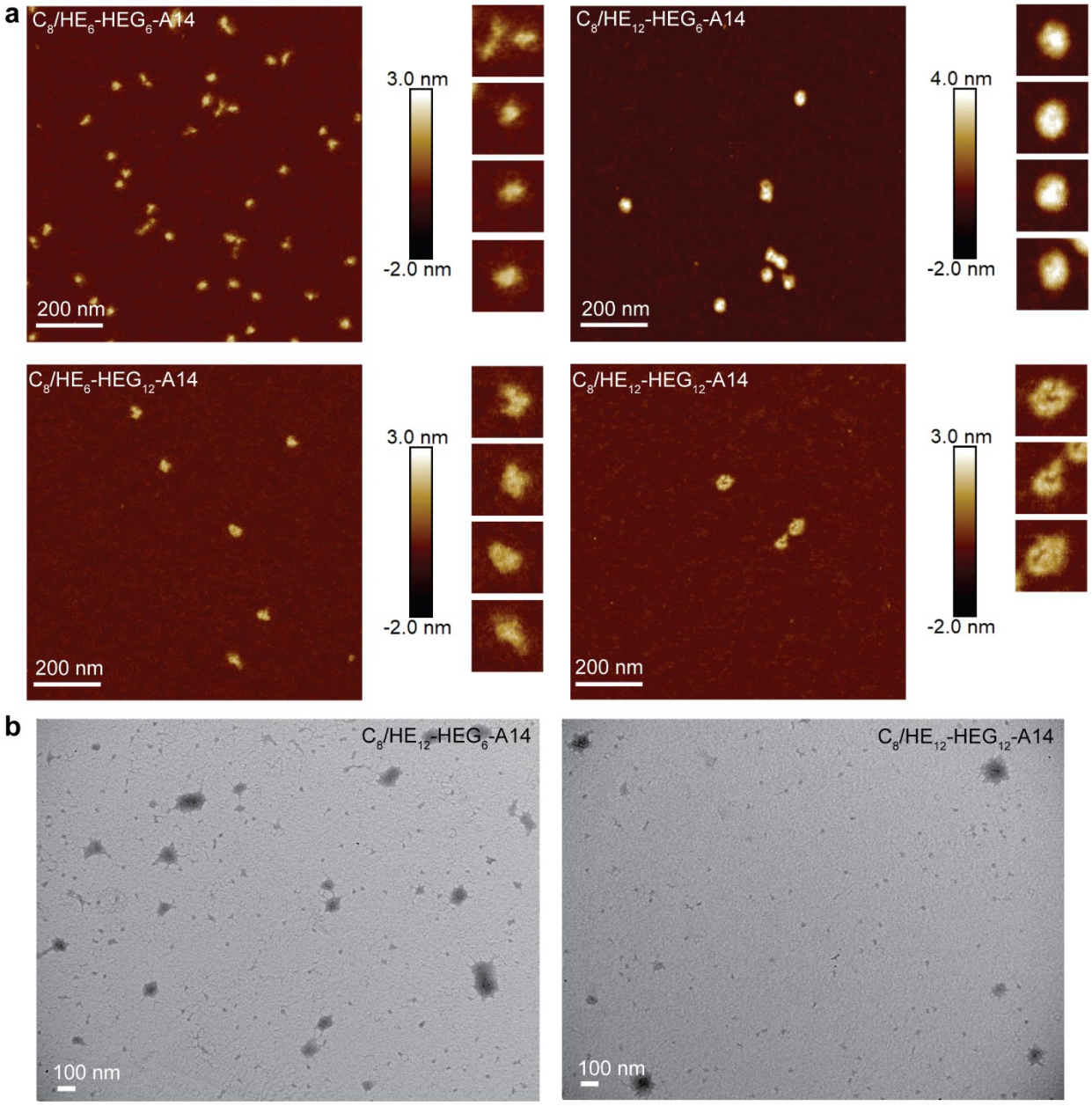

Figure 2.11 | Structural characterization of C_8 decorated with HE/HEG-DNA. a) AFM images of C_8 assembled with HE_n-HEG_m-A14 (n=6,12 and m=6,12) show small aggregates and DNA-cage rings as the assembly products for short (n=6) and long (n=12) HE blocks. b) TEM images show big aggregates and small spherical aggregates for both C_8/HE_{12}-HEG_6-A14 and C_8/HE_{12}-HEG_{12}-A14.

2.3.5 Structures and sizes of DNA cages

2.3.5.1 Assembly of trigonal and pentagonal prisms with HE-DNA conjugates

The geometric variation of DNA cages offers another design parameter to control the number and orientation of polymers on DNA cages. It allows us to answer the question: can the cage geometry change the onset of assembly? To investigate this effect, trigonal prism (TP) and pentagonal prism (PP) were assembled with HE_n-A14 (n=1-12) in an analogous manner to the cube. With these chains on one face, the aggregation numbers for TP_3 and PP_5 were indeed different from those of C_4. In the case of HE_6-A14, TP_3 gave dimer, trimer, and tetramer (Figure 2.12a) while C_4 and PP_5 gave only dimer and trimer (Figure 2.12b). Also, cage dimers started forming from HE_5-A14 to HE_9-A14 in the case of TP_3 and C_4, but only from HE_5-A14 to HE_7-A14 in PP_5. This can be explained by the smaller size of TP, allowing more cages to fit around the hydrophobic core. Thus, aggregation number can also be tuned by the cage geometry.

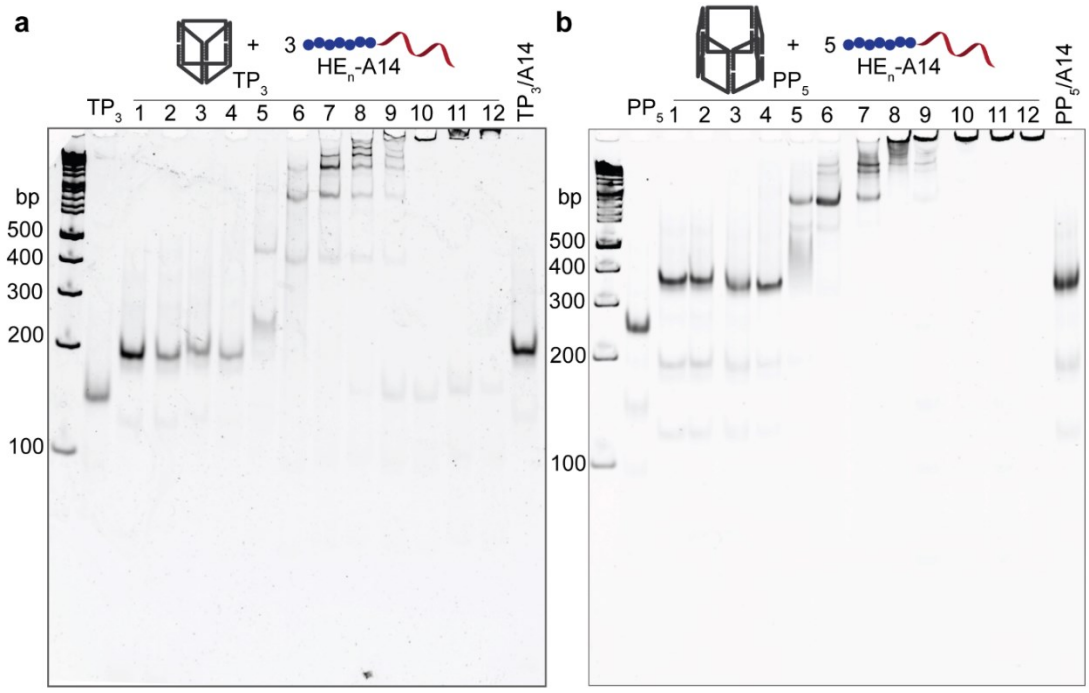

Figure 2.12 | Decoration of TP_3 and PP_5 with HE-DNA. Non-denaturing PAGE (5%) shows the assembly of a) TP_3 and b) PP_5 with HE_n-A14 (n=1-12). Monomeric cages were generated from HE_1-A14 to HE_5-A14. Small higher-order structures started forming from HE_5-A14 to HE_9-A14.

With HE_n-A14 on both faces of DNA cage, we expect that the smaller TP could accommodate shorter polymer chains in its core than the cube, and the larger PP would encapsulate larger polymer chains (Figure 2.13). Indeed, TP_6 could accommodate lengths up to HE_5 within its core (capacity of 30 HE repeats), before the cage started to dimerize with HE_6. This transition occurred from HE_6 to HE_7 for C_8 (capacity of 48 HE repeats), and from HE_7 to HE_8 for PP_{10} (capacity of 70 HE repeats).

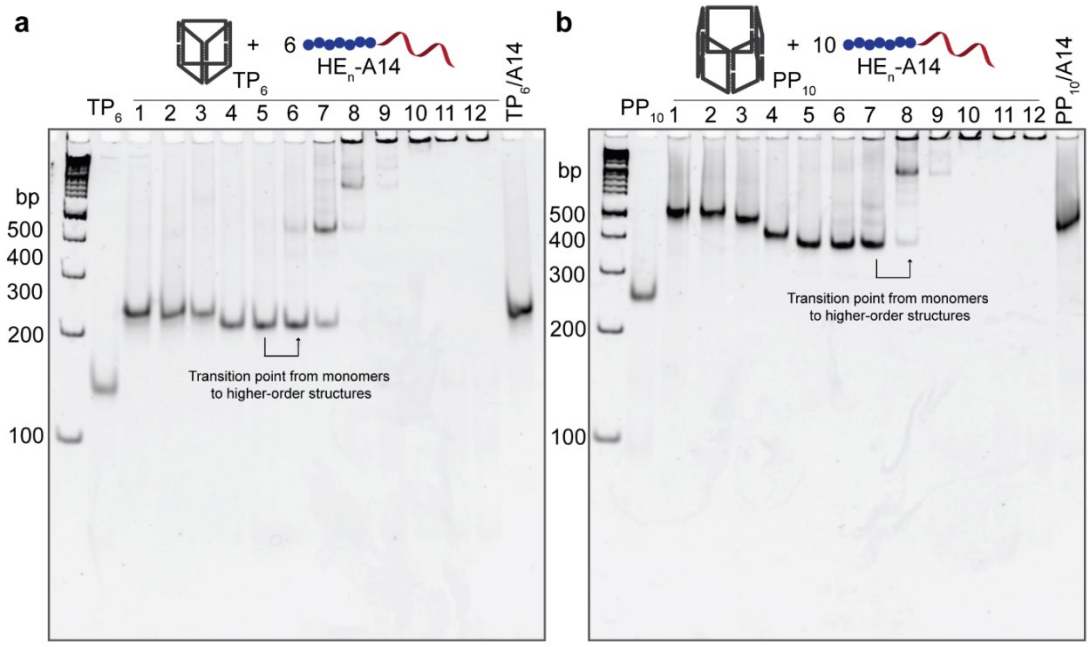

Figure 2.13 | Decoration of TP_6 and PP_{10} with HE-DNA. Non-denaturing PAGE (5%) shows the assembly of a) TP_6 and b) PP_{10} with HE_n-A14 (n=1-12). The structural compaction due to the formation of a hydrophobic core inside the cage was also evidenced by increased electrophoretic mobility of monomeric bands. A higher number of HE repeats led to aggregation.

2.3.5.2 Loading capacity of guest molecules

The larger cages and higher total number of HE repeats per cage can in principle increase the loading capacity of hydrophobic guests. To verify this, we compared the loading capacity of three different cages decorated with HE_6-A14 (see Section 2.5.10 for experimental details). Briefly, the cage assemblies were incubated with Nile Red for 19 hours to allow the dyes to diffuse into the hydrophobic core. After removal of non-encapsulated Nile Red, the concentrations of DNA cages and Nile Red were quantified by gel electrophoresis and fluorescence measurement, respectively. This allows us to determine Nile Red loading capacity per cage. Figure 2.14 shows an

approximately 2.5-fold increase in Nile Red loading capacity when the cage size and the total number of HE_6-A14 increased: 9.1±1.7 molecules per PP_{10}/HE_6-A14, 3.6±1.2 molecules per C_8/HE_6-A14 and 1.5±0.4 molecules per TP_6/HE_6-A14

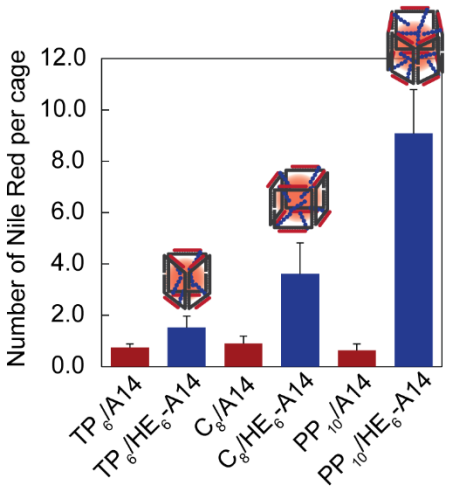

Figure 2.14 | Loading capacity of Nile Red in different cages. There was a ~2.5-fold increase in loading capacity with increased cage size. Red bars represent double-stranded cages, while blue bars denote DNA cages functionalized with HE_6-A14.

We had previously shown that HE_6-A14 conjugate forms micelles with a diameter of ~13 nm.[19] Yet if this polymer is fully stretched, it has a ~7 nm long DNA portion and a ~12 nm long hydrophobic chain. Considering the efficient chain packing of polyethylene[23] and the fact that HE chains are punctuated by phosphate groups, it is possible that they fold upon themselves to enable tight packing between adjacent HE repeats[19] in a similar way to the arrangement of phospholipid bilayers and bola-amphiphiles.[24-25] This would result in a smaller micelle size and a tighter, more densely packed hydrophobic core. The same tight chain packing may be present in the core of DNA-micelle cages, which may explain their relatively low loading capacity. It has been shown that the crystallinity of the hydrophobic core of block copolymer micelles tends to decrease the loading capacity for guest molecules, because of lower chain mobility that hinders the diffusion of hydrophobic molecules.[26-28]

2.3.5.3 Estimation of cage aggregation number

With the complete sets of quantized cage assembly, we would like to estimate the cage aggregation number by increasing the separation of higher-order structures on non-denaturing PAGE at lower gel percentage (3.5%). Figure 2.15 shows the assembly of cages with $HE_{6\text{-}8}$-A14, where higher-order bands were clearly resolved. We note that lowering the gel percentage makes it difficult to handle the gel, so we mainly used 5-6% PAGE to follow the assembly formation in other sections. Comparing the assembly bands to DNA ladder allows the estimation of relative 'molecular weight' for individual higher-order structures.

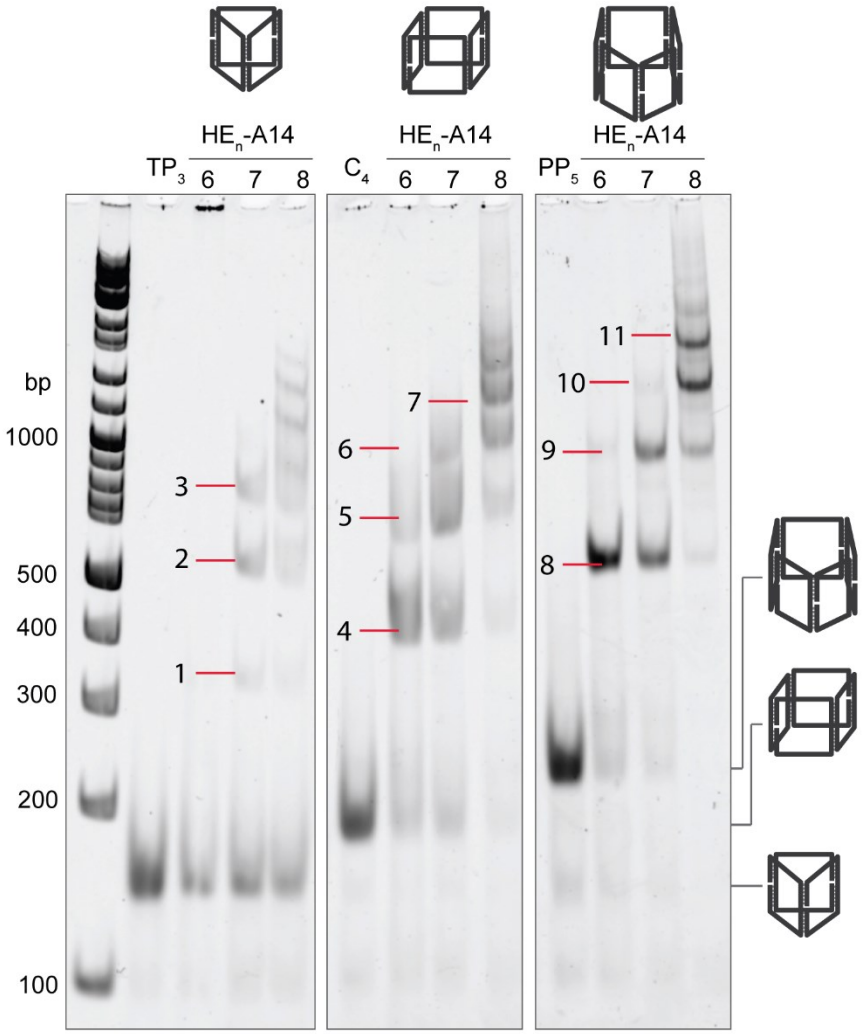

Figure 2.15 | Estimation of cage aggregation number. The assembly of TP_3, C_4, and PP_5 with HE_n-A14 (n=6-8) was analyzed by non-denaturing PAGE (3.5%). The bands corresponding to higher-order structures were well-resolved, and their 'molecular weight' can be estimated from DNA ladder on the leftmost lane.

The first higher-order band of C_4/HE_6-A14 (band 4, middle gel) was assigned as the cube dimer. By comparing the position of this band to DNA ladder, its estimated size was 420 bp. Assuming that one polymer-decorated cube can migrate by ~210 bp, we can calculate the cube number in other higher-order bands (bands 5-7), which corresponded to trimer, pentamer, and hexamer. It should be noted that the smaller higher-order structures such as cube dimer might be more compact than the larger higher-order structures such as cube pentamer, possibly due to less electrostatic repulsion between DNA structures on their corona. Thus, an alternative reference is based on monomeric cubes. This structure typically appears at ~250 bp based on other gels, which gave ~250 bp for one cube component. This was used to calculate cube aggregation number of the higher-order bands (bands 5-7), which corresponded to trimer tetramer, and pentamer. The analysis of other cages (TP_3 and PP_5) is summarized in Table 2.1.

Table 2.1 | Estimation of cage aggregation numbers by non-denaturing PAGE.

Cage	**Band number**[a]	**Size (bp)**	**Cage aggregation number**	
			Monomeric cage method[b]	Cage dimer method[c]
TP_3	1	340	1.7	**2.0**
	2	530	2.7	3.1
	3	800	4.0	4.7
C_4	4	420	1.7	**2.0**
	5	640	2.6	3.0
	6	1050	4.2	5.0
	7	1320	5.3	6.3
PP_5	8	520	1.5	**2.0**
	9	900	2.6	3.5
	10	1400	4.0	5.4
	11	1750	5.0	6.7

[a] band numbers are according to Figure 2.15.
[b] calculated from the electrophoretic mobility of monomeric cages (200, 250 and 350 bp for TP_3, C_4, and PP_5).
[c] calculated from the half value of the electrophoretic mobility of cage dimers (170, 210 and 260 bp for TP_3, C_4, and PP_5).

The estimation of cage aggregation number by monomeric cage method seems to be more consistent for all cage types. Therefore, we believe that the increment by one (such as dimer, trimer, tetramer, and others) would be more likely to represent the choice of the quantized cage assembly. We can conclude that C_4/HE_6-A14 generates dimer and trimer, further supporting the analysis in Section 2.3.2.2. A combination of dimer, trimer, and tetramer are the assembly products of C_4/HE_7-A14, while C_4/HE_8-A14 yields dimer, trimer, tetramer, and pentamer. C_4/HE_9-A14 to C_4HE_{12}-A14 give non-penetrating bands, which are potentially composed of incrementally higher cube aggregation numbers.

2.3.5.4 Assembly of trigonal and pentagonal prisms with HE/HEG-DNA conjugates

In the same manner to the cube, TP and PP were assembled with HE/HEG-A14 containing copolymers of 6 HE and 6 HEG repeats of different sequences. In Figures 2.16a and 2.16b, the decoration of HE/HEG-A14, with one exception (see below), on either one face or both faces of the cages generated monomeric cages.

Aggregate formation was observed in all cages decorated with HE_m-HEG_n-A14 (Figures 2.16c and 2.16d). AFM images (insets in Figures 2.16a and 2.16b) reveal the formation of polygonal rings for both TP_3/HE_6-HEG_6-A14 and PP_5/HE_6-HEG_6-A14. The size of these rings was similar to that of C_4/HE_6-HEG_6-A14, which was previously discussed in Section 2.3.3.

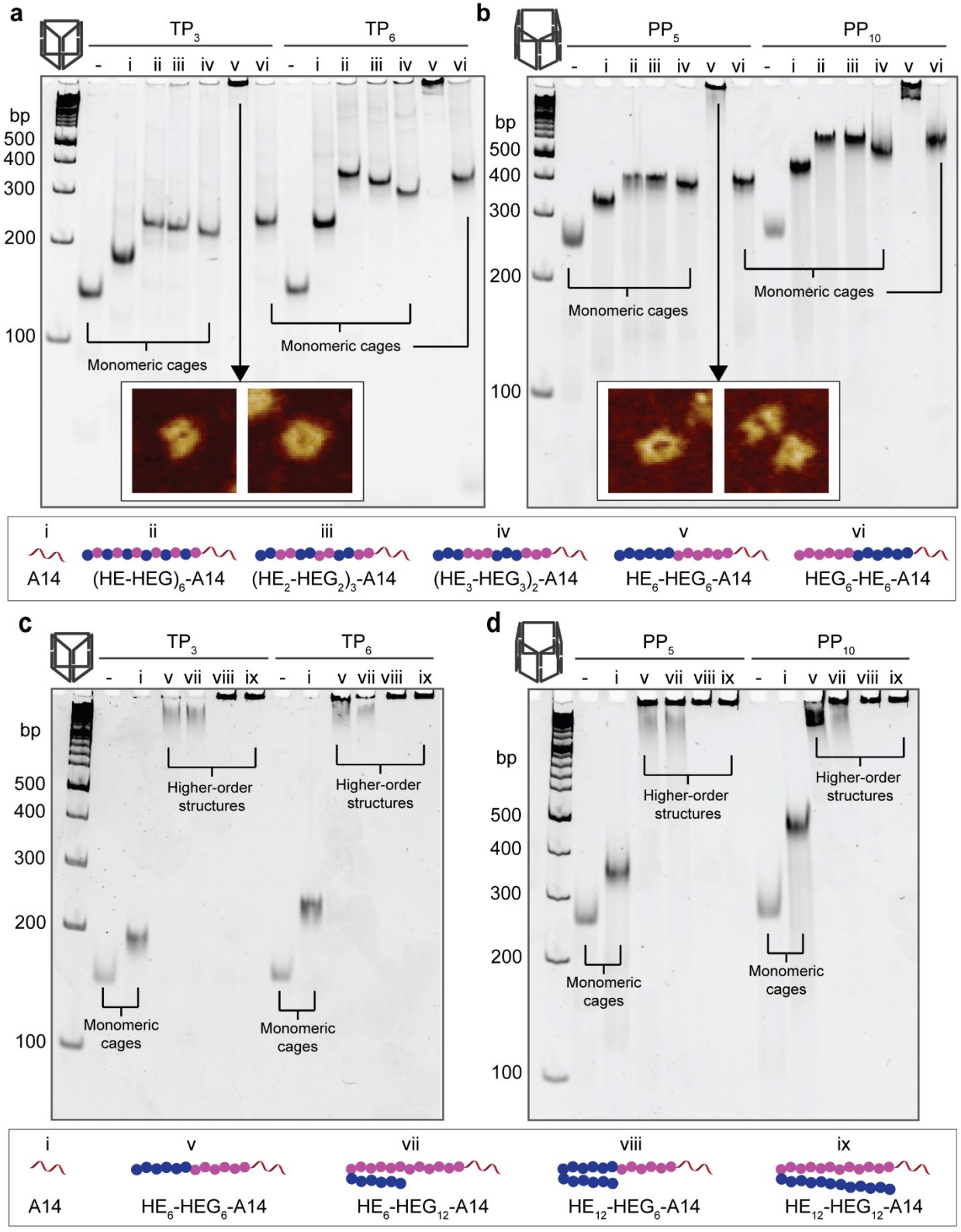

Figure 2.16 | Decoration of TP and PP with HE/HEG-DNA. Non-denaturing PAGE (5%) of a) TP_3/TP_6 and b) PP_5/PP_{10} assembly with HE/HEG-A14 shows that monomeric cages formed in all copolymer sequences, except HE_6-HEG_6-A14 that led to higher-order structures. On the other

hand, c) TP_3/TP_6 and d) PP_5/PP_{10} assembly with HE_n-HEG_m-A14 (n=6,12 and m=6,12) all generated higher-order structures. The insets in the top gel panel show AFM images of TP_3/HE_6-HEG_6-A14 and PP_{10}/HE_6-HEG_6-A14.

2.3.6 Assembly dynamics and thermodynamic properties

2.3.6.1 Concentration-dependent assembly and stability

The cage concentration for all assemblies described above was 125 nM. We were interested to find out whether changing the concentration could affect the assembly products. In Figure 2.17a, C_4 assembly with HE_n-A14 at high cube concentration (10-fold increase) generated higher-order structures for C_4/HE_6-A14 and C_4/HE_7-A14, similarly to lower concentration. However, the assembly products were not as clean as those assembled directly at a lower concentration. In the case of HE_8-A14, we observed mostly non-penetrating materials, suggesting that the assembly is concentration-dependent.

We also examined the stability of C_4/HE_6-A14 upon dilution. It was assembled at 125 nM relative to C_4 and diluted with the buffer. Figure 2.17b indicates good stability of C_4/HE_6-A14 up to 40-fold dilution (~3 nM), which was the sample concentration used in the stepwise photobleaching study in Section 2.3.2.2.

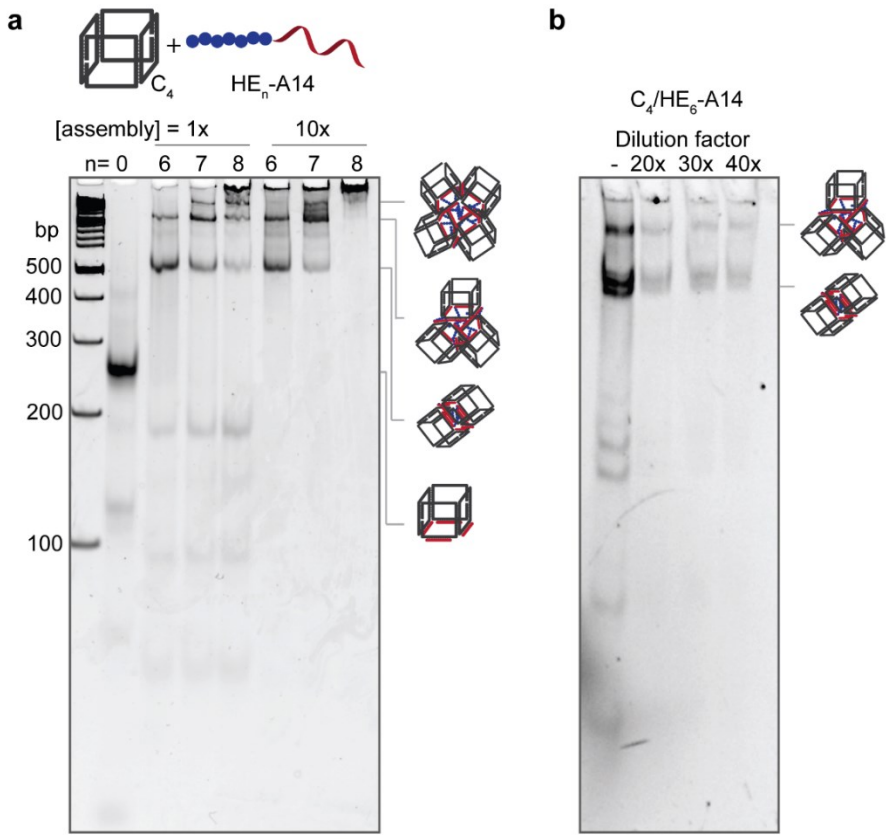

Figure 2.17 | Concentration-dependent assembly and stability of C_4 with HE-DNA. a) Non-denaturing PAGE (5%) shows that small higher-order structures could form in C_4/HE_6-A14 and C_4/HE_7-A14 at high cube concentration (10-fold increase). b) C_4/HE_6-A14 was stable against the dilution down to ~3 nM as evaluated by non-denaturing PAGE (5%).

2.3.6.2 Divalent-cation concentration-dependent assembly

The micellization of HE_n-A14 conjugates is dependent on divalent cations. This is because the HE repeats are punctured with phosphate groups, and HE chain association results in electrostatic repulsion. Addition of Mg^{2+} to HE_6-A14 and HE_{12}-A14 can induce the aggregation of these polymer-DNA conjugate, whereas adding EDTA to remove Mg^{2+} results in the de-aggregation.[19] Thus, a screening of Mg^{2+} concentrations in quantized cube assembly could provide some insights into the role of Mg^{2+} in the assembly process. We note that 12.5 mM Mg^{2+} was used in a typical assembly. Figure 2.18b validates that C_4/HE_7-A14 assembly is dependent on Mg^{2+} concentrations. No higher-order assembly formed at extremely low Mg^{2+} concentration (0-2 mM). Interestingly, cube dimer started forming and was the only product at 4 mM Mg^{2+}, whereas cube trimer and cube tetramer were generated at 6 mM and 12 mM Mg^{2+}, respectively. At higher Mg^{2+} concentrations,

the formation of larger higher-order structures was promoted as indicated by a gradual increase in the band intensity of cube trimer. We believe that the presence of Mg^{2+} is most likely to shield the electrostatic repulsion between phosphate groups on the polymer chains, allowing hydrophobic associations of HE_7 chains to happen. Larger higher-order structures will require a larger amount of Mg^{2+} to stabilize higher number of polymer chains in the hydrophobic domains (8 HE_7 chains for cube dimer and 16 HE_7 chains for cube tetramer). At extremely high Mg^{2+} concentrations (200 mM), the product was no longer efficiently generated.

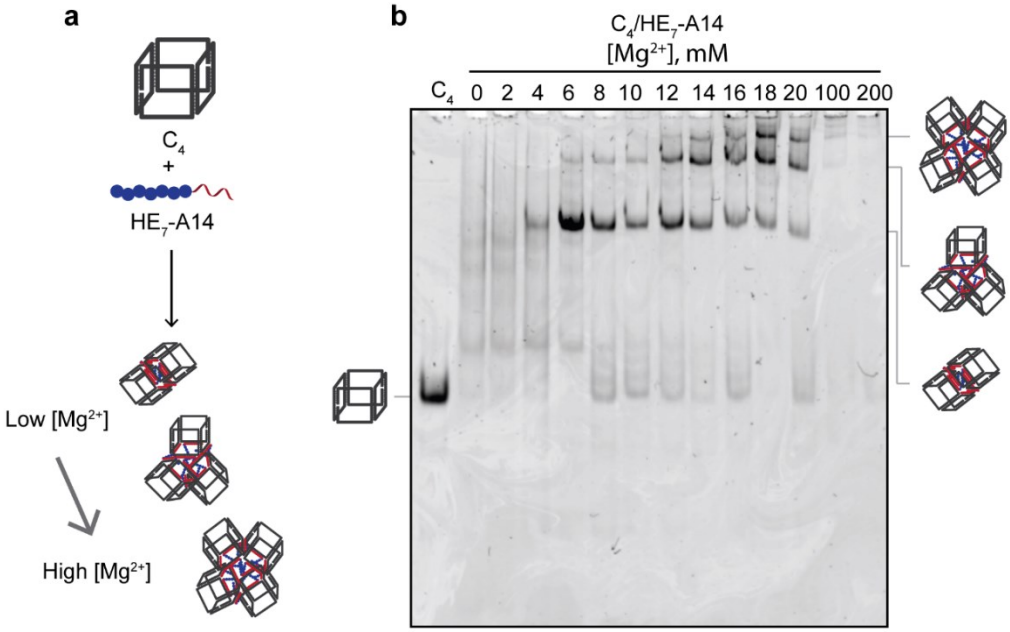

Figure 2.18 | Mg^{2+}-dependent assembly of C_4/HE_7-A14. a) The formation of larger higher-order structures was favorable at higher Mg^{2+} concentrations. b) Non-denaturing PAGE (5%) shows the assembly of C_4/HE_7-A14 in TA buffer supplemented with 0-200 mM $MgCl_2$.

2.3.6.3 Polymer concentration-dependent assembly

The concentration of polymer-DNA conjugates could control whether the conjugates will aggregate, depending on their critical micelle concentration, above which the micellization happens.[14] In our system, decorating HE_n-A14 on DNA cages likely increases the effective concentration of HE chains, favoring the interscaffold or intrascaffold associations of HE chains. It is of note that we used 1.5 equivalents of polymer-DNA conjugates per binding site on DNA

cage (rather than 1 equivalent) for all assemblies. Excess polymer-DNA conjugates were usually added to ensure complete hybridization of polymer-DNA conjugates to the cages.

To study the concentration effect of polymer-DNA conjugate, we screened a concentration range of HE_n-A14 in their assembly with C_4. Figure 2.19 shows that the binding of short HE chains to the cubes was efficient at all tested concentrations. However, the formation of higher-order structures with longer HE-chain lengths was concentration-dependent. The percentage of cube dimer of C_4/HE_5-A14 increased when using 8 equivalents of HE_5-A14 per cube (i.e., 2:1 polymer:binding site), and cubes of HE_8-A14 and HE_{10}-A14 showed higher-order structure at this ratio. Thus, we were able to tune product distributions by HE_n-A14 concentration, where the larger higher-order structure can be promoted by using a higher ratio of HE_n-A14 relative to C_4. It might be possible that excess HE_n-A14 conjugates were incorporated into the hydrophobic core of higher-order structures.[14] This could increase both the hydrophobicity and size of hydrophobic core, which will be more favorable to form larger higher-order structures.

Another aspect of this experiment is that we observed some degree of binding cooperativity of long HE_n-A14 to DNA cube. In the left panel of Figure 2.19, there were three major species for C_4 with 4.8 equivalents of HE_6-A14, which could be assigned as naked cube, cube dimer, and cube tetramer. There were also faint bands of C_4 containing one and two HE_6-A14, followed by the smearing. This suggests that there is a certain cooperativity degree in the binding of HE_6-A14 to C_4. In contrast, we observed no cooperative binding for C_4/HE_5-A14, where there were multiple bands corresponding to intermediate structures (C_4 containing one, two, three and more HE_5-A14).

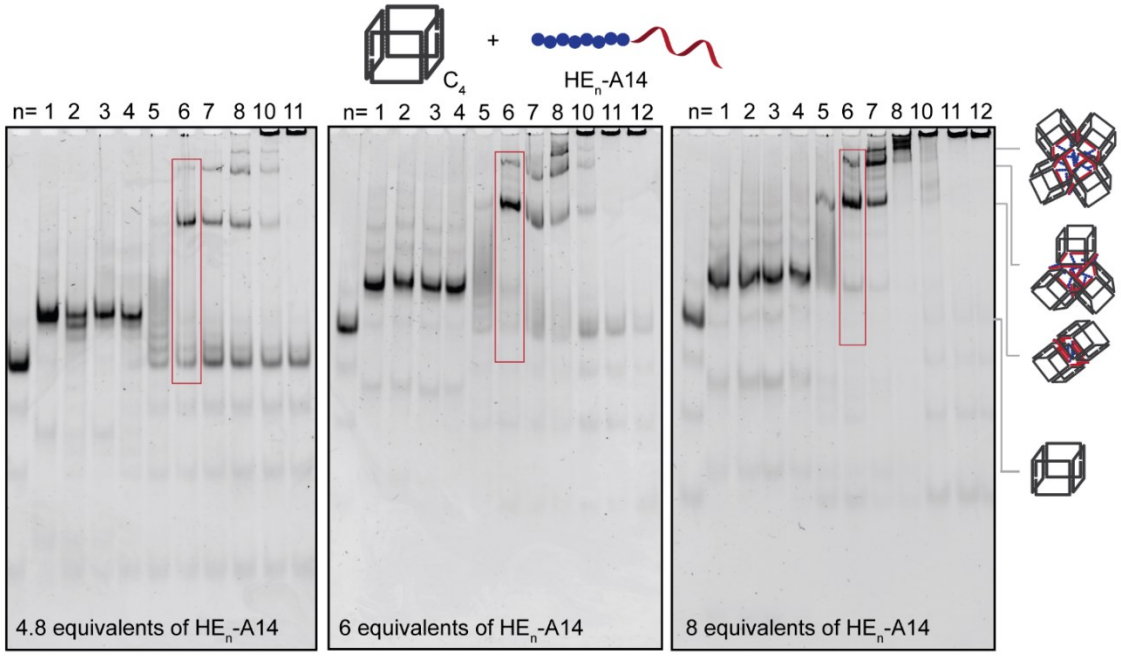

Figure 2.19 | Effect of HE-DNA concentration on quantized cube assembly. Non-denaturing PAGE (5%) shows C_4 assembly with HE_n-A14 (n=1-12, except 9) at different concentrations. The actual HE_n-A14 concentrations were 600, 750 and 1000 nM for 4.8, 6 and 8 equivalents per cube (125 nM). The formation of large higher-order structures could be promoted by using a higher ratio of HE_n-A14 relative to C_4. Red boxes show the binding cooperativity of HE_6-A14 to C_4.

We also performed titration experiments of C_4 with HE/HEG-A14 to study the assembly cooperativity. In Figure 2.20, higher HE/HEG-A14 concentrations promoted the formation of fully-bound cubes. However, the band ladder corresponding to C_4 containing 1-4 strands of HE/HEG-A14 was observed, suggesting that the binding of HE/HEG-A14 to C_4 was not cooperative. One exception is HE_6-HEG_6-A14, which showed a behavior consistent with 'all-or-none' binding. We had previously shown (Section 2.3.3) that this is the only structure that forms doughnut-shaped nanostructures.

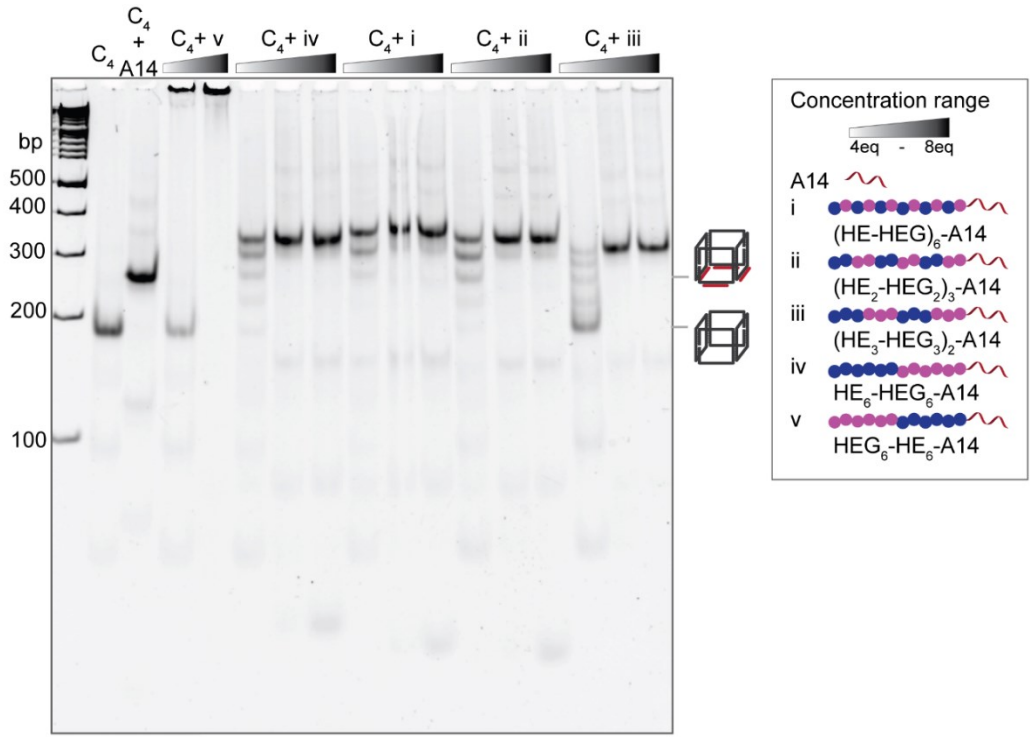

Figure 2.20 | Non-cooperative binding of HE/HEG-A14 to C_4. Non-denaturing PAGE (5%) shows the titration of C_4 with HE/HEG-A14. The concentrations of HE/HEG-A14 were 4, 6 and 8 equivalents per cube, except for HE_6-HEG_6-A14 where 4 and 8 equivalences were used. No binding cooperativity was observed for all HE/HEG-A14, except HE_6-HEG_6-A14.

We were interested in examining whether there was cooperative binding of HE_6-A14 to C_8 due to the strong intrascaffold association of HE_6 chains to form a hydrophobic core. To validate this hypothesis, we titrated C_8 with HE_6-A14. (Figure 2.21b). The all-or-none binding, as indicated by the co-existence of naked cubes and DNA-micelle cubes, was observed at sub-stoichiometric amounts of HE_6-A14 relative the cube. This suggests the cooperative binding of HE_6-A14 to C_8. On the other hand, the titration of C_8 with unmodified A14 strands led to multiple bands on the gel (Figure 2.21a). These intermediate structures (C_8 containing one, two, three and more A14 strands) indicate no binding cooperativity of A14 to C_8. This suggests that DNA base-pairing and hydrophobic interactions are acting synergistically, providing greater stability and assembly cooperativity to DNA-micelle cubes and some quantized cube assemblies.

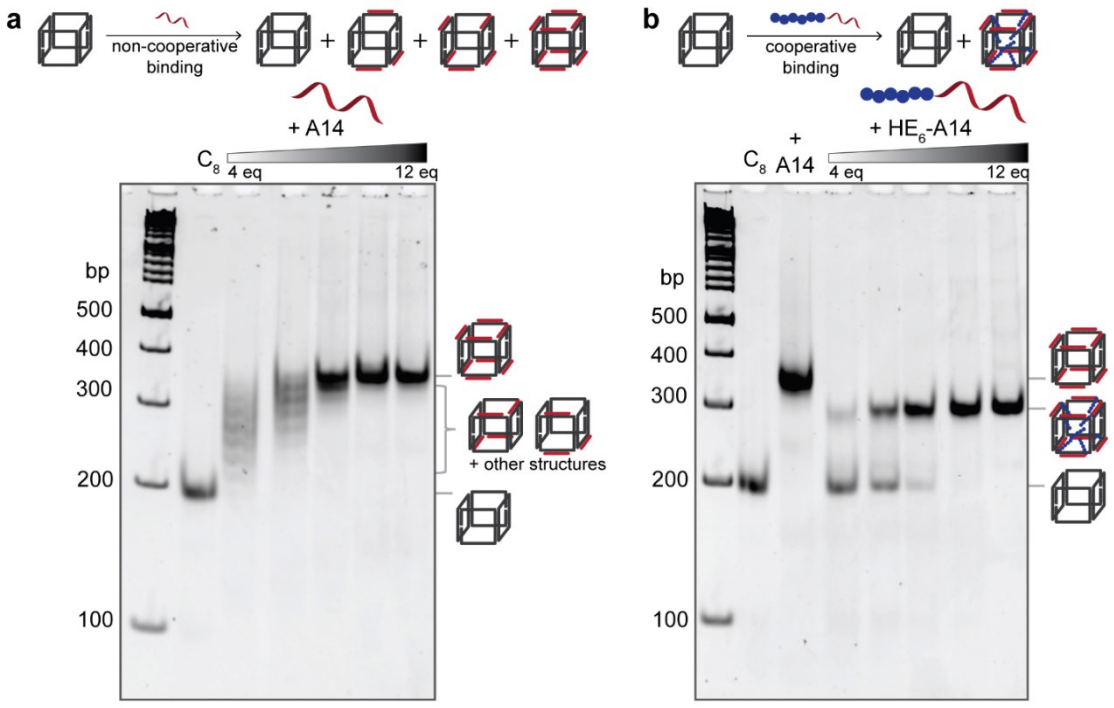

Figure 2.21 | Cooperative binding of HE_6-A14 to C_8. Non-denaturing PAGE (5%) shows the titration of C_8 with a) unmodified A14 and b) HE_6-A14. The concentrations of A14 or HE_6-A14 were 4, 6, 8, 10 and 12 equivalents per cube. All-or-none binding behavior was observed only in C_8/HE_6-A14, suggesting the binding cooperativity induced by hydrophobic interactions.

2.3.6.4 Cage combination and isolation of quantized assembly

We were interested to study the possibility of shape discrimination, i.e., whether two DNA cages of the same geometry would prefer to associate together via hydrophobic interactions. In a one-pot annealing of HE_6-A14 with both trigonal prism TP_3 and cube C_4 strands, we found no selectivity in the cage structures: for example, homo- and heterodimer combinations of TP_3-TP_3, TP_3-C_4 and C_4-C_4 were observed (Figure 2.22b, left gel). However, if TP_3-TP_3 and C_4-C_4 homodimers were separately assembled and mixed at room temperature for 30 minutes, no observable exchange occurred. (Figure 2.22b, right gel). This indicates the stability of the preformed assemblies at room temperature. At 37°C, scrambling started to happen, as indicated by faint bands of heterodimers (Figure 2.22b, middle gel). Because of its stability at room temperature, it is possible to isolate the heterodimer (for example, TP_3-C_4) to generate anisotropic nanoparticles, whose free single-stranded faces can be of different sequences and can provide unique sites for further functionalization.

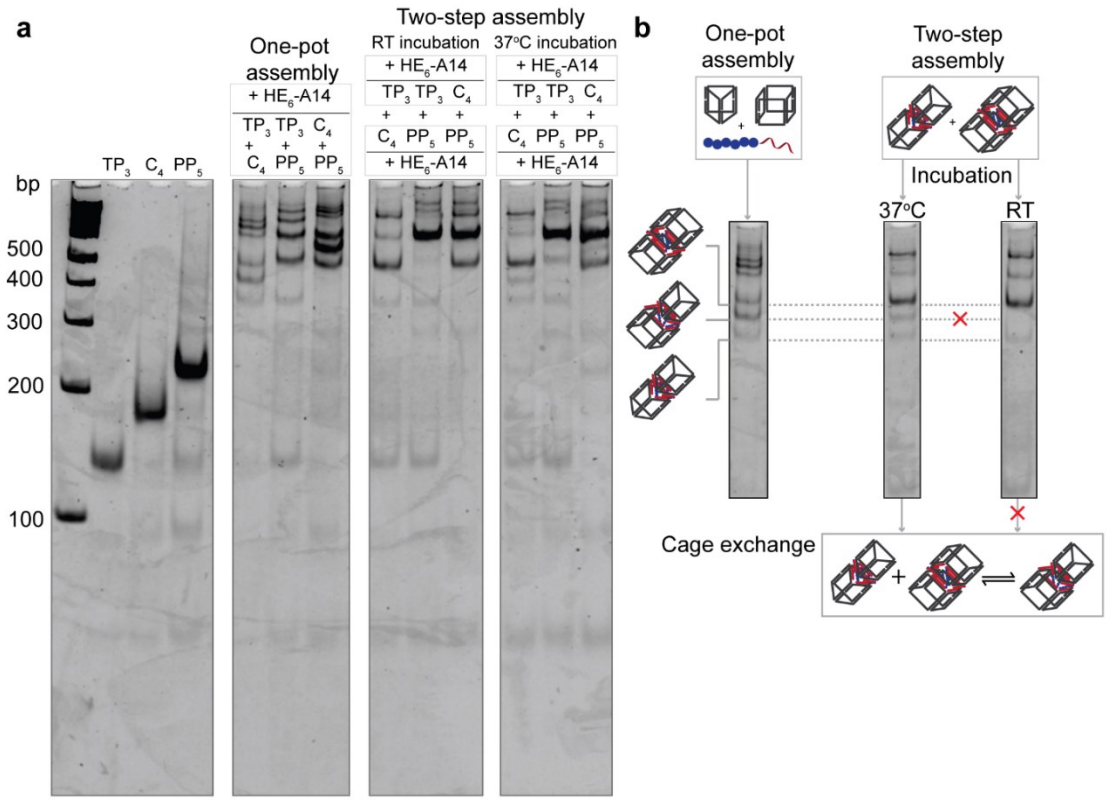

Figure 2.22 | Combination of DNA cages and their assembly with HE$_6$-A14. a) Non-denaturing PAGE (5%) shows that one-pot annealing of two choices of cages with HE$_6$-A14 generated all cage combinations. Mixing separately-preformed cage$_1$/HE$_6$-A14 and cage$_2$/HE$_6$-A14 at room temperature did not result in the cage exchange. However, 37°C incubation led to scrambling. b) As representative examples, only the bands corresponding to dimers were labeled for the combination of TP$_3$ and C$_4$ with HE$_6$-A14.

We also isolated the quantized cube assemblies of C$_4$/HE$_6$-A14 and C$_4$/HE$_7$-A14 by gel electrophoresis under non-denaturing conditions. Individual higher-order structures were collected by soaking the gel slices of target structures in the buffer. In Figure 2.23, all isolated higher-order bands were stable and survived the isolation process. Cube dimer did not seem to re-equilibrate back to the mixtures of the higher-order structures. Cube trimer and tetramer were stable at room temperature and that structures were mostly maintained at 37°C.

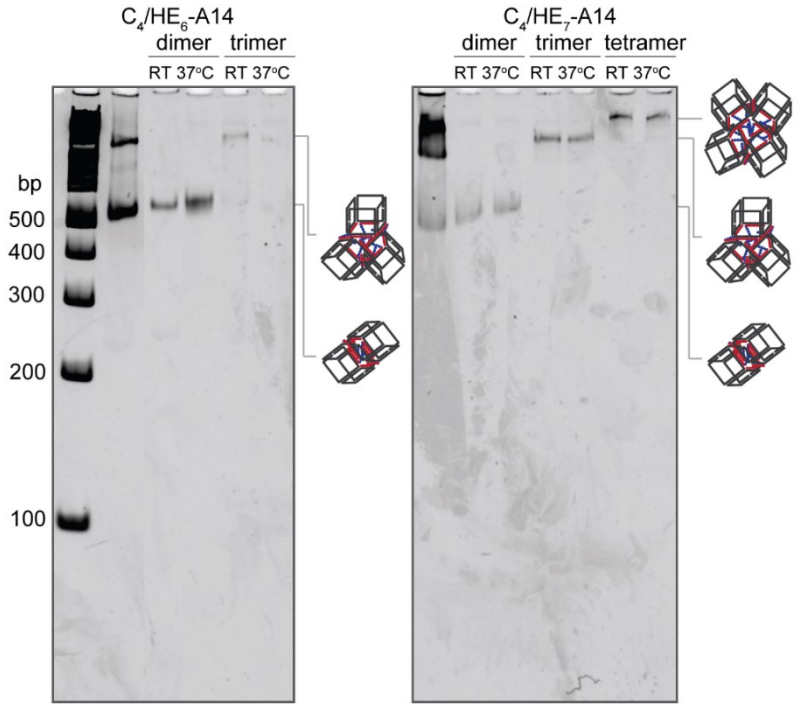

Figure 2.23 | Isolation of higher-order structures of C_4/HE_6-A14 and C_4/HE_7-A14. Non-denaturing PAGE (5%) shows good stability for all higher-order structures after isolation process.

DLS measurements were carried out for isolated dimers and trimers of C_4/HE_6-A14. Table 2.2 shows that both dimer and trimer had a similar size range, which was comparable to the mixture reported in Section 2.3.2.2. AFM was performed to characterize the morphology of isolated products; however, no structure was observed, likely because of the small quantity isolated (data not shown).

Table 2.2 | Hydrodynamic radii and polydispersity of isolated C_4/HE_6-A14.

Structures	R_h (nm)	% polydispersity
Dimer (lower) band	7.2±0.7	39.4±13.9
Trimer (upper) band	8.0±0.7	42.3±3.1

2.3.6.5 Thermal denaturation analysis

Decorating HE_6-A14 on C_8 led to a totally different mode of HE chain interactions, as compared to C_4. Here, the pre-organization of eight HE_6 chains on C_8 increase the extent of intrascaffold association of these chains over the interscaffold association. This is likely due to the lower entropic penalty of the intramolecular assembly, and the increased effective concentration of HE_6 in DNA cage's core, thus favoring the micellization below the critical micelle concentration of polymers.[19] We had previously noted 'all-or-none' cooperative binding of HE_6-A14 to C_8 (Section 2.3.6.3)

Thermal denaturation analysis was performed to investigate the thermodynamic properties of DNA-micelle cages. Interestingly, the presence of HE_6 chains led to higher thermal stability with an increase of 5.3°C in the melting temperature (T_m) compared to C_8/-A14 (Figure 2.24a). The full width at half-maximum (FWHM) determined from the first derivative of the melting curve can be used as the indication for cooperativity degree.[29-30] The dramatic decrease in FWHM of C_8/HE_6-A14 (4.0±0.1°C) in comparison to C_8/A14 (10.1±1.0°C) indicates a significantly increased positive cooperativity of DNA nanostructure assembly/disassembly.

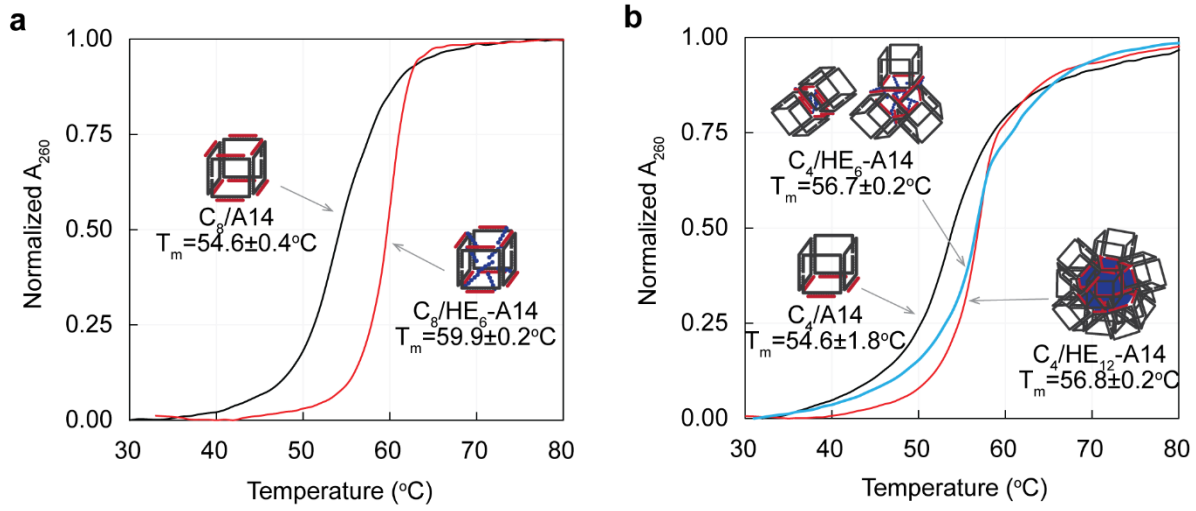

Figure 2.24 | Melting profiles of DNA cubes with HE-DNA. An increase in melting temperature (T_m) of a) C_8 and b) C_4 decorated with HE_n-A14 suggests the synergistic stabilization of DNA nanostructures by hydrophobic interactions. The narrow melting transition in the presence of polymers was consistent with a large increase in DNA assembly/disassembly cooperativity.

We hypothesized that the decoration of HE_6-A14 on only one face of the C_4 would not affect DNA hybridization to the same extent. C_4/HE_6-A14 exhibited a slight increase of 2°C in T_m compared to C_4/A14 (Figure 2.24b). Interestingly, the increased cooperativity was also observed in this system, as indicated by a significant decrease in FWHM (10.3±1.8°C for C_4/A14 and 4.5±0.7°C for C_4/HE_6-A14). A comparable increase in T_m and decrease in FWHM was observed for C_4/HE_{12}-A14. Moreover, an additional stabilization was also observed in the assemblies with copolymers HEG_n-HE_n-A14. There was a huge increase in T_m (> 7°C) for all C_8/HE_n-HEG_m-A14 (see Section 2.5.11 for melting profiles). Hence, the hydrophobic HE chains contribute to greater stabilization and cooperativity of DNA assemblies. This additional stabilization possibly stems from some additional intrascaffold interactions between HE chains, providing extra cohesion to the assembly. Therefore, the hydrophobic interactions not only introduce new DNA assembly modes but also synergistically work together with the base-pairing interactions to form and stabilize the DNA nanostructures.

2.3.6.6 Proposed assembly mechanism

To further explore the assembly mechanism, we carried out the C_4 assembly with HE_n-A14 in two steps: 1) separated thermal annealing of C_4 and HE_n-A14 from 95 to 4°C, and 2) incubation of both components at room temperature for 30 minutes. In Figure 2.25, short HE chains (HE_1-A14 to HE_4-A14) that are not expected to form stable micelles yielded monomeric structures similar to the one-pot assembly (Figure 2.3). On the other hand, the two-step assembly process with longer chains (HE_8-A14 to HE_{12}-A14) led to non-penetrating bands and unfunctionalized cubes. Thus, in this case, the cube cannot disassemble pre-formed micelles to hybridize with their individual chains at room temperature. (Figure 2.26, top scheme)

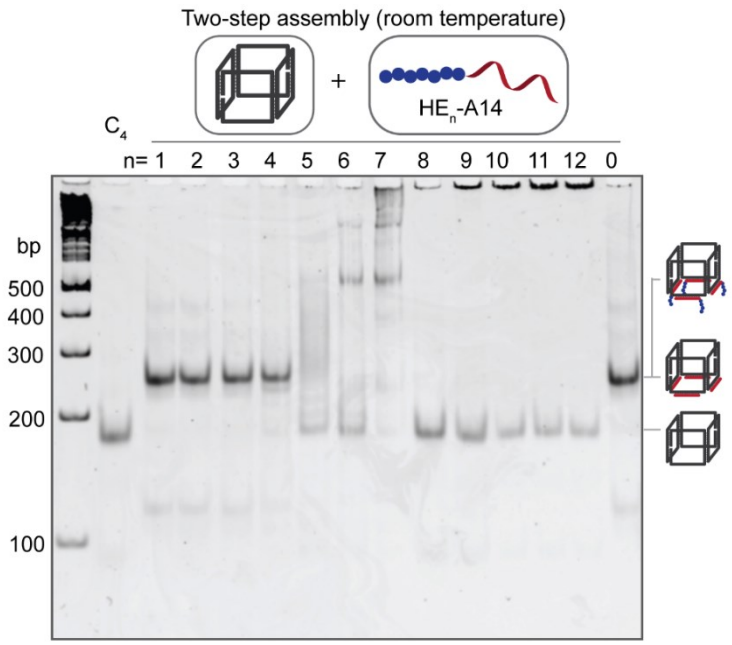

Figure 2.25 | Two-step assembly of C_4 with HE-DNA. Both C_4 and HE_n-A14 (n=1-12) were separately annealed from 95 to 4°C and incubated together at room temperature for 30 minutes. Non-denaturing PAGE (5%) shows that monomeric cubes could be generated from short polymer chains, but the formation of higher-order structures was inefficient with longer polymer chains.

Interestingly for HE_7-A14 and HE_8-A14, increasing the incubation temperature to 37°C converted the mixture of higher-order structures and cubes into the cube dimer and trimer (Figure 2.26). At the higher temperature, HE chains in the micelles may possibly rearrange into the more thermodynamically favorable cube-aggregate state. Thus, a pre-formed polymer-DNA spherical micelle can shape-shift into quantized cage assemblies, by adding DNA cages at 37°C. We also prepared HE_n-A14 at two concentrations (1.5 and 5 μM for low and high concentrations) in the first step to examine whether there will be concentration effect. The final HE_n-A14 concentration after mixing with C_4 was the same, and there was no significant difference in the product distribution using either low (Figure 2.26, left gel) or high (Figure 2.26, right gel) pre-annealed concentration of HE_n-A14.

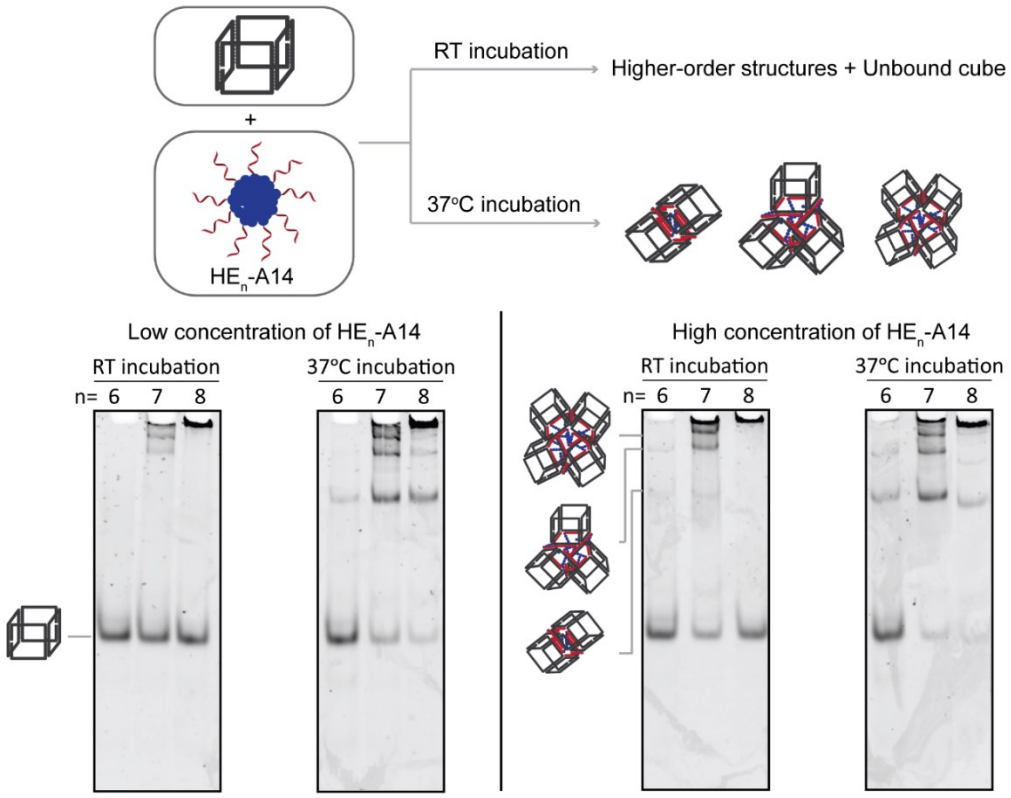

Figure 2.26 | Temperature effect in the two-step assembly of C_4 with HE-DNA. Both C_4 and HE_n-A14 (n=6-8) were separately annealed from 95 to 4°C and incubated together at room temperature or 37°C for 30 minutes. Two concentrations of HE_n-A14 annealed in the first step were used (low=1.5 μM and high=5 μM). Non-denaturing PAGE (5%) shows that increasing incubation temperature from room temperature to 37°C could convert the aggregates back to smaller higher-order structures (dimer, trimer, and tetramer).

Higher incubation temperature is undoubtedly a requirement to efficiently form small higher-order structures in the case of C_4/HE_8-A14. To find out the optimal temperature, the incubation temperature was varied from 37 to 55°C. Figure 2.27 shows that the formation of cube dimer and trimer was more efficient at higher temperatures, which were most likely to be optimized in the range of 45-50°C. However, thermal denaturation of C_4 (T_m of C_4/A14 ~55°C) and un-binding of HE_8-A14 from C_4 was observed at the highest temperatures. These observations can further support our hypothesis on the dynamic behavior of HE chains in the micelles that could lead to chain rearrangement at increased temperature.

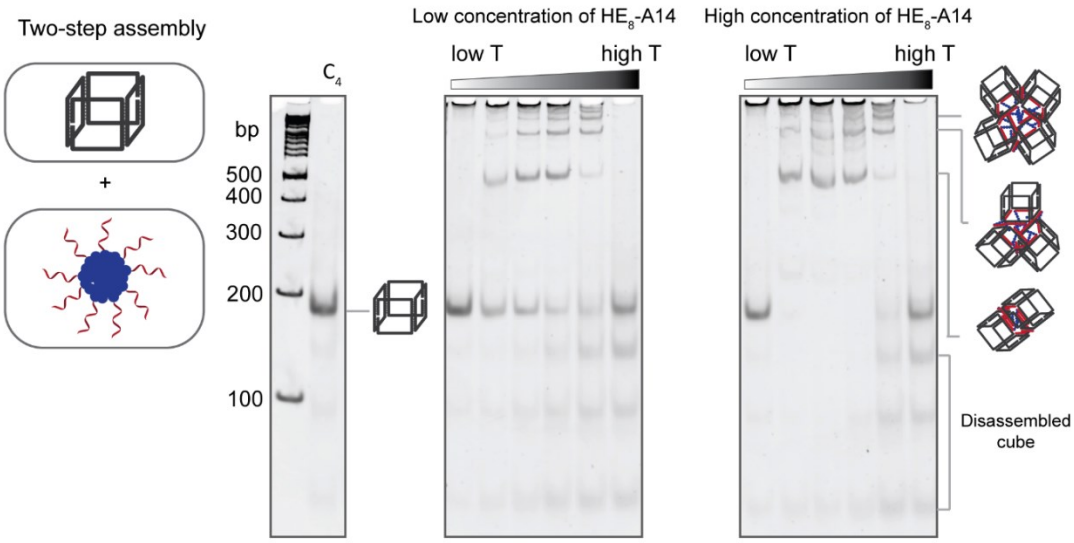

Figure 2.27 | Temperature effect in the two-step assembly of C_4 with HE_8-A14. Both C_4 and HE_8-A14 were separately annealed from 95 to 4ºC and incubated together at a range of temperatures (room temperature, 37.0ºC, 41.3ºC, 45.9ºC, 51.0ºC and 55.1ºC) for 30 minutes. There were also two concentrations of HE_n-A14 annealed in the first step (low=1.5 μM and high=5 μM). Non-denaturing PAGE (5%) shows that smaller higher-order structures can form more efficiently at a higher temperature.

We also carried out the two-step assembly of C_8 and HE_6-A14. In Figure 2.28, there was no difference between the products obtained from one-pot and two-step assembly. Interestingly in the two-step assembly, HE_6-A14 micelles can hybridize and fit themselves in the cube cavity, which is slightly smaller than HE_6-A14 micelles (R_h: C_8 = 5.4±0.6 nm, HE_6-A14 = 6.5±0.4 nm[19]). This generated only one product (DNA-micelle cube) without crosslinking the cubes. Therefore, it is likely that HE_6 chains are dynamic such that the hydrophobic core of HE_6-A14 micelles is not completely in 'frozen' state.

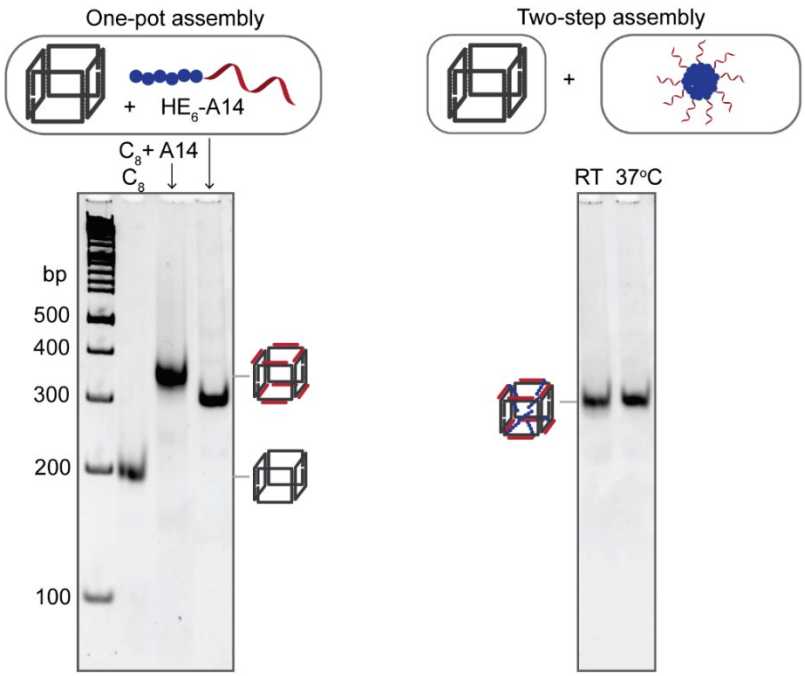

Figure 2.28 | Two-step assembly of C_8 with HE_6-A14. Both C_4 and HE_n-A14 (n=6-8) were separately annealed from 95 to 4°C and incubated together at room temperature or 37°C for 30 minutes. Non-denaturing PAGE (5%) shows that the DNA-micelle cubes formed efficiently at both incubation temperatures.

Therefore, there are two possible mechanisms for the quantized cage assembly. i) As the strands are cooled from 95°C, the cage assembles first, followed by the hybridization to individual polymer-DNA conjugates. Subsequent hydrophobic interactions drive the assembly of higher-order structures as the temperature further decreases (Figure 2.29a). This should happen with short HE chains. (ii) The DNA cage and the micelles pre-form separately, and the two objects hybridize together into the final structures, thus transitioning from a micelle morphology to higher-order structures. The rearrangement of polymer chains can also happen to generate smaller higher-order structures (Figure 2.29b). This is more favorable with intermediate to long HE chains.

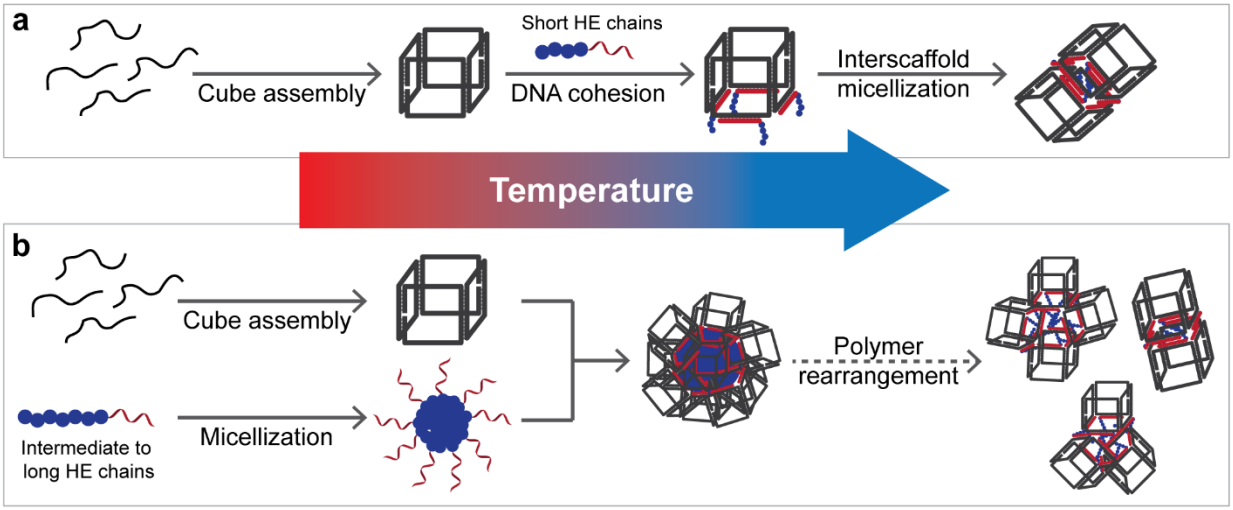

Figure 2.29 | Proposed assembly mechanism. a) Cage formation followed by polymer-DNA conjugate binding leads to monomeric cubes. Then, hydrophobic interactions can induce the interscaffold aggregation of hydrophobic chains to form small higher-order structures. b) Cages and micelles of polymer-DNA conjugates form separately and hybridize together as the temperature decreases to generate higher-order structures. Polymer rearrangement in the hydrophobic core can further generate smaller higher-order structures in intermediate length of polymer chains.

2.4 Conclusions

We have demonstrated the use of sequence-defined polymers to provide orthogonal assembly modes in DNA cages and to synergistically work together with base-pairing interactions. A range of unique self-assembled structures can be accessed by fine-tuning of the length of hydrophobic blocks, the polymer sequence, and the polymer orientation on DNA cages. Short hydrophobic chains result in monomeric DNA cages that are decorated with alkyl or oligoethylene glycol units. Longer hydrophobic chains arranged on one face of DNA cage lead to quantized cage higher-order structures, where the number of hydrophobic repeats defines the number of DNA cages that form these aggregates. When these hydrophobic chains are organized on both faces of DNA cage, these chains point to the interior of the cage and undergo an intrascaffold association. The sequence order of hydrophobic and hydrophilic monomers on the polymer chains can significantly control the interactions between hydrophobic blocks, resulting in monomeric cages and doughnut-shaped DNA cage-ring structures.

These DNA-polymer nanostructures can be alternatively viewed as amphiphilic block copolymers, where the hydrophilic block consists of DNA cages, and the hydrophobic block has hexaethylene chains. However, unlike block copolymers, the two components are monodisperse, sequence defined, and the placement of hydrophobic polymers on the DNA cage is anisotropic. This gives rise to entirely new morphologies that are not observed with block copolymers and provides guidelines for the design of DNA nanostructures mediated by hydrophobic interactions. It is remarkable that high specificity is achieved in these assembled structures despite the fact that the hydrophobic effect is one of the least directional supramolecular interactions.

2.5 Experimental Section

2.5.1 Chemicals

Tris(hydroxymethyl)aminomethane (tris), ethylenediaminetetraacetate (EDTA), urea, 40% acrylamide/bis-acrylamide (19:1), ammonium persulfate (APS), *N,N,N′,N′*-tetramethylethane-1,2-diamine (TEMED), and agarose were purchased from BioShop Canada Inc. Acetic acid, ammonium hydroxide, and boric acid were used as received from Fisher Scientific. GeneRuler DNA Ladder Mix (cat.# SM1173), GeneRuler Ultra Low Range DNA Ladder Mix (cat.# SM1223), and DNA Gel Loading Dye (6X) were obtained from Thermo Scientific. 1000 Å 1 μmole universal synthesis column and reagents used for automated DNA synthesis were purchased from BioAutomation. Sephadex G-25 (superfine DNA grade) was purchased from Glen Research. DMT-hexaethyloxy-glycol (HEG, cat.# CLP-9765), DMT-dodecane-diol (HE, cat.# CLP-1114) and symmetrical branching (cat.# CLP-5215) phosphoramidites were purchased from ChemGenes Corporation. Dithiol (cat.# 10-1937) and Cyanine 3 (cat.# 10-5913-95) phosphoramidites were purchased from Glen Research. GelRed nucleic acid stain (10,000x in water) was obtained from Biotium Inc. Nile Red, $MgCl_2 \cdot 6H_2O$, acetone, acetonitrile, and triethylamine were purchased from Sigma-Aldrich. Ruby mica sheets (V1/V2 quality, grade 2) was purchased from S&J Trading. TEM grids (cat.# CF400-Cu) were obtained from Electron Microscopy Sciences. 1xTBE buffer is composed of 90 mM tris, 90 mM boric acid and 2 mM EDTA with a pH ~8.3. 1xTAMg buffer is composed of 45 mM tris, 20 mM acetic acid, and 12.5 mM $MgCl_2 \cdot 6H_2O$, and its pH was adjusted to ~8.0 using glacial acetic acid.

2.5.2 Instrumentation

All standard DNA oligonucleotides were synthesized on solid supports using BioAutomation MerMade MM6 DNA synthesizer. DNA quantification was performed by NanoDrop Lite spectrophotometer (Thermo Scientific). Eppendorf Mastercycler 96-well thermocycler and Bio-Rad T100^{TM} thermal cycler were used to anneal all DNA structures. Polyacrylamide gel electrophoresis was performed using 20x20 cm vertical Hoefer 600 electrophoresis units. Owl Mini gel electrophoresis unit was used to perform agarose gel electrophoresis. HPLC purification was carried out on Agilent Infinity 1260. Gels were imaged by BioRad ChemiDoc MP. LC-ESI-MS data were obtained on Dionex Ultimate 3000 coupled to Bruker MaXis Impact^{TM} QTOF. Fluorescence data were measured by BioTek Synergy H4 Hybrid Multi-Mode Microplate Reader. Melting profiles of DNA structures were monitored by Cary 300 UV-Vis spectrophotometer equipped with Cary temperature controller (Agilent Technology). Multimode 8 scanning probe microscope and Nanoscope V controller (Bruker, Santa Barbara, CA) was used to acquire AFM images. DynaPro (model MS) molecular-sizing instrument was used to measure the particle size distributions. TEM micrographs were acquired on FEI Tecnai 120 kV 12 microscope equipped with AMT XR80C CCD Camera System (FEI electron optics).

2.5.3 Solid-phase synthesis and purification

DNA synthesis was performed on a 1 μmole scale on a universal 1000 Å CPG solid support by using standard method. Briefly, a phosphoramidite was activated by 0.25 M 5-(ethyl)-1H-thiotetrazole in acetonitrile and coupled to DNA chains on the solid support. Failed coupling was capped by THF/lutidine/acetic anhydride and 16% 1-methylimidazole/THF. Phosphorus (III) was oxidized to phosphorus (V) with 0.02 M I_2 in THF/pyridine/H_2O. Coupling efficiency was monitored after the removal of dimethoxytrityl (DMT) 5'-OH protecting groups by 3% dichloroacetic acid in dichloromethane. For the coupling of non-nucleoside phosphoramidites, DMT-hexaethyloxy-glycol phosphoramidite and DMT-dodecane-diol phosphoramidite were dissolved in acetonitrile to obtain 0.1 M solution under a nitrogen atmosphere in a glove box and added on the DNA synthesizer. The coupling time was extended to 5 minutes. The coupling of 0.1 M solution of Cyanine 3 phosphoramidite, dithiol phosphoramidite and symmetrical branching phosphoramidite in acetonitrile was performed in a glove box for 10 minutes, followed by capping,

oxidation and deblocking steps on the synthesizer. After the synthesis, the strand was deprotected and cleaved from the solid support by treating with 28% aqueous ammonium hydroxide for 16 hours at 60ºC. The crude product was isolated, dried, and re-suspended in 1:1 H_2O/8M urea before loading to polyacrylamide/urea gel (12% for cage components and 15% for polymer-DNA conjugates). The gel was run at 250 V for 30 minutes followed by 500 V for 45-60 minutes with 1xTBE as the running buffer. The gel was then imaged and excised on TLC plate under a UV lamp. DNA was extracted from the excised gel slabs by crushing and soaking in 11-12 mL of Milli-Q water at 60ºC overnight. The solution was dried to approximately 1 mL before loading to Sephadex G-25 column. The purified DNA was quantified by the absorbance at 260 nm. The strand purity was then evaluated by denaturing PAGE (12-15%). Approximately 0.02 nmole of strands was loaded on the gel, and the gel was run at 250 V for 30 minutes then 500 V for 60 minutes with 1xTBE as the running buffer. The gel was stained with a GelRed solution before imaging.

Alternatively, the crude products of polymer-DNA conjugates were directly purified by reversed-phase HPLC (Hamilton PRP-C18 5 μm 100 Å 2.1x150 mm). The sample was filtered using centrifuge tube filter with 0.22 μm cellulose-acetate membrane, after which 0.5-1 OD_{260} of the sample in Milli-Q water was injected into RP-HPLC. Two mobile phases comprise of 50 mM triethylammonium acetate (TEAA, pH 8.0) and acetonitrile. The elution gradient of 3-50% acetonitrile over 30 minutes at 60ºC was used to purify polymer-DNA conjugates. Detection was carried out using a diode-array detector, monitoring the absorbance at 260 nm.

2.5.4 DNA sequences and characterization

The sequences of DNA clips necessary for cage assembly are listed in Table 2.3. The strands were further analyzed by LC-ESI-MS in negative ESI mode, which is summarized in Table 2.4.

Table 2.3 | Sequences of DNA clips (6 = HEG).

Strand	Sequence (5'→ 3')
1AB	TCGCTGAGTA 6 TCCTATATGGTCAACTGCTC 6 GCAAGTGTGGGCACGCACAC 6 GTAGTAATACCAGATGGAGT 6 CACAAATCTG
2AC	CTATCGGTAG 6 TCCTATATGGTCAACTGCTC 6 TACTCAGCGACAGATTTGTG 6 AAAACTCTGCCGTAAGAGGA 6 CAACTAGCGG
3AD	CACTGGTCAG 6 TCCTATATGGTCAACTGCTC 6 CTACCGATAGCCGCTAGTTG 6 GCCTGGCCTTGGTCCATTTG 6 GGTTTGCTGA
4AE	CCACACTTGC 6 TCCTATATGGTCAACTGCTC 6 CTGACCAGTGTCAGCAAACC 6 TAACAGGATTAGCAGAGCGA 6 GTGTGCGTGC
TP3-AB	CCACACTTGC 6 TCCTATATGGTCAACTGCTC 6 CTACCGATAGCCGCTAGTTG 6 GTAGTAATACCAGATGGAGT 6 GTGTGCGTGC
PP4-AB	TACCGGATCG 6 TCCTATATGGTCAACTGCTC 6 CTGACCAGTGTCAGCAAACC 6 GTAGTAATACCAGATGGAGT 6 CCGTAATTGC
PP5-AB	CCACACTTGC 6 TCCTATATGGTCAACTGCTC 6 CGATCCGGTAGCAATTACGG 6 GTAGTAATACCAGATGGAGT 6 GTGTGCGTGC
1AA	TCGCTGAGTA 6 TCCTATATGGTCAACTGCTC 6 GCAAGTGTGGGCACGCACAC 6 TCCTATATGGTCAACTGCTC 6 CACAAATCTG
2AA	CTATCGGTAG 6 TCCTATATGGTCAACTGCTC 6 TACTCAGCGACAGATTTGTG 6 TCCTATATGGTCAACTGCTC 6 CAACTAGCGG
3AA	CACTGGTCAG 6 TCCTATATGGTCAACTGCTC 6 CTACCGATAGCCGCTAGTTG 6 TCCTATATGGTCAACTGCTC 6 GGTTTGCTGA
4AA	CCACACTTGC 6 TCCTATATGGTCAACTGCTC 6 CTGACCAGTGTCAGCAAACC 6 TCCTATATGGTCAACTGCTC 6 GTGTGCGTGC
TP3-AA	CCACACTTGC 6 TCCTATATGGTCAACTGCTC 6 CTACCGATAGCCGCTAGTTG 6 TCCTATATGGTCAACTGCTC 6 GTGTGCGTGC
PP4-AA	TACCGGATCG 6 TCCTATATGGTCAACTGCTC 6 CTGACCAGTGTCAGCAAACC 6 TCCTATATGGTCAACTGCTC 6 CCGTAATTGC
PP5-AA	CCACACTTGC 6 TCCTATATGGTCAACTGCTC 6 CGATCCGGTAGCAATTACGG 6 TCCTATATGGTCAACTGCTC 6 GTGTGCGTGC

Table 2.4 | Calculated and experimental masses (in g/mole) of DNA clips.

Strand	Calculated mass	Experimental mass
1AB	26063.61	26064.3699
2AC	26038.60	26038.6906
3AD	25953.46	25953.5017
4AE	25960.53	25960.5960
TP3-AB	25988.52	25988.4558
PP4-AB	25974.55	25974.4902
PP5-AB	26037.56	26037.4980
1AA	25901.49	25901.2963
2AA	25922.50	25922.2974
3AA	25905.46	25905.2799
4AA	25804.40	25804.2342
TP3-AA	25826.40	25826.4197
PP4-AA	25812.42	25812.3707
PP5-AA	25875.44	25875.4066

The sequences of polymer-DNA conjugates are listed in Table 2.5.

Table 2.5 | Sequences of polymer-DNA conjugates (6 = HEG, X = HE).

Strand	Sequence (5'→3')
A14	TTTTTCAGTTGACCATATA
HE_1-A14	XTTTTTCAGTTGACCATATA
HE_2-A14	XXTTTTTCAGTTGACCATATA
HE_3-A14	XXXTTTTTCAGTTGACCATATA
HE_4-A14	XXXXTTTTTCAGTTGACCATATA
HE_5-A14	XXXXXTTTTTCAGTTGACCATATA
HE_6-A14	XXXXXXTTTTTCAGTTGACCATATA
HE_7-A14	XXXXXXXTTTTTCAGTTGACCATATA
HE_8-A14	XXXXXXXXTTTTTCAGTTGACCATATA

Strand	Sequence (5'→3')
HE_9-NDA	XXXXXXXXXTTTTTCAGTTGACCATATA
HE_{10}-A14	XXXXXXXXXXTTTTTCAGTTGACCATATA
HE_{11}-A14	XXXXXXXXXXXTTTTTCAGTTGACCATATA
HE_{12}-A14	XXXXXXXXXXXXTTTTTCAGTTGACCATATA
$(HE\text{-}HEG)_6$-A14	X6X6X6X6X6X6TTTTTCAGTTGACCATATA
$(HE_2\text{-}HEG_2)_3$-A14	XX66XX66XX66TTTTTCAGTTGACCATATA
$(HE_3\text{-}HEG_3)_2$-A14	XXX666XXX666TTTTTCAGTTGACCATATA
$HE_6\text{-}HEG_6$-A14	XXXXXX666666TTTTTCAGTTGACCATATA
$HEG_6\text{-}HE_6$-A14	666666XXXXXXTTTTTCAGTTGACCATATA
$HE_6\text{-}HEG_{12}$-A14	XXXXXX666666666666TTTTTCAGTTGACCATATA
$HE_{12}\text{-}HEG_6$-A14	XXXXXXXXXXXX666666TTTTTCAGTTGACCATATA
$HE_{12}\text{-}HEG_{12}$-A14	XXXXXXXXXXXX666666666666TTTTTCAGTTGACCATATA

Polymer-DNA conjugates were purified by RP-HPLC. All samples were run using the same gradient of 3-50% acetonitrile to compare their relative hydrophobicity. Table 2.6 summarizes the retention times of all polymer-DNA conjugates. The strands were further analyzed by LC-ESI-MS in negative ESI mode, which is summarized in Table 2.6.

Table 2.6 | Characterization of polymer-DNA conjugates.

Strand	Retention time[a]	Calculated mass[b]	Experimental mass[b]
A14	-	5764.99	5765.0000
HE_1-A14	14.677	6029.14	6029.1250
HE_2-A14	18.624	6293.29	6293.2188
HE_3-A14	20.855	6557.44	6557.4063
HE_4-A14	22.490	6821.59	6821.5000
HE_5-A14	23.398	7085.74	7085.6875
HE_6-A14	24.154	7349.89	7349.7813
HE_7-A14	24.936	7614.03	7613.8672
HE_8-A14	25.289	7878.18	7878.1250
HE_9-A14	25.947	8142.33	8142.2656

Strand	Retention time[a]	Calculated mass[b]	Experimental mass[b]
HE_{10}-A14	26.302	8406.48	8406.4063
HE_{11}-A14	26.962	8670.63	8670.4297
HE_{12}-A14	27.232	8934.78	8934.7778
$(HE\text{-}HEG)_6$-A14	22.237	9414.63	9414.5000
$(HE_2\text{-}HEG_2)_3$-A14	23.102	9414.63	9414.5000
$(HE_3\text{-}HEG_3)_2$-A14	23.632	9414.63	9414.5000
$HE_6\text{-}HEG_6$-A14	24.399	9414.63	9414.5000
$HEG_6\text{-}HE_6$-A14	22.991	9414.63	9414.5000
$HE_6\text{-}HEG_{12}$-A14	23.618	11479.37	11484.5477
$HE_{12}\text{-}HEG_6$-A14	27.117	10999.52	11004.7412
$HE_{12}\text{-}HEG_{12}$-A14	26.838	13064.26	13070.0023

[a] Retention time (in minutes) was determined from RP-HPLC with the gradient of 3-50% acetonitrile for 30 minutes.
[b] mass unit is in g/mole.

2.5.5 Cage design and assembly with polymer-DNA conjugates

Cage design:

The clip combinations of different DNA cages are listed in Table 2.7

Table 2.7 | DNA clip combinations for the construction of different cages.

Cage	Clip strands	Number of binding sites
TP_3	1AB, 2AC, TP3-AB	3
C_4	1AB, 2AC, 3AD, 4AE	4
PP_5	1AB, 2AC, 3AD, PP4-AB, PP5-AB	5
TP_6	1AA, 2AA, TP3-AA	6
C_8	1AA, 2AA, 3AA, 4AA	8
PP_{10}	1AA, 2AA, 3AA, PP4-AA, PP5-AA	10

Assembly protocols:

1) One-pot assembly

To assemble a cage, equimolar amounts (1.25 pmole) of all required DNA clips were mixed in 1xTAMg buffer (10 µL) to obtain a final cage concentration of 125 nM. Polymer-DNA conjugates in appropriate ratios (1.5 equivalents per binding site) were added to the mixtures. The final concentrations of polymer-DNA conjugates were 562.5, 750, 937.5, 1125, 1500 and 1875 nM for TP_3, C_4, PP_5, TP_6, C_8, PP_{10}, respectively. The samples were heated at 95°C for 5 minutes, at 80°C for 3 minutes, cooled to 60°C (2 min/°C), and slowly cooled to 4°C (3 min/°C). The assemblies were examined by non-denaturing PAGE (5%) by mixing with 2 µL of glycerol mix (7:1 glycerol/H_2O) and loaded on the gel with 1xTAMg as the running buffer. The gel was run at 250 V for 2.5 hours and stained with GelRed.

2) Two-step assembly

Cube (250 nM) and HE_n-A14 (1.5 µM and 5 µM for 'low' and 'high' concentrations as mentioned in Section 2.3.6.6) were separately prepared in 1xTAMg buffer and thermally annealed from 95 to 4°C. To 5 µL of C_4 solution was added either i) 5 µL of 1.5 µM HE_n-A14 or ii) 1.5 µL of 5 µM HE_n-A14 and 3.5 µL of 1xTAMg. In the case of C_8, 3 µL of 5 µM HE_6-A14 and 2 µL 1xTAMg were added to 5 µL of C_8. The mixtures were incubated at room temperature or 37°C in a water bath for 30 minutes and analyzed by non-denaturing PAGE.

3) Combination of DNA cages with HE_6-A14

The concentrations of individual cage were maintained at 125 nM, and HE_6-A14 was added in 1.5 equivalents per binding site. One-pot assembly was performed by mixing all required components in 10 µL of 1xTAMg buffer and thermally annealed from 95 to 4°C. For two-step assembly, individual cage (125 nM) was annealed with HE_6-A14 from 95 to 4°C in 10 µL of 1xTAMg. Then, 5 µL of one mixture was mixed with 5 µL of another mixture (i.e., TP_3/HE_6-A14 and C_4/HE_6-A14). The combined mixture was incubated for 30 minutes at either room temperature or 37°C. All samples were analyzed by non-denaturing PAGE.

4) Isolation of higher-order structures of C_4/HE_6-A14 and C_4/HE_6-A14

C_4 (125 nM) and HE_6-A14/HE_7-A14 (750 nM) were thermally annealed in 1xTAMg buffer. Then, 100 μL of samples was mixed with 20 μL of glycerol mix. On the non-denaturing PAGE (5%), 12 μL of the mixtures was loaded as a reference in one lane, while the remaining 108 μL were loaded in other lanes for the isolation process. The gel was run at 250 V for 2.5 hours with 1xTAMg as the running buffer. The part of the gel containing reference band was cut and stained with GelRed to measure the distances of the target bands from the well. The bands on another part of the gel were then excised according to the calculated distances, cut into small pieces and soaked in 1xTAMg for 1-2 days at 4°C.

2.5.6 Atomic force microscopy

The sample was diluted with 1xTAMg from 125 nM to 41.7-62.5 nM with respect to the cages. 5 μL of sample was deposited on freshly cleaved mica for 5 seconds and washed three times with 50 μL of H_2O. Excess liquid was blown off by the stream of nitrogen for 30 seconds. The sample was then dried under vacuum for at least 20 minutes prior to imaging. Measurements were acquired in ScanAsyst mode under dry condition using ScanAsyst-Air triangular silicon nitride probe (tip radius = 2 nm, k = 0.4 N/m, f_o = 70 kHz; Bruker, Camarillo, CA).

Images were processed by NanoScope Analysis 1.40 Software. Raw data were treated with flattening to correct tilt, bow and scanner drift. Average particle sizes, heights, and numbers of particles (N) were obtained from Particle Analysis function, and edge lengths of some particles were measured by Section function. Table 2.8 summarizes the diameter, height, and number of analyzed particles for all assemblies. Figure 2.30 shows additional AFM images of the structures presented in Section 2.3 and images for other assemblies.

Table 2.8 | AFM analysis of DNA cages decorated with polymer-DNA conjugates.

Structure	Diameter (nm)	Height (nm)	Number of particles
C_4/HE_6-A14	22.7±3.4	2.1±0.3	171
C_4/HE_7-A14	23.3±5.6	2.3±0.4	840
C_4/HE_6-HEG_6-A14	26.4±8.2	2.0±0.3	178
C_4/HE_6-HEG_{12}-A14	25.4±10.0	2.1±0.4	49
C_4/HE_{12}-HEG_6-A14	53.9±8.8	4.4±1.1	271
C_4/HE_{12}-HEG_{12}-A14	47.7±9.8	2.6±0.8	353
C_8	17.0±2.8	1.8±0.2	568
C_8/HE_6-A14	19.1±4.8	1.8±0.4	236
C_8/HE_8-A14	29.6±7.4	2.6±0.8	251
C_8/HE_{12}-A14	48.8±14.8	6.9±2.5	135
C_8/HE_6-HEG_6-A14	26.7±7.3	2.2±0.2	333
C_8/HE_6-HEG_{12}-A14	46.3±9.7	2.2±0.4	136
C_8/HE_{12}-HEG_6-A14	45.6±10.7	5.0±1.6	86
C_8/HE_{12}-HEG_{12}-A14	50.7±7.2	2.8±0.6	40
PP_5	20.8±6.0	1.6±0.2	710
PP_5/HE_6-A14	24.4±3.8	5.3±7.9	222
PP_5/HE_7-A14	25.8±4.4	2.4±0.4	298
PP_5/HE_6- HEG_6-A14	28.9±6.8	1.9±0.2	58
TP_3/HE_7-A14	21.2±4.5	2.0±0.4	243
TP_3/HE_6- HEG_6-A14	27.8±8.4	2.2±0.3	156

a) C_4/HE_6-A14

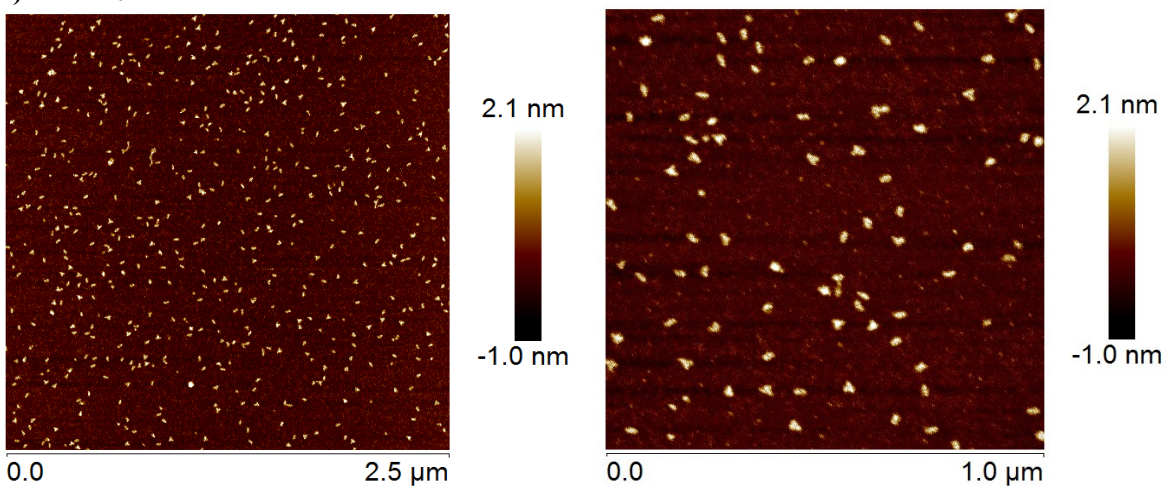

b) C_4/HE_7-A14

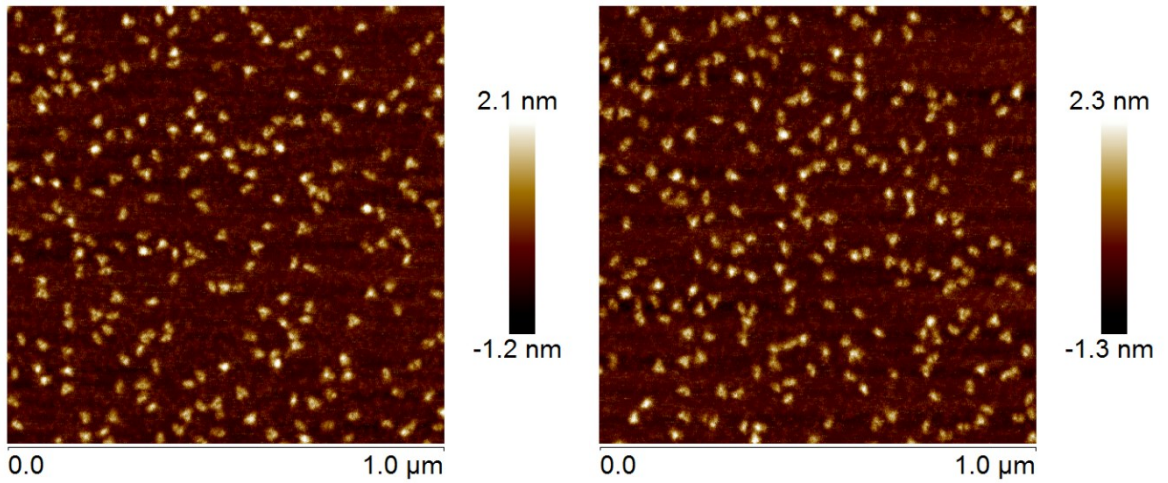

c) C_4/HE_6-HEG_6-A14

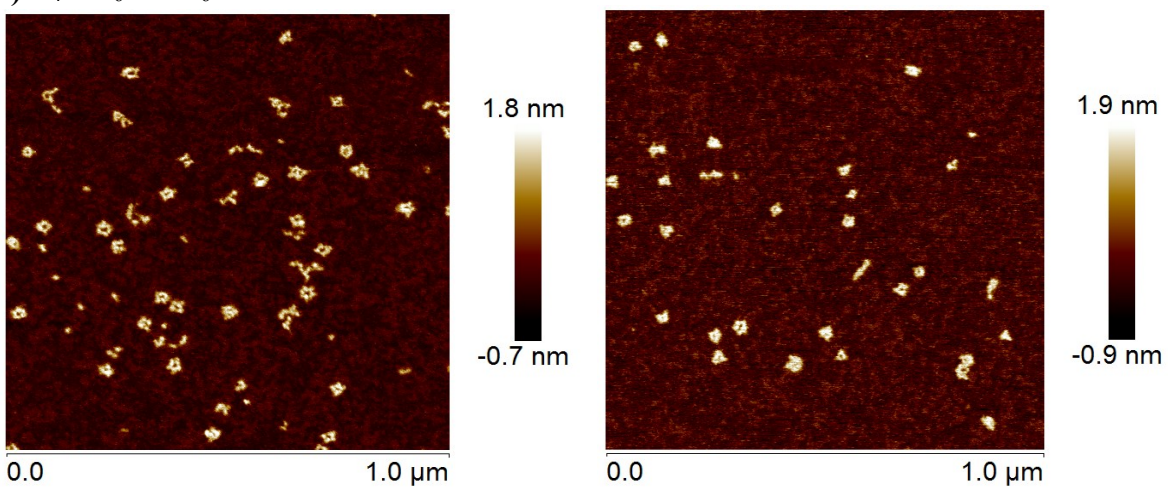

d) C_4/HE_6-HEG_{12}-A14

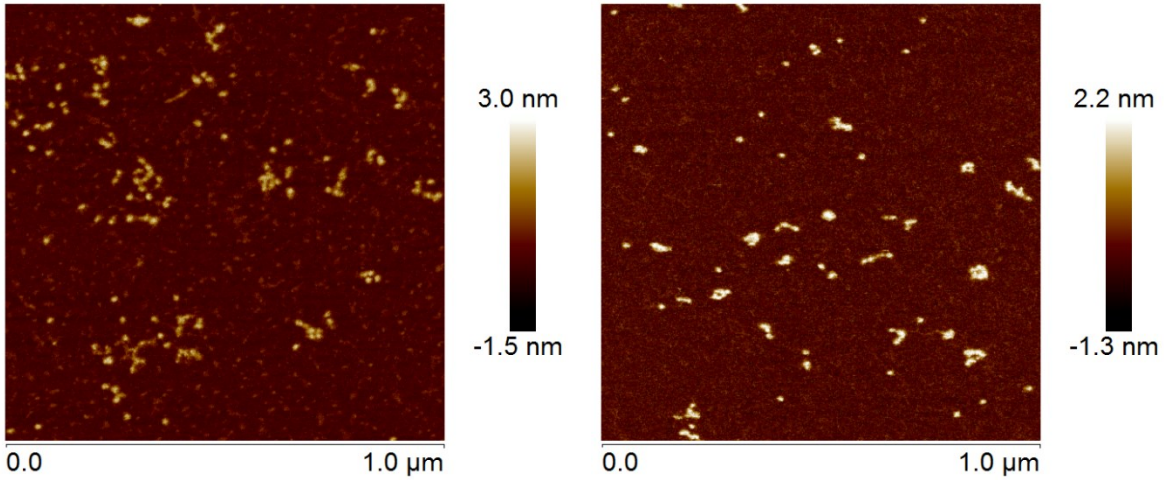

e) C_4/HE_{12}-HEG_6-A14

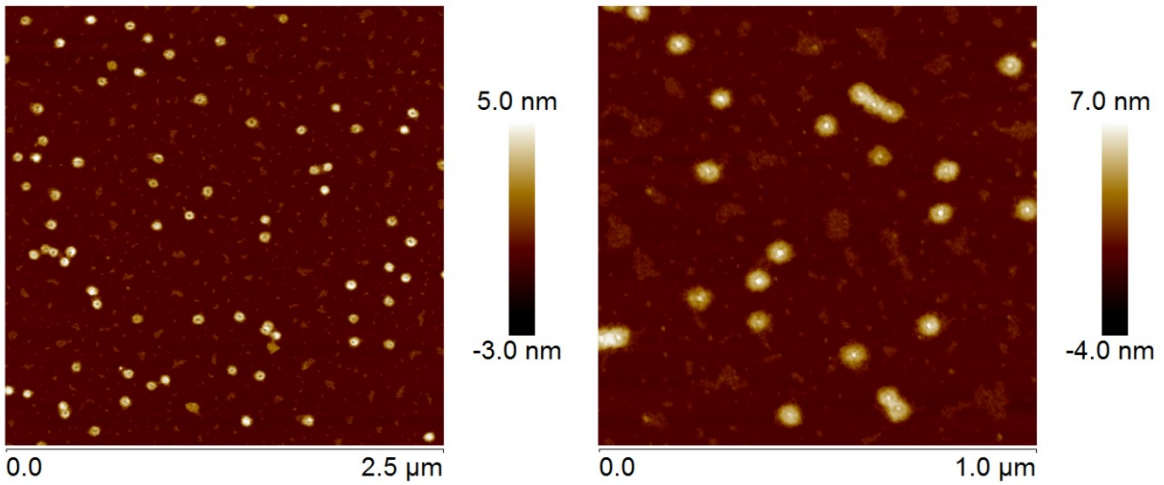

f) C_4/HE_{12}-HEG_{12}-A14

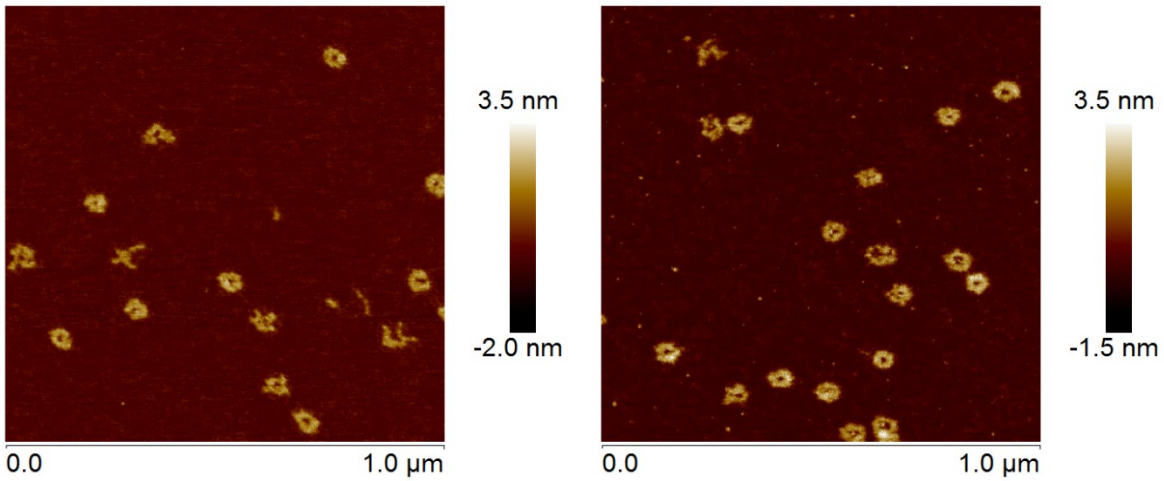

g) C_8

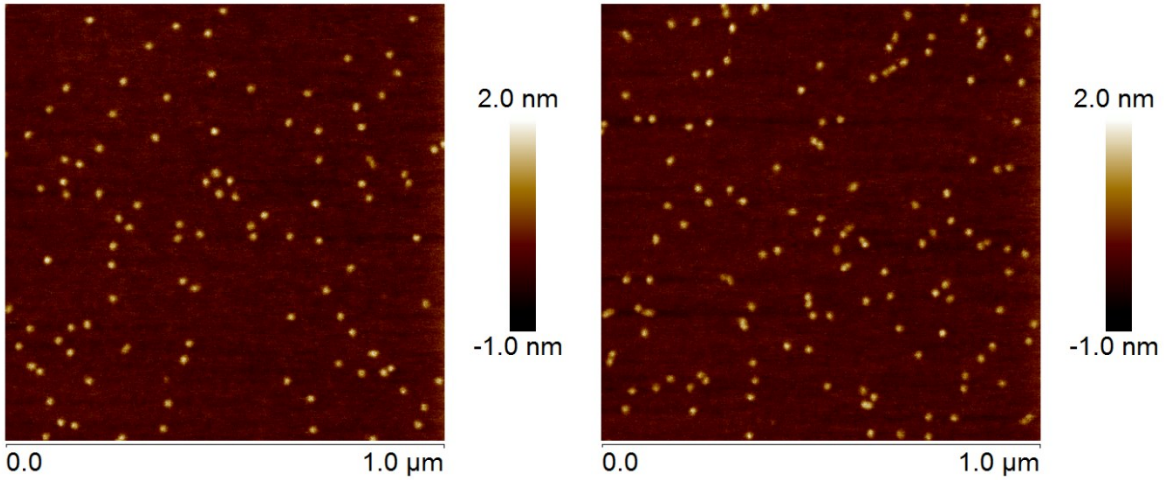

h) C_8/HE_6-A14

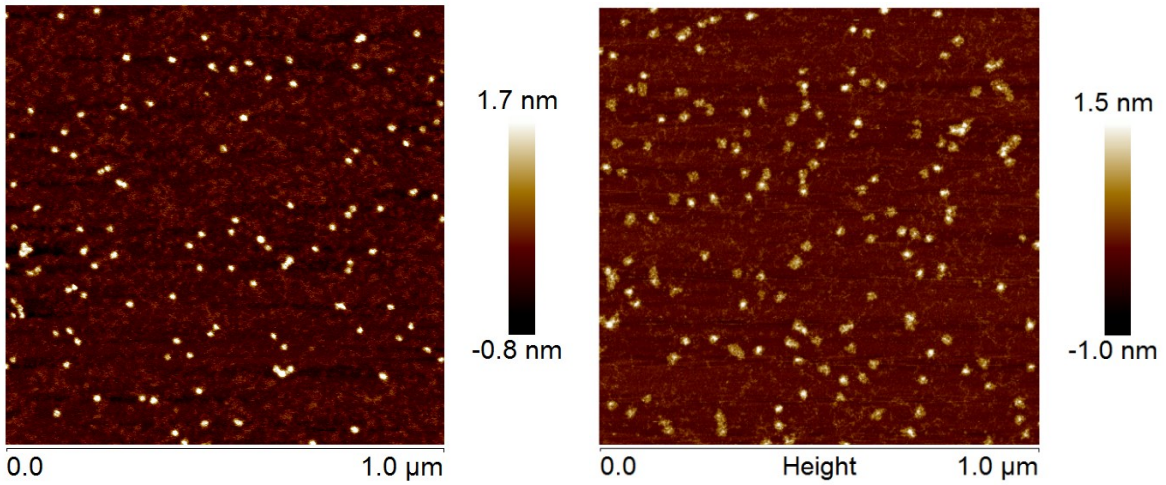

i) C_8/HE_8-A14

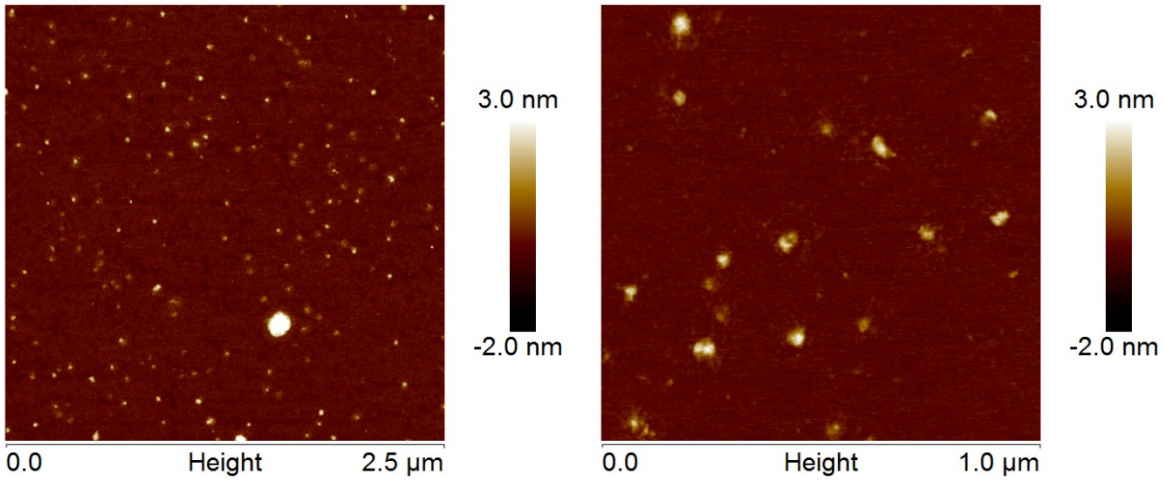

j) C_8/HE_{12}-A14

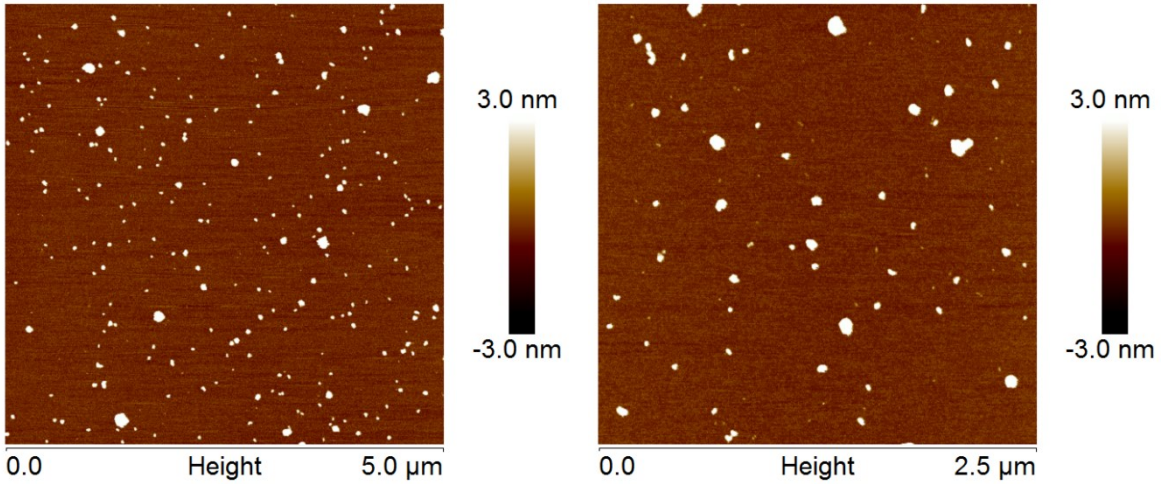

k) C_8/HE_6-HEG_6-A14

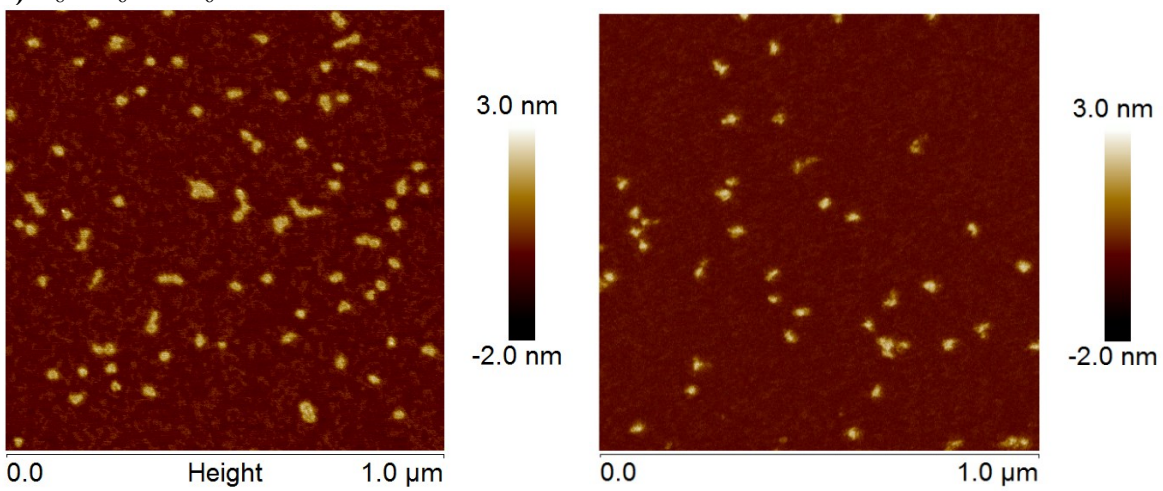

l) C_8/HE_6-HEG_{12}-A14

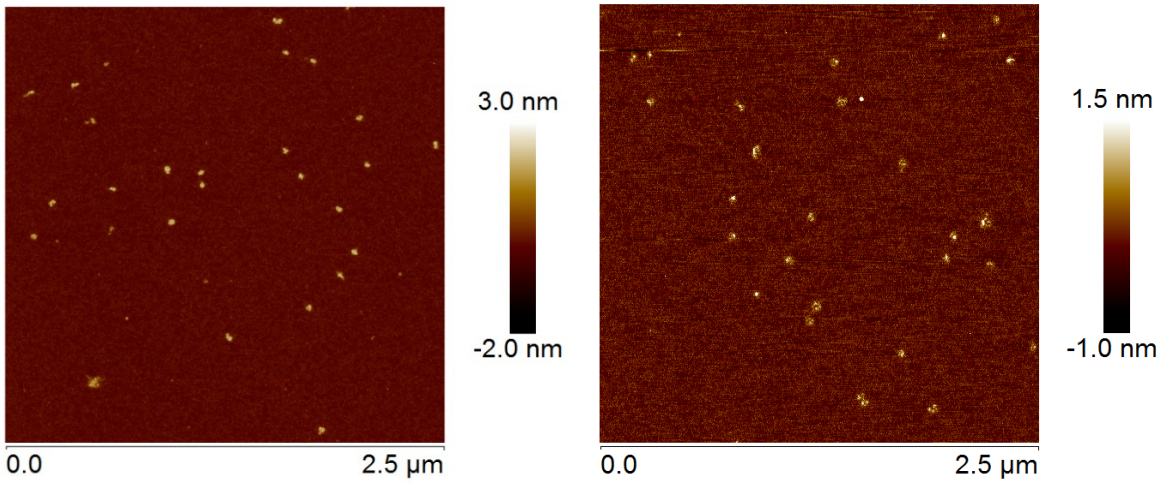

m) C_8/HE_{12}-HEG_6-A14

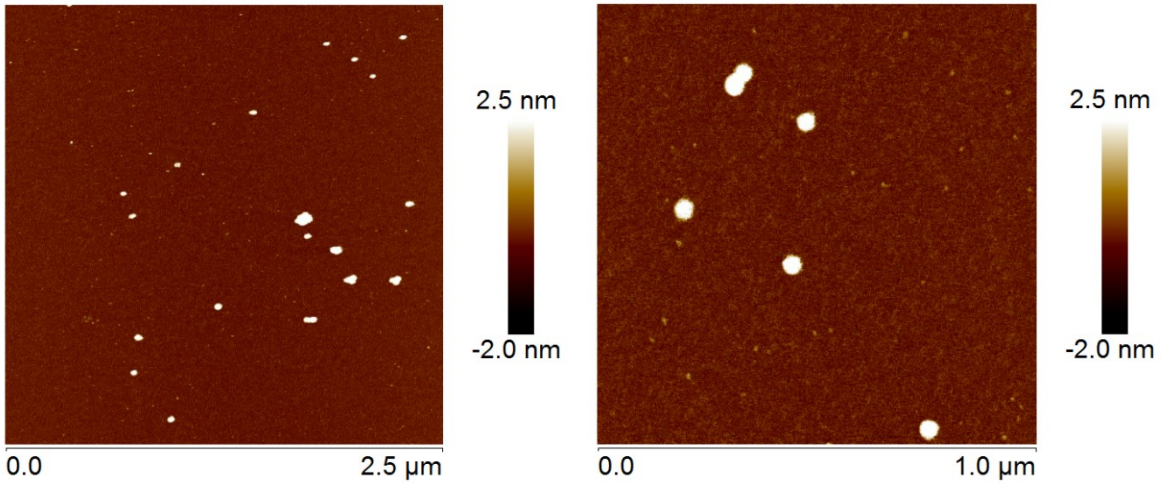

n) C_8/HE_{12}-HEG_{12}-A14

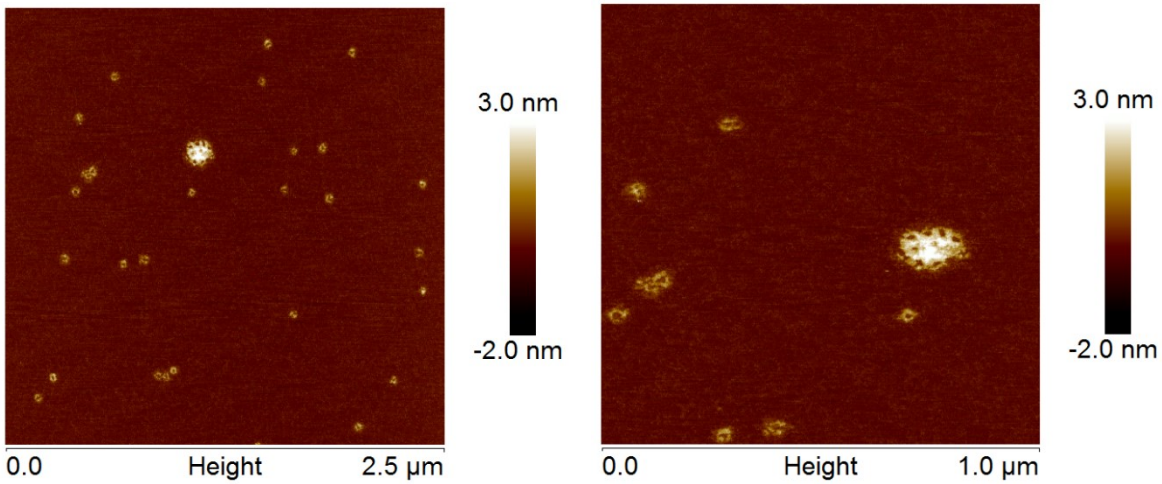

o) PP_5

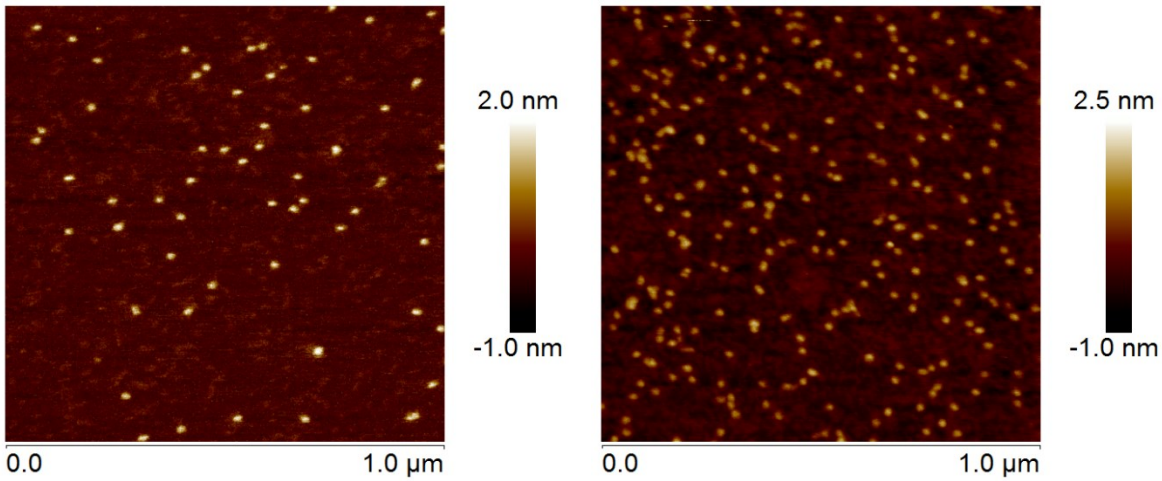

p) PP_5/HE_6-A14

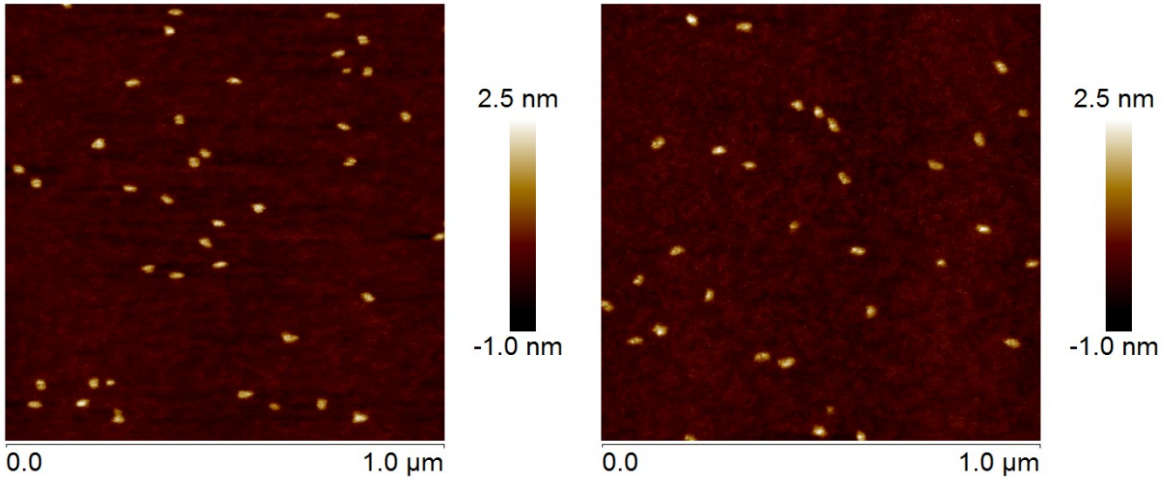

q) PP_5/HE_7-A14

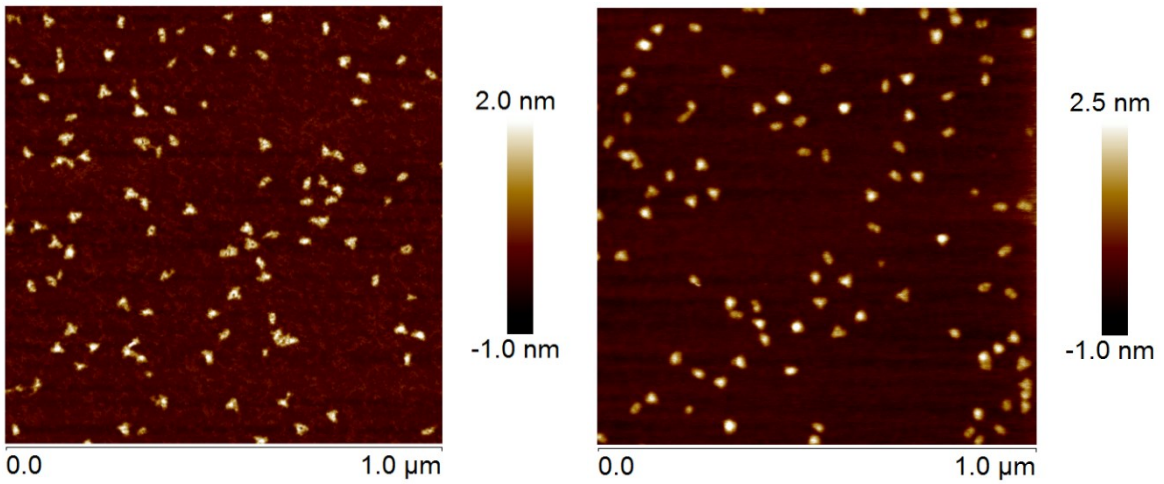

r) PP_5/HE_6-HEG_6-A14

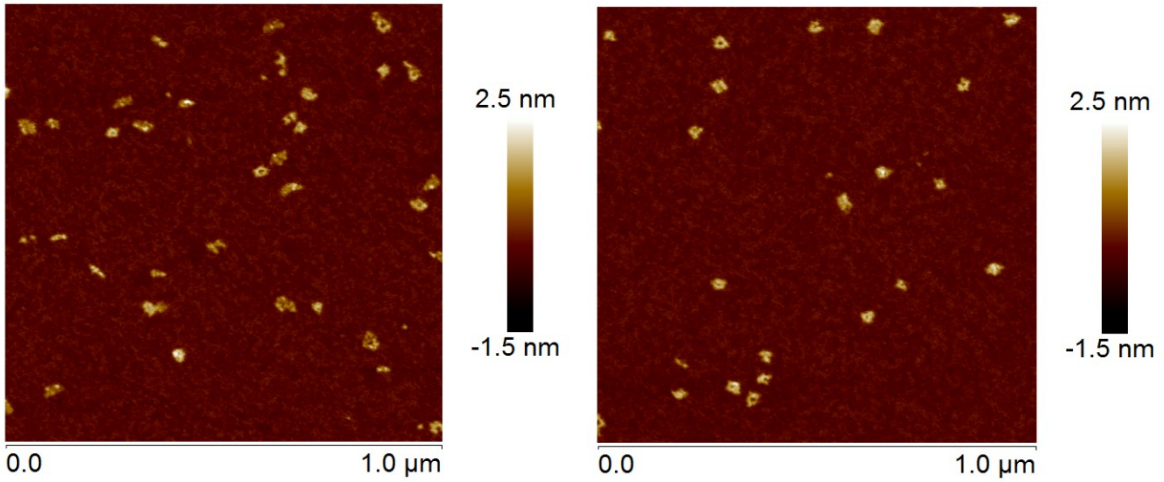

s) TP_3/HE_7-A14

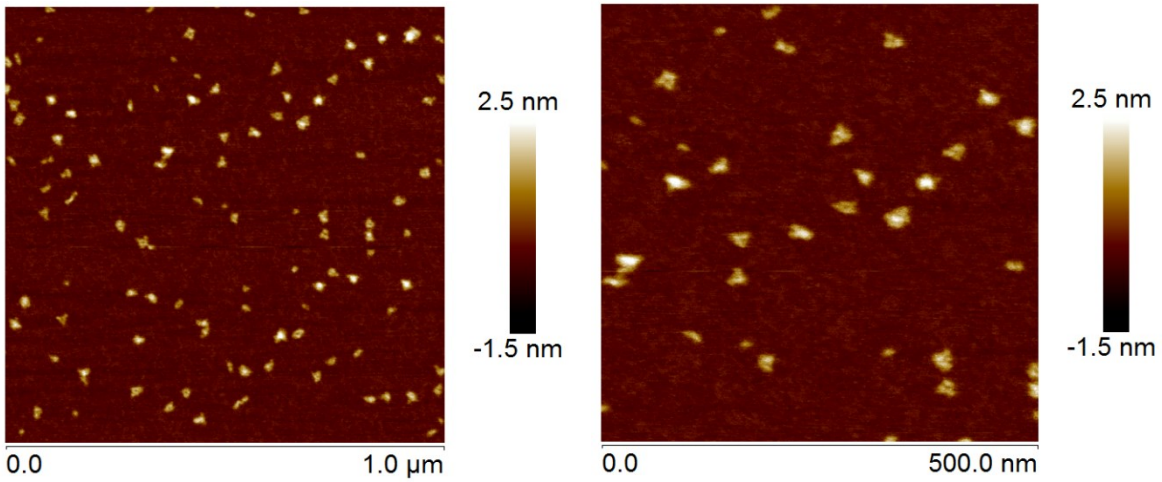

t) TP_3/HE_6-HEG_6-A14

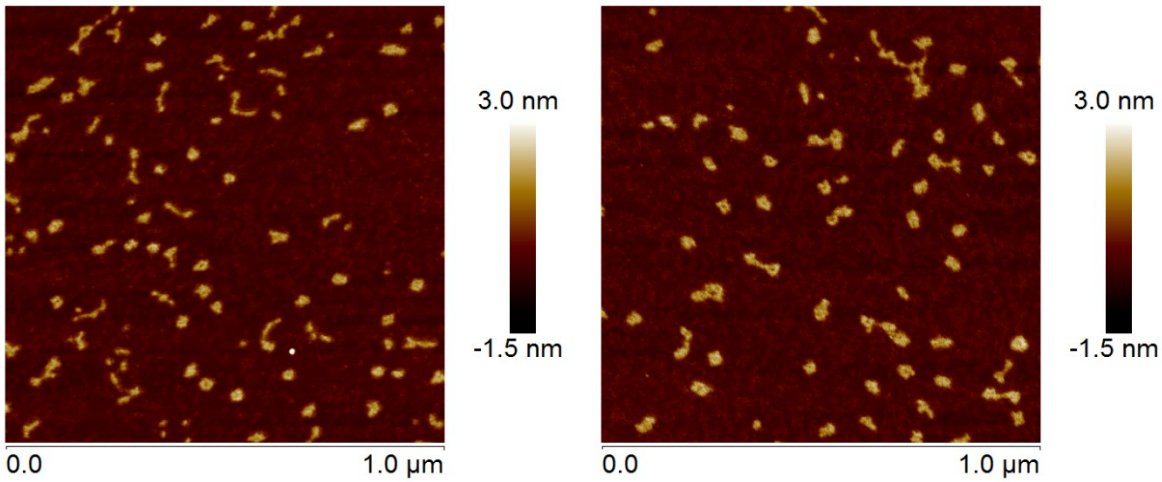

Figure 2.30 | AFM images of DNA cages decorated with polymer-DNA conjugates.

2.5.7 Transmission electron microscopy

Cube assembly with HE/HEG-DNA:

2 μL of sample was deposited on the carbon film coated 400-mesh copper grids for one minute. Excess liquid was blotted off with the edge of a filter paper. The sample was washed three times with 20 μL H_2O and blotted with filter paper. The sample was dried under vacuum at least 30 minutes prior to the imaging. Average particle sizes and numbers of particles (N) were analyzed by ImageJ software. Table 2.9 summarizes the size analysis of C_4 and C_8 with HE_{12}-HEG_6-A14.

Table 2.9 | TEM analysis of DNA cubes decorated with HE/HEG-DNA.

Structure	Diameter (nm)	Number of particles	Note
C_4/H_{12}-HEG_6-A14	24.7±3.9	337	
C_4/H_{12}-HEG_{12}-A14	30.3±5.4	462	
C_8/H_{12}-HEG_6-A14	107.5±28.5,	124	Large aggregates
	22.1±3.9	282	Monodisperse small spheres
C_8/H_{12}-HEG_{12}-A14	138.7±45.3	40	Large aggregates
	23.3±5.0	63	Monodisperse small spheres

a) C_4/HE_{12}-HEG_6-A14

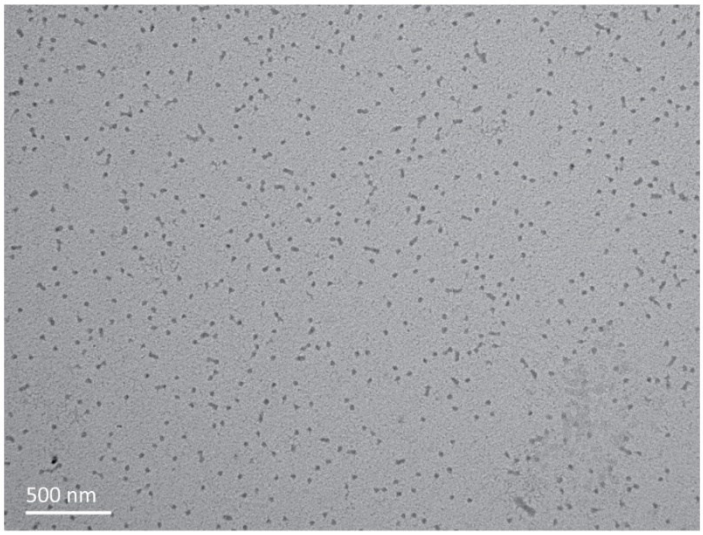

b) C_4/HE_{12}-HEG_{12}-A14

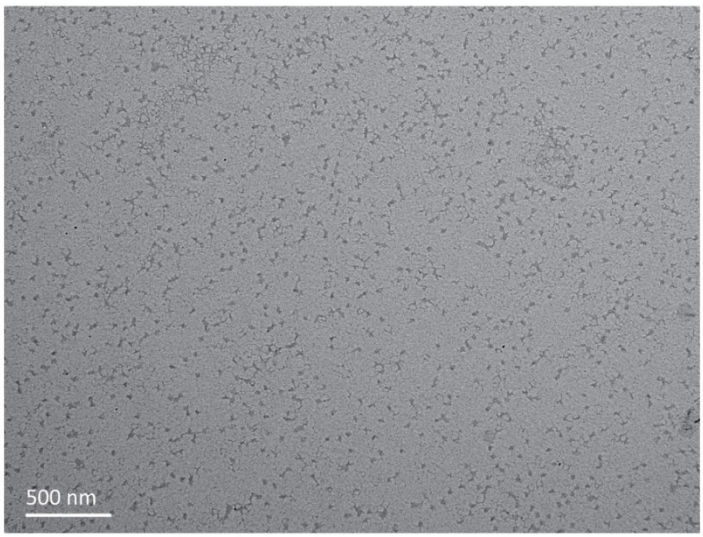

c) C_8/HE_{12}-HEG_6-A14

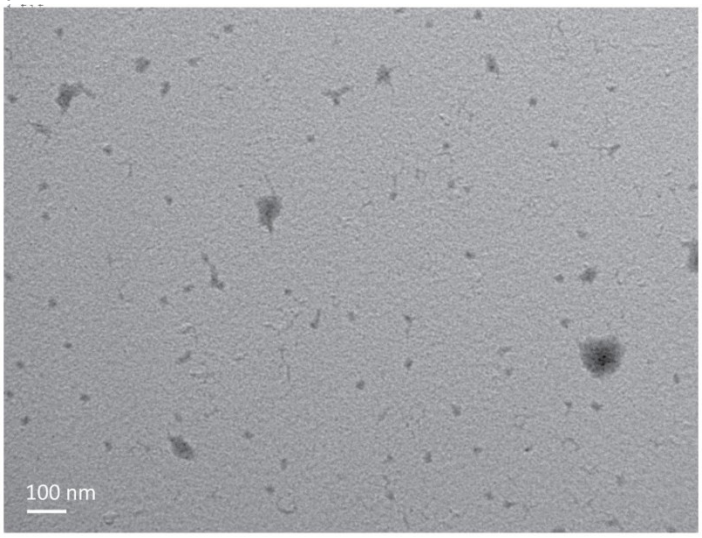

d) C_8/HE_{12}-HEG_{12}-A14

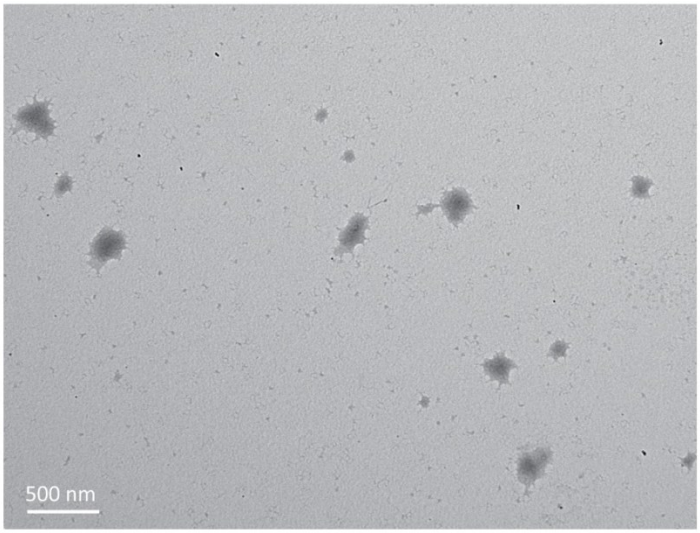

Figure 2.31 | TEM images of DNA cubes decorated with HE/HEG-DNA.

Gold nanoparticle labeled C_4/HE_6-A14:

DNA strands, named SBIS, containing two cyclic disulfide moieties at their 5' termini were decorated on the B face of cube $C_{AB,}$ which have four A edges on one face and four B edges on another face. This cube C_{AB} can be assembled from the clips 1AB, 2AB, 3AB, and 4AB. The sequences of all DNA strands for this experiment are listed in Table 2.10

Table 2.10 | Sequences of DNA clips for C_{AB} and SBIS (6 = HEG, X = HE, B = symmetrical branching, S = cyclic dithiol).

Strand	Sequence (5'→ 3')
1AB	TCGCTGAGTA 6 TCCTATATGGTCAACTGCTC 6 GCAAGTGTGGGCACGCACAC 6 GTAGTAATACCAGATGGAGT 6 CACAAATCTG
2AB	CTATCGGTAG 6 TCCTATATGGTCAACTGCTC 6 TACTCAGCGACAGATTTGTG 6 GTAGTAATACCAGATGGAGT 6 CAACTAGCGG
3AB	CACTGGTCAG 6 TCCTATATGGTCAACTGCTC 6 CTACCGATAGCCGCTAGTTG 6 GTAGTAATACCAGATGGAGT 6 GGTTTGCTGA
4AB	CCACACTTGC 6 TCCTATATGGTCAACTGCTC 6 CTGACCAGTGTCAGCAAACC 6 GTAGTAATACCAGATGGAGT 6 GTGTGCGTGC
SBIS	SXB TTTTACCATCTGGTATTAC

To assemble C_{AB}/SBIS, 1.25 µM (100 µL) of C_{AB} was mixed with SBIS (31.25 µL of 5 µM SBIS, 1.25 equivalent) in 1xTBE supplemented with 150 mM NaCl (TBEN). The samples were annealed from 95°C to 4°C over 6 hours. To 50 µL solution of 1 µM BSPP-coated 10-nm AuNP in 1xTBEN were added 90.1 µL of 555 nM C_{AB}-SBIS (1:1 ratio) and 16 µL of 10 mg/mL BSPP in 1xTBEN to obtain final BSPP concentration of 1 mg/mL. After incubation at room temperature overnight, 5 µL of 0.2 M HOOC-PEG_8-S-S-PEG_8-COOH in 1xTBEN was added to the mixtures and incubated at room temperature for 30 minutes. The crude mixtures were then loaded on 3% AGE, and the gel was run at 80 V for 1 hour with 1xTBE as the running buffer. The band corresponding to AuNP-C_{AB} monoconjugates was excised (Figure 2.32, the upper band in lane 1), cut into small pieces and soaked in 1xTAMg at 4°C. After 1-2 days, the liquid was isolated from the gel slices and centrifuged at 12000xg for 30 minutes in the cold room to collect the AuNP-C_{AB}. As a control, unbound AuNPs were also isolated using the same method.

The purity of isolated products was evaluated by 3% AGE. In lane 3 of Figure 2.32, there were two bands for the AuNP-C_{AB} monoconjugates. The upper band was the target structure, and the lower band could be AuNP-SBIS without C_{AB} (AuNP-$SBIS_4$) as this band showed lower electrophoretic mobility than free AuNPs in lane 2. The concentration of AuNP-C_{AB} was quantified by the absorption of AuNP at 450 nm using the extinction coefficient of 10-nm AuNP ($\varepsilon_{450\ nm}$ = $6.15x10^7$ $M^{-1}cm^{-1}$) reported in the literature.[31] The AuNP-C_{AB} was used for the next experiment without further purification.

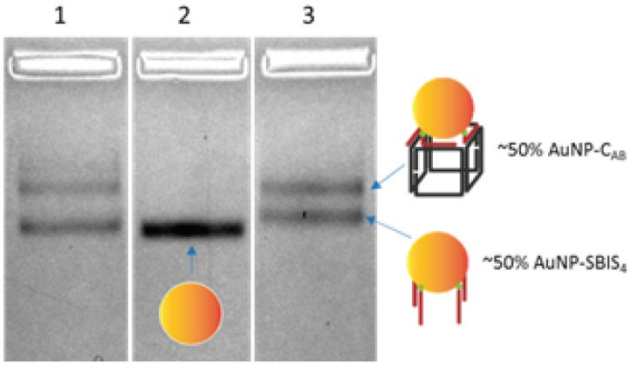

Figure 2.32 | Preparation and purity of gold/cube constructs. The bands on AGE assay (3%) are 1) crude mixture, 2) free AuNPs isolated from the lower band in lane 1, and 3) AuNP-C_{AB} isolated from the upper band in lane 1. The upper band in lane 3 was AuNP-C_{AB} while the lower band was AuNP-$SBIS_4$ that lost the cube components during the extraction process.

To assemble higher-order structures, AuNP-C_{AB} and HE_6-A14 were mixed in 1xTAMg buffer and incubated at room temperature overnight. While the concentrations of AuNP and HE_6-A14 were maintained at 125 and 750 nM, the actual concentration of AuNP-C_{AB} was lower than 125 nM due to the presence of AuNP-$SBIS_4$. HE_6-A14 was also added to the isolated AuNP as the control. The assembly products were run on 3% AGE at 80 V for 1.5 hours with 1xTAMg as the running buffer. In Figure 2.33, there was no change in the band of AuNP after addition of HE_6-A14 (lane 1 and 2), suggesting little or no interaction between HE_6-A14 and AuNPs. In contrast, the addition of HE_6-A14 to AuNP-C_{AB} led to the smearing on the gel although most of the products remained as unbound structures (lane 3 and 4).

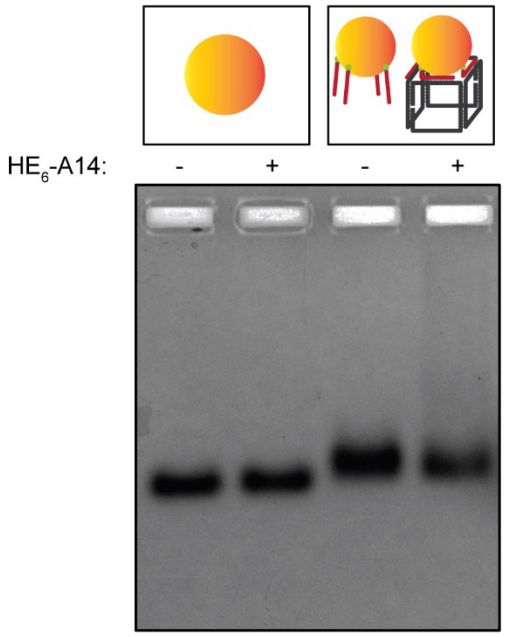

Figure 2.33 | Assembly of AuNP and AuNP-C_{AB} with HE_6-A14. AGE assay (3%) shows that there was no change after addition of HE_6-A14 to AuNP control and the smear could only be seen in case of AuNP-C_{AB} with HE_6-A14.

The structures were further characterized by TEM. For the sample preparation, 5 µL of 500 µg/mL bacitracin was deposited on the carbon-coated grid then wicked off by using filter paper after 1 min. Then, the grid was washed with 5 µL of water then wicked off excess. The samples were diluted 6x, and 5 µL was deposited on the grid then washed with 5 µL of water before drying under vacuum for 4 hours. TEM images of AuNP-C_{AB} and AuNP-C_{AB}/HE_6-A14 are shown in Figure 2.34.

a) AuNP-C_{AB}

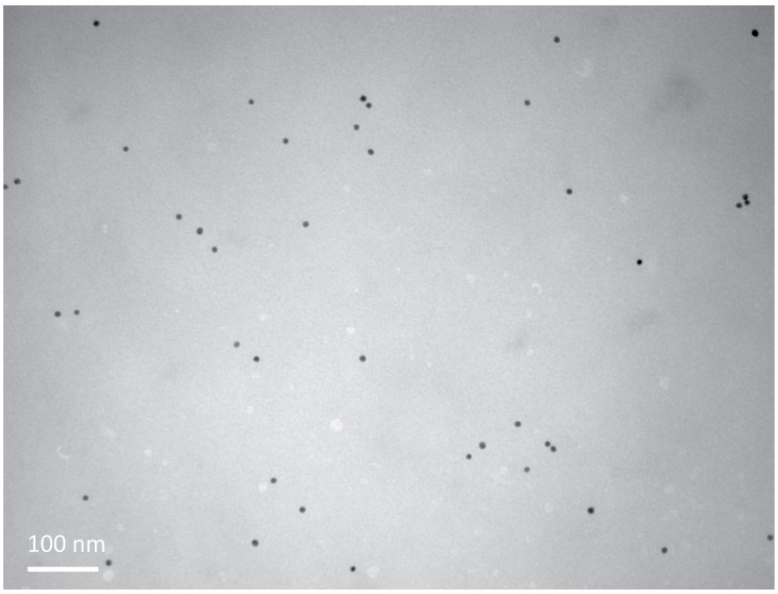

b) AuNP-C_{AB}/HE_6-A14

Figure 2.34 | TEM images of gold/cube constructs.

2.5.8 Dynamic light scattering

A 20-μL aliquot of the sample was analyzed on a DynaPro molecular-sizing instrument using a laser wavelength of 824 nm at 20°C or 25°C. Each sample was measured at least three times. Table 2.11 summarizes the hydrodynamic radii (R_h) and the polydispersity percentages of cube assembly with polymer-DNA conjugates. Although the polydispersity of size distribution of C_8/polymer-DNA conjugates was considerably narrow (<15%), we note that the size of large structures varied to some degree from one measurement to another. As such, the R_h values for these structures might not truly represent the actual size in solution. However, these values could be useful to provide their relative sizes.

Table 2.11 | DLS analysis of cube assembly with polymer-DNA conjugates.

Structure	R_h (nm)	% polydispersity
C_4	5.4±0.3	17.2±7.4
C_4/AT	6.0±0.6	19.1±9.8
C_4/HE_6-A14	7.7±1.0	25.5±8.4
C_4/HE_7-A14	11.0±1.6	25.0±12.6
C_4/HE_{12}-A14	17.4±1.5	19.4±7.8
C_4/HE_6-HEG_6-A14	13.6±1.1	14.7±7.1
C_4/HEG_6-HE_6-A14	6.9±0.9	25.2±16.1
C_4/HE_6-HEG_{12}-A14	17.7±1.4	17.3±8.9
C_4/HE_{12}-HEG_6-A14	19.7±0.9	15.6±7.9
C_8	5.4±0.6	23.2±9.5
C_8/A14	7.1±0.6	16.3±7.3
C_8/HE_6-A14	6.4±0.4	22.1±2.9
C_8/HE_8-A14	32.6±1.8	32.6±2.0
C_8/HE_{12}-A14	63.0±1.8	11.7±4.8
C_8/HE_6-HEG_6-A14	22.0±3.2	47.8±5.7
C_8/HEG_6-HE_6-A14	8.3±0.7	30.4±12.9
C_8/HE_6-HEG_{12}-A14	145.0±2.8	13.7±0.4
C_8/HE_{12}-HEG_6-A14	91.9±10.9	11.9±1.4
C_8/HE_{12}-HEG_{12}-A14	148.6±14.6	9.5±3.4

Figure 2.35 shows the histograms and the corresponding correlation curves of all structures.

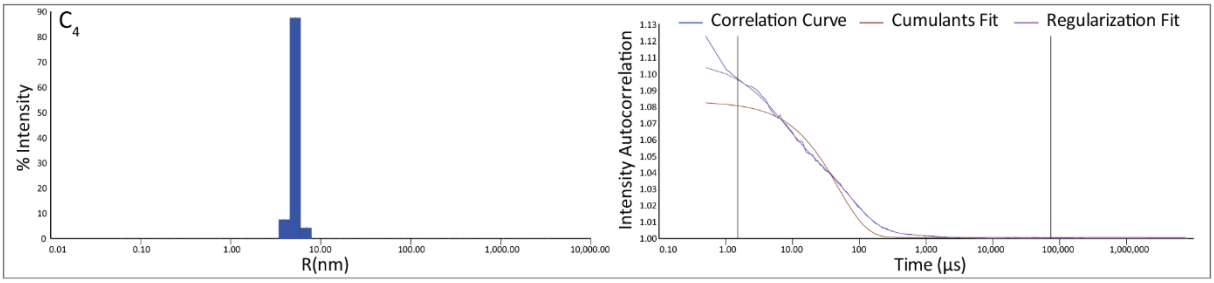

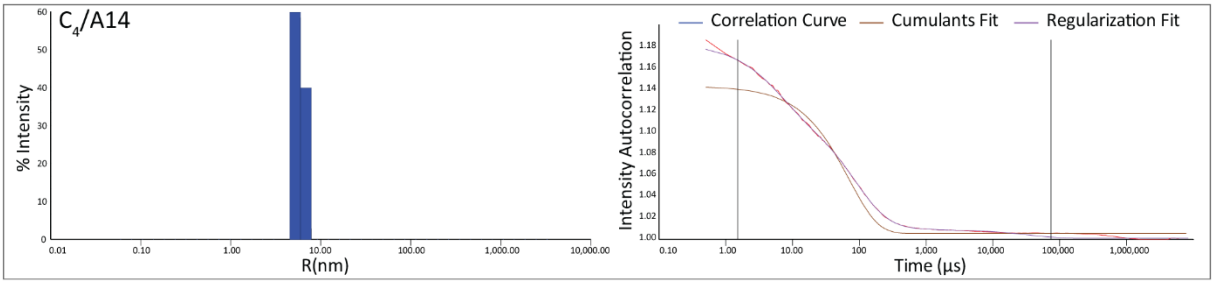

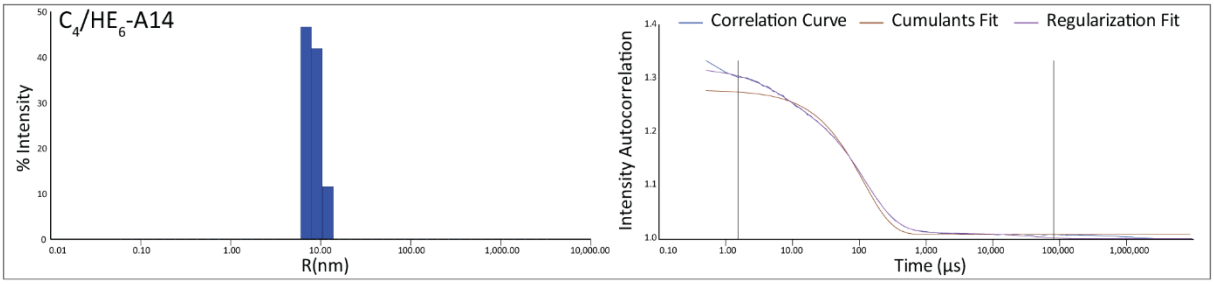

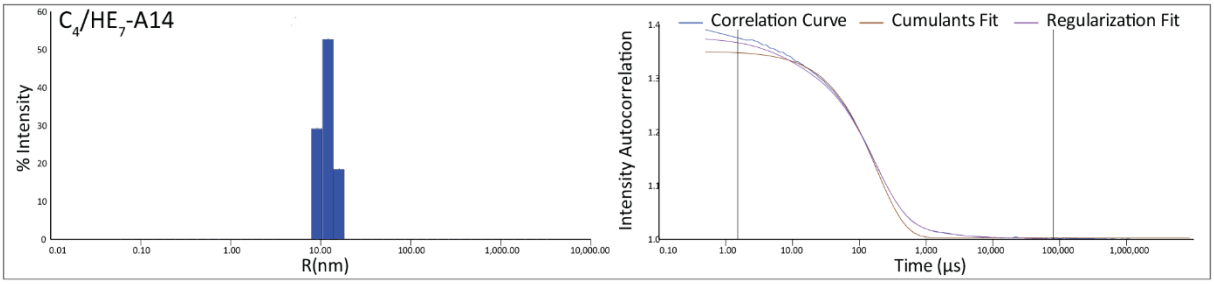

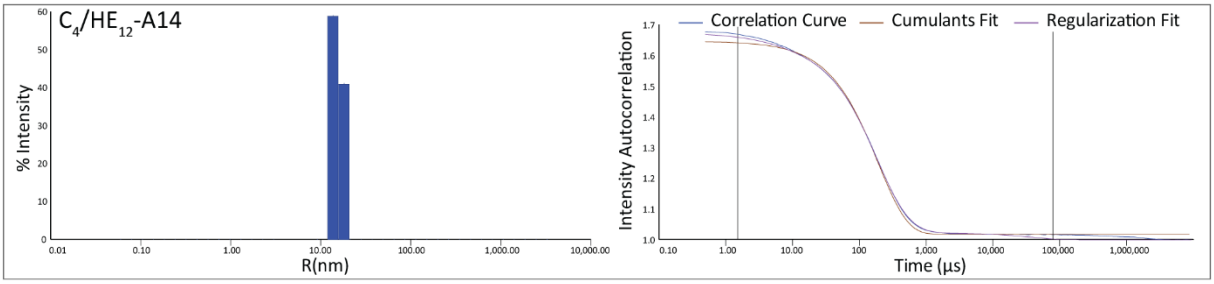

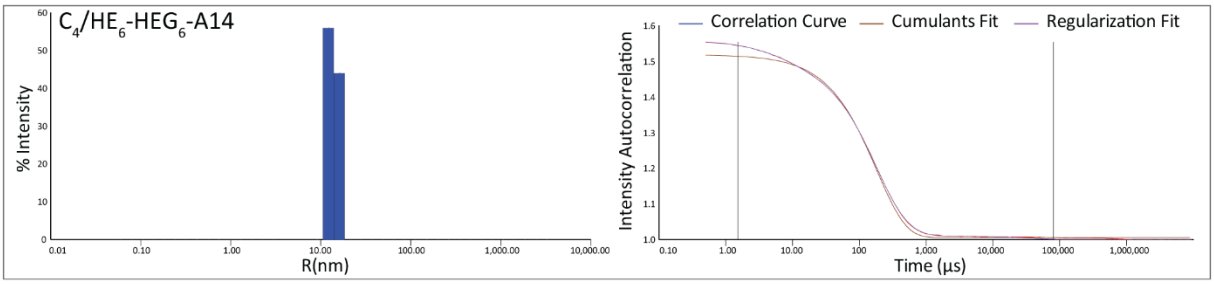
C4/HE6-HEG6-A14
% Intensity
R(nm)
Correlation Curve
Cumulants Fit
Regularization Fit
Intensity Autocorrelation
Time (µs)

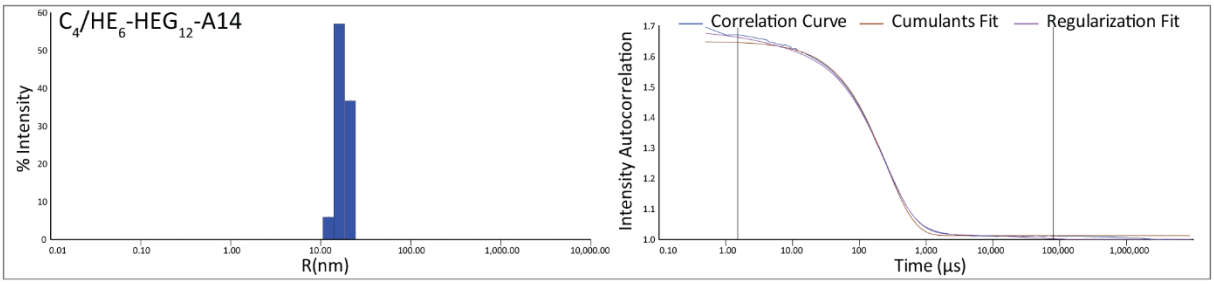
C4/HE6-HEG12-A14
% Intensity
R(nm)
Correlation Curve
Cumulants Fit
Regularization Fit
Intensity Autocorrelation
Time (µs)

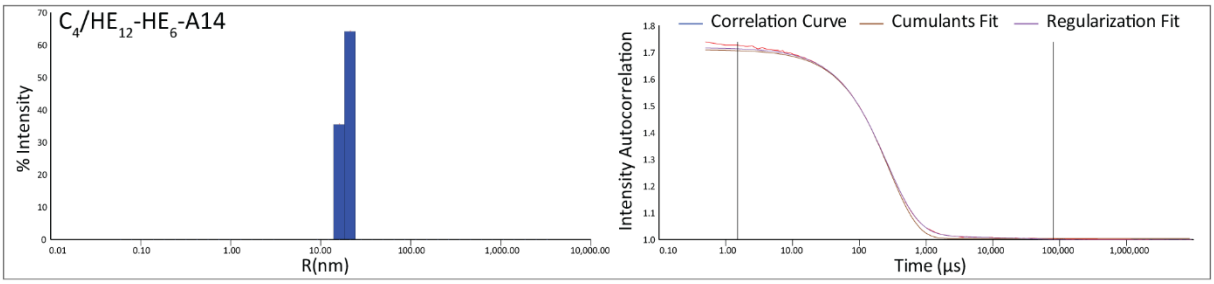
C4/HE12-HE6-A14
% Intensity
R(nm)
Correlation Curve
Cumulants Fit
Regularization Fit
Intensity Autocorrelation
Time (µs)

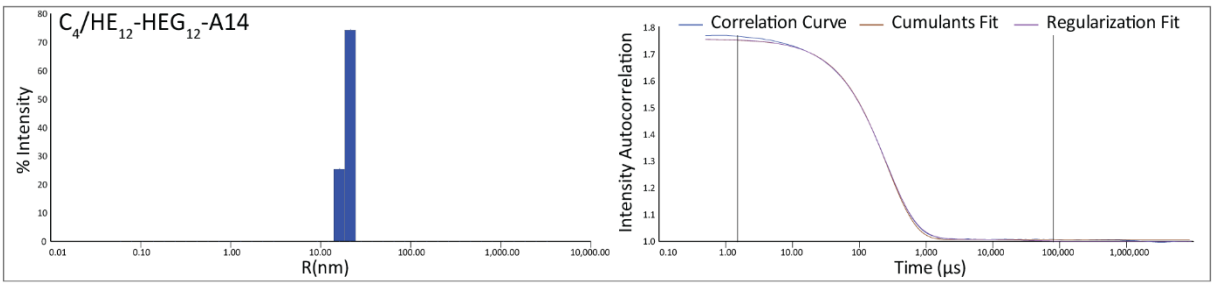
C4/HE12-HEG12-A14
% Intensity
R(nm)
Correlation Curve
Cumulants Fit
Regularization Fit
Intensity Autocorrelation
Time (µs)

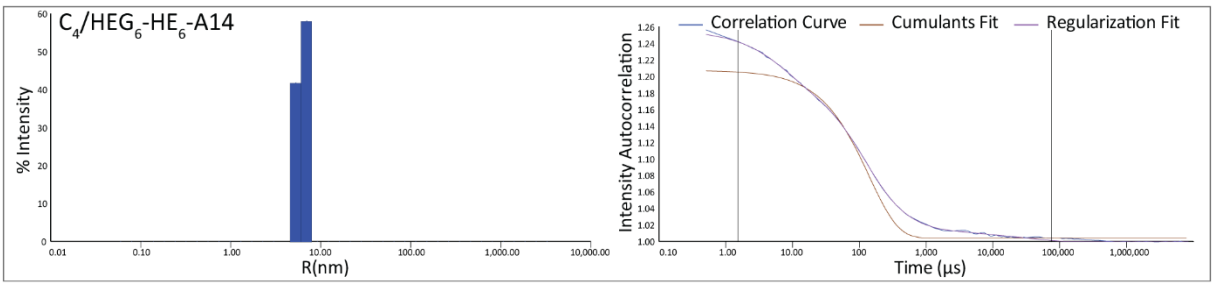
C4/HEG6-HE6-A14
% Intensity
R(nm)
Correlation Curve
Cumulants Fit
Regularization Fit
Intensity Autocorrelation
Time (µs)

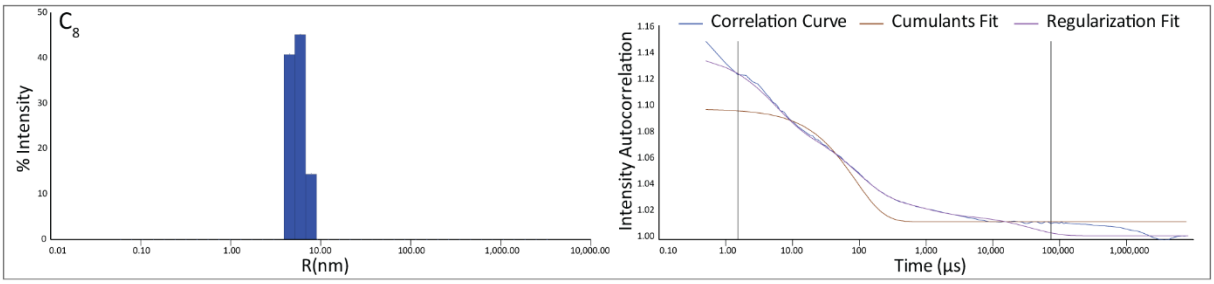
C8
% Intensity
R(nm)
Correlation Curve
Cumulants Fit
Regularization Fit
Intensity Autocorrelation
Time (µs)

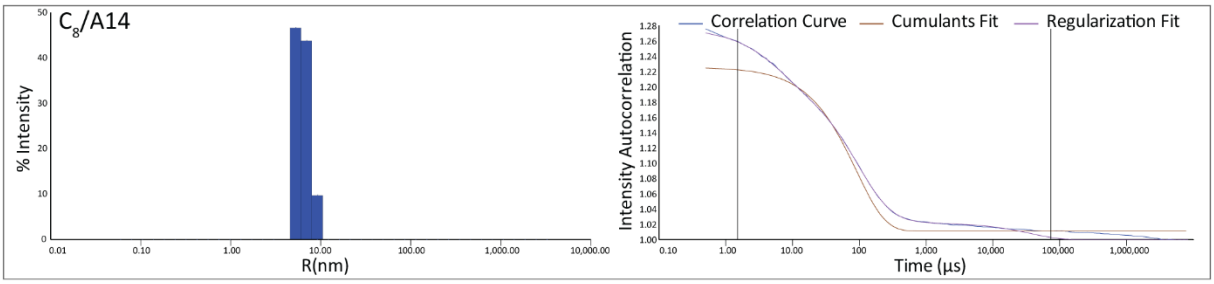
C8/A14
% Intensity
R(nm)
Correlation Curve
Cumulants Fit
Regularization Fit
Intensity Autocorrelation
Time (µs)

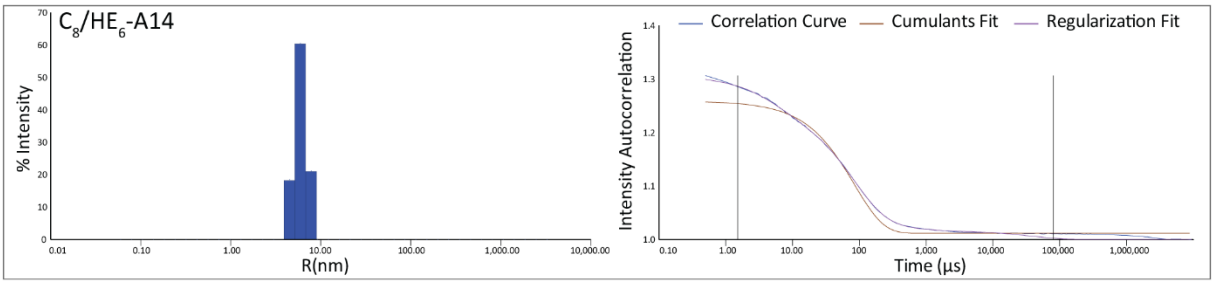
C8/HE6-A14
% Intensity
R(nm)
Correlation Curve
Cumulants Fit
Regularization Fit
Intensity Autocorrelation
Time (µs)

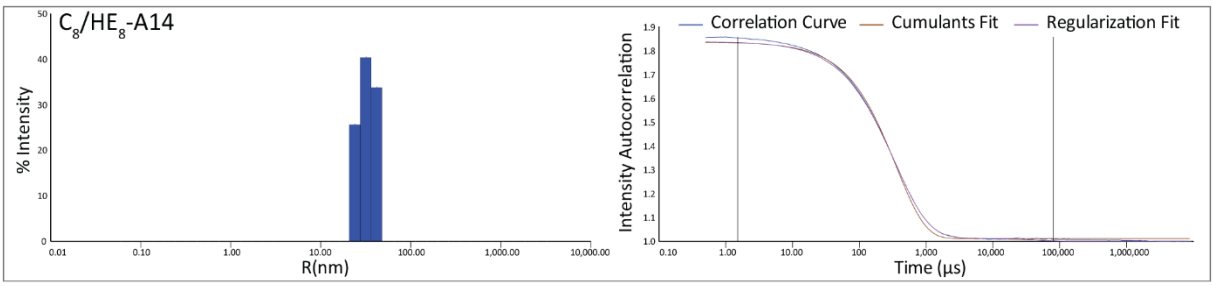
C8/HE8-A14
% Intensity
R(nm)
Correlation Curve
Cumulants Fit
Regularization Fit
Intensity Autocorrelation
Time (µs)

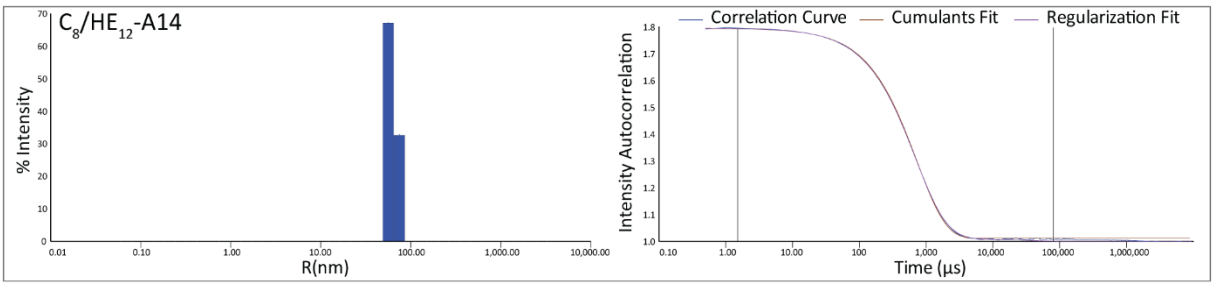
C8/HE12-A14
% Intensity
R(nm)
Correlation Curve
Cumulants Fit
Regularization Fit
Intensity Autocorrelation
Time (µs)

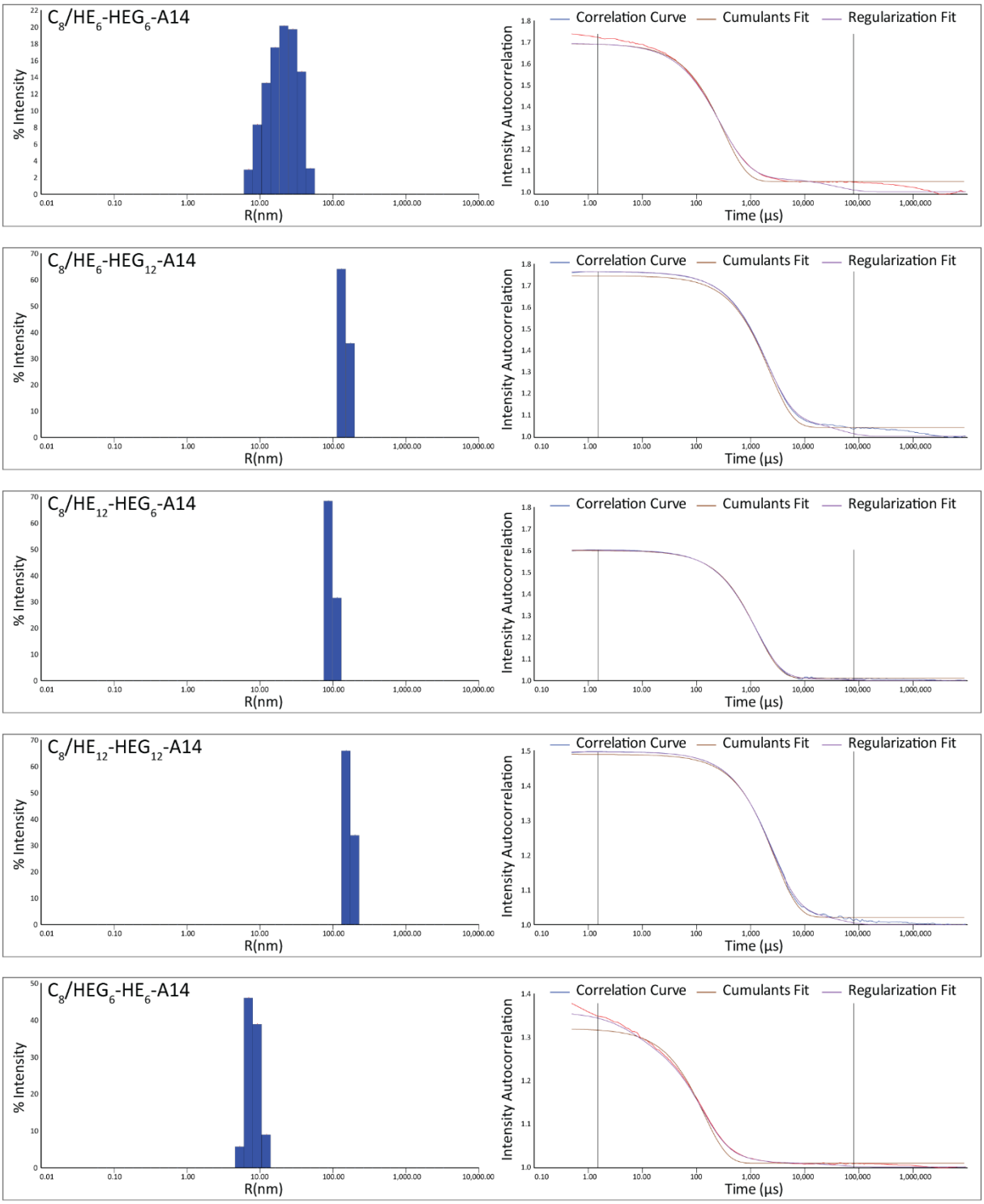

Figure 2.35 | DLS measurements of DNA cubes decorated with polymer-DNA conjugates. The histograms on the left panel show the size distribution of the assemblies. The corresponding intensity correlation function of individual measurements is shown in the right panel.

2.5.9 Stepwise photobleaching by single-molecule total internal reflection microscopy

The instrumental setup, preparation of imaging chambers and experimental procedures were based on the protocol reported by Hariri *et al*.[32]

Instrumentation:

The TIRFM setup consisted of an inverted microscope (IX71, Olympus) equipped with a laser-based TIRFM illumination module (IX2-RFAEVA-2, Olympus) coupled to a diode-pumped solid-state green laser (532 nm was used, lasers from CrystaLaser). The beam position was adjusted using the illuminator to attain total internal reflection through an oil-immersion objective (N.A. 1.45, Olympus U PLAN SAPO 60x). Fluorescence emission was collected through the objective and images were captured with an EMCCD camera (CascadeII: 512B, Photometrics, Roper Scientific). Emission was chromatically separated using dichroic mirrors (640dcxr, Chroma) with the green emission filtered through bandpass filters (HQ590/70M from Chroma) before being captured by the EMCCD camera. The camera was controlled using ImagePro Plus 5.1 (Media Cybernetics), capturing 8-bit 512x512-pixel images with an exposure time of 200 ms, a conversion gain of 3, and multiplication gain of 4095. Excitation was carried out with a power output of 9-21 mW from the power supply.

Preparation of imaging chambers:

Glass coverslips were first soaked in piranha solution (H_2O_2:H_2SO_4=1:3) and sonicated for 1 hour, followed by multiple rinses with water (molecular biology grade) and acetone (HPLC grade). Dry coverslips were then treated with Vectabond/acetone (1% v/v) solution for 5 minutes and rinsed with H_2O. To prevent non-specific adsorption onto the glass surface, coverslips were functionalized with a mixture of poly(ethylene glycol) succinimidyl valerate (mPEG-SVA, MW = 5000) and biotin-PEG-SVA at a ratio of 99/1 (w/w) in a 0.1 M sodium bicarbonate solution for 2.5-3 h. Excess PEG was rinsed with water, and the coverslips were dried under a N_2 stream. Imaging chambers were constructed by pressing a polycarbonate film with an adhesive gasket onto a PEG-coated coverslip. Two silicone connectors were glued onto the predrilled holes of the film and served as inlet and outlet ports.

Experimental procedure:

The surface was incubated with 10 µL of 0.2 mg/mL streptavidin solution for 5 minutes. Excess streptavidin was then washed with 100 µL of 1xTAMg buffer. Next, 10 µL of C_4/HE_6-A14 (15- to 30-fold dilution in 1xTAMg) was injected into the imaging chamber. C_4 was monolabeled with Cy3 dye by hybridizing Cy3-B14 strand (Cy3-TTTTTCCATCTGGTATTAC) to clip 1AB. To immobilize the assembly on the coverslips, we hybridized the clip 2AC with C-biotin strand (CCTTATCCTCTTACGGCAGAGTTTTTTTTT-biotin). Unbound DNA assembly was then washed away with 100 µL of 1xTAMg buffer. Multiple injections (usually 2-3) of the samples were performed in some cases to obtain proper sample density on the surface. To lower the photobleaching rate, 10 µL of oxygen scavenger solution (a triplet quencher agent, 1% v/v β-mercaptoethanol and an oxygen scavenger system (3% w/v D(+)glucose, 0.1 mg/mL glucose oxidase, and 0.02 mg/mL catalase)) was injected in the chamber. The movie of the photobleaching event was then acquired. The fluorescence intensity-time trajectories were extracted from the movie using a self-written algorithm in IDL and MATLAB software. The photobleaching steps were counted manually.

2.5.10 Nile Red encapsulation in DNA-micelle cages

Cages (125 nM) and HE_6-A14 or unmodified A14 (1.125, 1.5 and 1.875 µM for TP_3, C_4, and PP_5, respectively) were annealed together in 1xTAMg. In separated glass vials, 50 µL of 1 mM Nile Red solution in acetone was dried at room temperature to obtain films of Nile Red. Then, 400 µL of DNA solutions was added to the vials (final concentration of Nile Red = 125 µM or 1000-fold excess relative to cage concentration), mixed by a vortexer for 1 minute and gently shaken in the dark using the rotator for 19 hours. Excess Nile Red molecules were removed by centrifugation at 13.4 krpm for 10 minutes in the cold room. Then, the samples were concentrated by 10k MWCO centrifugal devices at 13.4 krpm for 10 minutes in the cold room.

To determine the cage concentration after removing excess Nile Red, the cages decorated with unmodified A14 or HE_6-A14 were analyzed by denaturing PAGE (12%) as shown in Figure 2.36a. The linear regression of known cage concentrations and their band intensities was fitted to determine the concentration of purified cages (Figure 2.36b). Furthermore, to confirm the cage integrity after Nile Red encapsulation, the concentrated cages were analyzed by non-denaturing

PAGE (5%). In Figure 2.36c, the major products were DNA-micelle cages, indicating that all cages with either unmodified A14 or HE_6-A14 remained intact after removal of excess Nile Red.

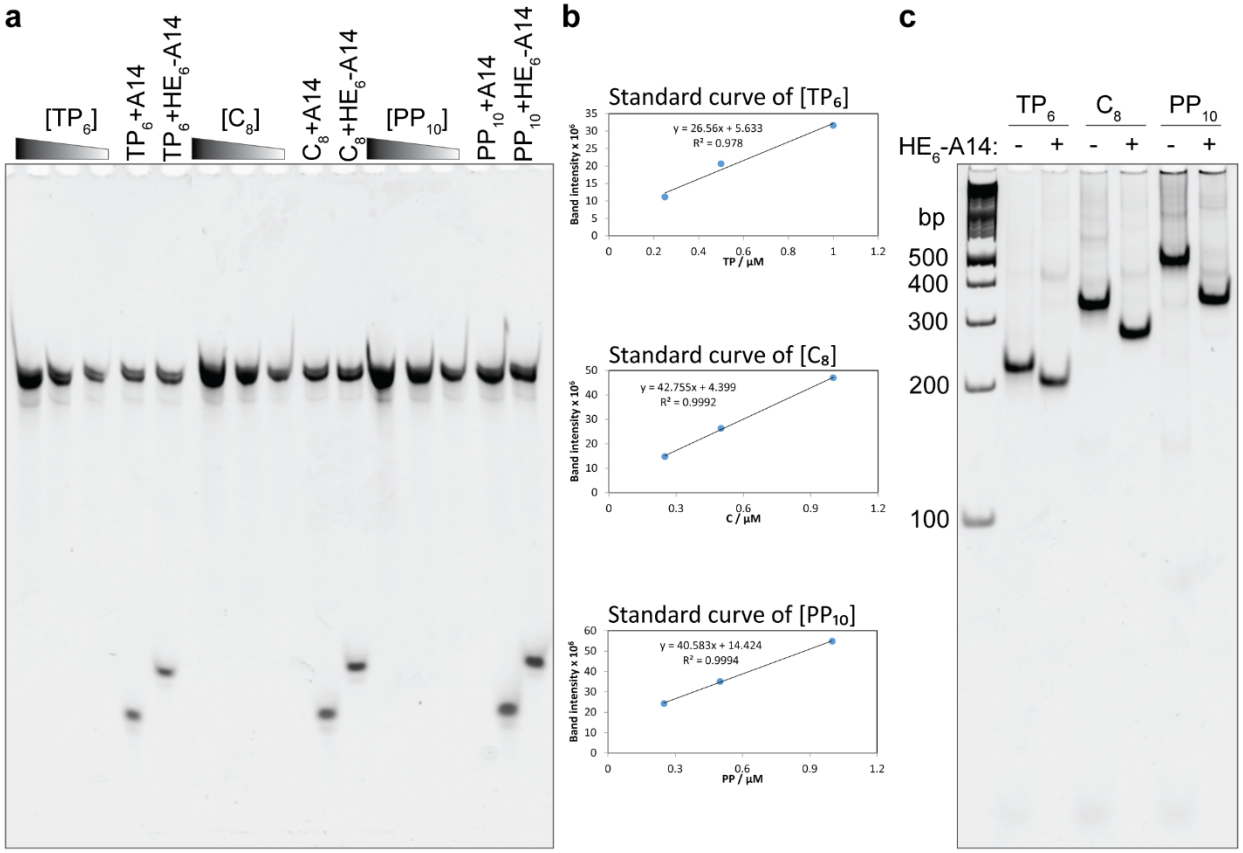

Figure 2.36 | Nile Red encapsulation in DNA-micelle cages. a) Denaturing PAGE (12%) was used to determine cage concentrations after removal of excess Nile Red. Known cage concentrations were 1, 0.5 and 0.25 μM. b) Standard curves of cage concentrations were constructed from the linear fitting of concentration and band intensity. c) Non-denaturing PAGE (5%) shows that the good structural integrity after Nile Red encapsulation and purification.

To measure fluorescence signals of encapsulated Nile Red, 20 μL of concentrated samples was mixed with 80 μL of acetone and transferred to a 96-well plate. The plate was read using the BioTek Synergy well-plate fluorometer. The excitation wavelength was 535 nm with a slit width of 9 nm, and the fluorescence emission was monitored from 560 to 750 nm. A series of Nile Red of known concentrations was also prepared to construct the standard curve to determine the concentration of Nile Red encapsulated within the cages (Figure 2.37). It should be noted that Nile Red fluorescence emission can be influenced by the polarity of the surrounding environment. Thus, acetone was added to the samples prior to the fluorescence measurement. Although DNA/DNA

amphiphilic components in the sample might have a possible effect on the fluorescence of Nile Red, Nile Red should mainly dissolve in the organic phase due to its high solubility in acetone. With a constant volume ratio between the buffer and acetone, it is most likely that Nile Red molecules in different samples sharing similar solvent environments could behave similarly. Thus, a calibration curve can be used to determine Nile Red concentrations in different cage samples.

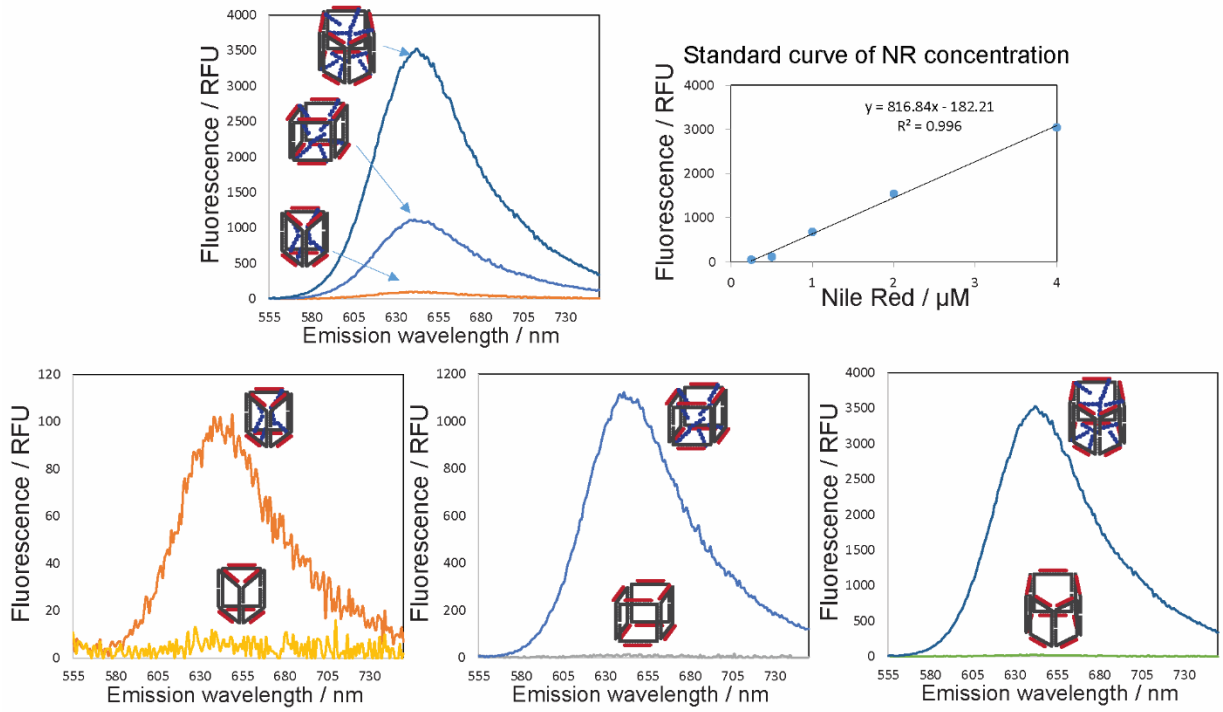

Figure 2.37 | Emission spectra of Nile Red encapsulated in DNA-micelles cages. The standard curve of Nile Red concentrations was used to determine the concentration of Nile Red in the assembly.

2.5.11 Thermal denaturation

Cube (375 nM) and polymer-DNA conjugates (2.25 μM for C_4 and 4.5 μM for C_8) were mixed and thermally annealed in 1xTAMg buffer. Then, 100 μL of samples was transferred to a quartz cuvette, and few drops of silicone oil were added on top. The absorbance at 260 nm was monitored in response to a temperature change (Figure 2.38, left panel). The temperature was increased from 25°C to 95°C with 1°C increment per minute. The first derivatives of the normalized melting curves were fitted with Lorentzian distribution function using OriginPro 2015 software. Then, the melting temperatures (T_m) were determined from the highest values of the first derivatives and the full

width at half-maximum (FWHM) values of the curves, which can be used to indicate the degree of cooperativity in DNA binding, were also obtained (Figure 2.38, right panel).

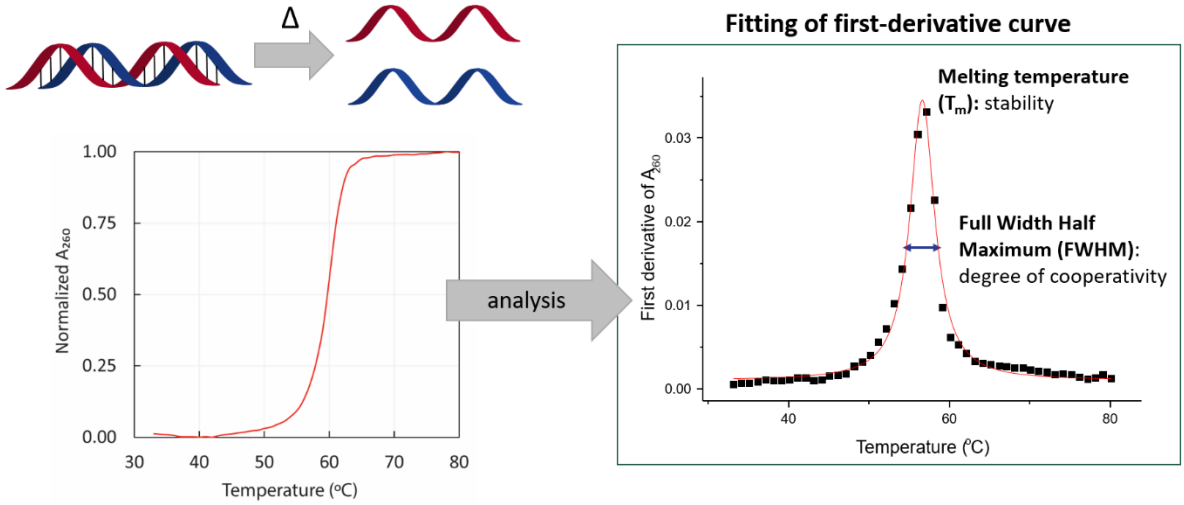

Figure 2.38 | Representative example of a melting curve and its first derivative curve. Lorentzian distribution was used to fit the first derivative curve to obtain two parameters: the peak maximum indicating the melting temperature (T_m) of DNA nanostructures and the full width at half-maximum (FWHM) indicating the degree of assembly cooperativity.

All T_m and FWHM values are listed in Table 2.12. Melting curves for all structures are shown in Figure 2.39.

Table 2.12 | Melting temperatures of cube assembly with polymer-DNA conjugates.[a]

DNA-polymer conjugates	C_4		C_8	
	T_m (°C)	FWHM (°C)	T_m (°C)	FWHM (°C)
A14	54.6±1.8	10.3±1.8	54.6±0.4	10.1±1.0
HE_6-A14	56.7±0.2	4.5±0.7	59.9±0.2	4.0±0.1
HE_6-HEG_6-A14	57.1±0.2	3.8±0.3	62.8±0.7	8.2±2.5
			(57.8±0.3, 62.6±0.6)	(4.1±1.6, 6.1±1.4)
HEG_6-HE_6-A14	54.9±0.4	7.7±1.1	55.9±0.1	7.3±0.4
HE_{12}-A14	56.8±0.2	5.3±0.3	65.8±1.0	6.7±1.6

DNA-polymer conjugates	C_4		C_8	
	T_m (°C)	FWHM (°C)	T_m (°C)	FWHM (°C)
HE_6-HEG_{12}-A14	56.4±0.3	4.2±0.5	61.9±0.8 (59.8±0.6, 64.7±0.4)	10.5±1.2 (5.7±0.6, 5.7±0.6)
HE_{12}-HEG_6-A14	57.7±0.2	3.8±0.1	66.0±1.7 (63.0±0.5, 67.1±1.2)	7.6±1.3 (3.5±3.0, 5.8±0.4)
HE_{12}-HEG_{12}-A14	57.6±0.3	3.7±0.4	66.3±1.0 (62.3±0.1, 66.9±0.5)	10.1±1.3 (6.6±0.2, 6.6±0.2)

[a] Some of the first derivative curves contained two local maxima. In addition to the values obtained from the fitting of the global maximum of the curves, the numbers in the parentheses were obtained from the multi-peak fitting of the two local maxima.

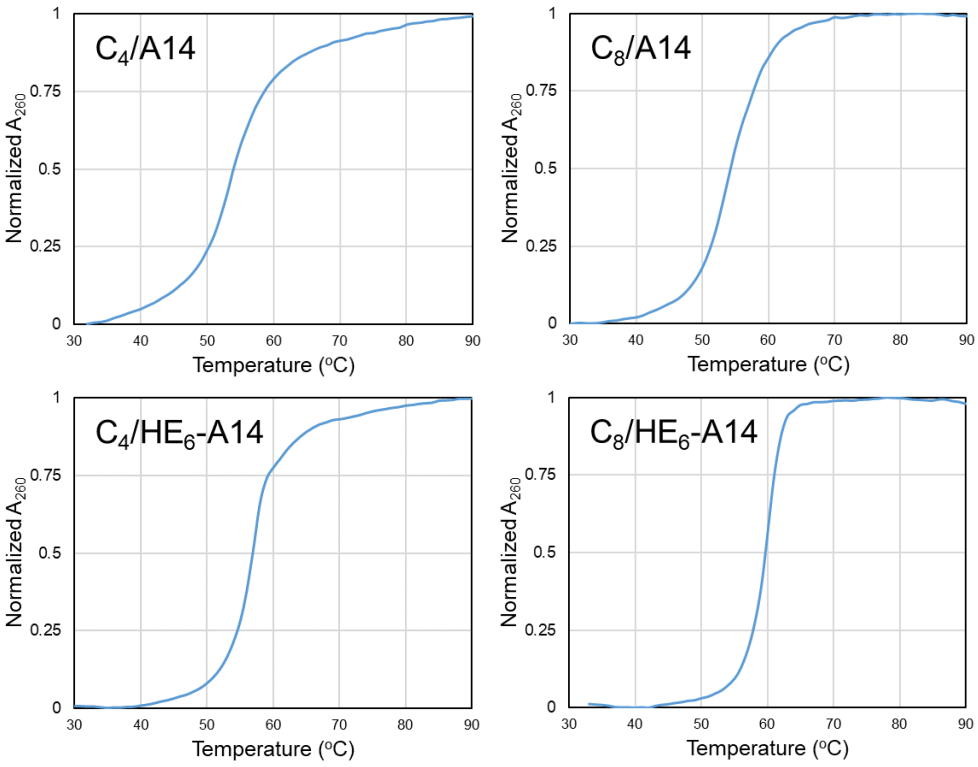

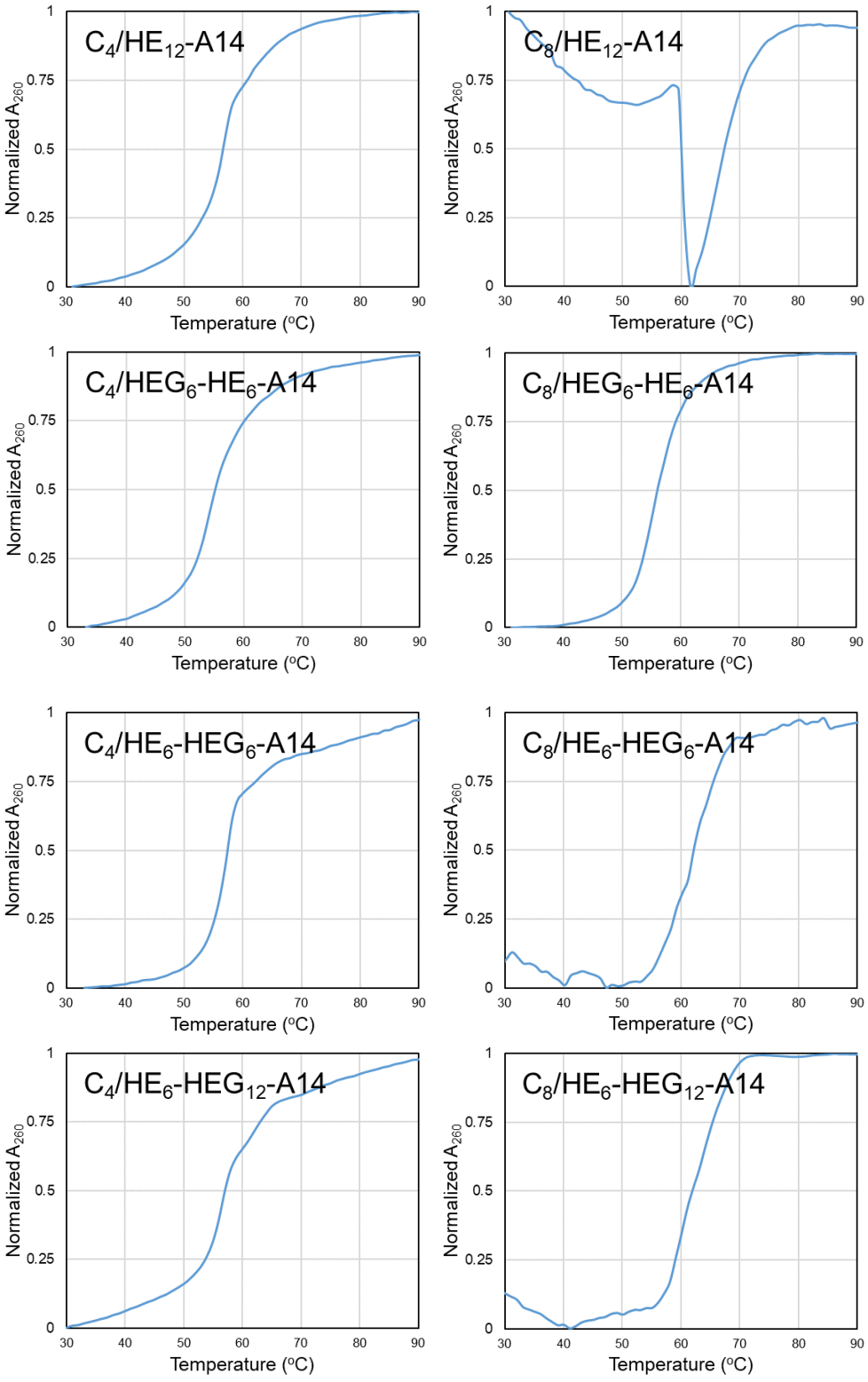
C4/HE12-A14
C8/HE12-A14
C4/HEG6-HE6-A14
C8/HEG6-HE6-A14
C4/HE6-HEG6-A14
C8/HE6-HEG6-A14
C4/HE6-HEG12-A14
C8/HE6-HEG12-A14
Normalized A260
Temperature (°C)
0
0.25
0.5
0.75
1
30
40
50
60
70
80
90

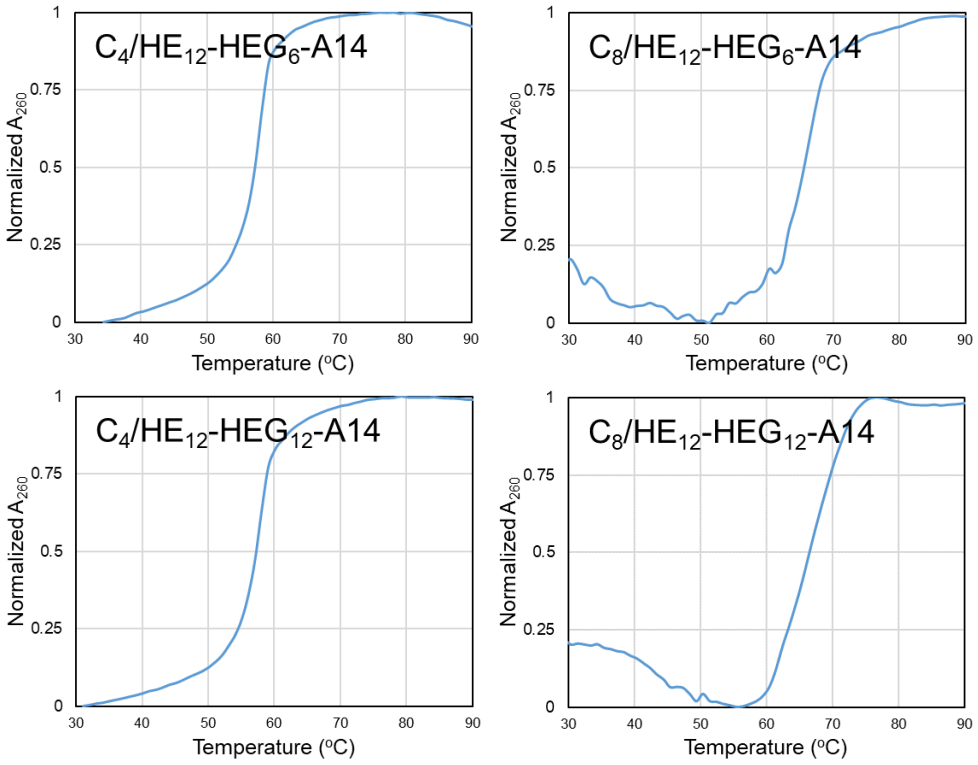

Figure 2.39 | Melting curves of DNA cubes decorated with polymer-DNA conjugates.

2.6 References

1. Lutz, J. F.; Ouchi, M.; Liu, D. R.; Sawamoto, M. *Science* 2013**,** 341, 1238149.
2. Aldaye, F. A.; Palmer, A. L.; Sleiman, H. F. *Science* 2008**,** 321, 1795-1799.
3. Winfree, E.; Liu, F.; Wenzler, L. A.; Seeman, N. C. *Nature* 1998**,** 394, 539-544.
4. Yan, H.; Park, S. H.; Finkelstein, G.; Reif, J. H.; LaBean, T. H. *Science* 2003**,** 301, 1882-1884.
5. Liu, D.; Wang, M.; Deng, Z.; Walulu, R.; Mao, C. *J. Am. Chem. Soc.* 2004**,** 126, 2324-2325.
6. He, Y.; Chen, Y.; Liu, H.; Ribbe, A. E.; Mao, C. *J. Am. Chem. Soc.* 2005**,** 127, 12202-12203.
7. Chen, J. H.; Seeman, N. C. *Nature* 1991**,** 350, 631-633.
8. Rothemund, P. W. *Nature* 2006**,** 440, 297-302.
9. Aldaye, F. A.; Sleiman, H. F. *J. Am. Chem. Soc.* 2007**,** 129, 13376-13377.
10. McLaughlin, C. K.; Hamblin, G. D.; Aldaye, F. A.; Yang, H.; Sleiman, H. F. *Chem. Commun.* 2011**,** 47, 8925-8927.
11. Wei, B.; Dai, M.; Yin, P. *Nature* 2012**,** 485, 623-626.
12. Mai, Y.; Eisenberg, A. *Chem. Soc. Rev.* 2012**,** 41, 5969-5985.
13. Woo, S.; Rothemund, P. W. *Nat. Chem.* 2011**,** 3, 620-627.
14. Edwardson, T. G.; Carneiro, K. M.; McLaughlin, C. K.; Serpell, C. J.; Sleiman, H. F. *Nat. Chem.* 2013**,** 5, 868-875.
15. List, J.; Weber, M.; Simmel, F. C. *Angew. Chem. Int. Ed.* 2014**,** 53, 4236-4239.

16. Zhou, C.; Wang, D.; Dong, Y.; Xin, L.; Sun, Y.; Yang, Z.; Liu, D. *Small* 2015**,** 11, 1161-1164.
17. Wilks, T. R.; Bath, J.; de Vries, J. W.; Raymond, J. E.; Herrmann, A.; Turberfield, A. J.; O'Reilly, R. K. *ACS Nano* 2013**,** 7, 8561-8572.
18. Serpell, C. J.; Edwardson, T. G.; Chidchob, P.; Carneiro, K. M.; Sleiman, H. F. *J. Am. Chem. Soc.* 2014**,** 136, 15767-15774.
19. Edwardson, T. G.; Carneiro, K. M.; Serpell, C. J.; Sleiman, H. F. *Angew. Chem. Int. Ed.* 2014**,** 53, 4567-4571.
20. Edwardson, T. G.; Lau, K. L.; Bousmail, D.; Serpell, C. J.; Sleiman, H. F. *Nat. Chem.* 2016**,** 8, 162-170.
21. Buckhout-White, S.; Ancona, M.; Oh, E.; Deschamps, J. R.; Stewart, M. H.; Blanco-Canosa, J. B.; Dawson, P. E.; Goldman, E. R.; Medintz, I. L. *ACS Nano* 2012**,** 6, 1026-1043.
22. Greenspan, P.; Mayer, E. P.; Fowler, S. D. *The Journal of Cell Biology* 1985**,** 100, 965-973.
23. Ehrenstein, G. W.; Theriault, R. P., *Polymeric materials : structure, properties, applications*. Hanser ; Hanser Gardner Publications: Munich; Cincinnati, OH, 2001.
24. Fuhrhop, J.-H.; Wang, T. *Chem. Rev.* 2004**,** 104, 2901-2938.
25. Blume, A.; Drescher, S.; Meister, A.; Graf, G.; Dobner, B. *Faraday Discuss.* 2013**,** 161, 193-213.
26. Shuai, X.; Ai, H.; Nasongkla, N.; Kim, S.; Gao, J. *J. Controlled Release* 2004**,** 98, 415-426.
27. Glavas, L.; Odelius, K.; Albertsson, A.-C. *Polym. Adv. Technol.* 2015**,** 26, 880-888.
28. Gou, J.; Feng, S.; Xu, H.; Fang, G.; Chao, Y.; Zhang, Y.; Xu, H.; Tang, X. *Biomacromolecules* 2015**,** 16, 2920-2929.
29. Eryazici, I.; Prytkova, T. R.; Schatz, G. C.; Nguyen, S. T. *J. Am. Chem. Soc.* 2010**,** 132, 17068-17070.
30. Greschner, A. A.; Toader, V.; Sleiman, H. F. *J. Am. Chem. Soc.* 2012**,** 134, 14382-14389.
31. Haiss, W.; Thanh, N. T.; Aveyard, J.; Fernig, D. G. *Anal. Chem.* 2007**,** 79, 4215-4221.
32. Hariri, A. A.; Hamblin, G. D.; Hardwick, J. S.; Godin, R.; Desjardins, J.-F.; Wiseman, P. W.; Sleiman, H. F.; Cosa, G. *Bioconjugate Chem.* 2017**,** 28, 2340-2349.

| 3 |

Functionalization of DNA cubes with cholesterol units and interactions with lipid bilayers

3.1 Preface

DNA cages are excellent scaffolds for the site-specific organization of functional groups such as sequence-defined polymers in 3D space as previously discussed in Chapter 2. DNA cages have also been extensively examined for the cellular delivery of therapeutics.[1-3] The first barrier encountered by these molecules as they interact with cells is the cellular lipid bilayer membrane. It is thus important to understand the interaction mechanisms of DNA cages with lipid bilayers. An early contribution in the Sleiman group has demonstrated the dynamic anchoring of DNA trigonal prism monofunctionalized with a cholesterol unit on microbead-supported bilayers to generate stimuli-responsive membrane-floating structures.[4] To extend the scaffolding concept in Chapter 2, this chapter aims to demonstrate a DNA-minimal strategy to systematically organize multiple cholesterol units on DNA cubes to tune their binding behavior on lipid bilayers. The solution assembly of cube/cholesterol constructs can be controlled by the number, orientation, and flexibility of cholesterol units tethered on the cubes. The binding behavior of cube/cholesterol constructs was then examined on free-floating lipid vesicles. Both number and orientation of cholesterol units on the cubes can be used to tune the surface mobility of cube/cholesterol constructs on the vesicle's surface, whereas the surface clustering of the constructs depends mainly on the number of cholesterol units. This strategy provides a simple method to create hybrid DNA nanostructures with high control of component organization. Cube/cholesterol constructs could be potentially applied as a platform to control the interactions of other materials with lipid bilayers, which have important applications for lipid membrane engineering and drug delivery.

3.2 Introduction

Structural organization in biomacromolecules is essential for regulating their assembly and function. The precise positioning of amino acid residues, for instance, not only directs protein folding but also significantly controls interactions of proteins with their environment. Mimicking such an organization degree in synthetic materials can provide tools to investigate biologically-relevant processes and to construct artificial functional devices.[5-6] In this regard, DNA assembly is a powerful approach that allows the rational design of nanoscale materials with arbitrary shape and size. The programmability of DNA base-pairing can be exploited to site-specifically functionalize molecules or materials of interest on DNA nanostructures with nanoscale resolution.[7]

As such, the versatility of DNA nanostructures has proven to be advantageous as a platform in many research areas where structural organization is a requirement.[8-9]

Among many applications is to integrate DNA nanostructures with lipid membranes.[10-11] This is of considerable interest as lipid bilayers are fundamental components for cellular compartmentalization, providing physical barriers for cells from their external environment. Another important class of membrane components is membrane proteins which facilitate cellular communication and regulate the transport of ions and biomolecules across the membranes.[12] They display a dynamic range of binding modes and affinity to cellular membranes. This can be attributed to how binding domains of membrane proteins are presented on their 3D structures.[13-14] Considering the power of DNA nanotechnology in size and shape control, there are consequently tremendous efforts in designing DNA nanostructures to synthetically mimic the roles of membrane proteins for many membrane-related applications (Figure 3.1).[15]

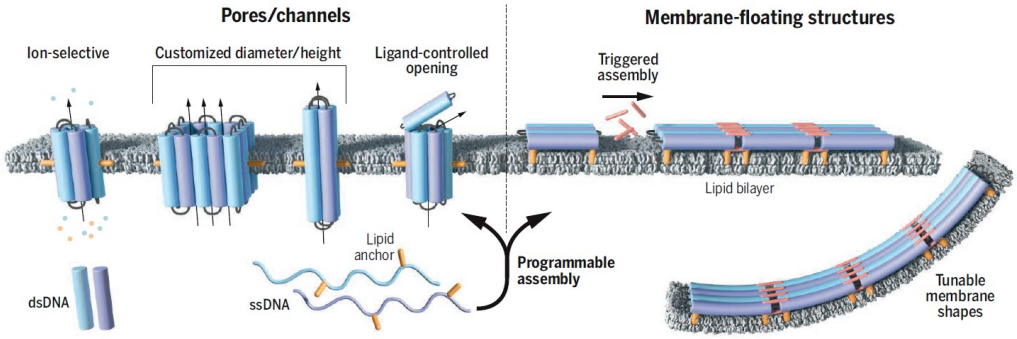

Figure 3.1 | DNA nanostructures interfacing with lipid bilayers. Adapted with permission from reference 15 (AAAS, 2016).

DNA-based nanochannels, akin to transmembrane proteins, are one of the main applications of DNA nanostructures interfacing with lipid membranes. Many hydrophobically-modified membrane-spanning DNA constructs, ranging from simple DNA duplexes to large DNA origami, have been demonstrated for ion and small molecule transport across membranes.[16-19] A second emerging area focuses on the surface functionalization of lipid bilayers with DNA nanostructures[20-21] and surface-mediated 2D assembly of DNA nanostructures on lipid membranes[22-24] with an aim to control physical properties of the bilayers. For instance, monodisperse size-defined liposomes can be produced from DNA-ring templates.[25] Oligomerization of cholesterol-functionalized massive DNA monoliths on giant lipid vesicles was

shown to display membrane-deforming activity, mimicking the process of membrane-curving proteins.[26]

A unique feature of DNA nanostructures is their capability to organize functional groups into well-defined, arbitrary patterns. We are thus interested in exploring the possibility to control the interaction modes of amphiphilic DNA cubes with lipid bilayers. In this chapter, we examine the orientation-dependent decoration of multiple cholesterol units on DNA cubes and its effect on the interactions with lipid bilayers. We found that the 3D organization and the spacing between cholesterol units can significantly affect cholesterol self-interactions within and between the cubes, leading to different assembly modes in solution. Upon binding to lipid vesicles, cube/cholesterol constructs showed tunable surface mobility and clustering degree on the lipid membranes that depends on the number and position of cholesterol units on the cubes. Moreover, the vesicle binding can provide shielding from enzymatic digestion for the cube/cholesterols constructs that have a high binding affinity to the bilayers. Finally, we preliminarily study the membrane poration activity of cube/cholesterol constructs, and the results suggest that some constructs are able to span the membranes and function as synthetic nanopores.

3.3 Results and Discussion

3.3.1 Design of cube scaffolds and cholesterol-DNA conjugates

Our goal is to control how deep the DNA structure is embedded into lipid bilayers by tuning the orientation and number of cholesterol units on a 3D DNA scaffold. A DNA cube is chosen as a single DNA-minimal scaffold to achieve different configurations of cholesterol units. To generate a cube, four 80-mer single-stranded DNA strands, called DNA clips, were assembled in a 'clip-by-clip' approach (Figure 3.2a). The resulting cube has a total of eight binding sites, consisting of 20-mer single-stranded DNA segments on its two opposite faces. Cholesterol units will be positioned through the hybridization with cholesterol-DNA conjugates of complementary sequences. In this study, there are four arrangements of cholesterol units on the cubes (Figure 3.2b): i) cube with one cholesterol unit (C_1), ii) cube with four cholesterol units on one face (C_4), iii) cube with eight cholesterol units (C_8), and iv) cube with two cholesterol units on one face and two units on another face, arranged in a diagonal manner ($C_{2,2}$).

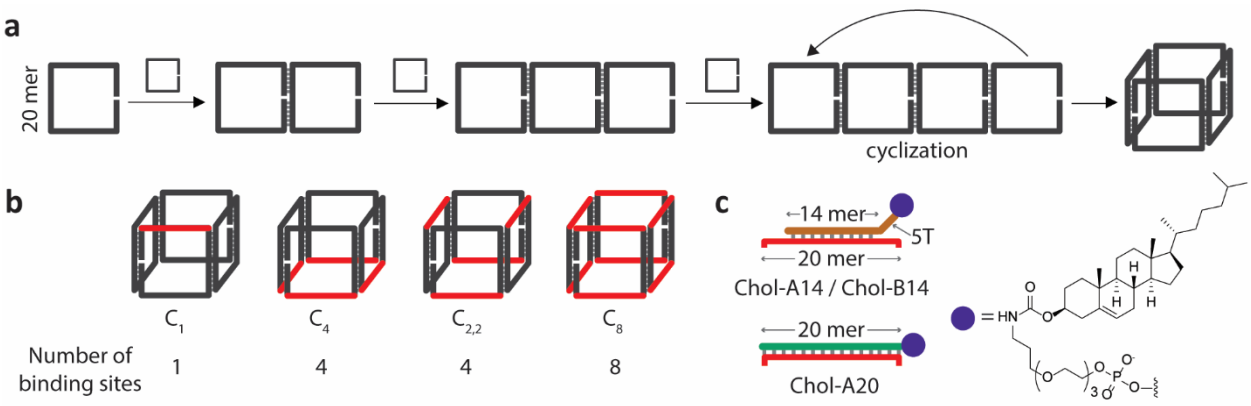

Figure 3.2 | Design of cube scaffolds and cholesterol-DNA conjugates. a) DNA cubes can be constructed from four DNA clips by 'clip-by-clip' approach. b) There are four cholesterol configurations on the cubes. The red lines show the binding sites of cholesterol-DNA conjugates on the cubes. c) Two versions of cholesterol-DNA conjugates were designed. Blue circle represents cholesteryl triethylene glycol unit at the 5' termini of cholesterol-DNA conjugates. We note that Chol-A14 was used to functionalize all cubes, except C_1 which used Chol-B14.

We designed two versions of cholesterol-DNA conjugates (Figure 3.2c) to control the degree of cholesterol self-interactions on the DNA cube. The first DNA sequences, named A14 and B14, are only complementary to 14 bases of the single-stranded segments on the cubes and have a 5 thymidine (T) spacer at the 5' terminus. We had noted that this partially complementary design gives flexibility to DNA cage, and allows an intrascaffold association of alkyl chains (see Chapter 2).[27-28] Another DNA sequence, named A20, was designed to be fully complementary to single-stranded segments on the cubes. Upon hybridizing Chol-A20 to the cube, the cholesterol units are positioned toward the corners of the cubes. We hypothesize that the longer distance between cholesterol units, compared to Chol-A14, and the increased nanostructure's rigidity are likely to reduce the self-interactions of cholesterol units of the same cube. This could also increase an exposure of cholesterol units of Chol-A20 on the cubes to the environment, which may strengthen the interactions between cube/cholesterol constructs and lipid bilayers.

Cholesterol-DNA conjugates were synthesized by a solid-phase DNA synthesis, where cholesterol units were functionalized at the 5' termini of DNA strands using a commercially available cholesteryl triethylene glycol phosphoramidite. This TEG unit serves as a linker to bypass hydrophilic head groups of lipids, facilitating the embedding of cholesterol unit into lipid bilayers.[29]

3.3.2 Assembly and structural characterization

There are two possible interaction modes for cube/cholesterol constructs. If the scaffold is flexible, and the hydrophobic units can meet intramolecularly, an intrascaffold association of the hydrophobic units is possible. On the other hand, if the hydrophobic units cannot meet intramolecularly, we may observe intermolecular hydrophobic aggregation (interscaffold association).[27-28] This would be more likely to happen with Chol-A14 than Chol-A20. The assembly of DNA cube with cholesterol-DNA conjugates was carried out by mixing all component strands in tris/acetate/magnesium buffer followed by thermal annealing from 95 to 4ºC over the course of 4 hours. The assembly products were characterized by non-denaturing polyacrylamide gel electrophoresis (PAGE) and atomic force microscopy (AFM).

3.3.2.1 Cube C_1 with one cholesterol unit

Upon C_1 assembly with a single cholesterol-DNA strand (Chol-B14), we observed a monomeric cube as the only product on the gel (Figure 3.3). There was a slight decrease in electrophoretic mobility of the band upon hybridization with either unmodified B14 or Chol-B14. High flexibility of the constructs is expected in this case, because of the presence of 7 remaining single-stranded segments on C_1/B14 and C_1/Chol-B14.

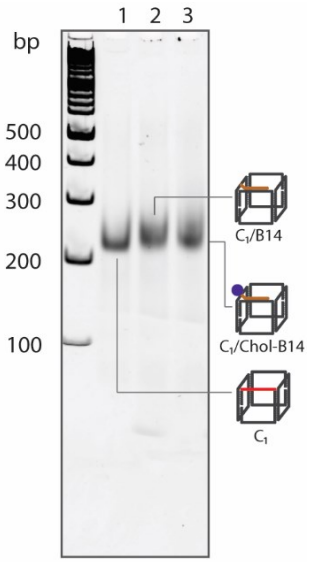

Figure 3.3 | Decoration of C_1 with cholesterol-DNA conjugate. Non-denaturing PAGE (5%) shows that monomeric cube was the main product for C_1/Chol-B14.

3.3.2.2 Cube C_4 with four cholesterol units on its face

C_4/Chol-A14 has four cholesterol-DNA conjugates positioned on one face of the cube. Its assembly on non-denaturing PAGE showed smearing bands of lower electrophoretic mobility, as compared to unfunctionalized C_4/A14 (Figure 3.4b, 6 equivalents). This suggests an aggregation of cubes, most likely mediated by interscaffold hydrophobic interactions between cholesterol units. AFM image in Figure 3.4d reveals some particle aggregates for C_4/Chol-A14, along with discrete spherical particles. The average size of these particles (diameter = 20.6±7.1 nm) was slightly bigger than unsubstituted cubes (diameter = 17.0±2.8 nm, see Chapter 2). Sample deposition on the mica surface followed by washing possibly breaks the aggregates. In the case of the more rigid C_4/Chol-A20, there was a discrete band showing similar electrophoretic mobility to unfunctionalized C_4/A20 (Figure 3.4c, 6 equivalents). This band could be assigned as a monomeric cube, which appeared as spherical particles by AFM (Figure 3.4e) This was consistent with the absence of intermolecular hydrophobic interactions mediated by cholesterol units for this rigid architecture.

We were interested to probe whether the hydrophobic interactions can induce the assembly cooperativity of cholesterol-DNA conjugates, possibly resulting in the all-or-none binding mode to the cubes.[28] At substoichiometric amounts of Chol-A20 with respect to C_4, there were 5 bands, corresponding to unsubstituted cube, and C_4 containing one to four Chol-A20 (Figure 3.4c, 2-3 equivalents). This indicates non-cooperative binding of Chol-A20 to C_4. The long distance between cholesterol units on C_4/Chol-20 could hinder cholesterol self-interactions across the face of the cube and prevent interscaffold aggregation of C_4/Chol-A20 monomers.

Adding substoichiometric amounts of the shorter Chol-A14 to C_4 showed distinct bands assigned to C_4 functionalized with 1-2 Chol-A14, in addition to unsubstituted cube (Figure 3.4b, 2-3 equivalents). Following these structures, the band became smeary at increasing Chol-A14 amounts. It is possible that greater than two Chol-A14 hybridized on a single C_4 face associate into a hydrophobic space that can promote aggregate formation. The increased cholesterol self-interactions, in this case, could stem from the closer distance between cholesterol units across the face of C_4/Chol-A14 and the higher flexibility, compared to C_4/Chol-A20. In this case as well, no significant binding cooperativity could be detected.

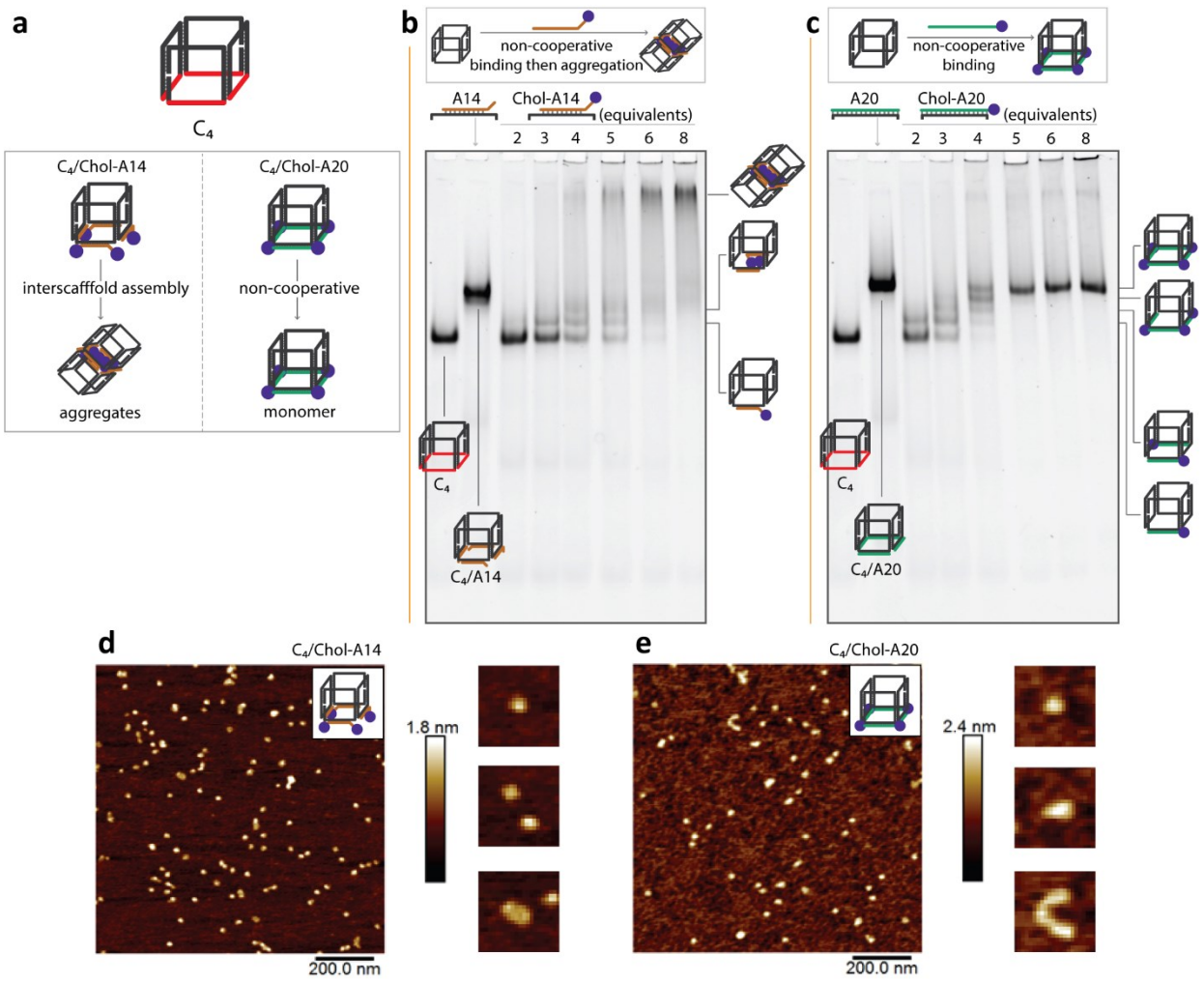

Figure 3.4 | Decoration of C_4 with cholesterol-DNA conjugates. a) Interscaffold hydrophobic interactions between cholesterol units led to C_4/Chol-A14 aggregation, whereas the main product of C_4/Chol-A20 was monomeric cube. Non-denaturing PAGE (5%) shows that b) aggregates were the main products for C_4/Chol-A14 and c) non-cooperative binding of Chol-A20 to C_4 resulted in monomeric cubes. The equivalents of cholesterol-DNA conjugates referred to their concentration with respect to C_4, where C_4 theoretically requires 4 equivalents of cholesterol-DNA conjugates to fill all 4 'A' binding sites. AFM images of d) C_4/Chol-A14 and e) C_4/Chol-A20 show discrete particles as the major products.

3.3.2.3 Cube $C_{2,2}$ with four cholesterol units on its two faces

The only difference between C_4 and $C_{2,2}$ is their cholesterol orientation. We hypothesized that the distribution of cholesterol-binding sites on both faces of $C_{2,2}$ could allow cholesterol units to meet inside the scaffold and facilitate intrascaffold association. This is most likely to happen with the more flexible Chol-A14. Figure 3.5b (6 equivalents) shows that the major product of $C_{2,2}$/Chol-

A14 was monomeric cube. The band mobility was higher than unfunctionalized $C_{2,2}$/A14, suggesting the scaffold compaction.[28] In this case, adding substoichiometric amounts of Chol-A14 to $C_{2,2}$ resulted in a single band corresponding to monomeric cube (Figure 3.5b, 2-3 equivalents), consistent with all-or-none cooperative binding mechanism. We note that the change in electrophoretic mobility of $C_{2,2}$/A14 and $C_{2,2}$/Chol-A14 was less than predicted, compared to C_4 in Figure 3.4b. This could be attributed to the higher flexibility of $C_{2,2}$/A14 arising from two half-single-stranded faces of the cubes, compared to only one fully-single-stranded face of C_4/A14.

Interestingly, no aggregation of $C_{2,2}$/Chol-A14 was observed by the gel. This could be rationalized by two possibilities. First, the binding of only two Chol-A14 on one face of $C_{2,2}$ may not provide sufficient interactions to bring together monomeric $C_{2,2}$/Chol-A14 to form aggregates. Second, the cooperative binding of Chol-A14 should be preferable in $C_{2,2}$ due to the intrascaffold association of cholesterol units, which is also supported by the cooperative assembly. Because of the increase in electrophoretic mobility and the binding cooperativity, we believe that $C_{2,2}$/Chol-A14 exhibits an intrascaffold hydrophobic interactions of its cholesterol units.[27-28]

In the case of $C_{2,2}$/Chol-A20, the monomeric cube was also the main product as indicated by a single band on the gel (Figure 3.5c, 6 equivalents). Unlike $C_{2,2}$/Chol-A14, no change in electrophoretic mobility of $C_{2,2}$/Chol-A20 in comparison to unfunctionalized $C_{2,2}$/A20 was observed, suggesting no scaffold compaction. Adding substoichiometric amounts of Chol-A20 to $C_{2,2}$ resulted in the formation of $C_{2,2}$ functionalized with 1-4 Chol-A14 (Figure 3.5c, 2-3 equivalents). This non-cooperative binding of Chol-A20 to $C_{2,2}$, in addition to increased rigidity of $C_{2,2}$ upon hybridization with Chol-A20, implies that $C_{2,2}$/Chol-A20 does not display an intrascaffold interactions of its cholesterol units.

AFM images show spherical particles and a minor population of short chain-like particles for both $C_{2,2}$/Chol-A14 (Figure 3.5d) and $C_{2,2}$/Chol-A20 (Figure 3.5e). Monomeric cubes were expected to be the main products in both constructs as indicated by the gels. We suspect that the formation of chain-like structures was driven by drying effects during sample preparation. However, PAGE may be more reliable, because this technique is less likely to affect the native state of cube/cholesterol constructs, as compared to strong DNA-mica interactions on AFM in the dry state. Thus, the assembly of $C_{2,2}$ with Chol-A14 and Chol-A20 leads to monomeric cubes as the major products.

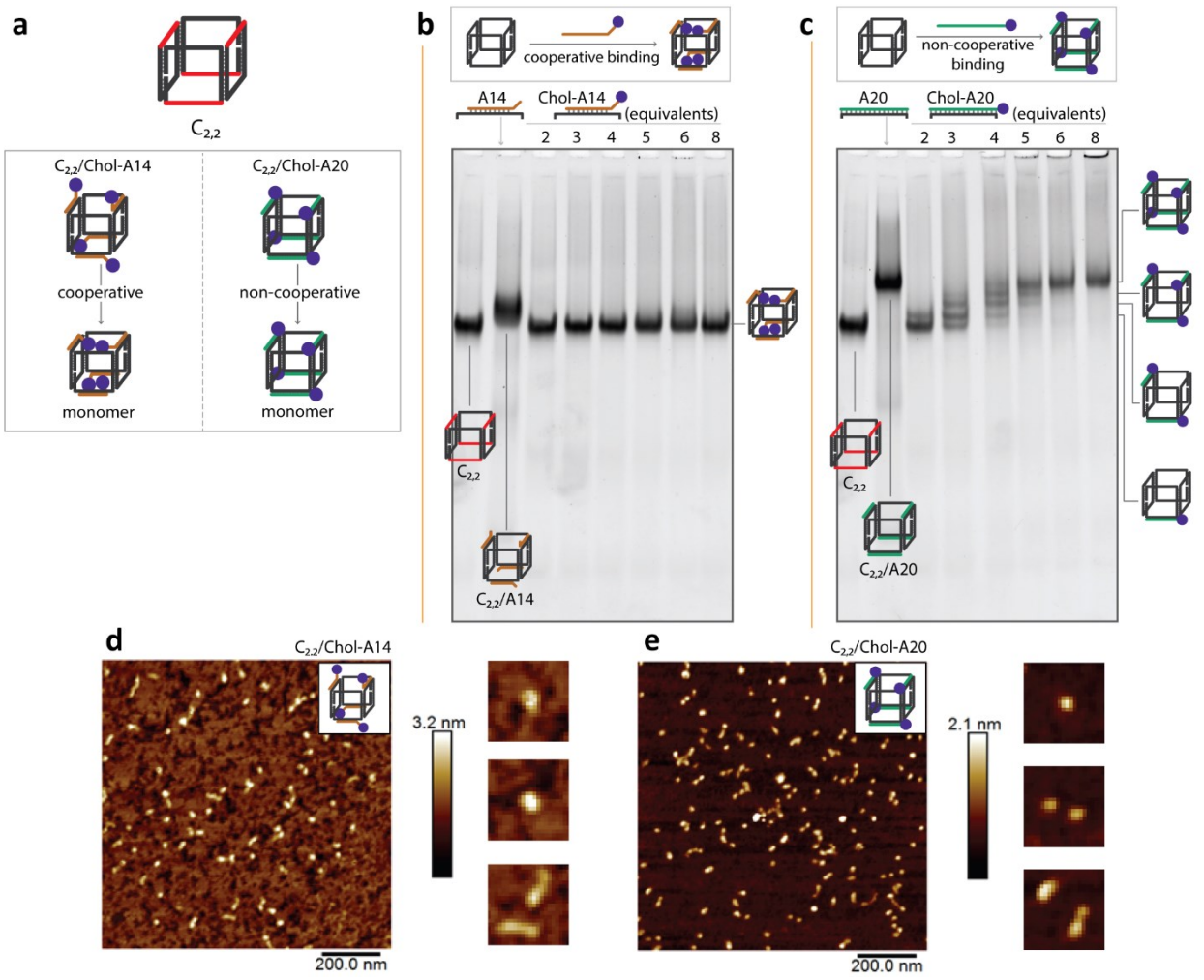

Figure 3.5 | Decoration of $C_{2,2}$ with cholesterol-DNA conjugates. a) The monomeric cubes were the main products for both $C_{2,2}$/Chol-A14 and $C_{2,2}$/Chol-A20. Non-denaturing PAGE (5%) shows b) cooperative binding of Chol-A14 but c) non-cooperative binding of Chol-A20 to $C_{2,2}$. The equivalents of cholesterol-DNA conjugates referred to their concentration with respect to $C_{2,2}$, where $C_{2,2}$ theoretically requires 4 equivalents of cholesterol-DNA conjugates to fill two 'A' binding sites on each face of the cube. AFM images of d) $C_{2,2}$/Chol-A14 and e) $C_{2,2}$/Chol-A20 show discrete particles and short chain-like particles, which were likely to be mediated by drying effects.

3.3.2.4 Cube C_8 with eight cholesterol units on its two faces

As C_8 has 8 binding sites distributed evenly on both faces, C_8/Chol-A14 can possibly form a monomeric cube with an intrascaffold association of cholesterol units. We observed two distinct bands on the gel for C_8/Chol-A14 (Figure 3.6b, 12 equivalents). The higher mobility band could be assigned as monomeric cube. The intrascaffold association of cholesterol units in this structure

was evidenced by the increased band mobility, compared to unfunctionalized C_8/A14. The cooperative binding of Chol-A14 to C_8 was supported by the formation of unsubstituted and fully functionalized cubes at substoichiometric Chol-A14 amounts (Figure 3.6b, 4-6 equivalents). We assigned the less intense, lower mobility band as cube dimer, which formed by interscaffold hydrophobic interactions. AFM images (Figure 3.6d) further support the gel by revealing single spherical particles as the major products and linear dimeric particles as the minor products.

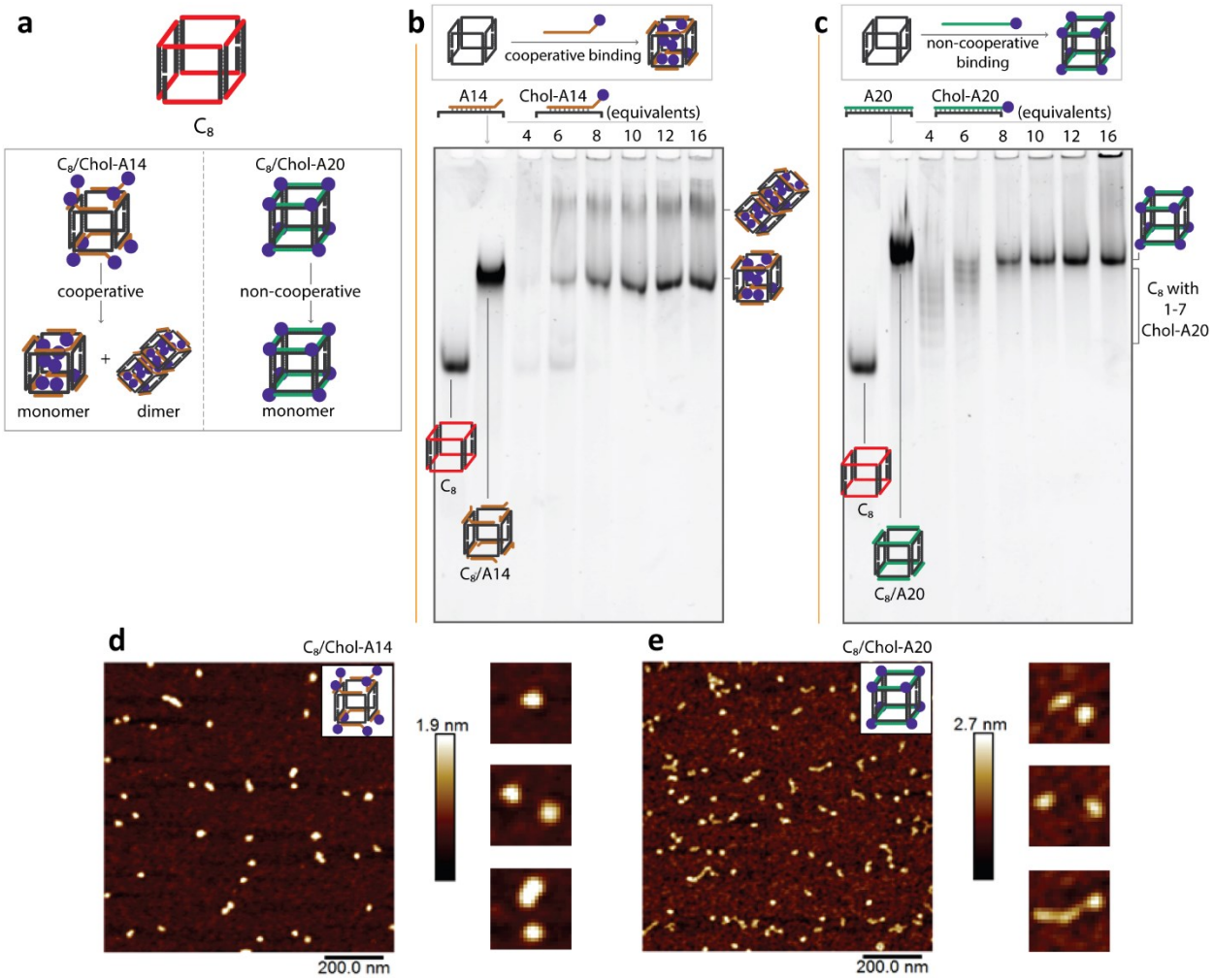

Figure 3.6 | Decoration of C_8 with cholesterol-DNA conjugates. a) Monomeric cube and cube dimer were the assembly products of C_8/Chol-A14, whereas monomeric cube was the main product for C_8/Chol-A20. Non-denaturing PAGE (5%) shows b) cooperative binding of Chol-A14 but c) non-cooperative binding of Chol-A20 to C_8. The equivalents of cholesterol-DNA conjugates referred to their concentration with respect to C_8, where C_8 theoretically requires 8 equivalents of cholesterol-DNA conjugates to fill all 8 'A' binding sites. AFM images of d) C_8/Chol-A14 show single particles and some dimers, and e) single particles and short chain-like particles for C_8/Chol-A20. The formation of aggregates was likely mediated by drying effects.

We predicted that C_8/Chol-A20 would form a monomeric cube without intrascaffold association of cholesterol units. Figure 3.6c (12 equivalents) validates this hypothesis, showing only one band with similar electrophoretic mobility to C_8/A20 on the gel. At substoichiometric Chol-A20 amounts, multiple bands corresponding to C_8 functionalized with 1-7 Chol-A20 were clearly observed (Figure 3.6c, 4-6 equivalents), indicating non-cooperative binding of Chol-A20 to C_8. In Figure 3.6e, there were single particles and some chain-like particles on mica surface as observed by AFM.

Therefore, DNA cube functionalization with the shorter, flexible Chol-A14 can generate two assembly modes mediated by cholesterol self-interactions. The cholesterol units on both cube faces can engage in an intrascaffold association within the cube, resulting in monomeric products as in $C_{2,2}$/Chol-A14. The cubes can form aggregates when cholesterol self-interactions on the same face are strong as in C_4/Chol-A14. Both assembly modes can occur in C_8/Chol-A14. Importantly, the intramolecular association of cholesterol units across the cube faces results in cooperative binding of Chol-A14 units to the cube ($C_{2,2}$/Chol-A14 and C_8/Chol-A14). This behavior can weaken lipid interactions as shown in the following section. On the other hand, the formation of monomeric cubes as the only products in DNA cubes functionalized with Chol-A20 could be attributed to the increased scaffold rigidity and longer distance between cholesterol units, preventing cholesterol self-interactions and leading to non-cooperative binding of Chol-A20 to the cubes.

3.3.3 Interaction of cube/cholesterol constructs with lipid vesicles

Lipid-binding experiments of cube/cholesterol constructs were then carried out to study the effect of design parameters on binding behavior. For these experiments, giant unilamellar vesicles (GUVs) composed of 1,2-dioleyl-*sn*-glycero-3-phosphocholine (DOPC) were used. DOPC GUVs were prepared by agarose-assisted film hydration method, yielding vesicles with tens of micrometers in diameter (the procedure is detailed in Section 3.5.8).[30] To aid the fluorescence visualization by confocal laser scanning microscopy (CLSM), all DNA cubes were monolabeled with a Cy3 fluorescent dye at the 5' terminus of one of the DNA clips. We found that all cube/cholesterol constructs showed significantly higher fluorescence signals on the vesicle's surface than unfunctionalized cubes, suggesting that the GUV binding of these constructs is mediated by cholesterol-lipid interactions. As an example, Figure 3.7 shows the binding of

C_4/Chol-A20 to the GUV. The regular distribution on the vesicle's surface and good colocalization with a lipid-labeling dye, DiD, could be clearly observed.

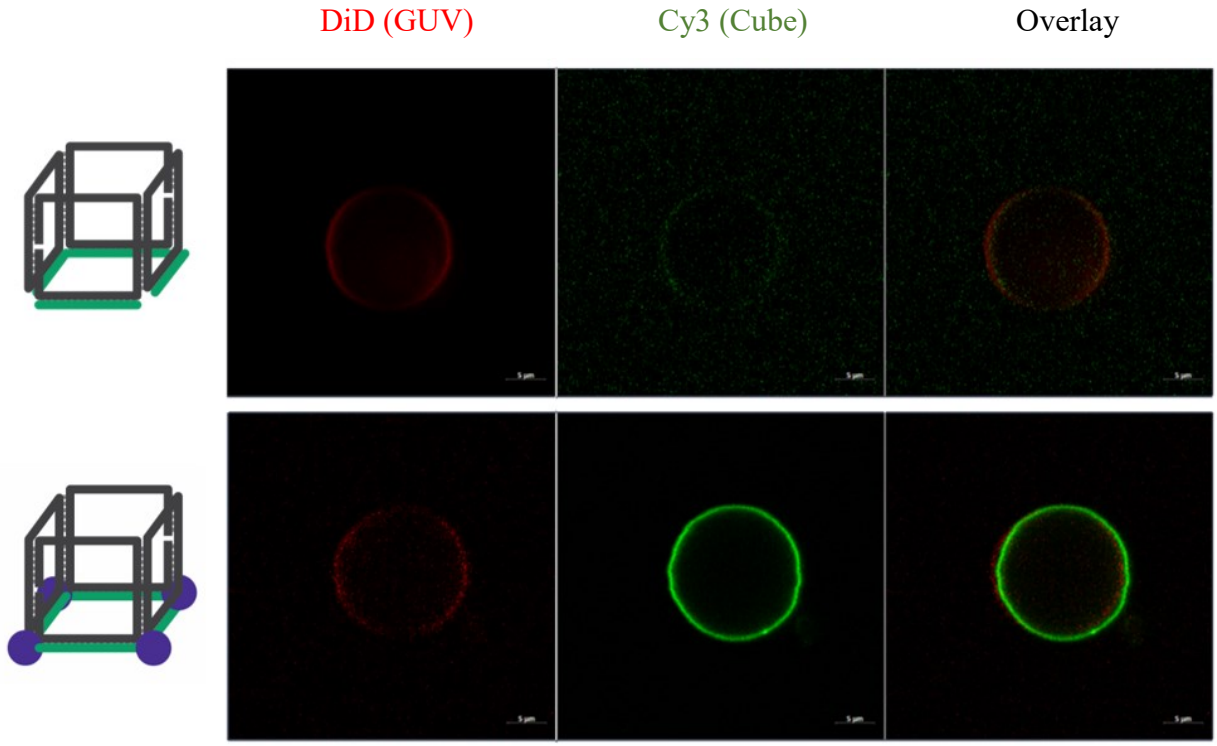

Figure 3.7 | GUV binding of cube/cholesterol constructs. The first panel is DiD channel, labeling DOPC lipids. The middle panel is Cy3 channel from the cubes. The top row shows the binding of unfunctionalized cube, C_4/A20, and the bottom row shows binding of cube/cholesterol construct, C_4/Chol-A20 to GUVs. There was a significant increase in Cy3 intensity in C_4/Chol-A20, compared to C_4/A20. The scale bar is 5 μM.

3.3.3.1 Surface mobility of cube/cholesterol constructs

Fluorescence recovery after photobleaching (FRAP) was performed to quantitatively compare the bilayer-binding characteristics of cube/cholesterol constructs. First, we examined the effect of the number of cholesterol units on the surface mobility of cube/cholesterol constructs. Figure 3.8a shows a decrease in diffusion rate as the cholesterol number increases from 1 to 8 units per construct. Thus, the diffusion rate of cube/cholesterol constructs inversely correlates with the cholesterol number. An increase in cholesterol number is expected to enhance the anchoring of the constructs on the GUVs, hindering their surface diffusion on the bilayers due to collective interactions from multiple cholesterol units. C_1/Chol-B14 showed a similar diffusion rate to the

single-stranded cholesterol-DNA conjugate (Chol-A14-Cy3). This suggests that the perturbation from the large hydrophilic 3D cube on the surface mobility is minimal.

Cholesterol units on DNA cubes functionalized with Chol-20 should have a higher exposure to the aqueous environment than Chol-A14 functionalized constructs, where cholesterol units tend to undergo self-interactions (see Section 3.3.2). In Figure 3.8b, there was a significant reduction in the diffusion rates of C_8 when switching from Chol-A14 to Chol-A20. On the other hand, no change in the diffusion rates was observed in C_4, consistent with the absence of intrascaffold association of cholesterol units. This implies that the surface mobility of cube/cholesterol constructs can be modulated by tuning the self-interactions of cholesterol units within the scaffolds (Figure 3.8c).

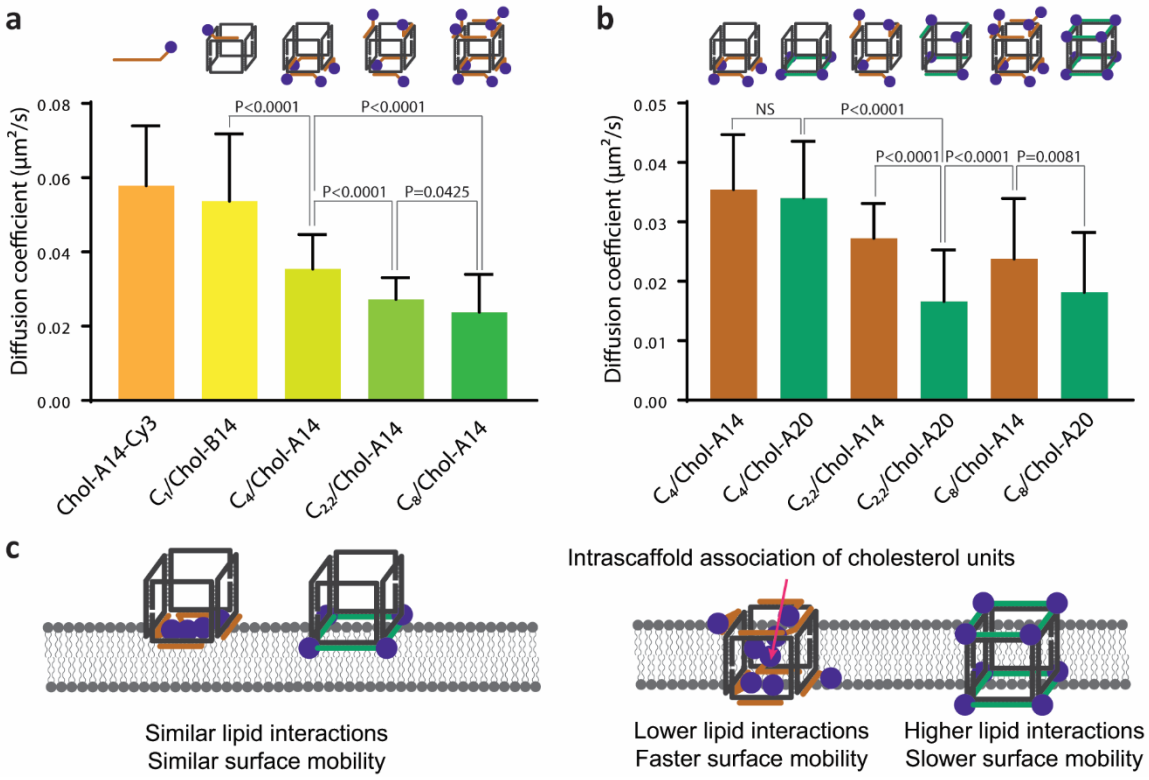

Figure 3.8 | Surface mobility of cube/cholesterol constructs. a) The diffusion coefficients decreased as cholesterol number increased, suggesting that the surface mobility inversely correlates with cholesterol number. b) Substitution of Chol-A14 with Chol-A20 further lowered the diffusion coefficients. This could be attributed to the increased nanostructure's rigidity and lower degree of intrascaffold association of cholesterol units in cube/Chol-A20 constructs. NS means the data are not significantly different. c) Schematic representation of GUV binding of cube/cholesterol constructs shows how intrascaffold association of cholesterol units can lower the surface mobility of the constructs.

Regarding the cholesterol orientation, distributing four cholesterol units on both faces of $C_{2,2}$ should allow its entire structure to embed deeper in the bilayers, compared to C_4/cholesterol constructs. Indeed, we observed lower diffusion rate in $C_{2,2}$/cholesterol constructs than C_4/cholesterol constructs (Figure 3.8b). Thus, despite having the same number, cholesterol orientation could increase the interfacial interactions of cube/cholesterol constructs with the bilayers and hinder the surface mobility. Interestingly, this effect was far more pronounced when Chol-A20, rather than Chol-A14, was used. We had earlier noted that $C_{2,2}$ shows an intrascaffold association of cholesterol units with Chol-A14, but not with Chol-A20. Thus, the intrascaffold association of $C_{2,2}$/Chol-A14 appears to be sequestering the cholesterol units inside the cube and dampens the effect of their orientation on the cube's surface mobility.

We can conclude that the surface mobility of cube/cholesterol constructs on GUVs depends strongly on both number and orientation of cholesterol units. Slower mobility can be achieved by i) increasing cholesterol number and ii) distributing the cholesterol units on both faces of the cubes rather than clustering them on the same face. In addition, the surface mobility can be further decreased by preventing the self-interactions of cholesterol units within the cubes, thus enhancing the interactions between the constructs and the bilayers.

3.3.3.2 Surface clustering of cube/cholesterol constructs

We examined the surface binding of cube/cholesterol constructs on GUVs. Figures 3.9c to 3.9e show reconstructed Z-stacked images of DNA cubes functionalized with Chol-A14. The surface coverage of C_4/Chol-A14 and $C_{2,2}$/Chol-A14 on the vesicle was very homogenous. We also measured the mobile fraction, another quantitative FRAP parameter, to quantify the clustering degree. The mobile fraction refers to the percentage of molecules contributing to fluorescence recovery, and it is normally associated with transient interactions with immobile components in the environment being measured.[31] Figure 3.9a shows high fluorescence recovery for the constructs with 1-4 cholesterol units as indicated by >90% mobile fraction. These observations suggest that these constructs present as monomeric cubes or small clusters on the surface. Although we had observed that C_4/Chol-A14 formed aggregates in solution as observed by PAGE (Figure 3.4b), we believe that the aggregates are breaking apart on the vesicles' surface.

On the other hand, there are multiple high fluorescence patches on the vehicle's surface in the case of C_8/Chol-A14. This construct also showed significantly reduced mobile fraction compared to other constructs (Figure 3.9a). Thus, a likely interpretation of the reduced mobile fraction for C_8/Chol-A14 is its clustering, which can physically impede the exchange of certain populations of cube/cholesterol constructs between bleached and non-bleached areas. Surface clustering of C_8/Chol-A14 on GUVs was consistent with previously noted aggregation in PAGE and AFM for C_8/Chol-A14. Thus, the surface clustering degree correlates well with the number of cholesterol units presented on the constructs.

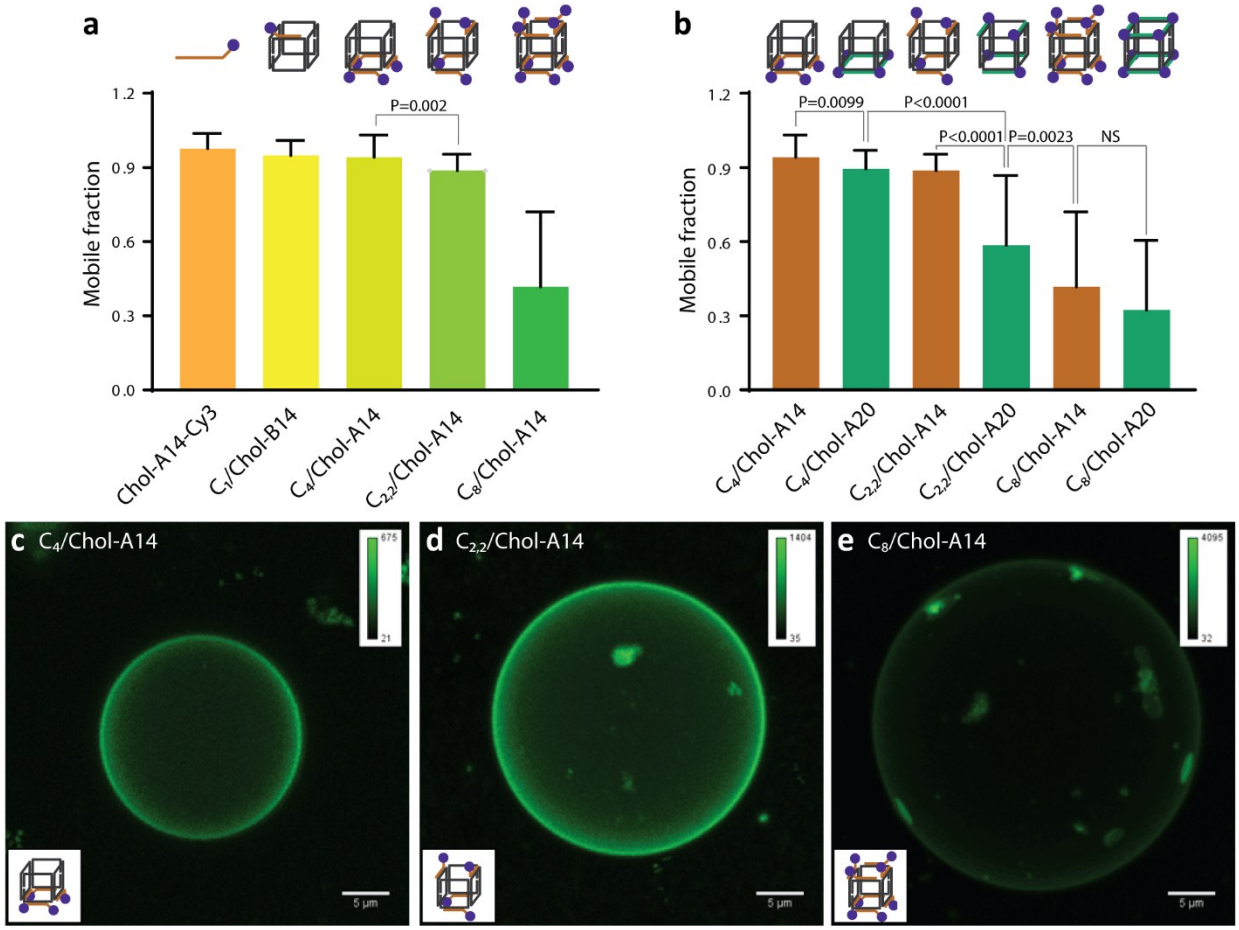

Figure 3.9 | Clustering of cube/cholesterol constructs on GUVs. a) Mobile fractions decreased significantly for C_8/Chol-A14, suggesting that the surface clustering strongly depends on cholesterol number. b) Substitution of Chol-A14 with Chol-A20 could further increase the clustering degree of some cube/cholesterol constructs, most likely due to the absence of intrascaffold association of cholesterol units. NS means the data are not significantly different. Reconstructions of z-stacked images show different surface homogeneity degrees from the bindings of c) C_4/Chol-A14, d) $C_{2,2}$/Chol-A14 and e) C_8/Chol-A14 on GUVs. The color scale bar indicates Cy3 fluorescence intensity of cube/cholesterol constructs. The scale bar is 5 µM.

There was no visible difference in the fluorescence distribution on the vesicle's surface when switching from Chol-A14 to Chol-A20. However, Chol-20 substitution significantly decreased the mobile fraction and increased the surface clustering of $C_{2,2}$ and to a lesser extent, C_8 (Figure 3.9b). This is consistent with the intrascaffold association, which sequesters the cholesterol units in these constructs and decreases the interfacial contact of cholesterol units to the bilayers, thus lowering the clustering degree on the bilayers. This difference was less pronounced for C_4/cholesterol constructs, which was consistent with the absence of intrascaffold interactions of cholesterol units.

In Figure 3.9e, we could observe the heterogeneous binding of C_8/Chol-A14 on GUVs, often seen as patches of high fluorescence intensity. Surprisingly, the low-intensity areas on the GUVs mostly showed lower mobile fraction (< 20%) and lower diffusion coefficients than those of high-intensity patches (Figure 3.10). It is likely that the clusters of C_8/Chol-A14 on the vesicle's surface are the main components responsible for high fluorescence intensity on the patches.

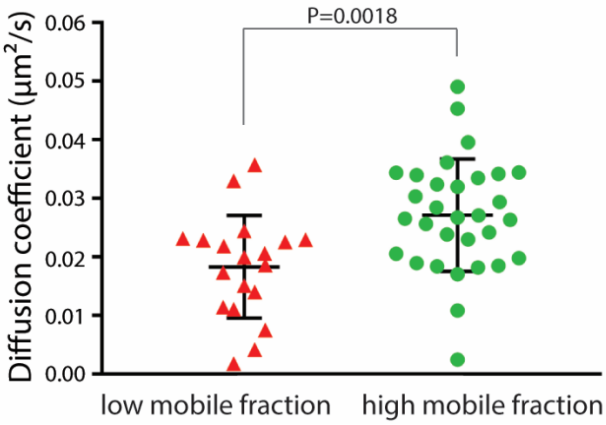

Figure 3.10 | Comparison of diffusion coefficients of C_8/Chol-A14 on GUVs. The diffusion coefficients were separated into two groups, depending on their corresponding mobile fractions. The mobile fraction value of < 20% is used as the higher limit for 'low mobile fraction' group. Each triangle and circle represent individual diffusion coefficients calculated from separated FRAP measurements. The error bars indicate mean values and standard deviations.

It was reported that there is a limited solubility of cholesterols in phosphatidylcholine lipids, above which leads to the precipitation of cholesterol monohydrates.[32] These cholesterol clusters, however, are not stable in the bilayers because they tend to immerse deeply within the bilayers, which disturbs lipid organization and destabilizes the bilayers.[33-34] We suspect that C_8/Chol-A14 clusters, which contain a higher cholesterol number than monomeric C_8/Chol-A14, may also

similarly destabilize the bilayers, resulting in the increased population of 'mobile' species on the vesicle surface. However, an additional study will be required to elucidate the structural identity of the structures showing high mobile fraction on high-intensity patches on the GUVs.

We can conclude that the cholesterol number strongly determines the surface clustering degree of cube/cholesterol constructs on GUVs. In addition, the clustering degree can be lowered by introducing an intrascaffold cholesterol association, which could reduce their accessibility from cholesterol units of other constructs and decrease the clustering degree.

3.3.3.3 Surface mobility of small-molecule dye

We note that the diffusion coefficient of C_1/Chol-B14 was one order of magnitude lower than the similar system in our previous report.[4] To further investigate this, we measured the surface mobility of small-molecule dye. It is of note that DiO-C18 dye was used instead of DiD dye for FRAP analysis because of the excitation wavelength of DiO-C18 dye that allows more efficient photobleaching under our CLSM settings than DiD dye. FRAP analysis in Figure 3.11 showed that the diffusion rate and mobile fraction of DiO-C18 were comparable to Chol-A14-Cy3. However, the diffusion rate of DiO-C18 on DOPC GUVs in our study (0.065±0.004 $\mu m^2/s$) is two orders of magnitude lower than other reported values (~1-7 $\mu m^2/s$).[35-37] It is known that there is a residual agarose contamination in the GUVs formed by film-assisted hydration.[30, 38] In addition to different experimental setup and data analysis, it is possible that this contamination could affect FRAP measurements in our system even if it had been shown that agarose does not alter the mobility of the lipids[30]. Therefore, we would like to emphasize that the diffusion coefficients will serve as a quantitative comparison within this study, but they are not intended for a comparison across studies.

We also performed FRAP analysis of DiO-C18 dye on GUVs in the presence of C_8/Chol-A14. DiO-C18/DOPC GUVs were incubated with C_8/Chol-A14 for 1.5 hours before the measurements. Figure 3.11 shows that the presence of C_8/Chol-A14 did not change the diffusion rate and mobile fraction of DiO-C18 dye on the bilayers.

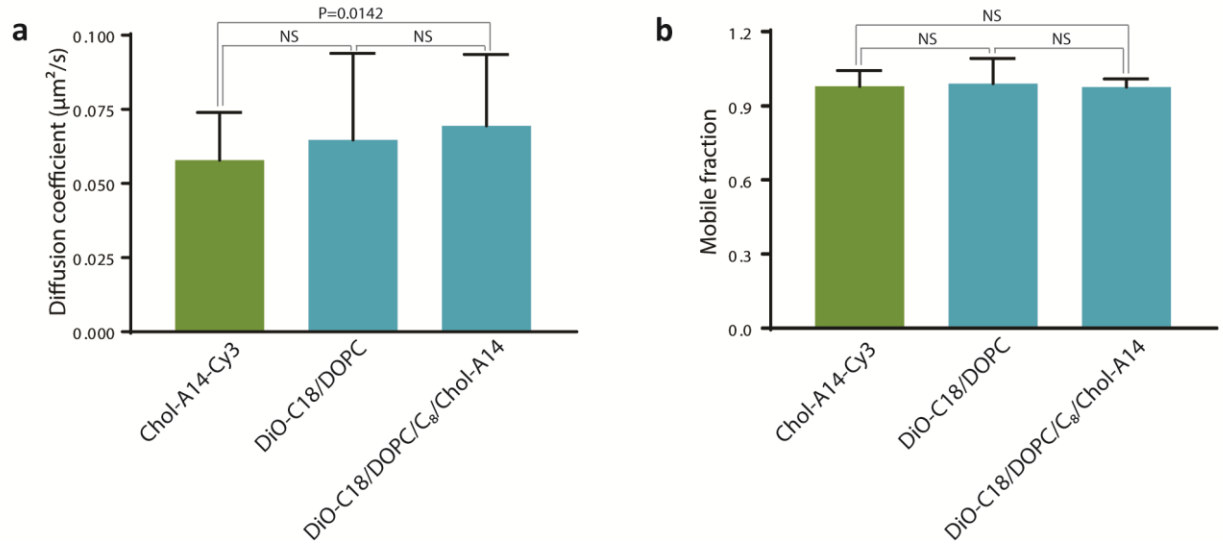

Figure 3.11 | Binding characteristics of DiO-C18 dye on GUVs. FRAP analysis showed that there was no significant difference in a) the diffusion rate and b) mobile fraction of DiO-C18 dye compared to Chol-A14-Cy3.

3.3.3.4 Effect of incubation time on vesicle binding

In an incubation period of a few hours, it is possible that the binding of cube/cholesterol constructs is under kinetic control. As some of the constructs show clustering behavior on the vesicle's surface, we hypothesized that the binding and organization of these constructs on the bilayers might reach an equilibrium state, given sufficiently long incubation period. To preliminarily evaluate this, the cube/cholesterol constructs were incubated with DOPC GUVs at 10ºC for 24 hours. FRAP analysis in Figure 3.12 showed that long incubation led to significantly decreased diffusion rate and increased clustering degree in the case of C_8/Chol-A14. In contrast, the change on binding characteristics of C_4/Chol-A14 was not significantly different at prolonged incubation time. Thus, it is possible that the reorganization of C_8/Chol-A14 on lipid bilayers may slowly happen, leading to the more optimal distribution of this construct on the vesicle surface.

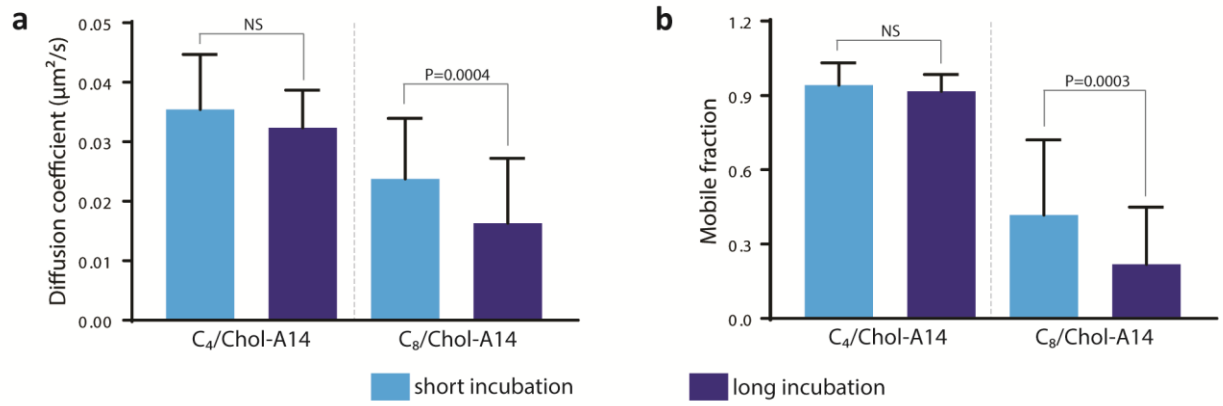

Figure 3.12 | Effect of incubation time on GUV binding characteristics. Longer incubation (24 hours) lowered both a) diffusion coefficient and b) mobile fraction of C_8/Chol-A14, but not in the case of C_4/Chol-A14. NS means the data are not significantly different.

3.3.3.5 Effect of cube/cholesterol construct concentrations on vesicle binding

It is difficult to avoid the clustering of cube/cholesterol constructs in the present assembly conditions because the critical micelle concentration (CMC) of free cholesterol is in the nanomolar regime.[39] We attempted to reduce their surface clustering to obtain a uniform GUV binding. This is an important aspect for applications where consistent behavior of the constructs throughout the vesicle's surface will be essential. As such, we carried out a simple dilution of C_8/Chol-A14 before mixing with GUVs. In Figures 3.13a to 3.13c, the reconstructed z-stacked images show that higher C_8/Chol-A14 dilution led to higher surface homogeneity upon GUV binding.

To gain a better understanding on the surface behavior, FRAP analysis of the GUVs incubated with 50-fold diluted C_8/Chol-A14 was performed. In Figures 3.13d and 3.13e, C_8/Chol-A14 showed high recovery of mobile fraction and diffusion coefficient as comparable to Cy3-Chol-A14. Similar behavior was also observed for C_8/Chol-A20. The increased mobile fractions of both constructs suggest that the dilution can prevent their clustering on the vesicle's surface. This could be possibly accounted by the lower density of the constructs bound on the vesicle's surface, which can increase an interspacing between the constructs and allow them to diffuse more freely than on hindered, dense surface in the case of non-diluted constructs.

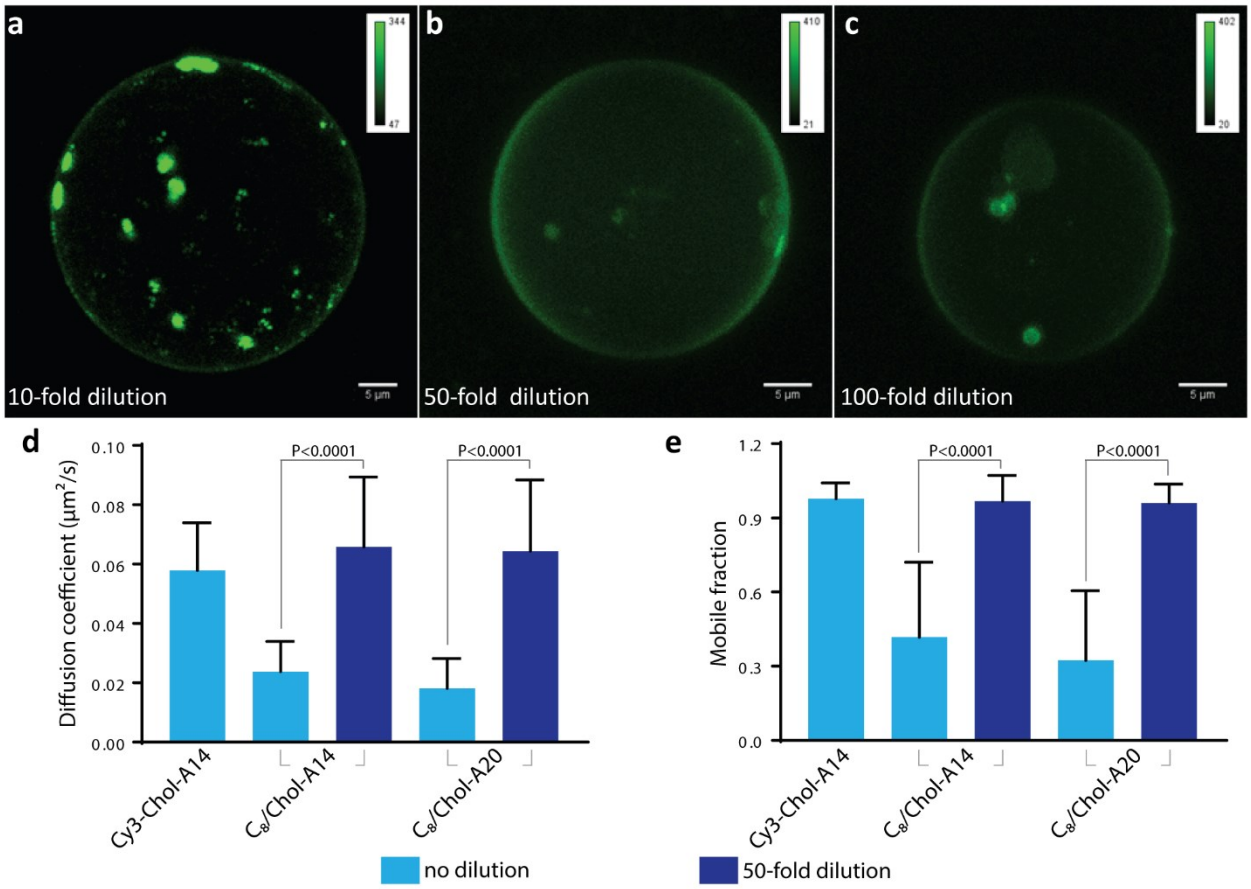

Figure 3.13 | Concentration effect of C_8/cholesterol constructs on their GUV binding characteristics. Reconstructions of z-stacked images show increased surface homogeneity of C_8/Chol-A14 when diluted at a) 10-fold, b) 50-fold and c) 100-fold prior to GUV addition. FRAP analysis showed the increase in d) diffusion coefficients and e) mobile fractions at 50-fold dilution of both constructs. The color scale bar indicates Cy3 fluorescence intensity of cube/cholesterol constructs. The scale bar is 5 μM.

We also examined the behavior of other constructs under dilute conditions. In Figure 3.14b, $C_{2,2}$/Chol-A14 showed a slight but significant change in mobile fraction, indicating lower clustering degree on the vesicle's surface upon dilution. Similar to the case of C_8/Chol-A14, there was a significant increase in diffusion rates for both C_4/Chol-A14 and $C_{2,2}$/Chol-A14 (Figure 3.14a). This further supports that the surface-binding density could have a substantial influence on the surface mobility of cube/cholesterol constructs.

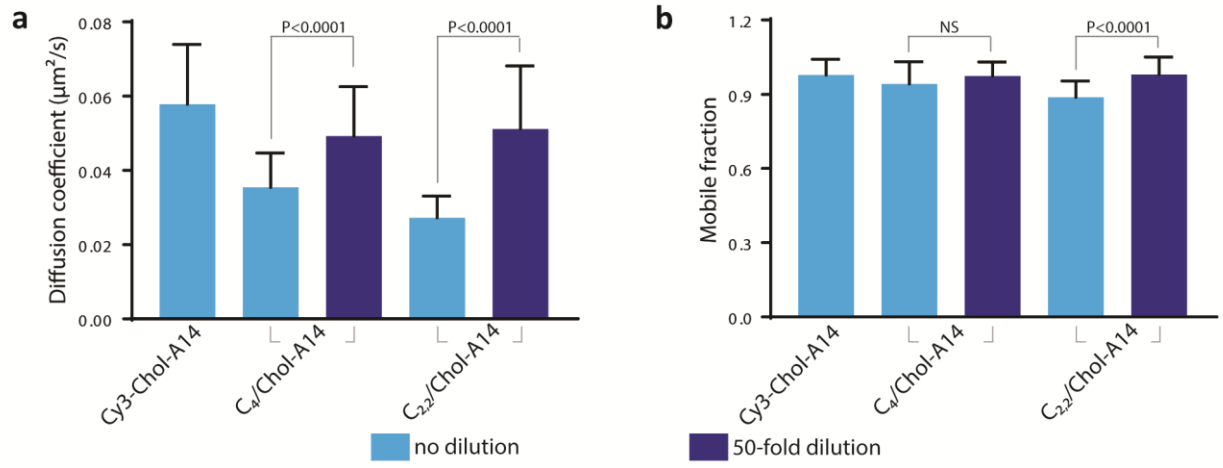

Figure 3.14 | FRAP analysis of 50-fold diluted C_4/Chol-14 and $C_{2,2}$/Chol-A14 on GUVs. a) There was a significant increase in diffusion rates of the diluted constructs. b) Only $C_{2,2}$/Chol-A14 showed increased mobile fraction upon dilution, suggesting lower clustering on the vesicle surface.

3.3.3.6 Addition of free cholesterol in DOPC/cholesterol GUVs

Cholesterol is naturally found in plasma membranes of mammalian cells and plays an essential role in regulating the lateral organization and membrane fluidity. It has been evidenced that cholesterols are important components of lipid rafts, of significance to cellular communication.[40] Therefore, we were interested in studying the binding of cube/cholesterol constructs on DOPC GUVs containing free cholesterols. This aspect can provide some insights into the structural design if our constructs are to be further used to interface with cellular membranes.

We chose 10% and 40% w/w cholesterol as low and high cholesterol concentration regimes in the DOPC/cholesterol GUVs (Figure 3.15a). FRAP analysis in Figure 3.15b indicates that cholesterol addition slows down the diffusion of C_8/Chol-A14, but the change is not proportional to the cholesterol concentration. Thus, it is very likely that the cholesterol units on C_8/Chol-A14 interact with free cholesterol in the bilayers. In terms of mobile fraction (Figure 3.15c), we observed a higher C_8/Chol-A14 clustering degree on the GUVs of 10% cholesterol. This also implies the interactions between free cholesterol and C_8/Chol-A14. Interestingly, there was no change in C_8/Chol-A14 clustering degree on the GUVs of 40% cholesterol in comparison to DOPC-only GUVs. We suspect that the mobile fraction recovery may be attributed to lipid

instability due to the formation of cholesterol clusters at high cholesterol concentration in the bilayers.[33-34]

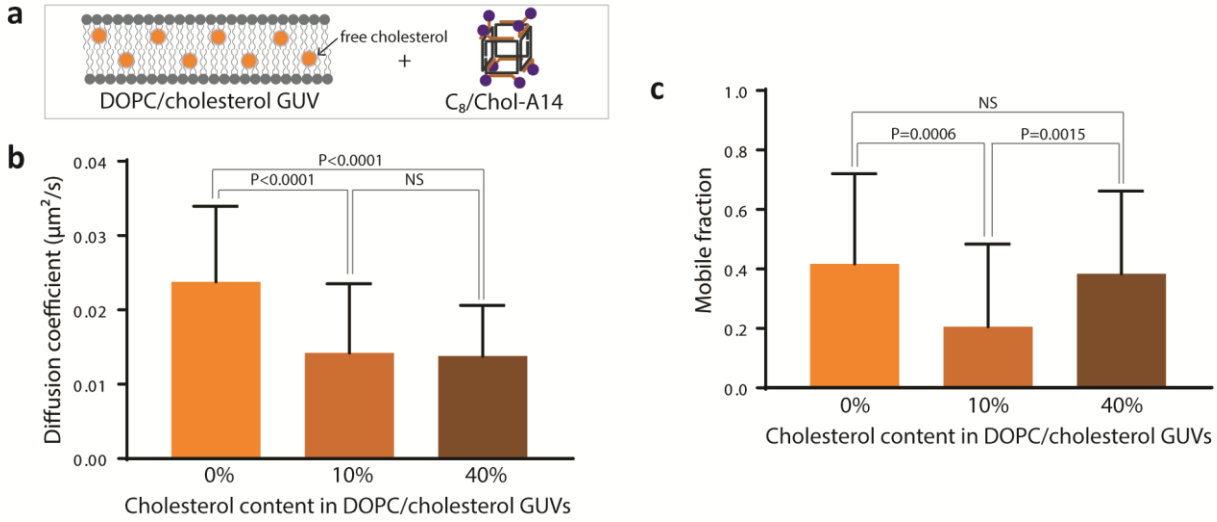

Figure 3.15 | Effect of free cholesterol in GUVs. a) GUVs composed of DOPC and cholesterols at different weight ratios (10% and 40% cholesterol) were mixed with C_8/Chol-A14. FRAP analysis showed that b) higher cholesterol concentration lowered the diffusion rate of C_8/Chol-A14 on the vesicle's surface, but) mobile fraction decreased only at low cholesterol concentration.

3.3.3.7 Binding of cube/cholesterol constructs on DPhPC GUVs

We also examined the interactions of some cube/cholesterol constructs on GUVs composed of branched 1,2-diphytanoyl-*sn*-glycero-3-phosphocholine (DPhPC, Figure 3.16b). This phospholipid has been widely used to fabricate highly stable bilayers as a platform to study synthetic membrane channels.[17, 41] DPhPC GUVs were prepared in the same manner as DOPC GUVs. On DPhPC GUVs, the diffusion rate and mobile fraction of C_4/Chol-A14 were significantly higher than C_8/Chol-A14 (Figures 3.16c and 3.16d). Thus, the behavior of cube/cholesterol constructs on DPhPC lipids followed the same trend as on DOPC lipids. The comparison between two lipid types suggests that the constructs interact more strongly with DPhPC than DOPC, as suggested by lower diffusion rate and higher clustering degree on DPhPC GUVs.

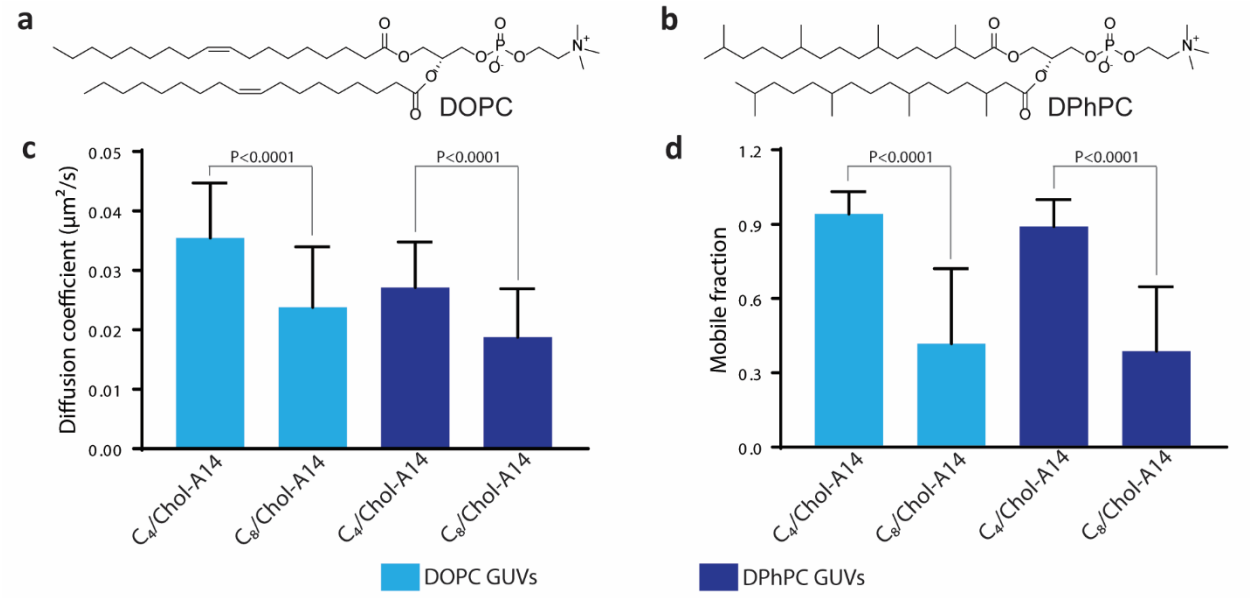

Figure 3.16 | Binding characteristics of C_4/Chol-A14 and C_8/Chol-A14 on DPhPC GUVs. The schematics show chemical structures of a) DOPC and b) DPhPC. FRAP analysis showed that b) the diffusion rate and c) mobile fraction of C_4/Chol-A14 were higher than C_8/Chol-A14.

3.3.4 Accessibility of cube/cholesterol constructs on GUVs to enzymatic digestion

Embedding or enclosing DNA nanostructures within lipid bilayers has been demonstrated to improve their stability towards nuclease digestion.[4, 42] As cube/cholesterol constructs showed tunable bilayer-binding characteristics, we were interested in studying whether this binding behavior could influence the accessibility of nuclease to the constructs bound on GUVs. Pre-incubated GUVs and cube/cholesterol constructs were mixed together with DNase I. After incubation at room temperature, the mixtures were denatured and analyzed by denaturing PAGE.

Figures 3.17 shows the gel analysis of the cube constructs after DNase I treatment for 15 minutes. We note that only intact DNA clips, which have the electrophoretic mobility between 50-75 bps compared to DNA ladder on the leftmost lane, will be used to determine the nuclease resistance degree. Intensities of the bands corresponding to intact clips for individual constructs were quantified and compared with the first three lanes (C_4, $C_{2,2}$, and C_8), which are the cubes that were not treated with DNase I. The band intensity of the control (C_4, $C_{2,2}$, and C_8) was used as a reference for 100% nuclease resistance.

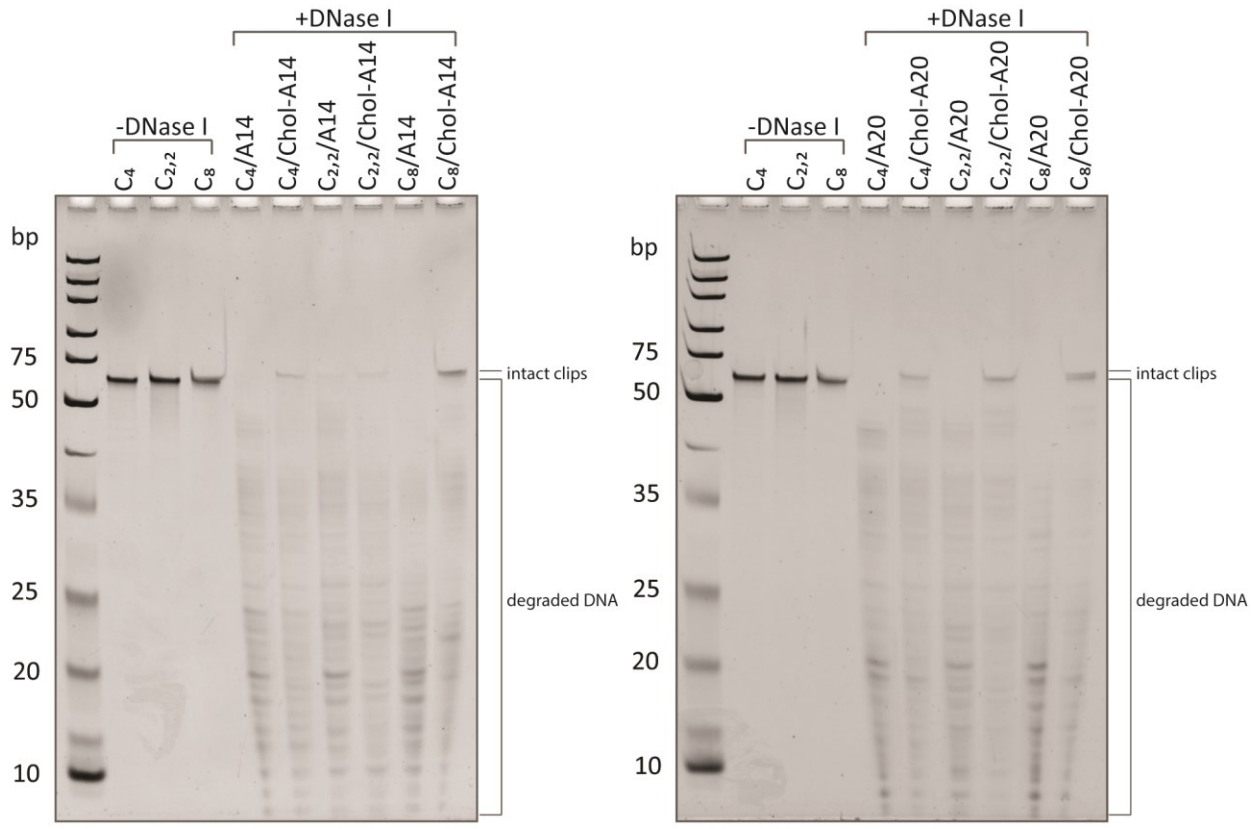

Figure 3.17 | DNase I treatment of cube/cholesterol constructs bound on GUVs. Denaturing PAGE (15%) shows the analysis of: left) cubes decorated with A14 and Chol-A14, and right) cubes decorated with A20 and Chol-A20. The cubes which were not treated with DNase I were used as the references for 100% resistance to DNase I digestion. The cube/cholesterol constructs showed higher nuclease resistance than unfunctionalized cubes when treated with DNase I for 15 minutes.

The cube/cholesterol constructs that show higher binding affinity and/or more embedding in the bilayers may possibly be more resistant to DNase I. Figure 3.18 shows the percentages of 'intact' DNA clips, which survive the nuclease digestion. There was a greater nuclease resistance in C_8/cholesterol constructs than in C_4/cholesterol constructs, consistent with deeper embedding in the bilayers. All cubes decorated with Chol-A20 were more resistant towards enzymatic digestion, likely due to the greater interactions of cholesterol units with the bilayers and reduced intrascaffold interactions between cholesterol units on the constructs. In addition, Chol-A20 decoration can further increase the nanostructure's rigidity, which also leads to higher nuclease resistance than DNA cubes functionalized with Chol-A14.

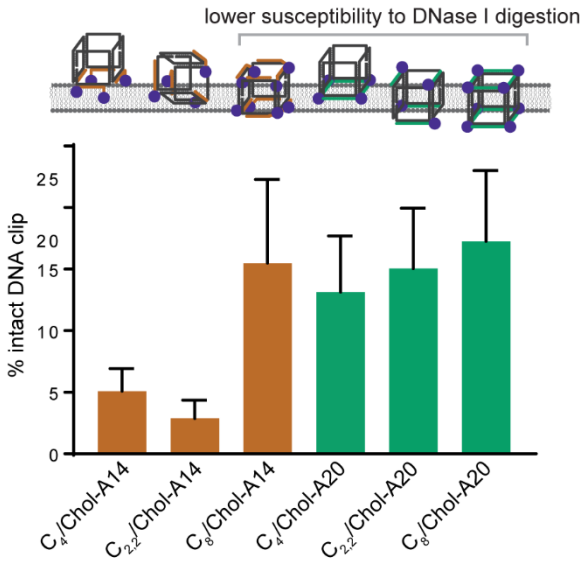

Figure 3.18 | Stability of cube/cholesterol constructs on GUVs against DNase I digestion. Cube/cholesterol constructs could have different degrees of membrane embedding, resulting in different susceptibility to DNase I digestion. The percentage of intact DNA clips was an indicator for the resistance of cube/cholesterol constructs to nonspecific enzymatic degradation, where higher number represents greater stability. NS means the data are not significantly different.

We expected $C_{2,2}$/Chol-A14 to show higher nuclease resistance than C_4/Chol-A14 because the cholesterol orientation should allow it to embed deeper in the bilayers. It is possible that lowered nuclease resistance in this construct is due to higher degree of cholesterol self-interactions, which reduces their interactions with the bilayers. Therefore, it can be concluded that the GUV binding of cube/cholesterol constructs can partially shield them from DNase I digestion. The higher interactions between cube/cholesterol constructs and the bilayers as well as the rigidity and fully double-stranded nature of the constructs can contribute to the protection of the constructs from nuclease digestion.

3.3.5 Membrane poration activity (work in progress by Daniel Offenbartl-Stiegert in Prof. Stefan Howorka's lab at University College London)

The observation from enzyme-accessibility experiments also implies that some of the cube/cholesterol constructs are likely to be inserted in the bilayers more than others. To further explore this aspect, we, in collaboration with the Howorka group, would like to investigate the membrane poration activity of these constructs. One set of the experiments to realize puncturing behavior was through a flux monitoring of fluorescent dyes across the vesicle wall (Figure 3.19). In this case, fluorescent dyes were added to the GUV suspension preincubated with cube/cholesterol constructs. If these constructs could function as nanopores, the dye-influx into GUVs can happen due to the dye concentration gradient. The preliminary results suggest that C_8/Chol-A20 and $C_{2,2}$/Chol-A20/B20 could allow the passage of small dyes across the vesicle wall (data not shown). More evidences to support the poration activity of these constructs are underway.

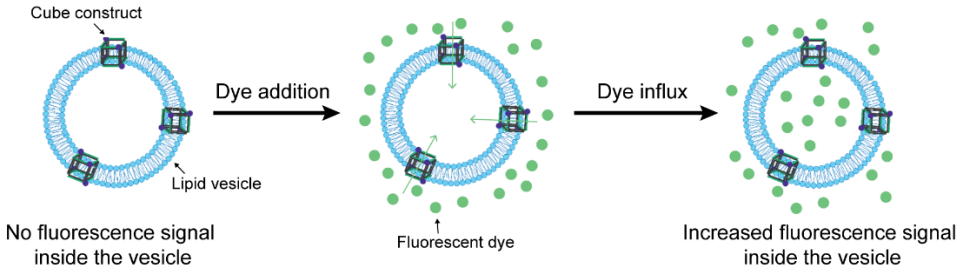

Figure 3.19 | Dye-influx experiment. Fluorescent dyes are added to the solution of lipid vesicles preincubated with the cube/cholesterol constructs. There will be an increase in fluorescence signal inside the vesicles if the constructs can function as nanopores.

The design principle of our cube/cholesterol constructs, if their poration activity is established, can give an additional feature to synthetic DNA nanopores. The typical nanopores reported by several research groups are 'barrel-like' objects (Figure 3.20a). Enclosing parallel-aligned DNA duplexes can form a channel with DNA-dense walls which will protect the channel from being in contact with the bilayer environment, thus allowing ions or charged molecules to pass through.[43] In contrast, our cube/cholesterol constructs are wireframe structures with large gaps on their faces (Figure 3.20b). These cubes constitute the first design of 'wall-less' DNA nanopores, and our strategy could potentially provide an alternative design of reconfigurable DNA-minimal nanopore as different cage geometries can be easily generated.

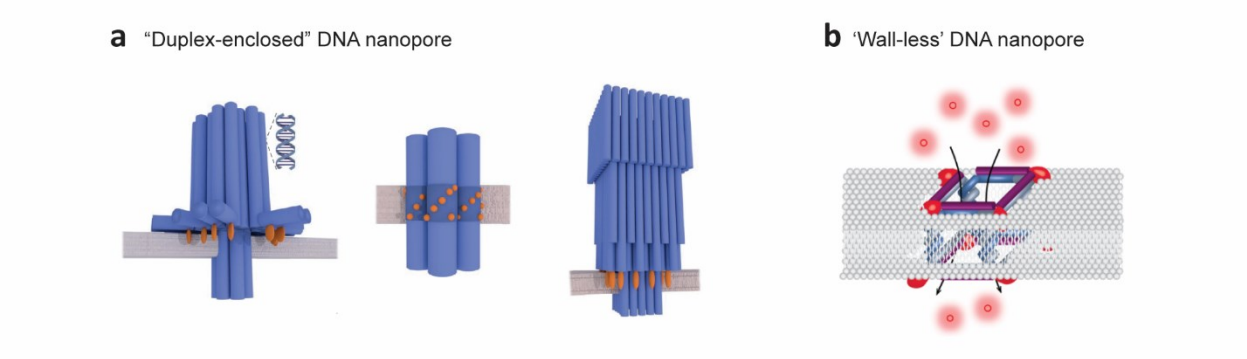

Figure 3.20 | Synthetic DNA nanopore designs. a) 'Barrel-like' DNA nanopore formation by enclosing parallelly-aligned DNA duplexes. Adapted with permission from reference 43 (NPG, 2017). b) Wireframe cube/cholesterol construct as a potential 'wall-less' DNA nanopore.

3.4 Conclusions

We have demonstrated the use of DNA cubes to functionalize cholesterol units with precise control of their configurations on the cubes. Three parameters on cube/cholesterol constructs were examined. i) The design of cholesterol-DNA conjugates to position cholesterol units on the cubes shows that the shorter and more flexible Chol-A14 can increase the self-interactions of cholesterol units within the cubes and induce cooperative assembly. This resulting intrascaffold association reduces the bilayer interactions of the constructs, increasing their surface mobility. In contrast, the longer and more rigid Chol-A20 prevents the intrascaffold association of cholesterol units, increasing the bilayer interactions of the constructs. This effect and the increased nanostructure's rigidity lead to increased nuclease resistance of the constructs within the bilayers. ii) An increase in cholesterol number decreases the construct's surface mobility and increase both nuclease resistance and clustering degree within the bilayers. iii) The cholesterol orientation controls the assembly direction of cholesterol units. If there are more than two Chol-A14 on a single cube face, there is an interscaffold association, leading to aggregation. On the other hand, the intrascaffold association of cholesterol units is favorable when Chol-A14 units are across from one another on the cube. Cholesterol decoration on both faces of the cubes can also increase their embedding and lower their surface mobility on the bilayers. We also found the protection of cube/cholesterol constructs on GUVs from enzymatic degradation, which can be applicable to design drug delivery vehicle. Finally, the preliminary results suggest that the cube/cholesterol constructs that can span

the bilayers display the membrane poration activity, allowing the membrane transport. This will be the first example of 'wall-less' DNA nanopore, which will be useful for further design of synthetic membrane channels.

3.5 Experimental Section

3.5.1 Chemicals

The reagents and buffers are as detailed in Section 2.5.1 in Chapter 2 with the following additions. DOPC and DPhPC were purchased from Avanti Lipids Polar, Inc. Agarose Type IX-A (ultra-low gelling temperature, cat.# A2576), sucrose, glucose, casein, cholesterol, chloroform, and methanol were purchased from Sigma-Aldrich. 5'-cholesteryl-TEG phosphoramidite (cat.# 10-1976-95) was obtained from Glen Research. 1-1'-dioctadecyl-3-3-3'-3'-tetramethylindodicarbocyanine perchlorate (DiD, cat.# D307), 3,3'-dioctadecyloxacarbocyanine perchlorate (DiO-C18, cat.# V22886) and Gibco 1xDPBS without calcium and magnesium (cat.# 14190-144) were obtained from Thermo Scientific. DNase I (cat# M0303S) and 10x DNase I reaction buffer (cat# B0303S) were purchased from New England Biolabs Inc.

3.5.2 Instrumentation

Instrumentation is as detailed in Section 2.5.2 in Chapter 2 with the following additions. Multimode 3 SPM connected to a Nanoscope NanoScope IIIa controller (Veeco, Plainview, NY) was also used to acquire AFM images. LSM 710 confocal microscope (Zeiss, Germany) was used for fluorescence imaging and FRAP.

3.5.3 Solid-phase synthesis and purification

DNA synthesis and purification are as detailed in Section 2.5.3 in Chapter 2. The coupling of 0.1 M solution of 5'-cholesteryl-TEG phosphoramidite in acetonitrile was performed in a glove box for 10 minutes, followed by capping, oxidation and deblocking steps on the synthesizer. For HPLC purification, cholesterol-DNA conjugates were run on Hamilton PRP-C18 column by using elution gradient of 3-80% acetonitrile in TEAA over 30 minutes.

3.5.4 DNA sequences and characterization

The sequences of DNA clips necessary for cube assembly are listed in Table 3.1. **Table 3.1 |** Sequences of DNA clips (6 = HEG).

Strand	**Sequence (5'→ 3')**
1AB	TCGCTGAGTA 6 TCCTATATGGTCAACTGCTC 6 GCAAGTGTGGGCACGCACAC 6 GTAGTAATACCAGATGGAGT 6 CACAAATCTG
2AB	CTATCGGTAG 6 TCCTATATGGTCAACTGCTC 6 TACTCAGCGACAGATTTGTG 6 GTAGTAATACCAGATGGAGT 6 CAACTAGCGG
3AB	CACTGGTCAG 6 TCCTATATGGTCAACTGCTC 6 CTACCGATAGCCGCTAGTTG 6 GTAGTAATACCAGATGGAGT 6 GGTTTGCTGA
4AB	CCACACTTGC 6 TCCTATATGGTCAACTGCTC 6 CTGACCAGTGTCAGCAAACC 6 GTAGTAATACCAGATGGAGT 6 GTGTGCGTGC
1AA	TCGCTGAGTA 6 TCCTATATGGTCAACTGCTC 6 GCAAGTGTGGGCACGCACAC 6 TCCTATATGGTCAACTGCTC 6 CACAAATCTG
2AA	CTATCGGTAG 6 TCCTATATGGTCAACTGCTC 6 TACTCAGCGACAGATTTGTG 6 TCCTATATGGTCAACTGCTC 6 CAACTAGCGG
3AA	CACTGGTCAG 6 TCCTATATGGTCAACTGCTC 6 CTACCGATAGCCGCTAGTTG 6 TCCTATATGGTCAACTGCTC 6 GGTTTGCTGA
4AA	CCACACTTGC 6 TCCTATATGGTCAACTGCTC 6 CTGACCAGTGTCAGCAAACC 6 TCCTATATGGTCAACTGCTC 6 GTGTGCGTGC
2BA	CTATCGGTAG 6 GTAGTAATACCAGATGGAGT 6 TACTCAGCGACAGATTTGTG 6 TCCTATATGGTCAACTGCTC 6 CAACTAGCGG

Strand	Sequence (5'→ 3')
4BA	CCACACTTGC 6 GTAGTAATACCAGATGGAGT 6 CTGACCAGTGTCAGCAAACC 6 TCCTATATGGTCAACTGCTC 6 GTGTGCGTGC
Cy3-1AB	Cy3-TCGCTGAGTA 6 TCCTATATGGTCAACTGCTC 6 GCAAGTGTGGGCACGCACAC 6 GTAGTAATACCAGATGGAGT 6 CACAAATCTG
Cy3-1AA	Cy3-TCGCTGAGTA 6 TCCTATATGGTCAACTGCTC 6 GCAAGTGTGGGCACGCACAC 6 TCCTATATGGTCAACTGCTC 6 CACAAATCTG

The sequences of cholesterol-DNA conjugates are listed in Table 3.2.

Table 3.2 | Sequences of cholesterol-DNA conjugates.

Strand	Sequence (5'→3')
A14	TTTTTCAGTTGACCATATA
A20	GAGCAGTTGACCATATAGGA
B14	TTTTTCCATCTGGTATTAC
Chol-A14	Cholesterol-TTTTTCAGTTGACCATATA
Chol-A20	Cholesterol- GAGCAGTTGACCATATAGGA
Chol-B14	Cholesterol- TTTTTCCATCTGGTATTAC
Chol-A14-Cy3	Cholesterol-TTTTTCAGTTGACCATATA-Cy3

Cholesterol-DNA conjugates were purified by reversed-phase HPLC (RP-HPLC), and their purity was evaluated by denaturing PAGE (15%) as shown in Figure 3.21

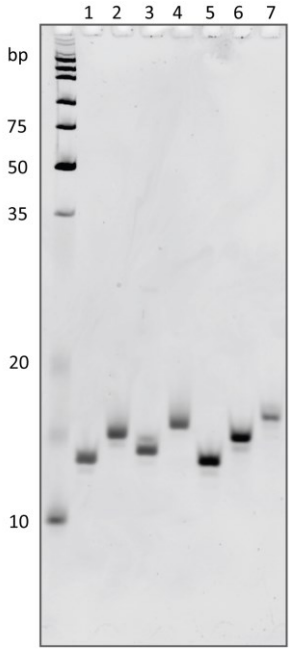

Figure 3.21 | Purity of cholesterol-DNA conjugates. Denaturing PAGE assay (15%). Lane 1: A14; lane 2: Chol-A14; lane 3: A20; lane 4: Chol-A20; lane 5: B14; lane 6: Chol-B14 and lane 7: Chol-A14-Cy3

All samples were run using the same gradient of 3-80% acetonitrile to compare their relative hydrophobicity. Table 3.3 shows the retention times of cholesterol-DNA conjugates. The strands were further analyzed by LC-ESI-MS in negative ESI mode, which is summarized in Table 3.3.

Table 3.3 | Characterization of cholesterol-DNA conjugates.

Strand	Retention time[a]	Calculated mass[b]	Experimental mass[b]
A14	-	5764.99	5765.0000
A20	-	6187.08	6186.8125
B14	-	5731.97	5731.6563
Chol-A14	23.675	6446.43	6446.1250
Chol-A20	23.499	6868.52	6868.5625
Chol-B14	23.743	6413.40	6413.1250
Chol-A14-Cy3	*17.792*	6953.67	6952.5625

[a] Retention time (in minutes) was determined from RP-HPLC with the gradient of 3-80% acetonitrile for 30 minutes.
[b] mass unit is in g/mole.

3.5.5 Design of cube/cholesterol constructs

Cage design:

Table 3.4 lists the combination of DNA clips to generate different cages. The sequence of A binding site (TCCTATATGGTCAACTGCTC) is complementary to all cholesterol-DNA conjugates. The exception is Chol-B14 which is designed to be complementary to B binding site (GTAGTAATACCAGATGGAGT) on the clips.

Table 3.4 | DNA clip combinations for the construction of different cages.

Cage	Clip strands	No. of A binding sites	No. of B binding sites
C_1	1AB, 2AA, 3AA, 4AA	7	1
C_4	1AB, 2AB, 3AB, 4AB	4	4
$C_{2,2}$	1AB, 2BA, 3AB, 4BA	4	4
C_8	1AA, 2AA, 3AA, 4AA	8	0
Cy3-C_1	Cy3-1AB, 2AA, 3AA, 4AA	7	1
Cy3-C_4	Cy3-1AB, 2AB, 3AB, 4AB	4	4
Cy3-$C_{2,2}$	Cy3-1AB, 2BA, 3AB, 4BA	4	4
Cy3-C_8	Cy3-1AA, 2AA, 3AA, 4AA	8	0

Assembly protocol:

In a typical assembly, equimolar amounts of DNA clips (1.25 pmole each) and cholesterol-DNA conjugates at 1.5 equivalents per binding site were mixed in 10 μL of 1xTAMg buffer. This will give final cube concentration of 125 nM. The final concentrations of cholesterol-DNA conjugates were 250, 750, 750 and 1500 nM for C_1, C_4, $C_{2,2,}$ and C_8. The samples were heated at 95^{o}C for 5 minutes, at 80^{o}C for 3 minutes, cooled to 60^{o}C (2 minutes/^{o}C), and slowly cooled to 4^{o}C (3 minutes/^{o}C). The assemblies were examined by non-denaturing PAGE (5%) by mixing with 2 μL of glycerol mix (7:1 glycerol/H_2O) and loaded the gel with 1xTAMg as the running buffer. The gel was run at 250 V for 2.5 hours and stained with GelRed.

For the titration experiments (Figures 3.4-3.6), the cube concentration was maintained at 125 nM. For C_4 and $C_{2,2}$, cholesterol-DNA conjugates were added at 250, 375, 500, 625, 750 and 1000 nM for 2, 3, 4, 5, 6 and 8 equivalents with respect to the cubes. For C_8, the cholesterol-DNA conjugates were added at 500, 750, 1000, 1250, 1500 and 2000 nM for 4, 6, 8, 10, 12 and 16 equivalents with respect to the cube.

3.5.6 Atomic force microscopy

The topology of cube/cholesterol constructs was characterized by AFM on the mica substrate under dry conditions. To prepare an AFM sample, 5 μL of diluted cube/cholesterol constructs was deposited on freshly cleaved mica for 5 seconds and washed twice with 50 μL of H_2O. Excess liquid was blown off by the stream of air for 30 seconds, following by vacuum drying overnight. The measurement was acquired in tapping mode using OTESPA-R3 rectangular silicon probe (tip radius = 7 nm, k = 26 N/m, f_o = 300 kHz; Bruker, Camarillo, CA).

Images were processed by NanoScope Analysis 1.50 Software. Raw data were treated with flattening function to correct tilt, bow and scanner drift. Average particle sizes, heights, and numbers of particles (N) were obtained from Particle Analysis function. Table 3.5 summarizes the diameter, height, and number of analyzed particles for all assemblies. Figure 3.22 shows additional AFM images of the structures presented in Section 3.3.2.

Table 3.5 | AFM analysis of cube/cholesterol constructs.

Structures	Diameter (nm)	Height (nm)	Number of particles
C_4/Chol-A14	20.6±7.1	1.1±0.3	333
C_4/Chol-A20	23.1±6.1	1.2±0.4	417
$C_{2,2}$/Chol-A14	22.9±8.2	1.3±0.8	676
$C_{2,2}$/Chol-A20	24.0±8.2	1.5±0.5	655
C_8/Chol-A14	24.8±5.5	1.6±0.5	202
C_8/Chol-A20	24.4±6.2	1.4±0.4	527

a) C_4/Chol-A14

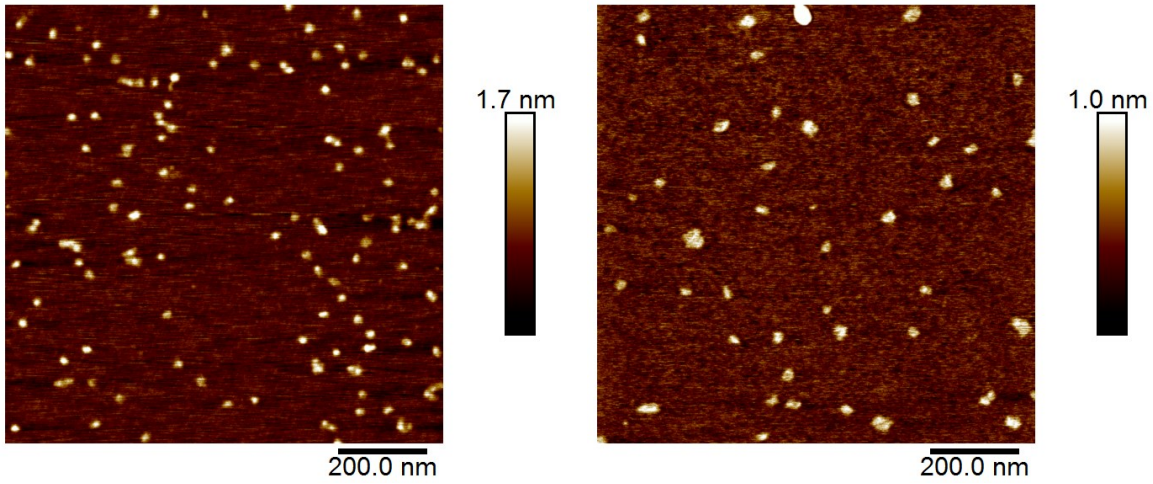

b) C_4/Chol-A20

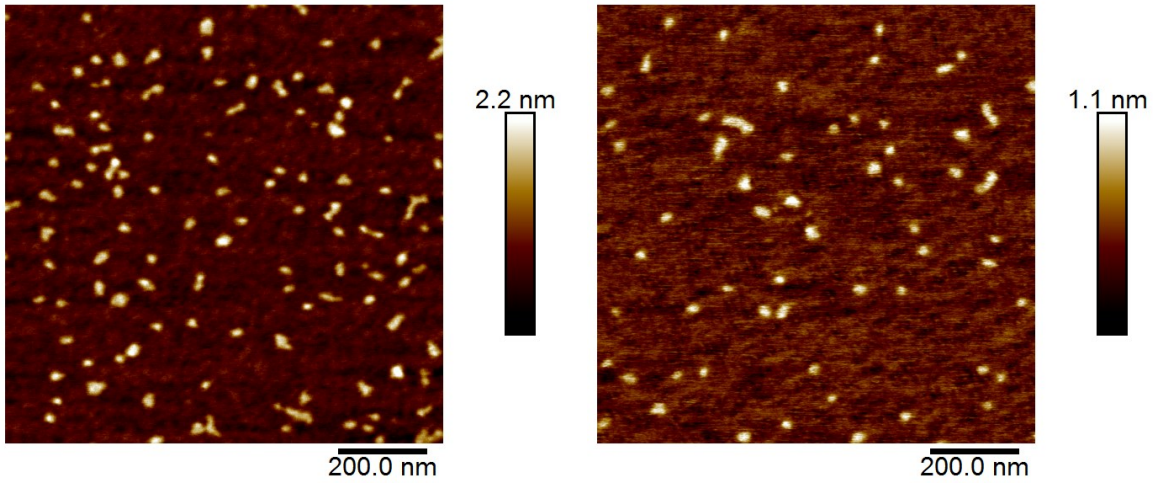

c) $C_{2,2}$/Chol-A14

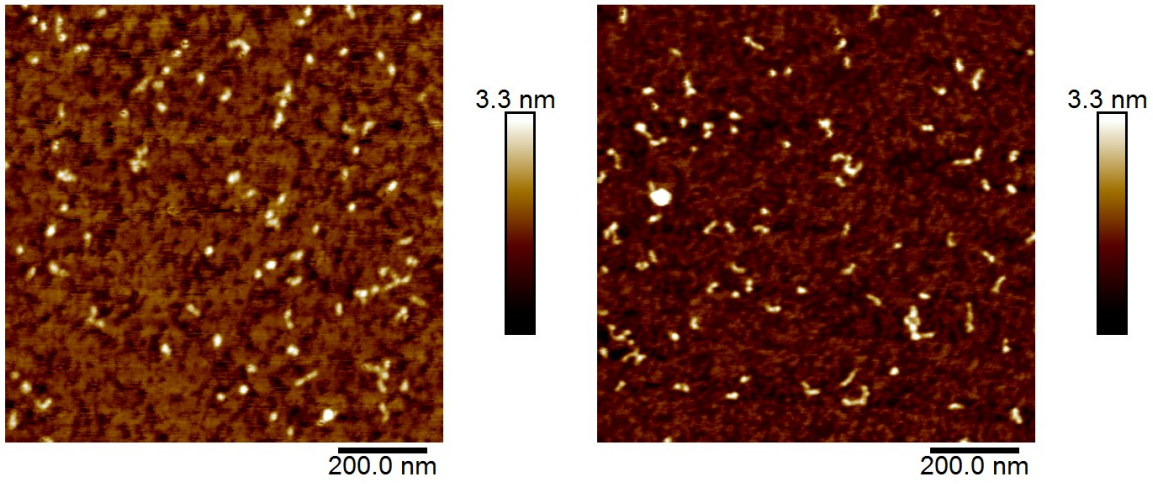

d) $C_{2,2}$/Chol-A20

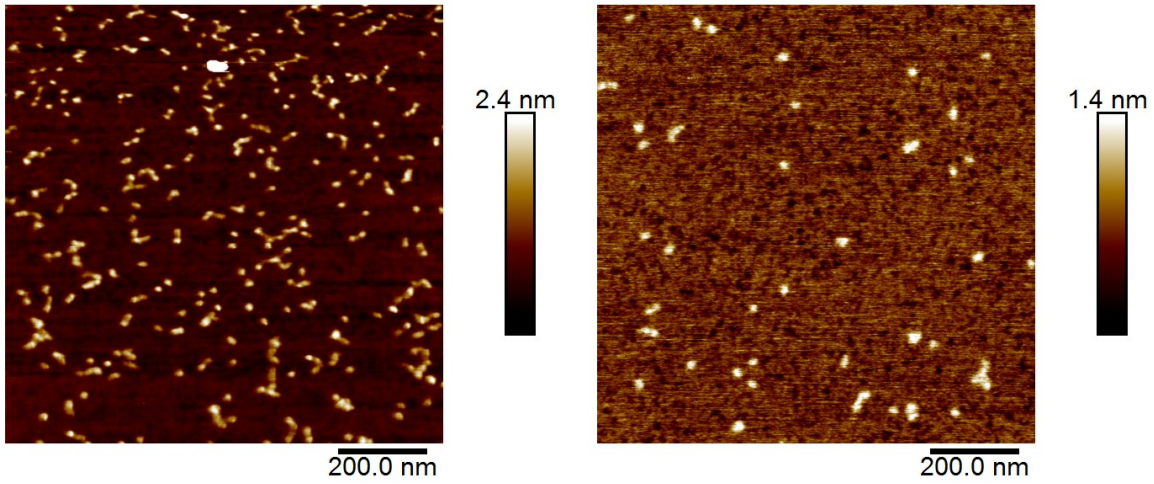

e) C_8/Chol-A14

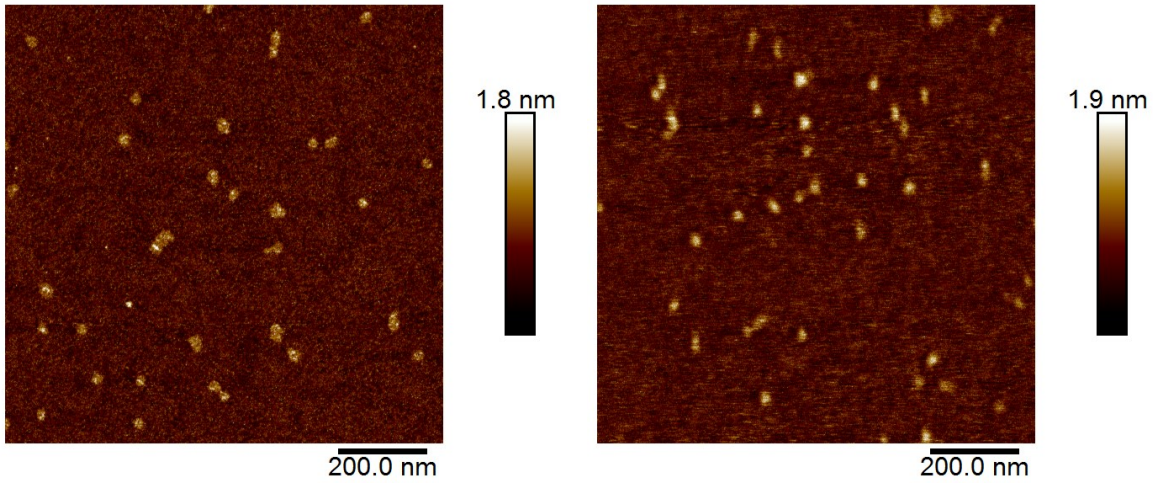

f) C_8/Chol-A20

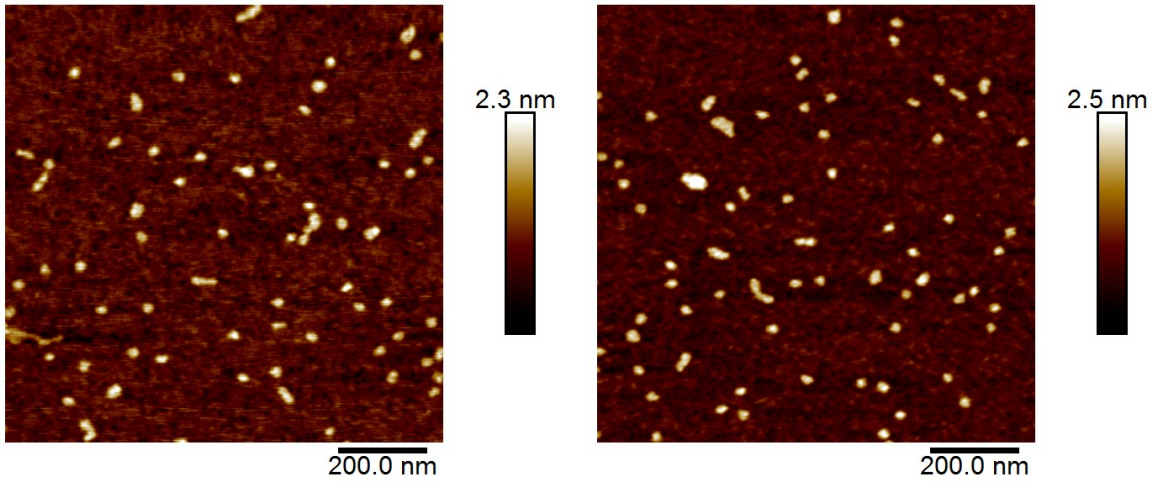

Figure 3.22 | Additional AFM images for cube/cholesterol constructs.

3.5.7 Thermal denaturation

C_8 (375 nM) and cholesterol-DNA conjugates (4.5 μM) were mixed and thermally annealed in 1xTAMg. Then, 100 μL of samples was transferred to a quartz cuvette, and few drops of silicone oil were added on top. The absorbance at 260 nm was monitored in response to a temperature change from 25°C to 95°C with 1°C increment per minute. The first derivative of the normalized melting curve was fitted with Lorentzian distribution function using OriginPro 2015 software. Then, the melting temperature (T_m) was determined from the highest value of the first derivative. Melting curves for C_8 constructs are shown in Figure 3.23.

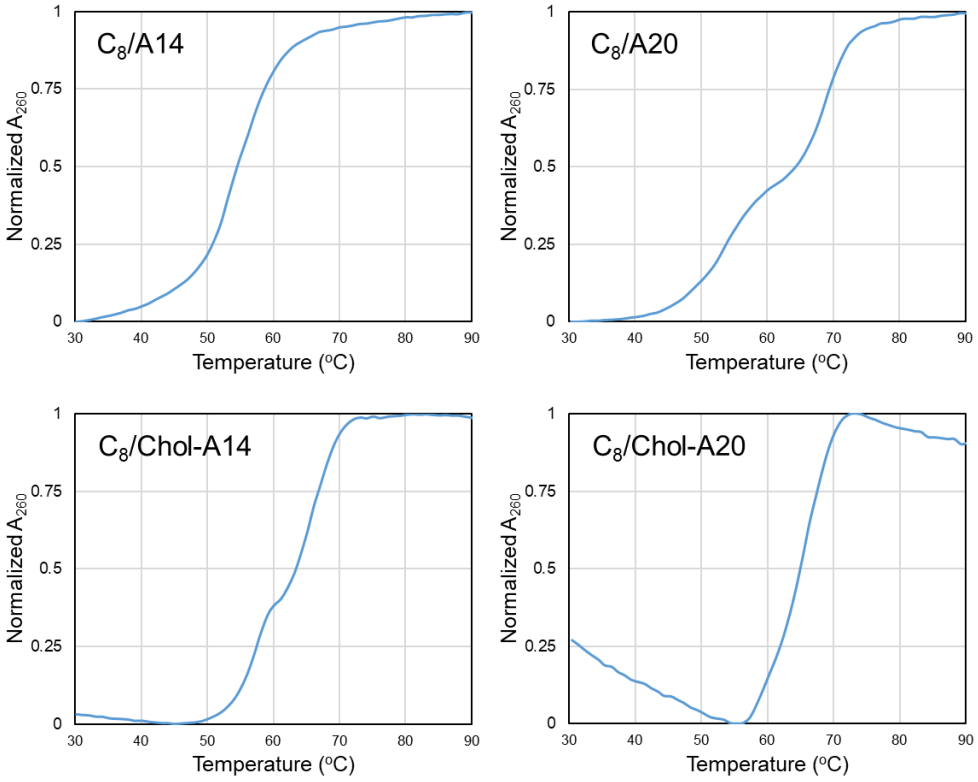

Figure 3.23 | Melting curves of C_8 constructs.

There were two transition points in the melting profiles of C_8 constructs. All T_m values are listed in Table 3.6. For A20 strands, the lower melting temperature should correspond to DNA clip disassembly while A20 dissociation from the clips should occur at a higher temperature. In the case of C_8/Chol-A14, we suspect that the lower melting temperature could be attributed to cube dimers, where cholesterol units aggregated intermolecularly. It is very likely that the monomeric

cubes have the T_m of 65.2ºC, which was to be expected from the strong intrascaffold association of cholesterol units. Nevertheless, the cholesterol interactions could increase thermal stability of the cube/cholesterol constructs, compared to nonfunctionalized cubes.

Table 3.6 | Melting temperatures of C_8 constructs.

Constructs	**T_m (ºC)**
C_8/A14	54.3±0.7
C_8/Chol-A14	56.9±0.4, 65.2±1.5
C_8/A20	53.8±0.5, 68.8±0.2
C_8/Chol-A20	60.3±1.2, 66.5±1.0

3.5.8 GUV formation and binding of cube/cholesterol constructs

Instrumentation:

The images were acquired using Zeiss LSM710 CLSM with 20x plan apochromatic objective. For an acquisition of the cross-sectional image of GUVs incubated with cube/cholesterol constructs, Cy3 and DiD dyes were excited using 514-nm Argon ion laser (3% laser intensity) and 633-nm HeNe633 laser (5% laser intensity). The emission ranges of 538-680 nm and 638-755 nm were collected for Cy3 and DiD. The image resolution was 1024x1024 pixels with the scan time of 6.25 s per image.

For 3D reconstruction of GUVs incubated with cube/cholesterol constructs, z-stacked images were acquired using 561-nm Argon ion laser (3% laser intensity) with emission range of 564-680 nm. The image resolution was 512x512 pixels with the scan time of 391 ms per image. The interval between z-stacked slides was kept between 0.3 to 1 μm, depending on the range of image depth. The reconstruction was performed by the Z-project function in Image J software (version 1.51n).

GUV and sample preparation:

DOPC GUVs were prepared by gel-assisted hydration method developed by Horger *et al*.[30] A 25x25 mm cover glass (Fisher Scientific, cat.# 12542C) was used as the substrate for film fabrication. Prior to agarose gel deposition, the cover glass was cleaned by sonicating in

isopropanol for 1 hour at room temperature, washing with water and drying with the air stream. Separately, an agarose solution was prepared by mixing 1% w/w agarose of ultra-low gelling temperature in Milli-Q water. After gentle heating to dissolve agarose, a 200-µL aliquot of agarose solution was evenly spread on the cover glass by using a 200-µL pipette tip. An excess solution was removed by tilting the cover glass on Kimwipes wipers. The films were then heated on a hot plate at 40^{o}C for 1 hour. The agarose films were kept in the refrigerator and used within a week.

To prepare a lipid mixture, 3.75 g/mL DOPC in $CHCl_3$ was mixed with 1 mol% DiD dye in methanol. A 10-µL aliquot of the lipid mixture was then deposited on the agarose films by using 100-µL Hamilton syringe. The needle was used to quickly spread the lipid mixture on the films until no solvent was visible. A total of 30 µL of the lipid mixture was applied on each cover glass. The hybrid films were then dried under vacuum for at least 30 minutes, kept in the refrigerator and used within a week.

The vesicle growth was typically carried out on the same day of the binding experiments. The film-casted cover glass was placed in a 35-mm cell culture dish (Corning Incorporated, cat.# 430165) with the films facing up. Film hydration was done by adding 2 mL of 1xDPBS supplemented with 200 mM sucrose to the dish. We noted that 1xDPBS was used as the working buffer to simulate the physiological conditions. After room-temperature incubation for 1.5-2 hours, GUVs were harvested by gentle pipetting using a 200-µL micropipette.

The glass slide and coverslip were passivated with 5 mg/mL casein solution for 5 minutes to prevent non-specific adsorption of lipids on the glass surface, followed by washing with water and air drying. The imaging chamber was assembled by placing a 25x25 mm silicone isolator (13 mm diameter x 1 mm depth, Electron Microscopy Sciences, cat# 70336-02) on the glass slide. Then, 50 µL of 1xDPBS supplemented with 200 mM glucose and 50 µL of GUV mixture were added to the well on the glass slide. The higher solution density inside the GUVs compared to the external solution will induce GUV sedimentation to the chamber's surface, resulting in enhanced GUV stability during image acquisition. Then, 10 µL of cube/cholesterol constructs at 125 nM with respect to the cube was added and mixed by gentle pipetting. The imaging chamber was closed by placing a passivated cover glass on top of the silicone isolator. The sample was incubated at room temperature in the dark for at least 1 hour prior to imaging.

3.5.9 Fluorescence recovery after photobleaching

Instrumentation:

FRAP measurements were performed by Zeiss LSM710 CLSM equipped with 20x plan apochromatic objective. The main beam splitter 488/561/633 was used with two laser lines: 488 nm argon ion laser (25 mW) and 561 nm DPSS laser (20 mW). A series of 42.5 µm x 42.5 µm images were acquired using 3% of the 561-nm laser with the image resolution of 512x512 pixels and the scan time of 391 ms per image (emission range of 564-680 nm). The time-dependent intensities of three circular bleach spots with a radius of 1.25 µm were collected for data analysis. These spots were bleached spot, reference spot, and background spot. The reference spot was used to correct the fluorescence intensity loss due to photobleaching during image acquisition of the bleach spot. Five images were acquired before FRAP bleaching to measure initial fluorescence intensity. FRAP bleaching was performed by using both lasers with 100% laser intensity for 10 consecutive bleach iterations. A total of 245 post-bleaching images were then collected.

Data analysis:

Time-dependent fluorescence intensity of the bleach spot was corrected for background signal and acquisition photobleaching by using double normalization method.[44]

$$I_{norm}(t) = \frac{I_{ref\_pre}}{I_{ref}(t) - I_{back}(t)} \cdot \frac{I_{frap}(t) - I_{back}(t)}{I_{frap\_pre}}$$

where frap, ref and back are FRAP, reference and background spots; subscript _pre means intensity average of the spots before bleach moment after subtracting background intensity. FRAP data from each measurement was fitted using a standard exponential equation.

$$I(t) = y_0 - Ae^{-\tau t}$$

Mobile fraction is calculated by

$$mobile\ fraction = \frac{I_\infty - I_{frap\_bleach}}{1 - I_{frap\_bleach}} = \frac{A}{1 - (y_0 - A)}$$

Half-life time of the recovery is calculated by

$$t_{1/2} = \frac{ln2}{\tau}$$

The diffusion coefficient is then calculated by using the equation developed by Soumpasis.[45]

$$D = \frac{0.224r^2}{t_{1/2}}$$

where r is the radius of bleach spot. Data normalization and curve fitting were performed using Microsoft Excel and Origin 2015 software. An example of FRAP curves and data analysis is shown in Figure 3.24.

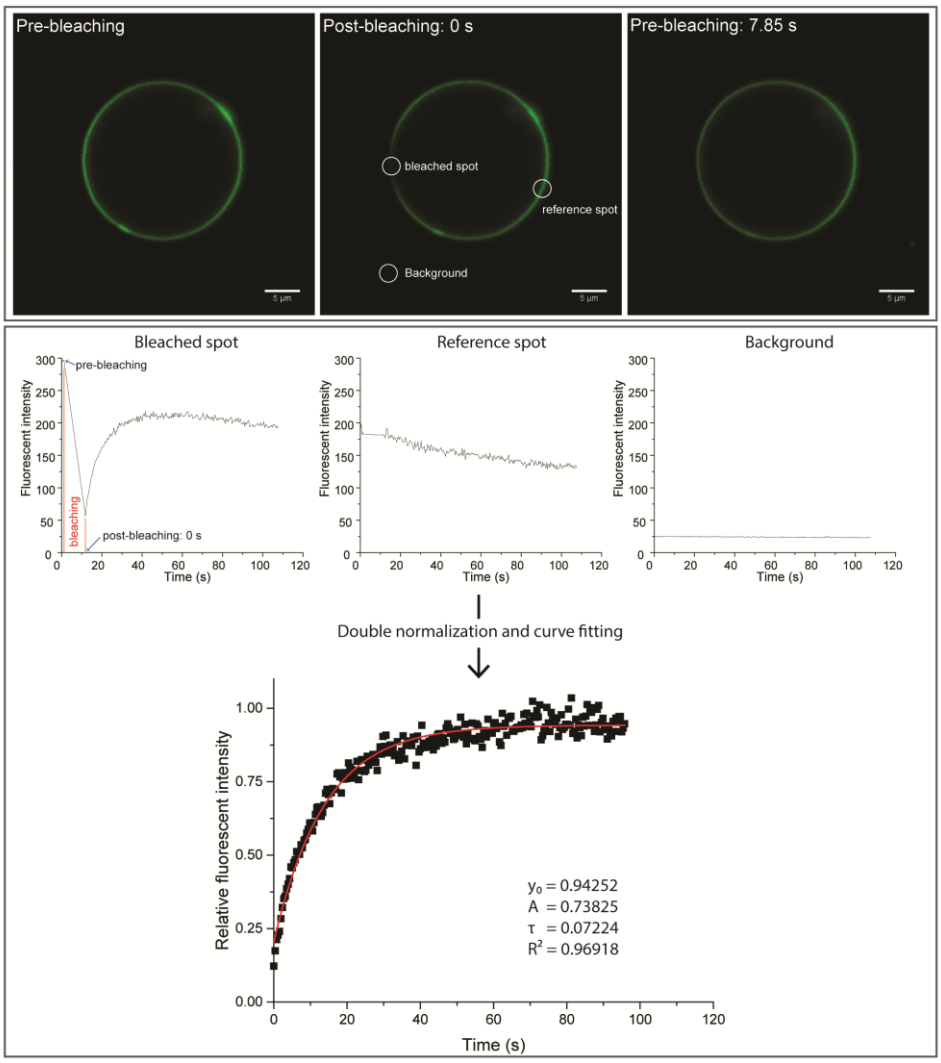

Figure 3.24 | Example of FRAP data analysis for C_4/Chol-A14 on GUV.

Correlation between mobile fractions and diffusion coefficients:

The purpose of these plots was to show data variations in FRAP measurements performed on different days with different sample batches. Each data point represents FRAP measurement of the individual GUVs. The data points labeled with the same marker (i.e., square, circle, diamond and triangle) were collected from the same batch. N indicates the number of measurements.

1) Number and orientation of cholesterol units

Chol-A14-Cy3 (N=36)

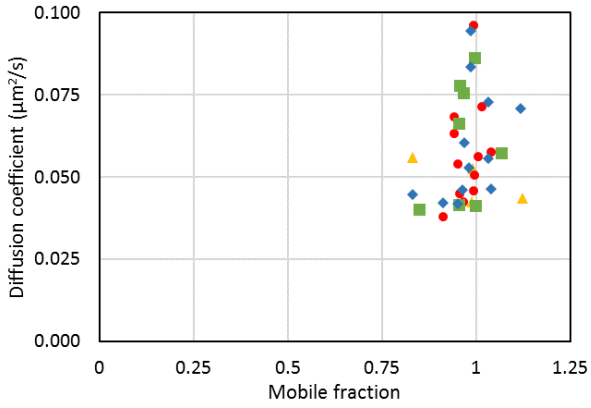

C_1/Chol-B14 (N=38)

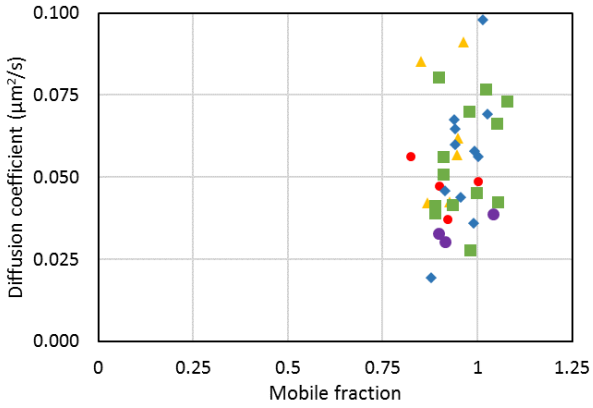

C_4/Chol-A14 (N=42)

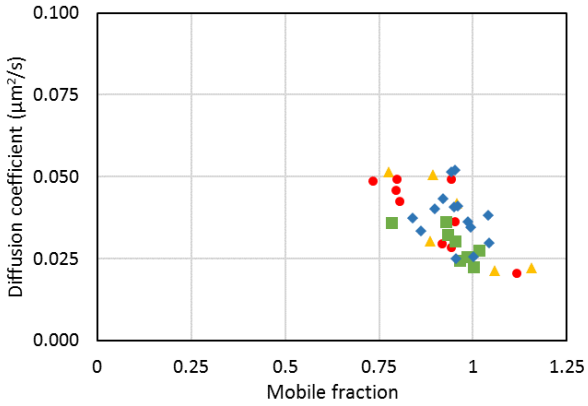

C_4/Chol-A20 (N=42)

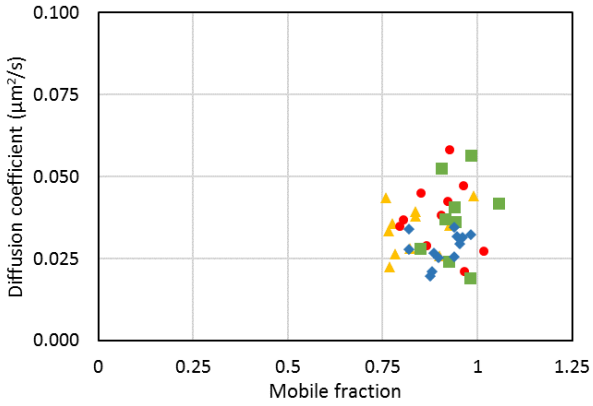

$C_{2,2}$/Chol-A14 (N=45)

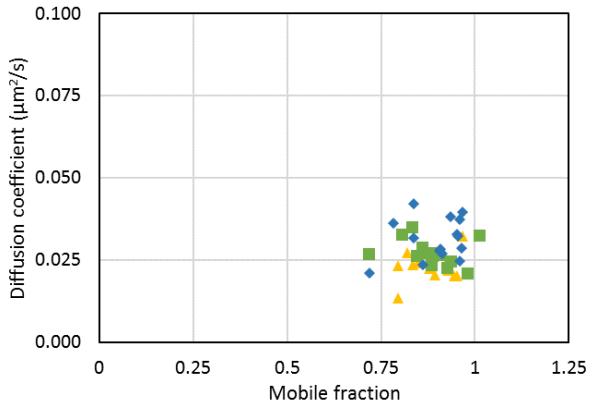

$C_{2,2}$/Chol-A20 (N=75)

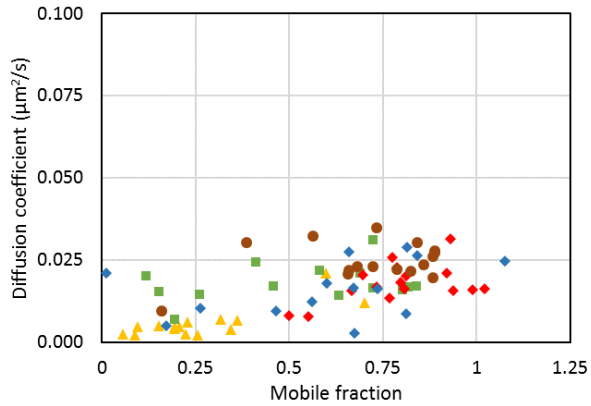

C_8/Chol-A14 (N=50)

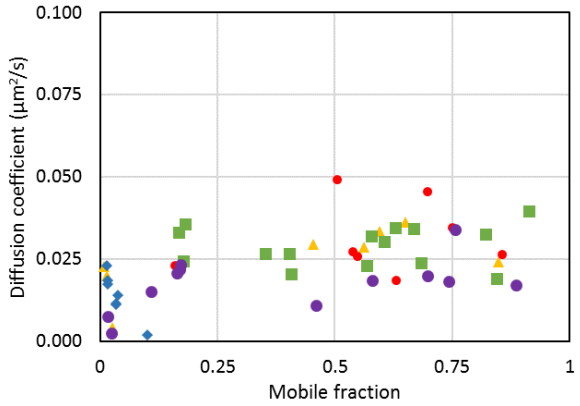

C_8/Chol-A20 (N=45)

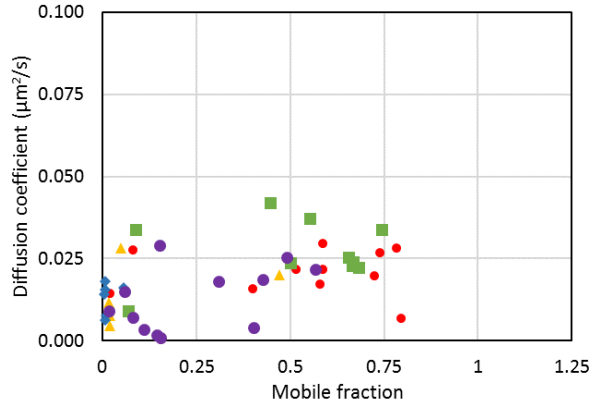

2) Incubation time (24-hour incubation at 10°C)

C_4/Chol-A14 (N=40)

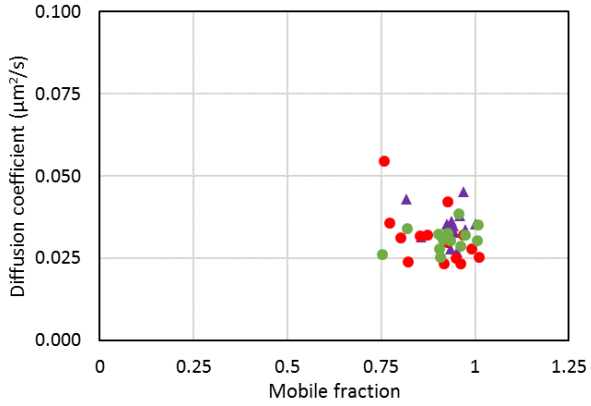

C_8/Chol-A14 (N=58)

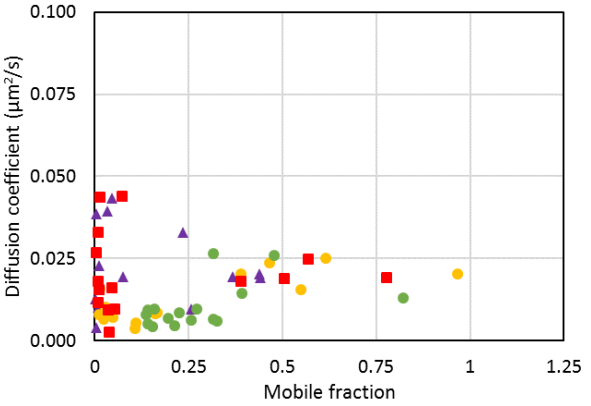

3) Concentration of cube/cholesterol constructs (50-fold dilution)

C_4/Chol-A14 (N=39)

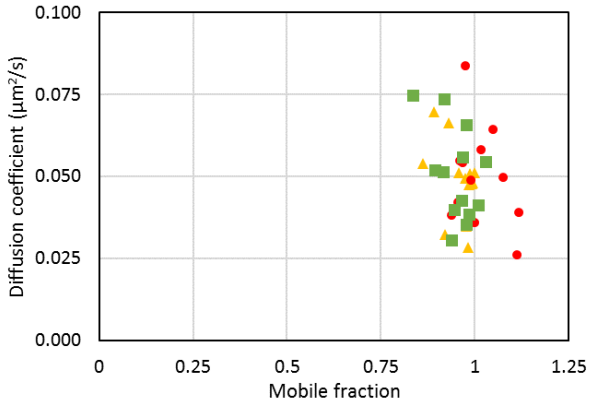

$C_{2,2}$/Chol-A14 (N=41)

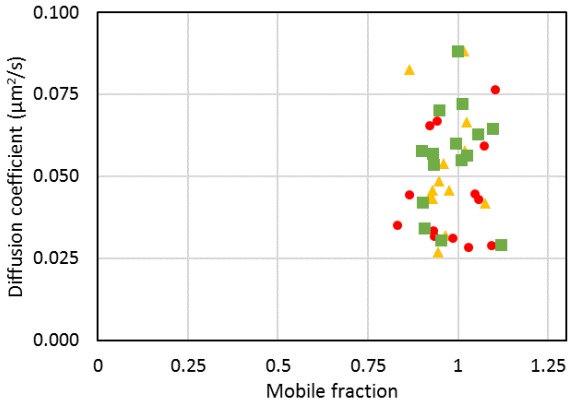

C_8/Chol-A14 (N=40)

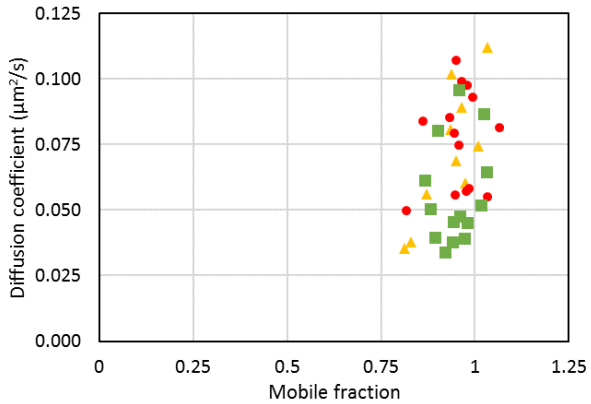

C_8/Chol-A20 (N=43)

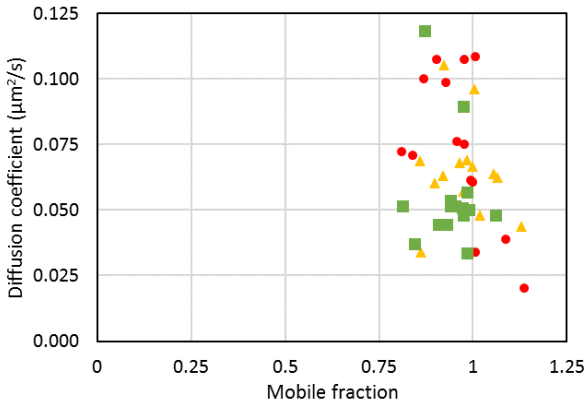

4) Addition of free cholesterol

10% (N=44)

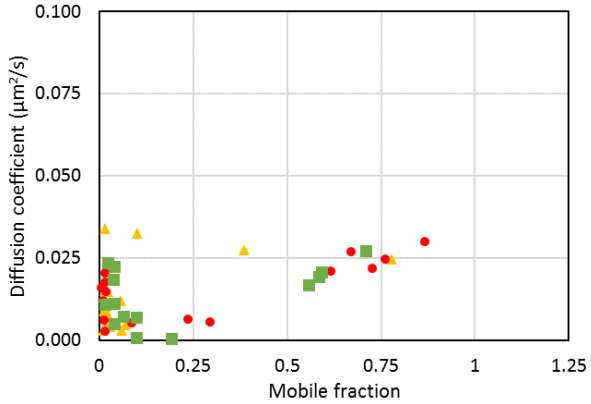

40% (N=64)

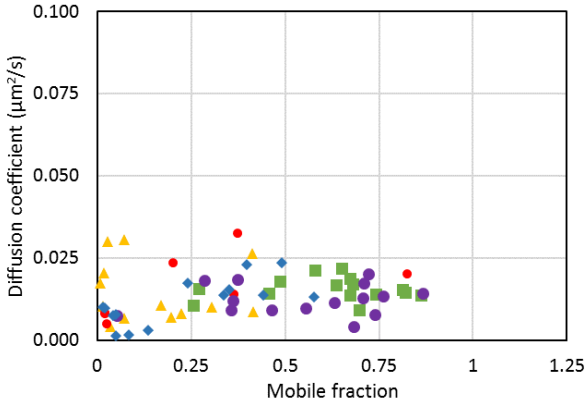

5) DPhPC GUVs

C_4/Chol-A14 (N=37)

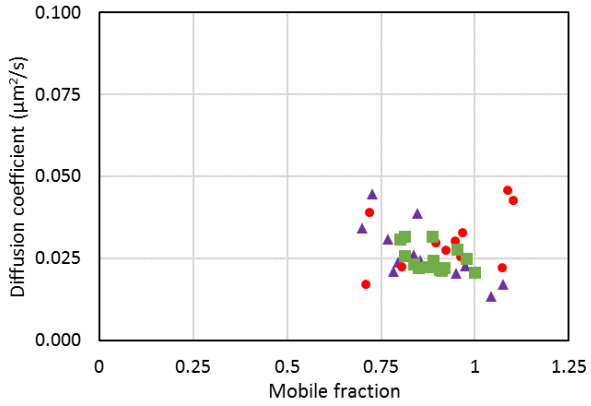

C_8/Chol-A14 (N=37)

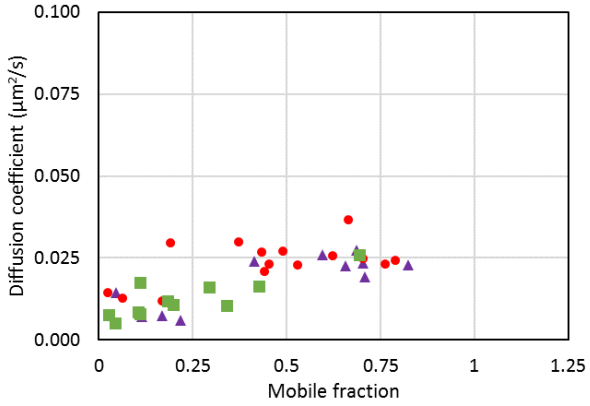

6) Small-molecule dye (DiO-C18)

DiO-C18 on DOPC GUV (N=46)

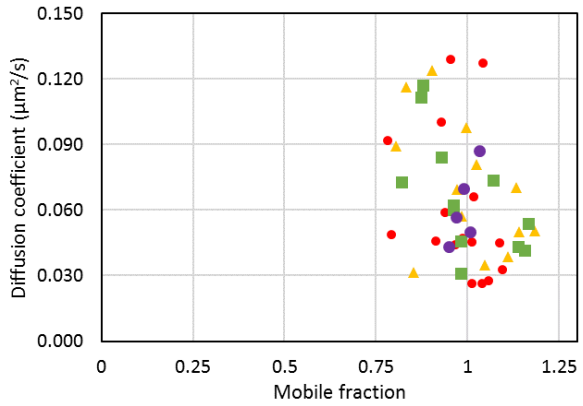

DiO-C18 on DOPC GUV incubated with C_8/Chol-A14 (N=41)

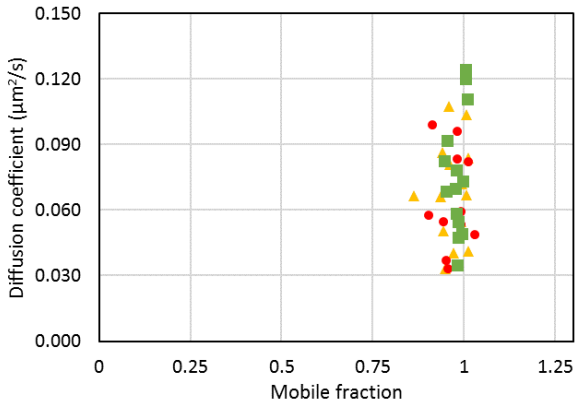

Additional reconstructed z-images:

The length scale bar is 5 μm.

1) Number and orientation of cholesterol units

a) Chol-A14-Cy3

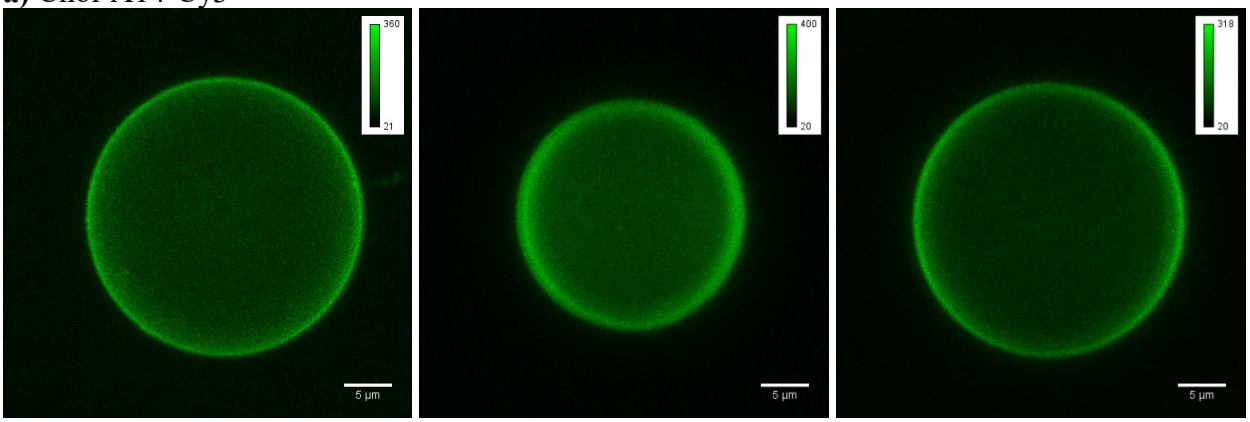

b) C_4/Chol-A14

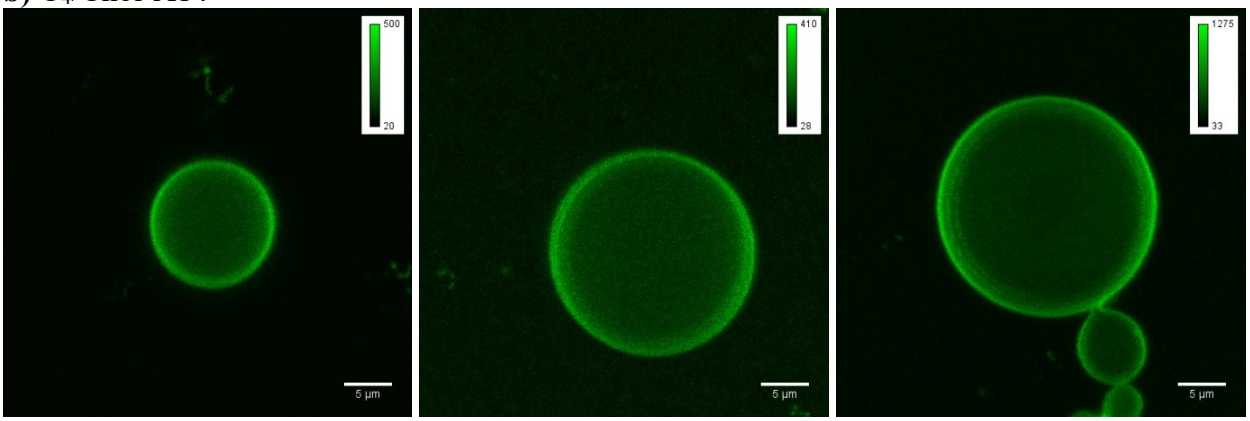

c) C_4/Chol-A20

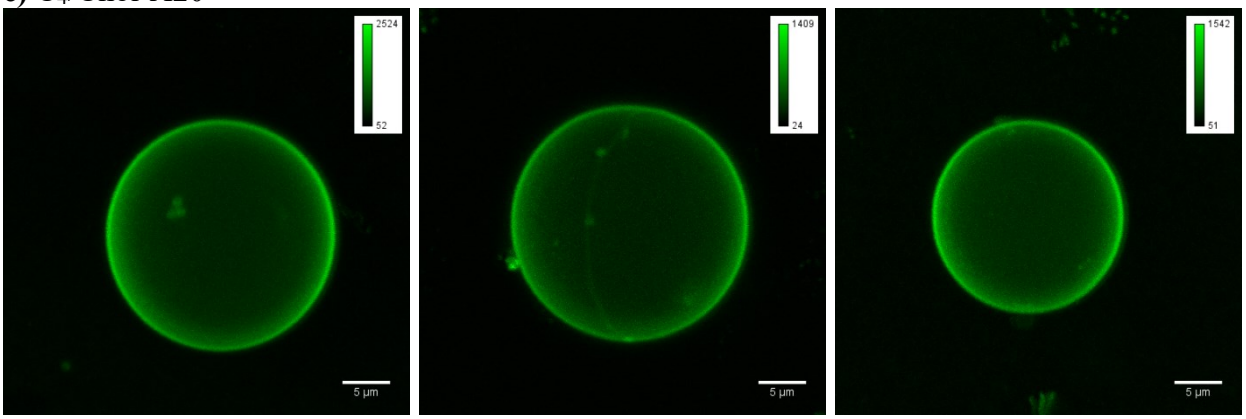

d) $C_{2,2}$/Chol-A14

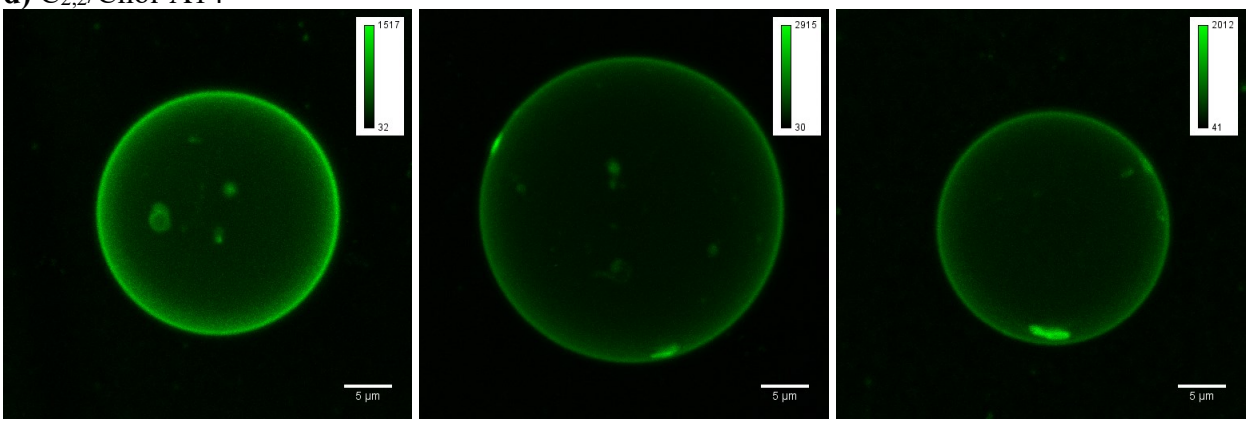

e) $C_{2,2}$/Chol-A20

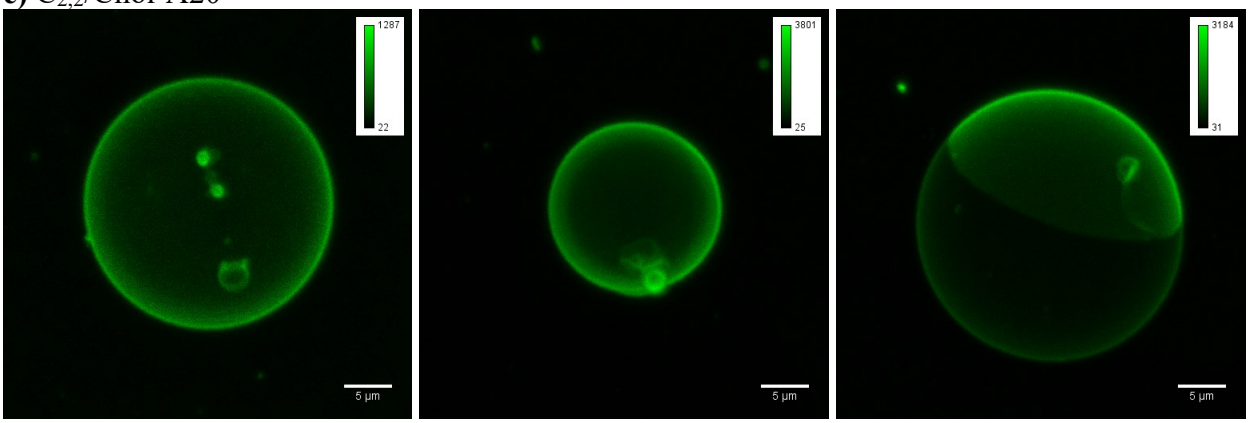

f) C_8/Chol-A14

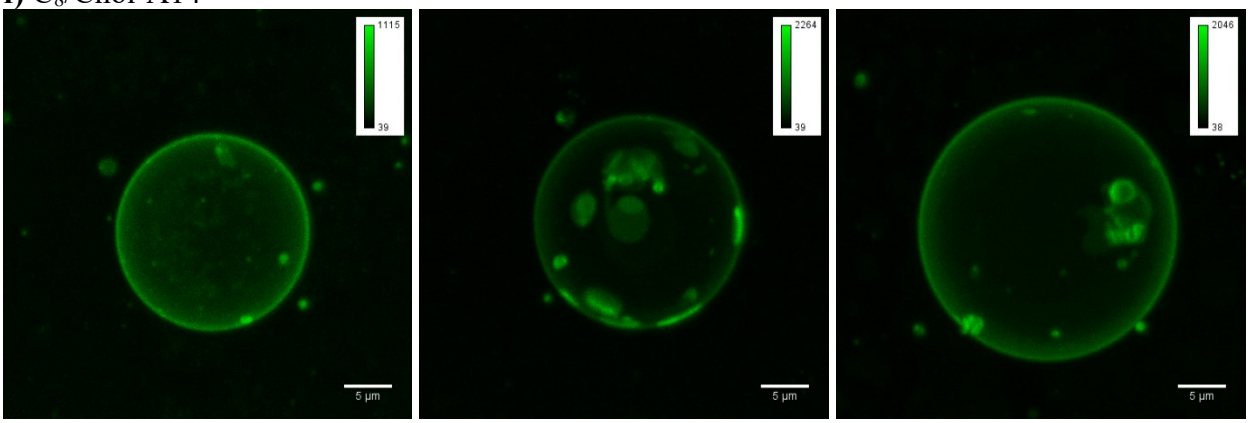

g) C_8/Chol-A20

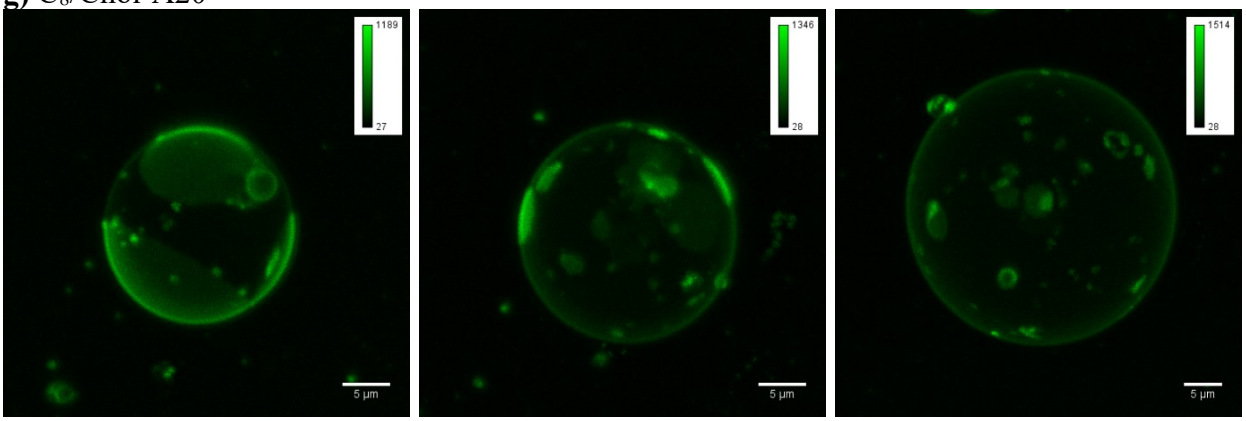

2) Concentration of cube/cholesterol constructs

a) C_8/Chol-A14 at 10-fold dilution

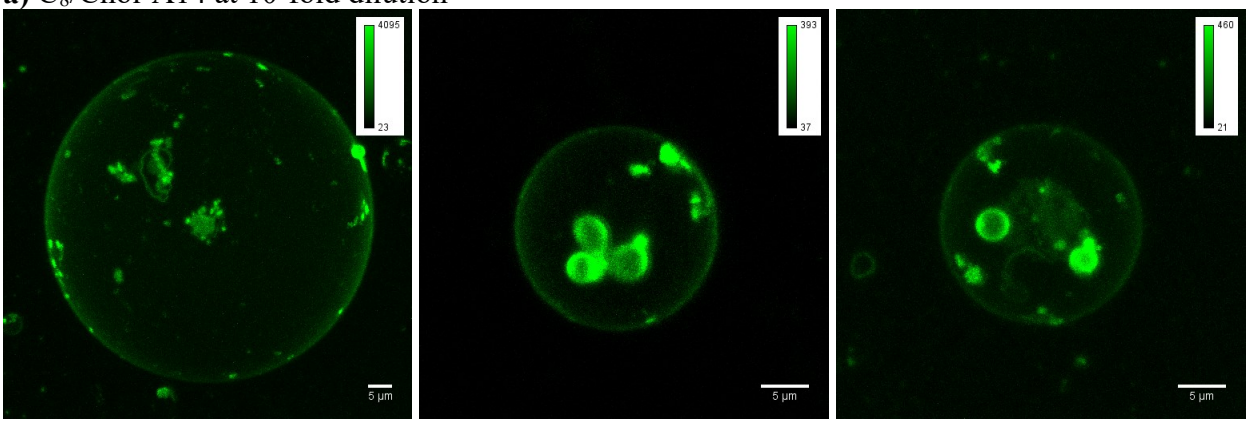

b) C_8/Chol-A14 at 50-fold dilution

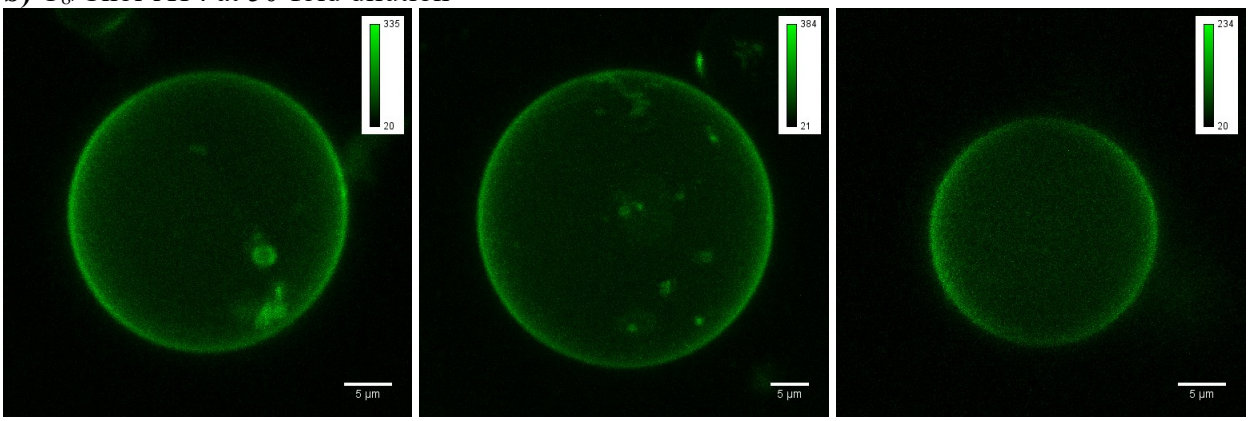

c) C_8/Chol-A14 at 100-fold dilution

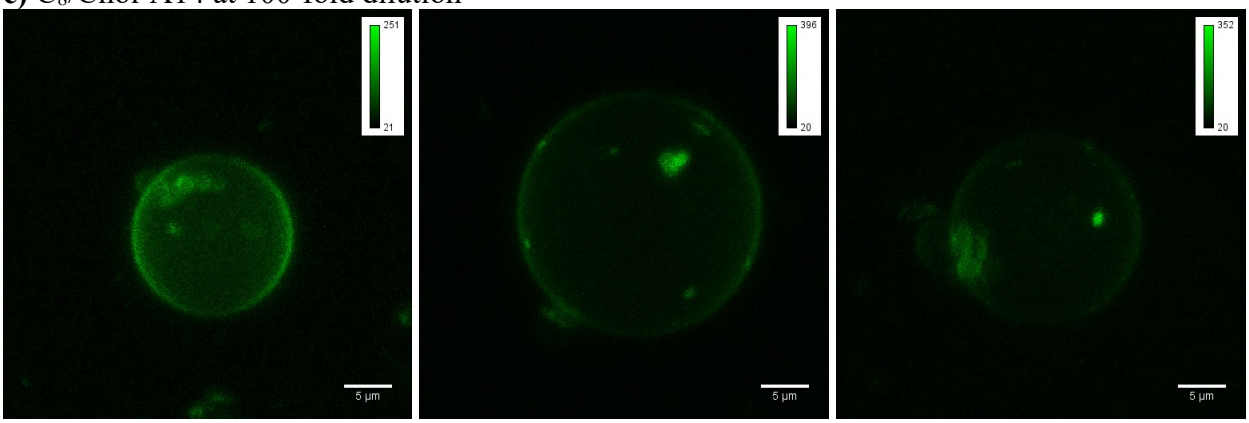

d) C_8/Chol-A20 at 50-fold dilution

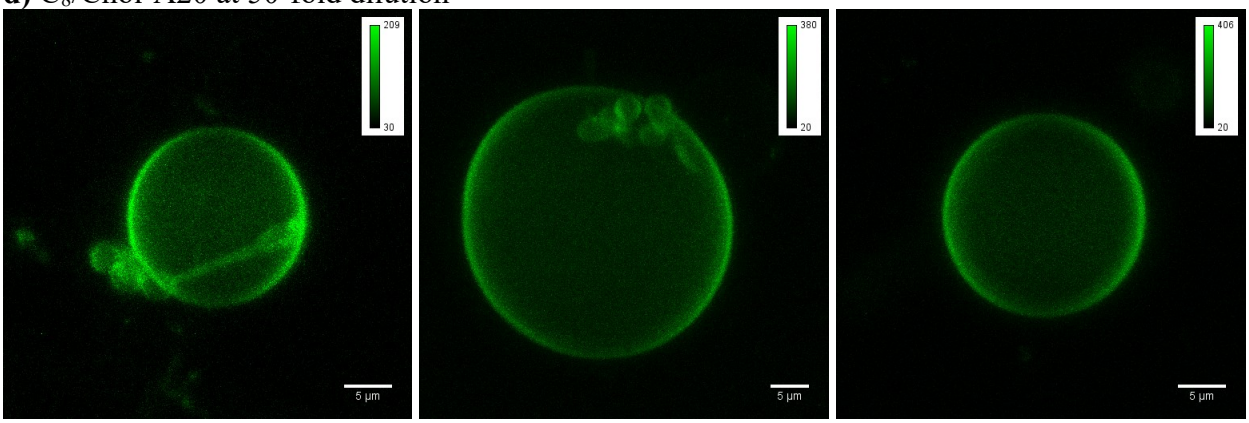

e) C_4/Chol-A14 at 50-fold dilution

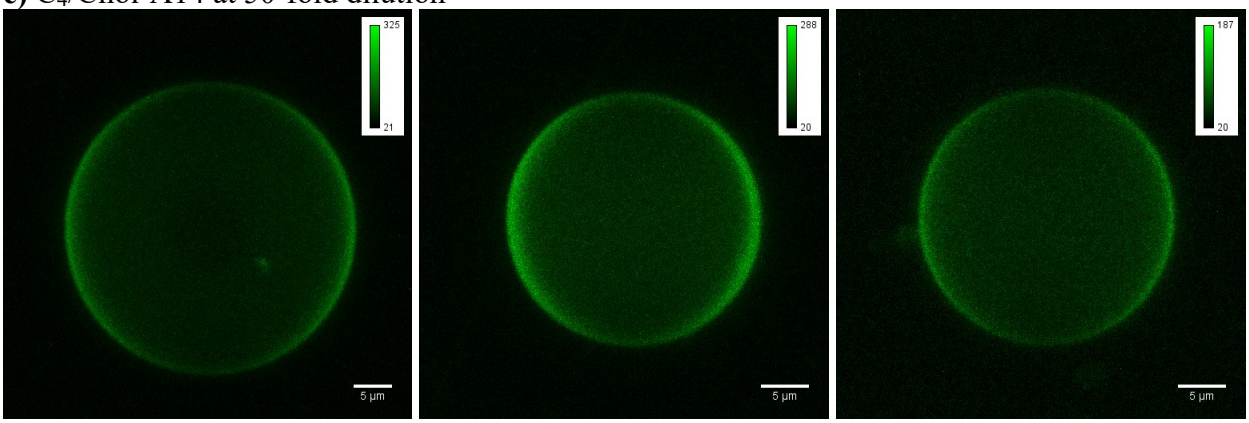

f) $C_{2,2}$/Chol-A14 at 50-fold dilution

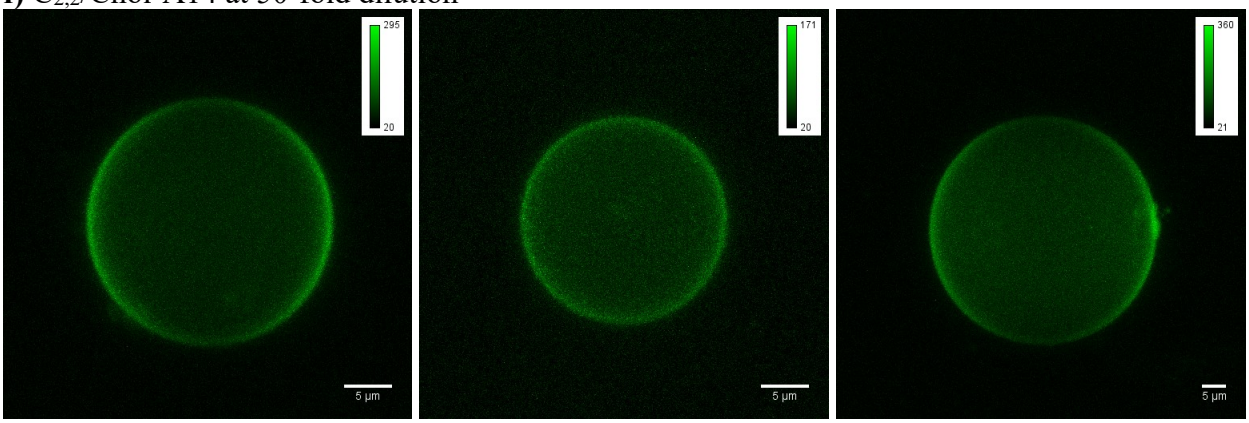

3.5.10 Enzymatic digestion of cube constructs by DNase I treatment

DOPC GUVs were prepared in the same manner as described in Section 3.5.8 with slight modifications. i) DOPC was used as the only component for the lipid mixture. ii) 1xDPBS without sucrose (1.5 mL) was added to hydrate the films, and the vesicle growth was carried out at room temperature for 1.5 hours. To bind cube constructs to GUVs, 10 µL of 125 nM cube/cholesterol constructs was added to 35 µL of the GUV suspension. The mixtures were mixed by gentle pipetting and incubated at room temperature for 1.5 hours. Then, 5 µL of 10x DNase I buffer was added to the mixtures, which resulted in a final volume of 50 µL. DNase I (1 µL) was then added to the mixture and quickly mixed by pipetting, followed by the incubation at room temperature. We note that the manufacturer's protocol recommends 37ºC incubation. However, our concern was the increased lipid dynamics. This might change the binding behavior of cube/cholesterol constructs that we previously observed on fluorescence technique. Therefore, we decided to maintain the working temperature at room temperature. After the 15-minute incubation, the mixture was heated to 75ºC for 10 minutes to inactivate the enzymes. To denature DNA assembly, 20 µL of 8 M urea was added to the mixtures. The samples were loaded on denaturing PAGE (15%). The gel was run at 250 V for 30 minutes then 500 V for 1 hour, using 1xTBE as the running buffer. The gel was finally stained with GelRed in 1xTBE solution before imaging.

The percentages of intact DNA clips for different cube constructs after 15-minute treatment with DNase I are summarized in Table 3.7. Cubes without cholesterol units showed very low amounts of intact DNA clips than cube/cholesterol constructs.

Table 3.7 | Percentage of intact DNA clips after DNase I treatment.

Constructs	% intact clips	Number of samples
C_4/A14	0.8±0.2	3
C_4/Chol-A14	5.1±1.8	4
$C_{2,2}$/A14	0.8±0.2	3
$C_{2,2}$/Chol-A14	2.9±1.5	4
C_8/A14	0.6±0.2	3
C_8/Chol-A14	15.5±6.8	4
C_4/A20	1.4±1.0	3
C_4/Chol-A20	13.1±4.6	4
$C_{2,2}$/A20	0.6±0.4	3
$C_{2,2}$/Chol-A20	15.0±4.9	4
C_8/A20	1.6±2.1	3
C_8/Chol-A20	17.2±5.8	4

We also performed a longer incubation of cube/cholesterol constructs with DNase I (30 minutes). In Figure 3.25, the amounts of intact DNA clips significantly reduced (less than 6%), compared to 15-minute incubation in Figure 3.17.

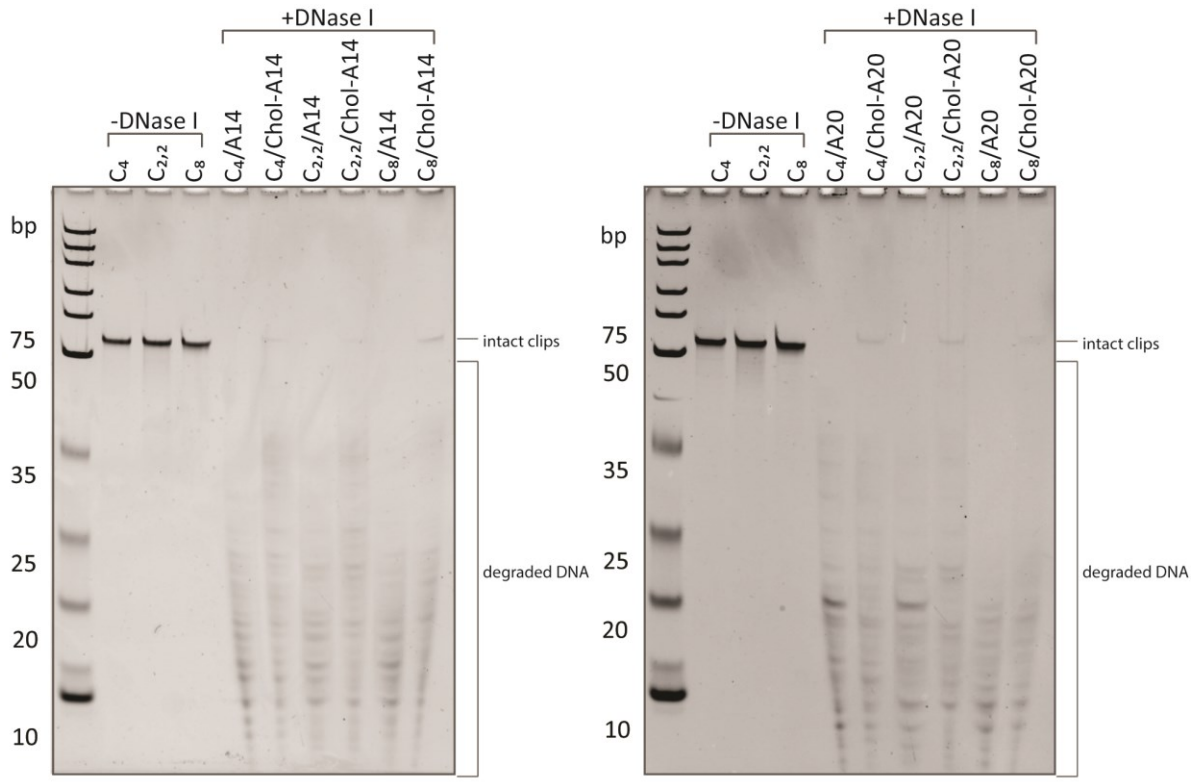

Figure 3.25 | 30-minute DNase I treatment of cube/cholesterol constructs bound on GUVs. Denaturing PAGE (15%) shows the analysis of: left) cubes functionalized with A14 and Chol-A14, and right) cubes decorated with A20 and Chol-A20. The cubes which were not treated with DNase I were used as the references for 100% resistance to DNase I digestion.

One of the concerns for this assay is on the possible interference of DOPC lipids with the analysis. As DNA may non-specifically interact with the lipids, DOPC/DNA complexes might adhere to the plastic PCR tubes during the sample handling due to the hydrophobicity of DOPC. If this happens, the detected amounts of DNA on PAGE will be lower than expected. To verify this hypothesis, the mixture of DOPC GUVs and the cube/cholesterol constructs without DNase I treatment were analyzed by denaturing PAGE. Figure 3.26 shows that most of DNA clips could be quantitatively recovered from the assay as they showed high band intensity on the gel, which was comparable to the cube control in the last lane.

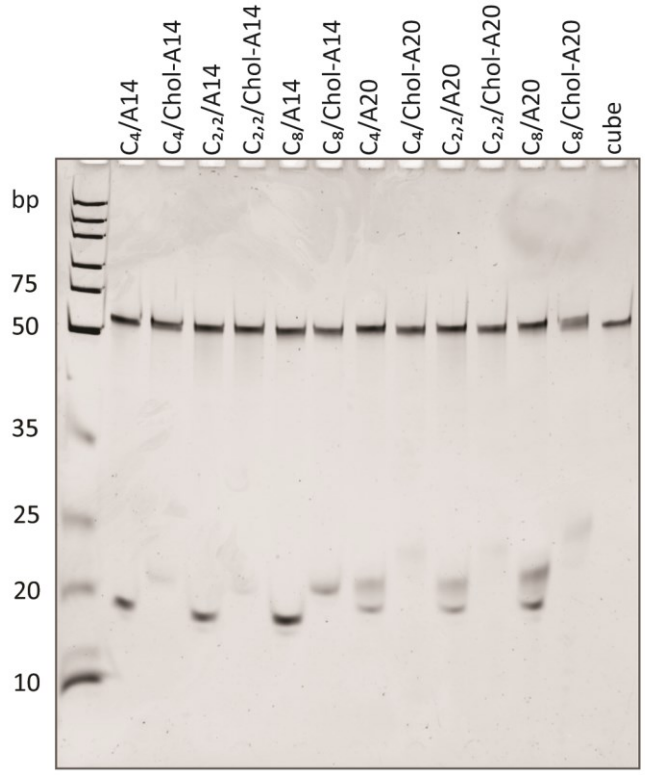

Figure 3.26 | Denaturation of cube/cholesterol constructs bound on GUVs. Denaturing PAGE (15%) shows that all samples could be fully recovered from the experiments.

3.6 References

1. Fakhoury, J. J.; McLaughlin, C. K.; Edwardson, T. W.; Conway, J. W.; Sleiman, H. F. *Biomacromolecules* 2014**,** 15, 276-282.
2. Bujold, K. E.; Fakhoury, J.; Edwardson, T. G. W.; Carneiro, K. M. M.; Briard, J. N.; Godin, A. G.; Amrein, L.; Hamblin, G. D.; Panasci, L. C.; Wiseman, P. W.; Sleiman, H. F. *Chem. Sci.* 2014**,** 5, 2449-2455.
3. Bujold, K. E.; Hsu, J. C.; Sleiman, H. F. *J. Am. Chem. Soc.* 2016**,** 138, 14030-14038.
4. Conway, J. W.; Madwar, C.; Edwardson, T. G.; McLaughlin, C. K.; Fahkoury, J.; Lennox, R. B.; Sleiman, H. F. *J. Am. Chem. Soc.* 2014**,** 136, 12987-12997.
5. Horne, W. S.; Gellman, S. H. *Acc. Chem. Res.* 2008**,** 41, 1399-1408.
6. Goodman, C. M.; Choi, S.; Shandler, S.; DeGrado, W. F. *Nat. Chem. Biol.* 2007**,** 3, 252-262.
7. Aldaye, F. A.; Palmer, A. L.; Sleiman, H. F. *Science* 2008**,** 321, 1795-1799.
8. Zhang, F.; Nangreave, J.; Liu, Y.; Yan, H. *J. Am. Chem. Soc.* 2014**,** 136, 11198-11211.
9. Yang, Y. R.; Liu, Y.; Yan, H. *Bioconjugate Chem.* 2015**,** 26, 1381-1395.
10. Langecker, M.; Arnaut, V.; List, J.; Simmel, F. C. *Acc. Chem. Res.* 2014**,** 47, 1807-1815.
11. Czogalla, A.; Franquelim, H. G.; Schwille, P. *Biophys. J.* 2016**,** 110, 1698-1707.
12. White, S. H. *Nature* 2009**,** 459, 344-346.

13. Hurley, J. H. *Biochim. Biophys. Acta* 2006**,** 1761, 805-811.
14. Lee, A. G. *Biochim. Biophys. Acta* 2003**,** 1612, 1-40.
15. Howorka, S. *Science* 2016**,** 352, 890-891.
16. Gopfrich, K.; Li, C. Y.; Mames, I.; Bhamidimarri, S. P.; Ricci, M.; Yoo, J.; Mames, A.; Ohmann, A.; Winterhalter, M.; Stulz, E.; Aksimentiev, A.; Keyser, U. F. *Nano Lett.* 2016**,** 16, 4665-4669.
17. Burns, J. R.; Seifert, A.; Fertig, N.; Howorka, S. *Nat. Nanotechnol.* 2016**,** 11, 152-156.
18. Langecker, M.; Arnaut, V.; Martin, T. G.; List, J.; Renner, S.; Mayer, M.; Dietz, H.; Simmel, F. C. *Science* 2012**,** 338, 932-936.
19. Krishnan, S.; Ziegler, D.; Arnaut, V.; Martin, T. G.; Kapsner, K.; Henneberg, K.; Bausch, A. R.; Dietz, H.; Simmel, F. C. *Nat. Commun.* 2016**,** 7, 12787.
20. List, J.; Weber, M.; Simmel, F. C. *Angew. Chem. Int. Ed.* 2014**,** 53, 4236-4239.
21. Johnson-Buck, A.; Jiang, S.; Yan, H.; Walter, N. G. *ACS Nano* 2014**,** 8, 5641-5649.
22. Suzuki, Y.; Endo, M.; Sugiyama, H. *Nat. Commun.* 2015**,** 6, 8052.
23. Kocabey, S.; Kempter, S.; List, J.; Xing, Y.; Bae, W.; Schiffels, D.; Shih, W. M.; Simmel, F. C.; Liedl, T. *ACS Nano* 2015**,** 9, 3530-3539.
24. Dohno, C.; Makishi, S.; Nakatani, K.; Contera, S. *Nanoscale* 2017**,** 9, 3051-3058.
25. Yang, Y.; Wang, J.; Shigematsu, H.; Xu, W.; Shih, W. M.; Rothman, J. E.; Lin, C. *Nat. Chem.* 2016**,** 8, 476-483.
26. Czogalla, A.; Kauert, D. J.; Franquelim, H. G.; Uzunova, V.; Zhang, Y.; Seidel, R.; Schwille, P. *Angew. Chem. Int. Ed.* 2015**,** 54, 6501-6505.
27. Edwardson, T. G.; Carneiro, K. M.; McLaughlin, C. K.; Serpell, C. J.; Sleiman, H. F. *Nat. Chem.* 2013**,** 5, 868-875.
28. Chidchob, P.; Edwardson, T. G.; Serpell, C. J.; Sleiman, H. F. *J. Am. Chem. Soc.* 2016**,** 138, 4416-4425.
29. Bunge, A.; Loew, M.; Pescador, P.; Arbuzova, A.; Brodersen, N.; Kang, J.; Dahne, L.; Liebscher, J.; Herrmann, A.; Stengel, G.; Huster, D. *J. Phys. Chem. B* 2009**,** 113, 16425-16434.
30. Horger, K. S.; Estes, D. J.; Capone, R.; Mayer, M. *J. Am. Chem. Soc.* 2009**,** 131, 1810-1819.
31. Phair, R. D.; Misteli, T. *Nat. Rev. Mol. Cell Biol.* 2001**,** 2, 898-907.
32. Huang, J.; Feigenson, G. W. *Biophys. J.* 1999**,** 76, 2142-2157.
33. Dai, J.; Alwarawrah, M.; Huang, J. *J. Phys. Chem. B* 2010**,** 114, 840-848.
34. Olsen, B. N.; Bielska, A. A.; Lee, T.; Daily, M. D.; Covey, D. F.; Schlesinger, P. H.; Baker, N. A.; Ory, D. S. *Biophys. J.* 2013**,** 105, 1838-1847.
35. Bacia, K.; Scherfeld, D.; Kahya, N.; Schwille, P. *Biophys. J.* 2004**,** 87, 1034-1043.
36. Chiantia, S.; Ries, J.; Kahya, N.; Schwille, P. *ChemPhysChem* 2006**,** 7, 2409-2418.
37. Sanchez, M. F.; Levi, V.; Weidemann, T.; Carrer, D. C. *FEBS Lett.* 2015**,** 589, 3527-3533.
38. Lira, R. B.; Dimova, R.; Riske, K. A. *Biophys. J.* 2014**,** 107, 1609-1619.
39. Haberland, M. E.; Reynolds, J. A. *Proc. Natl. Acad. Sci. U.S.A.* 1973**,** 70, 2313-2316.
40. Krause, M. R.; Regen, S. L. *Acc. Chem. Res.* 2014**,** 47, 3512-3521.
41. Gopfrich, K.; Zettl, T.; Meijering, A. E.; Hernandez-Ainsa, S.; Kocabey, S.; Liedl, T.; Keyser, U. F. *Nano Lett.* 2015**,** 15, 3134-3138.
42. Perrault, S. D.; Shih, W. M. *ACS Nano* 2014**,** 8, 5132-5140.
43. Howorka, S. *Nat. Nanotechnol.* 2017**,** 12, 619-630.

44. Phair, R. D.; Gorski, S. A.; Misteli, T., Measurement of Dynamic Protein Binding to Chromatin In Vivo, Using Photobleaching Microscopy. In *Chromatin and Chromatin Remodeling Enzymes, Part A*, Academic Press: 2003; Vol. Volume 375, pp 393-414.
45. Soumpasis, D. M. *Biophys. J.* 1983**,** 41, 95-97.

| 4 |

Crosslinking strategies to increase the stability of DNA nanostructures

4.1 Preface

In Chapter 2, the decoration of DNA nanostructures with sequence-defined polymer-DNA conjugates was demonstrated. The hydrophobicity introduced by the polymer chains can bring new assembly modes and functions in the assembly of amphiphilic DNA nanostructures. However, one of the challenges encountered with some structures was their instability and disassembly due to a change in concentration or sample-substrate interactions, which can potentially interfere with accurate structural characterization. The stability of DNA amphiphiles is also important for their *in vivo* applications. To overcome these issues, we sought to apply chemical crosslinking strategies to increase the assembly stability of polymer-DNA conjugates and amphiphilic DNA nanostructures. In this chapter, the core-crosslinking will be demonstrated by using three strategies, including amide-bond formation, *S*-alkylation of phosphorothioate backbones and anthracene photodimerization. We also examined the site-specific hydrophobic modifications of phosphorothioated DNA by *S*-alkylation strategy.

4.2 Introduction

An amphiphile is a molecule that contains both hydrophilic and hydrophobic components. Many amphiphiles have a strong aggregation tendency in an aqueous solution, generating a variety of self-assembled morphologies such as spherical micelles, bilayers, and vesicles. These structures have a great potential as carriers of hydrophobic guests and as confined chemical environments, enabling their extensive use in materials and biomedical sciences.[1] In the context of DNA materials, there have been tremendous efforts to introduce hydrophobic character to hydrophilic DNA. DNA strands can be modified with various types of hydrophobic moieties, from lipids to polymers. These DNA amphiphiles inherit the programmability of DNA and orthogonal functionality of hydrophobic components.[2-3] This opportunity has led to the use of DNA amphiphiles as hybrid materials interfacing with lipid bilayers such as in gene therapy, drug delivery, and membrane-protein mimicry.[4-5]

An interesting character of DNA amphiphiles is that their self-assembly is concentration-dependent, which is typically defined by a critical micelle concentration (CMC), above which the aggregation of DNA amphiphiles into micellar morphologies can happen. However, this

concentration-dependent behavior could be a major drawback in drug delivery applications. High dilution of amphiphilic DNA assembly in physiological conditions can potentially cause undesired leakages of hydrophobic cargos that are physically entrapped in the hydrophobic cores of micelles. Several strategies to enhance structural stability and to avoid premature cargo release have been successfully demonstrated such as component crosslinking and covalent conjugation of cargo in non-DNA materials.[6-7] There are few examples that apply these strategies in DNA amphiphiles. The Levy group modified the sequence of DNA amphiphiles by inserting multiple guanine units and were able to enhance the stability of DNA micelles by G-quadruplex formation.[8] A very recent work by the groups of Nguyen and Mirkin showed that crosslinking the DNA corona can increase the stability of spherical nucleic acids.[9]

The Sleiman group has reported a solid-phase synthetic method to prepare monodisperse, sequence-defined polymer-DNA conjugates based on phosphoramidite chemistry.[10] These DNA amphiphiles introduced hydrophobic interactions in DNA nanostructures as demonstrated in Chapter 2. However, we observed an instability of these DNA hybrid materials that seemed to interfere with the structural characterization of some structures. These could be attributed to their CMC values which were in molar to submicromolar regimes.[11] Thus, the focus of this chapter is to investigate three core-crosslinking strategies to increase the assembly stability of these polymer chains. Bifunctional linkers that can create amide bonds with DNA amphiphiles were first examined. Then, bifunctional iodoacetamide-based linkers were introduced to crosslink phosphorothioated DNA amphiphiles. Finally, anthracene photodimerization was applied to crosslink DNA amphiphiles. We also present an alternative method for hydrophobic modification of phosphorothioated DNA by using iodoacetamide-based alkylating reagents.

4.3 Results and Discussion

4.3.1 Dimerization of DNA amphiphiles by amide bond formation

Amino groups are arguably one of the most common modifications on DNA strands and can form amide bonds with various molecules containing activated carboxyl groups. As the starting point, we used amide bond formation to provide a linker between two DNA amphiphiles. The amino group (NH_2) from a commercially available phosphoramidite was incorporated into DNA

amphiphiles composed of hexaethylene (HE) repeats to generate a library of amino-modified DNA amphiphiles (NH_2-HE_n-A14). To study the position effect on dimerization efficiency, we inserted only one NH_2 group at the polymer chain-end of DNA amphiphiles (Figure 4.1a). We note that these amino-modified DNA strands were directly purified by reversed-phase HPLC (RP-HPLC) because the NH_2 groups can be rendered inactive under denaturing conditions in gel purification (see a detailed note in Section 4.5.3).

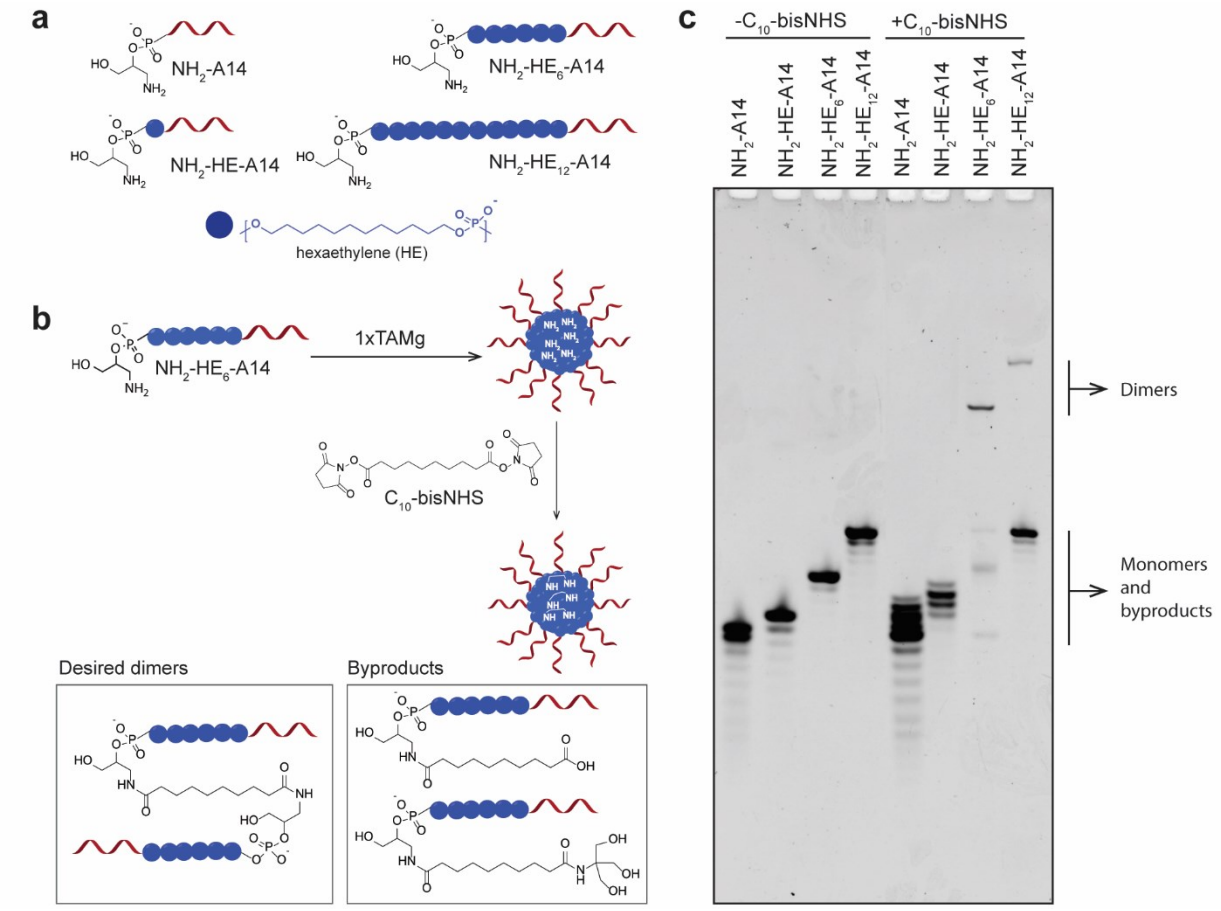

Figure 4.1 | Dimerization of amino-modified DNA amphiphiles with bifunctional alkyl linkers. a) The amino group (NH_2) was appended to the 5' termini of DNA amphiphiles. b) The dimerization was then carried out by incubating DNA amphiphile with C_{10}-bisNHS, leading to desired dimers and byproducts. c) Denaturing polyacrylamide gel electrophoresis (PAGE) (15%) shows that the dimerization was achieved with NH_2-HE_6-A14 and NH_2-HE_{12}-A14 but not with DNA amphiphile that was not able to form micelles (NH_2-HE-A14).

DNA amphiphiles were prepared at 5 μM and thermally annealed from 95°C to 4°C for 1 hour. It is of note that DNA amphiphiles that contained at least 6 HE units in a row were able to form

micelles in tris/acetate/magnesium (TAMg) buffer.[10] Their micelle formation was confirmed by atomic force microscopy (AFM, see AFM images in Section 4.5.10). The dimerization of the micellar core was then performed by using bifunctional sebacic acid bis(*N*-hydroxysuccinimide ester) (C_{10}-bisNHS). The desired products were two DNA amphiphiles connected via a C_{10}-bisamide linker (Figure 4.1b). We quantified the linking efficiency by analyzing the dimer yields on denaturing polyacrylamide gel electrophoresis (PAGE, Figure 4.1c). The highest yield was achieved with NH_2-HE_6-A14 (48%), followed by NH_2-HE_{12}-A14 (14%). On the other hand, no dimer formation was observed for DNA amphiphiles, NH_2-A14, that cannot form micelles. RP-HPLC analysis further supported the dimer formation in the case of NH_2-HE_6-A14 (36%) and NH_2-HE_{12}-A14 (21%) with C_{10}-bisNHS.

The reaction byproducts were NH_2-HE_n-A14/C_{10}-bisNHS monoconjugates where another end of C_{10}-bisNHS was either hydrolyzed back to free carboxyl group or formed amide bonds with tris(hydroxymethyl)aminomethane or tris (Figure 4.1b, see Section 4.5.6 for detailed characterization). However, these by-products were not observed in NH_2-HE_{12}-A14, suggesting that the side reactions are likely to happen before encapsulating C_{10}-bisNHS inside the hydrophobic core. It is possible that an increase in the hydrophobicity degree of NH_2-HE_{12}-A14 compared to NH_2-HE_6-A14 could hinder the diffusion of inactive NHS molecules containing free carboxyl groups which are more hydrophilic than the original NHS molecules. A large difference in dimerization efficiency between NH_2-HE_6-A14 and NH_2-HE_{12}-A14 also suggests that the NH_2 groups reside in different environments in the hydrophobic cores.

Having confirmed the dimerization of DNA amphiphiles, we then proceeded to study the dimerization of polymer strands in amphiphilic DNA nanostructures. DNA cube was used as the 3D scaffold to organize DNA amphiphiles. For cube C_8, which has eight polymer-DNA binding sites on its top and bottom faces, we previously found that the polymer chains could fold themselves inside the cube's cavity and generate a hydrophobic core (Figure 4.2a, see Chapter 2). To crosslink this DNA-micelle cube, C_8 was assembled with eight NH_2-HE_6-A14 strands, followed by the incubation with C_{10}-bisNHS (Figure 4.2a). The assembly products were characterized by PAGE. Figure 4.2b shows that the assembly products remained intact after the crosslinking process, as indicated by the single band similar to un-crosslinked C_8/NH_2-HE_6-A14. The

dimerization of NH_2-HE_6-A14 decorated on C_8 was confirmed by denaturing PAGE, with the dimer yield of 37% (Figure 4.2c).

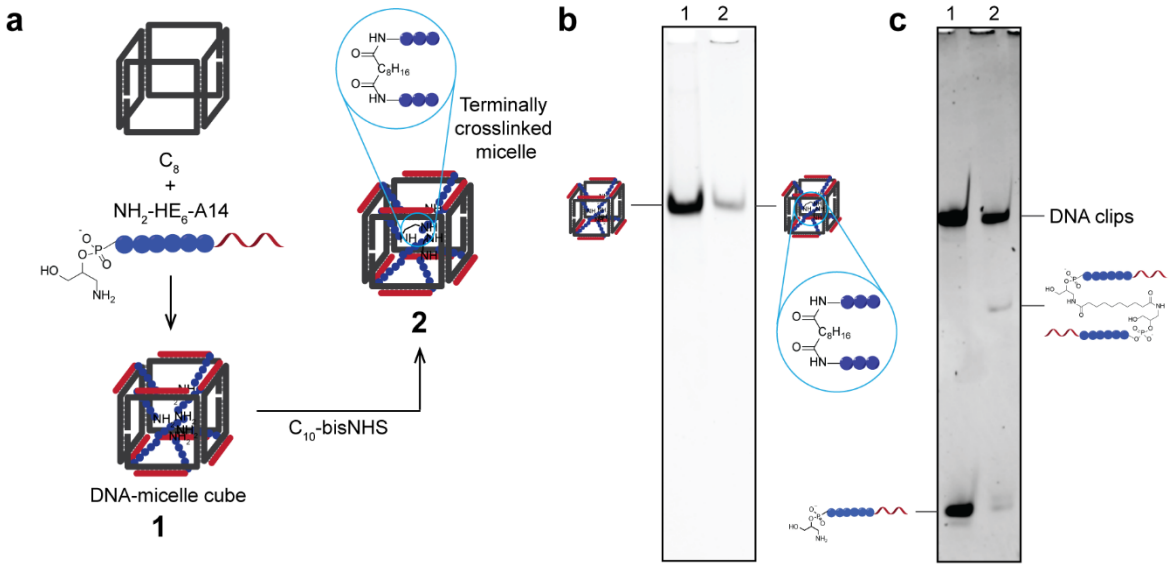

Figure 4.2 | Dimerization of DNA-micelle cubes with bifunctional alkyl linkers. a) The hydrophobic core of C_8/NH_2-HE_6-A14 was dimerized by C_{10}-bisNHS linkers. b) Non-denaturing PAGE (6%) confirms C_8/NH_2-HE_6-A14 stability after the dimerization. c) The dimerization of NH_2-HE_6-A14 was evidenced by the presence of dimer bands on denaturing PAGE (15%).

We would like to note that there are some issues associated with this strategy. DNA nanostructure assembly is mostly performed in the tris-based buffer. The nucleophilic tris molecules in the buffer can react with C_{10}-bisNHS linkers and render them inactive. This could be a serious issue when only one NHS moiety of the linkers is still active and available for the conjugation with DNA amphiphiles, thus decreasing the dimerization efficiency. Another issue is that the hydrolysis of NHS moieties depends strongly on the solution pH, where the half-life is usually few hours at pH 7 and decreases dramatically to less than 1 hour at pH 8.[12] TAMg buffer has a pH of ~8, which can decrease the half-life of C_{10}-bisNHS, also leading to lower dimer yields. These issues can be avoided by replacing tris with other non-nucleophilic bases such as 4-(2-hydroxyethyl)-1-piperazineethanesulfonic acid (HEPES) and decrease the solution pH. Nevertheless, the amide-based dimerization could be applied as a simple strategy to crosslink hydrophobic micellar cores of amino-modified DNA amphiphiles. Potentially, a higher

crosslinking degree could be further achieved by incorporating multiple NH_2 groups on the polymer chains of DNA amphiphiles.

4.3.2 Crosslinking of DNA amphiphiles by *S*-alkylation of phosphorothioate backbones

The phosphorothioate bond is another widely used DNA backbone modification, where one nonbridging oxygen atom on the phosphodiester linker is replaced by a sulfur atom. This simple substitution can greatly improve the stability of antisense oligonucleotides, which are synthetic DNA strands for inhibiting gene expression, against enzymatic digestion.[13-14] In the context of chemical addressability, it was suggested that the localization of negative charge is preferable on the sulfur atom.[15] Many groups have employed this nucleophilicity to post-synthetically functionalize phosphorothioated DNA.[16-22] Early works by the McLaughlin group showed that a molecule bearing activated leaving groups can be attached to phosphorothioated DNA, creating the phosphorothioate triester.[16-17] Lee and co-workers used bifunctional linkers containing iodoacetamide moiety to control the binding sites of gold nanoparticles and proteins on phosphorothioated DNA.[20-21] Thus, due to its versatility, we would like to apply this concept to crosslink the phosphorothioated hydrophobic micellar core of DNA amphiphiles.

Hydrophobic bifunctional linkers that contain iodoacetamide moieties at both ends were used to crosslink the phosphorothioated hydrophobic core of DNA amphiphiles (Figure 4.3b). The linker, *N,N'*-hexamethylene-bis(iodoacetamide) or C_6-bisI, was prepared by a two-step synthesis following the reported procedure (Figure 4.3a).[23-24] We chose HE_6(PS)-A14 containing three phosphorothioate modifications distributed along the hydrophobic HE_6 chain as the model amphiphile (Figure 4.3b). To perform the crosslinking, HE_6(PS)-A14 solution in 1xPBS was allowed to react with C_6-bisI in DMSO at 37ºC for 22 hours. The denaturing PAGE in Figure 4.3c shows the successful micelle crosslinking, indicating by the presence of multiple higher-order bands assigned to dimer, trimer and other higher-order species. Higher C_6-bisI concentration could also promote the crosslinking process, as evidenced by increased band intensity of the slower gel-migrating species.

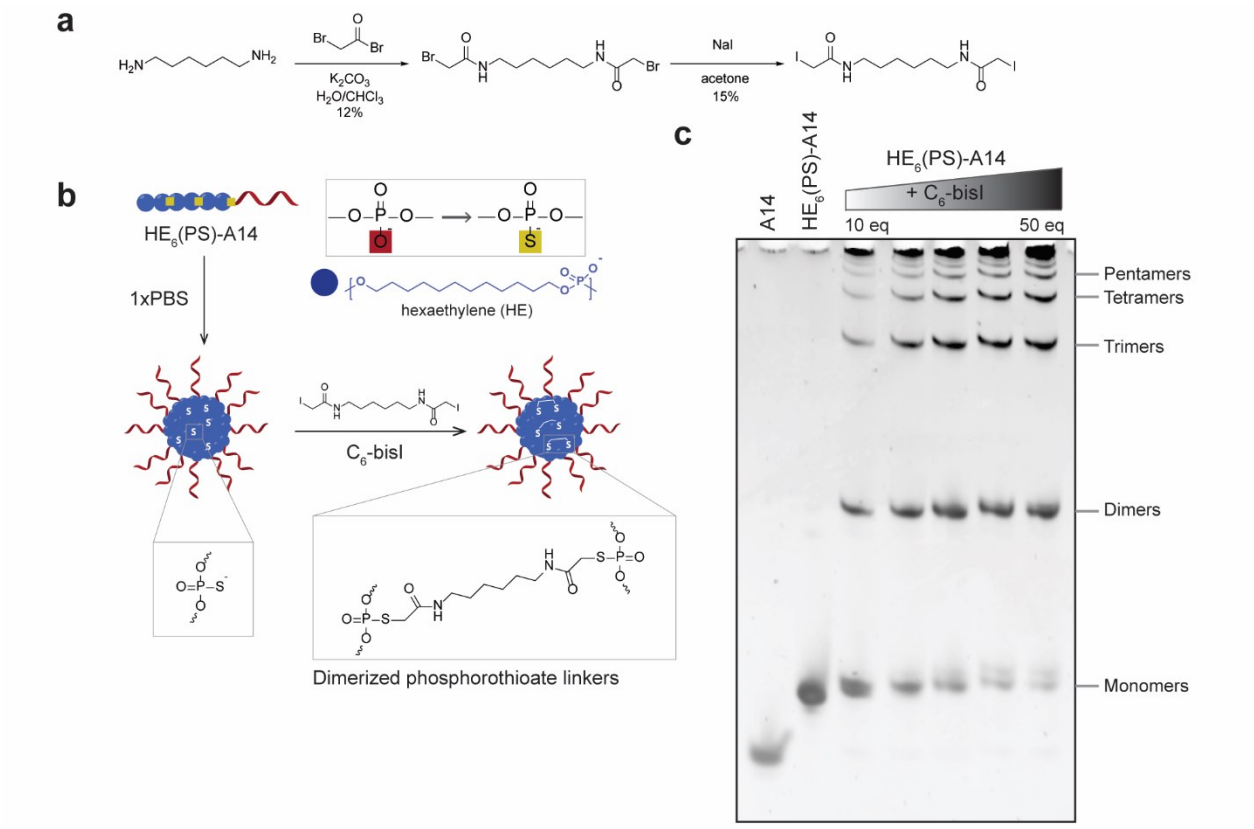

Figure 4.3 | Crosslinking of phosphorothioated DNA amphiphiles with bifunctional alkyl linkers. a) C_6-bisI was synthesized in two steps starting from *N,N'*-hexamethylenediamine. b) The crosslinking reaction was performed by incubating HE_6(PS)-A14 with C_6-bisI at 37°C for 22 hours. c) Denaturing PAGE (15%) shows that the crosslinking efficiency increased with C_6-bisI concentrations. The equivalents of C_6-bisI were relative to HE_6(PS)-A14 (5 μM). There were multiple bands corresponding to monomer, dimer, trimer and other higher-order species.

We then preliminarily proceeded to crosslink the hydrophobic cores of amphiphilic DNA nanostructures. Cubes C_8 and C_4 (the latter structure has four polymer-DNA binding sites on one of its faces) were combined with eight and four HE_6(PS)-A14 strands and thermally annealed (Figure 4.4a). DNA-micelle cube was the assembly product of C_8/HE_6(PS)-A14, while C_4/HE_6(PS)-A14 generated cube dimer, trimer, and tetramer. The crosslinking was performed by incubating preassembled C_8/HE_6(PS)-A14 or C_4/HE_6(PS)-A14 with C_6-bisI at 37°C overnight, and analyzed by non-denaturing PAGE. The preliminary gel results in Figures 4.4b and 4.4c showed that the product distribution shifted towards larger structures that remained in the well when C_6-bisI concentration was increased. This implies that the initial well-defined product distribution is greatly affected by the crosslinking process. Thus, we did not attempt to continue further although

it is possible to optimize the linker concentration that will yield internally crosslinked with intact overall structures.

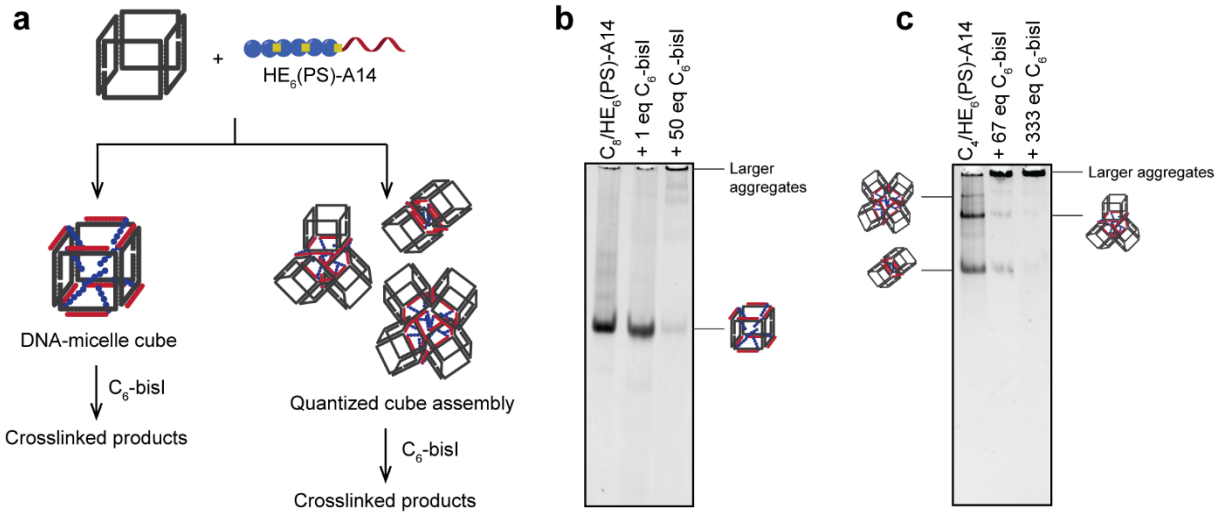

Figure 4.4 | Crosslinking of phosphorothioated amphiphilic DNA nanostructures with bifunctional alkyl linkers. a) The phosphorothioated hydrophobic cores of C_8/HE_6(PS)-A14 and C_4/HE_6(PS)-A14 were crosslinked by C_6-bisI linkers. The reaction was carried out in 1:10 v/v DMSO/1xTAMg at 37ºC overnight. Non-denaturing PAGE (5%) shows that adding C_6-bisI to b) C_8/HE_6(PS)-A14 and c) C_4/HE_6(PS)-A14 generated larger higher-order structures. The equivalents of C_6-bisI were relative to HE_6(PS)-A14 (1.5 µM for C_8 and 750 nM for C_4.)

The phosphorothioate crosslinking strategy is simple and highly accessible because it involves low-cost modification of DNA strands. The crosslinking degree can be increased by increasing the number of phosphorothioate linkages on the polymer chains. It is worth mentioning that the phosphorothioate modification of polymer chains results in increased hydrophobicity of polymer-DNA conjugates, which can also increase the stability of DNA amphiphiles against the dilution. Future improvement of this strategy is to optimize the crosslinking conditions that will give higher crosslinking degree at milder reaction conditions. The chemical structure of crosslinker is another parameter to be examined. We only used the C_6 chain in this work, but other alkyl chains might lead to better crosslinking efficiency. It is also attractive to incorporate stimuli-responsive moiety in the crosslinkers such that the disassembly of crosslinked DNA micelles could be triggered when needed.

4.3.3 Dimerization of DNA amphiphiles by anthracene photodimerization

The previously described crosslinking strategies involve the addition of external crosslinker molecules. We then asked whether the crosslinker moieties themselves can be incorporated directly into DNA amphiphiles. Among many potential candidates, an anthracene, which is a polycyclic molecule consisting of three fused benzene rings, is well known for its [4+4] photocycloaddition to generate eight-membered ring anthracene dimers (Figure 4.5). This property was used to photoligate anthracene-appended DNA strands hybridized on a DNA template by the Jyo group.[25-26] They later applied this strategy to detect a base mismatch.[27-28] In the design of DNA nanostructures, the photoligation was demonstrated in anthracene-functionalized 2'-amino-LNA oligonucleotides to construct covalently-linked higher-ordered DNA constructs.[29] Yu and co-workers used anthracene dimerization to crosslink 2D DNA networks composed of self-complementary three-way DNA junctions.[30]

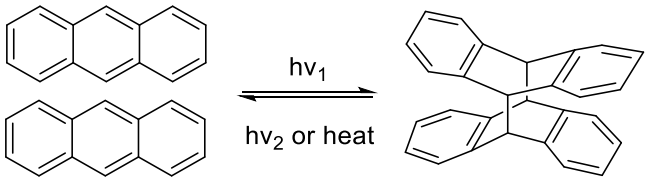

Figure 4.5 | Reversible photodimerization of anthracenes.

As the starting point, we would like to attach one anthracene unit to the 5' termini of DNA amphiphiles by using phosphoramidite chemistry.[30-31] The synthesis of a novel anthracene precursor is outlined in Figure 4.6a. The simplest hydroxyl anthracene derivative is 9-anthracenemethanol; however, it was reported that the cleavage of 9-anthracenemethanol from DNA strand could happen at the I_2 oxidation step in DNA synthesis cycle.[32] Thus, we attached an ethylene glycol spacer to 9-anthracenemethanol to make it less susceptible as a leaving group. Having prepared the anthracene precursor, we synthesized two monodisperse anthracene-appended DNA amphiphiles composed of HE and hexaethylene glycol (HEG) repeats (Figure 4.6b). As a control, Ant-A14 which cannot form micelles was also prepared.

Ant-HE_{12}-A14 and Ant-HE_{12}-HEG-A_{14} assembly in 1xTAMg was carried out by thermal annealing from 95°C to 4°C for 4 hours and examined by non-denaturing agarose gel electrophoresis (AGE). In Figure 4.6c, there was a single band for both Ant-HE_{12}-A14 and Ant-HE_{12}-HEG-A_{14} on the gel. Their electrophoretic mobility was slightly faster than the corresponding DNA amphiphiles without anthracene units, suggesting that anthracene-appended DNA amphiphiles can form micelles. Ant-HE_{12}-A14 assembly was further characterized by AFM and transmission electron microscopy (TEM). In Figure 4.6d, there were spherical structures and some short rods on the mica surface as observed by AFM, which can be further confirmed by TEM (Figure 4.6e). The formation of small rods might be driven by π-π stacking of anthracene units. However, these interactions might not be strong enough to switch the assembly from spherical to cylindrical micelles. This can also be supported by the electrophoretic mobility of Ant-HE_{12}-A14 on the gel, showing that this amphiphile form micelles rather than long fibers.

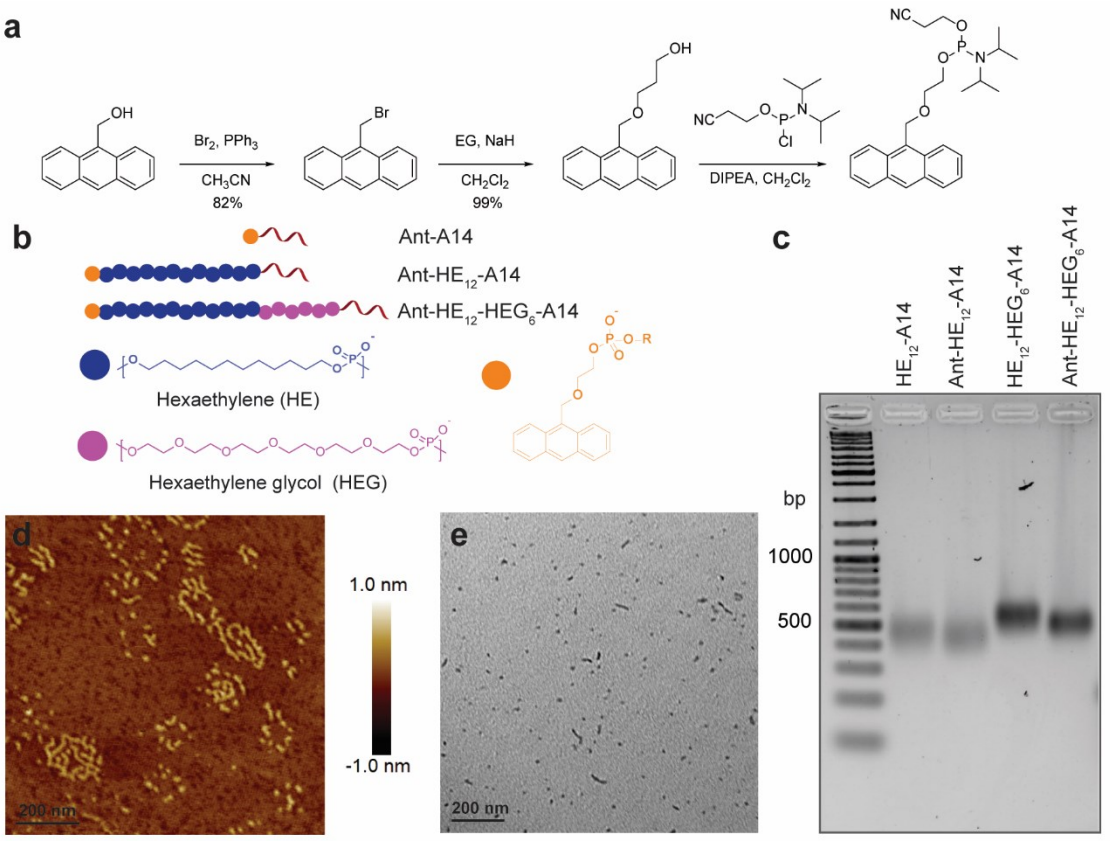

Figure 4.6 | Synthesis and self-assembly of anthracene-appended DNA amphiphiles. a) Anthracene precursor was synthesized in three steps from 9-anthracenemethanol. b) The anthracene-appended DNA amphiphiles were prepared by attaching the anthracene unit to the 5' termini of DNA amphiphiles. c) Non-denaturing AGE (2.5%) shows that both anthracene-

appended DNA amphiphiles could form micelles. Ant-HE_{12}-A14 assembly was further examined by d) AFM and e) TEM, revealing spherical micelles and a minor population of short rods. The length scale bar is 200 nm.

We then carried out the dimerization of anthracene-appended DNA amphiphiles (Figure 4.7a). The anthracene units on Ant-HE_{12}-A14 and Ant-HE_{12}-HEG_6-A14 micelles are expected to increase the dimerization yield due to the possibility of anthracene aggregation inside the hydrophobic core of the micelles. The samples in 1xTAMg were irradiated with 365-nm UV source for 15 minutes at room temperature, then analyzed by denaturing PAGE. Figure 4.7b shows that photoirradiation of Ant-HE_{12}-A14 and Ant-HE_{12}-HEG_6-A14 generated their dimers with the yield of 54% and 72%. We also observed small yields (<15%) in the samples that did not receive photoirradiation. This is likely due to an undesired dimerization that happened during sample handling. It is of note that there is no visible DNA cleavage due to prolonged exposure to UV light. In contrast, there was no visible dimer band for DNA amphiphiles without anthracene unit. Ant-A14 that did not contain a hydrophobic chain did not show a visible dimer band as well. These results suggest that anthracene dimerization is efficient in the presence of confined hydrophobic environments.

To find an optimal irradiation time that will maximize the dimer yield, we examined time-dependent dimerization of Ant-HE_{12}-A14 and Ant-HE_{12}-HEG_6-A14. Figures 4.7c and 4.7d show that dimerization process was very rapid. The dimer yields reached their maximum value in less than 5 minutes, and longer irradiation time did not significantly increase the dimer yields. We also did not observe complete anthracene dimerization within our time points. Interestingly, the dimerization of Ant-HE_{12}-HEG_6-A14 led to a higher yield (~60%) than that of Ant-HE_{12}-A14 (~50%). This might be due to different chain packing modes of HE_{12}-A14 and HE_{12}-HEG_6-A14. We can conclude that the hydrophobic core formation inside the micelles can increase effective concentration of anthracene units, which significantly improve the dimerization efficiency.

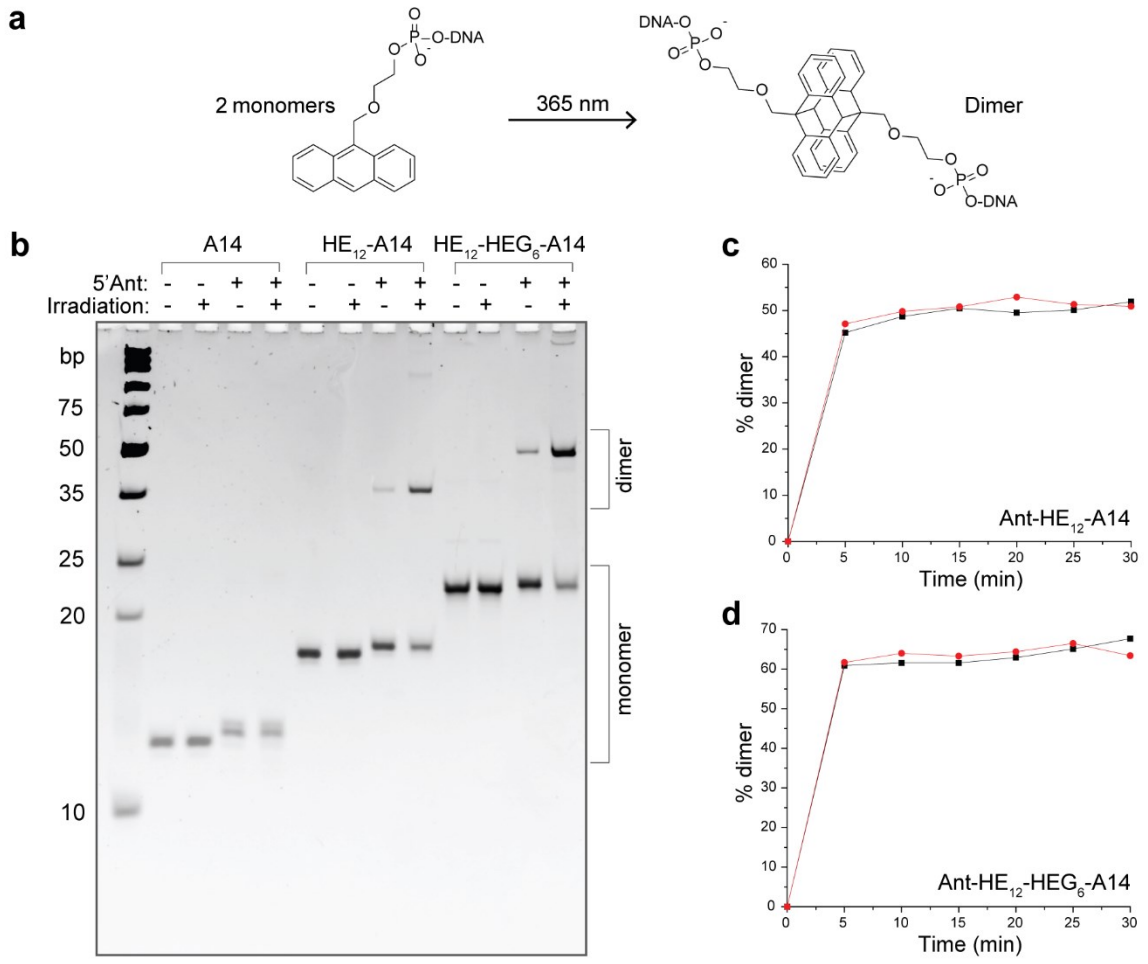

Figure 4.7 | Photodimerization of anthracene-appended DNA amphiphiles. a) Photoirradiation of anthracene-appended DNA amphiphiles with 365-nm UV source can generate anthracene dimers. b) Denaturing PAGE (15%) shows that anthracene dimerization happened efficiently when they were attached to DNA amphiphiles. Time-dependent dimerization of c) Ant-HE_{12}-A_{14} and d) Ant-HE_{12}-HEG_6-A14 indicated fast anthracene dimerization (in <5 minutes). Red and black spheres represent the data sets from two different experiments.

The initial purpose of this study is to increase the stability of amphiphilic DNA nanostructures by covalent crosslinking of their hydrophobic cores using anthracene dimerization. In Chapter 2, the decoration of cube C_4 with HE_{12}-A14 and HE_{12}-HEG_6-A14 led to the formation of monodisperse cube-micelles and cube-ring structures. For cube C_8, C_8/HE_{12}-A14 gave polydisperse aggregates while C_8/HE_{12}-HEG_6-A14 generated well-defined spherical structures.

The assembly of cubes C_4 and C_8 with anthracene-appended DNA amphiphiles was examined by non-denaturing AGE (Figure 4.8b). C_4 assembly with both anthracene-appended DNA

amphiphiles gave higher-order structures, which can migrate through the gel. Similarly, we observed non-penetrating materials in the case of C_8 functionalized with anthracene-appended DNA amphiphiles, suggesting that large structures also formed. There was a resolvable higher-order band in C_8/Ant-HE_{12}-HEG_6-A14, which might be small aggregates. Photoirradiation with 365-nm UV source did not change the band mobility in all cases, implying that there should be no change to the overall assembly morphology. More quantitative estimates of the dimerization were obtained from denaturing PAGE in Figure 4.8a. No dimer band was observed in all structures that had not received photoirradiation. However, a significant dimer amount was generated after photoirradiation. The dimer yield of Ant-HE_{12}-HEG_6-A14 on the cubes was higher than that of Ant-HE_{12}-A14 (Table 4.1).

Table 4.1 | Dimer yield of anthracene-appended DNA amphiphiles decorated on DNA cubes.

Cube	% dimer (repeat# 1)	% dimer (repeat# 2)
C_4/Ant-HE_{12} -A14	71	66
C_4/Ant-HE_{12}-HEG_6-A14	71	77
C_8/Ant-HE_{12} -A14	73	70
C_8/Ant-HE_{12}-HEG_6-A14	76	82

AFM image (Figure 4.8c) of photodimerized C_4/Ant-HE_{12}-A14 reveals aggregates with the size of 30-40 nm in diameter. These were similar in size but had higher polydispersity compared to C_4/HE_{12}-A14.[33] We also observed polydisperse aggregates for photodimerized C_8/Ant-HE_{12}-A14 by AFM (Figure 4.8e). Their diameter was more than 100-150 nm, which was significantly bigger than C_8/HE_{12}-A14 (see Chapter 2). For photodimerized C_4/Ant-HE_{12}-HEG_6-A14, there were relatively monodisperse spherical aggregates (60-70 nm in diameter, Figure 4.8d) whose structures resembled C_4/HE_{12}-HEG_6-A14 which gave doughnut-shaped structures. The photodimerized C_8/Ant-HE_{12}-HEG_6-A14 showed two types of structures on the mica surface as revealed by AFM (Figure 4.8f). The large aggregates (~75 nm in diameter) resembled the spherical structures of C_8/HE_{12}-HEG_6-A14 but were twice in size. The smaller spheres had a diameter of ~20 nm, which could be corresponding to cube monomers. More structural characterization is required to compare the morphology of pre- and post-photodimerized cube/anthracene constructs to examine whether anthracene dimerization can increase the assembly stability.

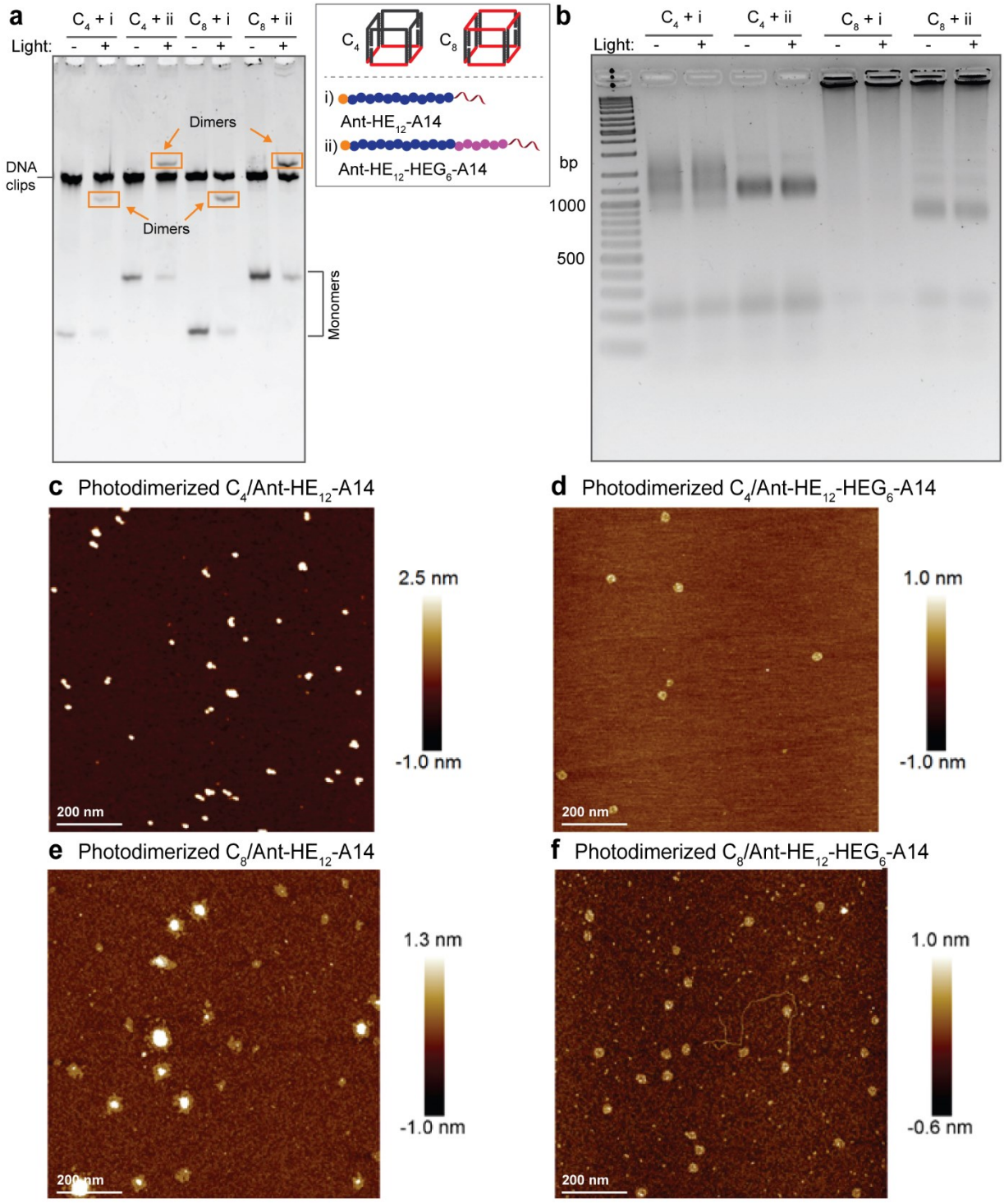

Figure 4.8 | Self-assembly and photodimerization of DNA cube/anthracene constructs. a) Denaturing PAGE (15%) shows that the dimerization of anthracene-appended DNA amphiphiles was very efficiency upon photoirradiation with the 365-nm light source. b) Non-denaturing AGE (2.5%) confirms the structural stability of cube/anthracene constructs after photoirradiation. c-f) Photodimerized assembly products were further characterized by AFM. The length scale bar is 200 nm.

Future work of this strategy is to incorporate multiple anthracene units (Figure 4.9) to further lock the hydrophobic chains. It was also reported that photoligation efficiency depends strongly on the substitution position on anthracene unit, where 2-substituted anthracene showed higher reactivity than 9-substituted anthracene.[26] This could provide a basis to improve the dimerization yields. Thus, the anthracene dimerization could be extended to increase the product stability that can aid more accurate structural characterization. This is also useful in the biomedical applications of these structures as they will be more resistant to the dilution and low-salt environments, which are challenging barriers. Anthracene dimerization can also introduce a stimuli-responsive mechanism in these structures such that light can be used to disassemble them.

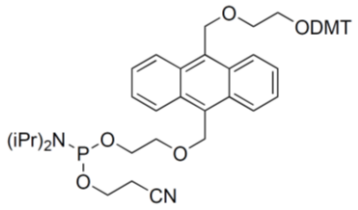

Figure 4.9 | Proposed anthracene precursor for internal modifications on DNA amphiphiles.

4.3.4 Hydrophobic modification of phosphorothioated DNA by *S*-alkylation

The reactivity of the phosphorothioate backbone provides an opportunity for site-specific functionalization of DNA. The Howorka group attached multiple ethyl groups on phosphorothioated DNA by using iodoethane to construct hydrophobic DNA nanopores that can span lipid bilayers.[22, 34] Inspired by this, we then asked whether it is possible to attach longer and more hydrophobic alkyl chains on phosphorothioated DNA. This will be an alternative method to prepare DNA amphiphiles. Two alkylating reagents (Figure 4.10) were used: *N*-hexyl-2-iodoacetamide (C_6-I) and *N*-dodecyl-2-iodoacetamide (C_{12}-I). As these molecules have low water solubility, we sought to perform the *S*-alkylation in an organic solvent to increase the conjugation yield by employing the surfactant approach reported by Liu *et al*. In their approach, a cationic surfactant, didodecyldimethylammonium bromide (DDAB), can electrostatically associate to phosphate backbones on DNA strands, resulting in the precipitation of DNA/surfactant complex from water. The isolated DNA/surfactant complexes show high solubility in DMF and THF, allowing the functionalization of DNA strands in organic solvents (Figure 4.10).[35]

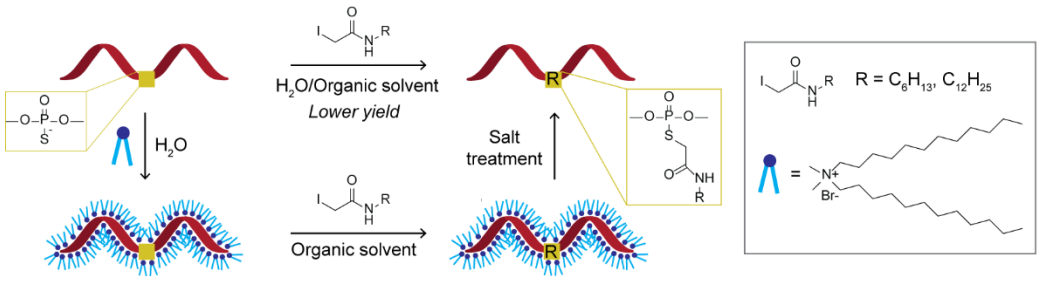

Figure 4.10 | Surfactant approach for *S*-alkylation of phosphorothioated DNA. The surfactant DDAB can form water-insoluble complexes with phosphorothioated DNA. The alkylation of DDAB/DNA complexes can be carried out in DMF. The alkylated product can be collected after the salt treatment to remove DDAB.

To perform the *S*-alkylation, the dried DDAB complex of A20-1PS, which is a 20-mer DNA containing a single phosphorothioate modification, was mixed with C_6-I (50 equivalents) in DMF. The reaction was kept at room temperature for 24 hours and analyzed by RP-HPLC (Figure 4.11a), giving a yield of 54%. An attempt to improve the yield by increasing the reaction temperature to 37ºC and using 100 equivalents of C_6-I resulted in slightly improved yield (59%) but with increased by-product formation. In the case of A20-2PS containing 2 phosphorothioate backbones (Figure 4.11b), there were two main species corresponding to partial (43%) and full alkylated products (36%). In addition to the alkylation efficiency, monoalkylated A20-2PS formation could also be a result of the presence of monosulfurized DNA in the starting materials due to an incomplete sulfurization of A20-2PS during the oxidation step, which cannot be easily isolated by gel electrophoresis. We further increase the length of an alkyl chain from 6 carbons to 12 carbons (Figure 4.11a). The alkylation of A20-1PS with C_{12}-I gave the yield of 58%.

The sample handling after the reaction was also important to recover the alkylated products. In Figure 4.11a, the intensity of A20-1PS/C_{12} was much lower than that of A20-1PS/C_6 although the same amounts of A20-1PS were used. We hypothesized that the increased hydrophobicity of alkylated A20-1PS could be a major issue as they can hydrophobically interact with the surfactant DDAB, resulting in a separation difficulty. In the protocol reported by Liu *et al.*, a saturated NaCl solution was added to the reaction mixture such that excess sodium ions can displace DDAB molecules that bound to DNA strands and induce their decomplexation. The solvent was then evaporated, followed by an addition of water. In this step, both Na^+-coated DNA and DDAB will remain soluble in water while the organic molecules will precipitate. DNA strands can then be

recovered by filtering out the precipitates and further purifications.[35] However, in our system, the association between DDAB and alkylated phosphorothioated DNA may lead to the loss of materials upon filtration and lower recovery yield.

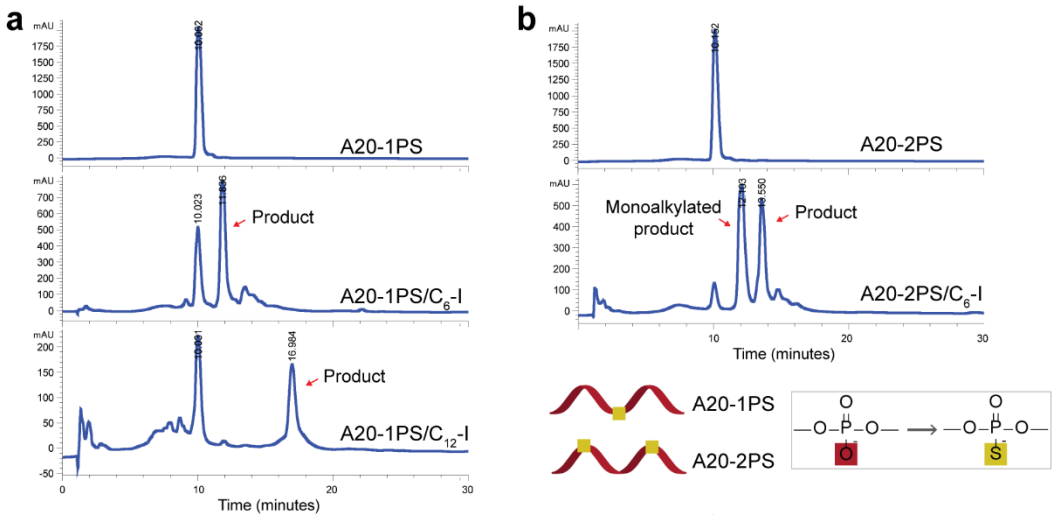

Figure 4.11 | HPLC chromatograms of *S*-alkylated phosphorothioated DNA. The samples were run on a gradient of 3-50% acetonitrile in triethylammonium acetate buffer (TEAA, pH 7) for 30 minutes. The signal was monitored at 260 nm.

We examined the use of $NaPF_6$ as an alternative for NaCl treatment. Unlike chloride ions, the electrostatic interactions between DDAB and hexafluorophosphate ions can create a less hydrophilic ion-pair and induce DDAB precipitation from aqueous solution. After the reactions, the mixture was dried and treated with $NaPF_6$. We obtained a good recovery of alkylated A20-1PS with C_6-I and C_{12}-I; however, lower recovery was still obtained in the case of A20-2PS. The peaks on HPLC chromatograms were also broadened, which is probably due to the presence of remaining DDAB. This makes it more difficult to isolate the product. Thus, the surfactant strategy gives higher alkylation yields but results in inefficient product recovery, particularly for long alkyl chains. One of the possible solutions is to screen the salt-treatment conditions, for instance, at a higher temperature, which might be able to disrupt the interactions between DDAB and alkylated DNA. A chemical additive such as urea can also be added to further denature hydrophobic interactions between DDAB and alkylated DNA.[36]

Finally, we performed a hybridization experiment between A20-1PS/C_6 and its complementary strands (A20') to examine the effect of *S*-alkylation on the stability of DNA strand. The strands were incubated in 1xTAMg and 1xPBS at 37°C for 40 minutes and analyzed by non-denaturing PAGE. In Figure 4.12a, the band of A20-1PS/C_6 showed lower electrophoretic mobility than A20-1PS, suggesting the presence of C_6-alkyl chain. The duplexes of A20-1PS/C_6:A'20 gave a single band in both 1xTAMg and 1xPBS, which were similar to that of A20-1PS:A'20. This indicates that the hybridization of alkylated DNA was not affected much by the presence of C_6-alkyl chain. To further study the stability of the duplexes, we carried out thermal denaturation analysis (Figure 4.12b).

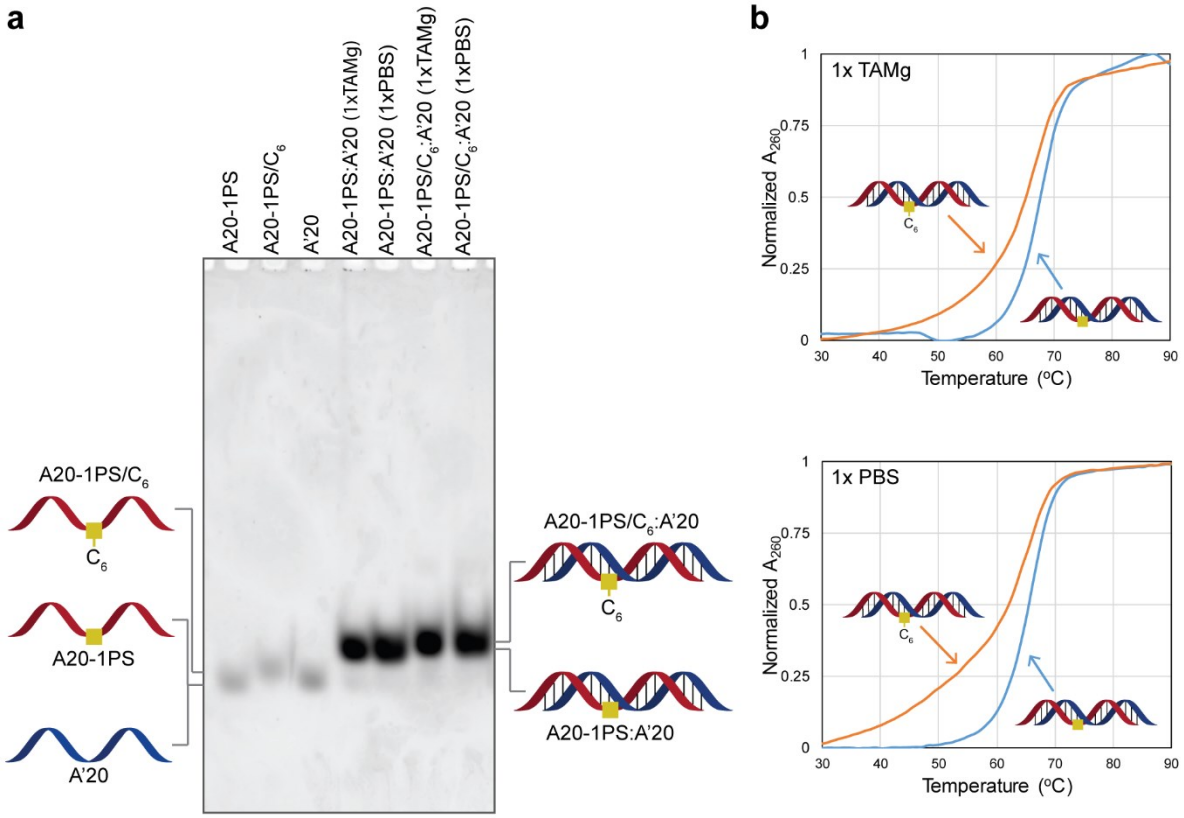

Figure 4.12 | Hybridization and stability of alkylated phosphorothioated DNA. a) Non-denaturing PAGE (6%) shows that *S*-alkylation of phosphorothioated DNA did not affect their hybridization property. b) Thermal denaturation indicated that the presence of C_6 chain slightly destabilized the duplexes of alkylated phosphorothioate DNA and its complementary strand.

Table 4.2 shows that *S*-alkylation of A20-1PS slightly destabilized the duplexes and lowered the hybridization cooperativity.

Table 4.2 | Thermal denaturation analysis of phosphorothioated DNA duplexes.

Duplexes	Buffers	T_m (°C)	FWHM (°C)
A20-1PS:A'20	TAMg	67.6	7.3
	PBS	65.7	7.2
A20-1PS/C_6:A'20	TAMg	66.0	8.8
	PBS	64.5	8.7

Therefore, the intrinsic reactivity of sulfur atom of phosphorothioate backbone could be exploited for site-specific attachment of alkyl chains. The future work of this strategy is to improve the alkylation yield and to increase the number of alkylation sites. However, one of the issues associated with this strategy is that the hydrolysis of phosphorothioate triesters can happen at pH>8, resulting in the loss of conjugation.[16-17, 37] The Gothelf group addressed this by using bromoethylammonium bromide as the precursor. The subsequent rearrangement can occur in the presence of a non-nucleophilic base to yield *N*-(2-mercaptoethyl)phosphoramidite, which is more stable at high pH.[37] The free thiol group can also be used as a site-specific functionalization site for maleimide-containing molecules via Michael addition reaction (Figure 4.13).[38]

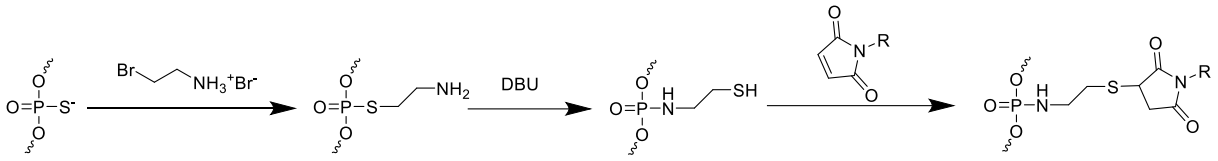

Figure 4.13 | Alternative strategy for functionalizing phosphorothioate backbone. Adapted with permission from reference 38 (RSC, 2008).

4.4 Conclusions

We have demonstrated the applicability of three chemical crosslinking strategies in the stability improvement of amphiphilic DNA nanostructures. The first two strategies are based on the addition of external linkers to covalently join hydrophobic polymer chains of DNA amphiphiles

which were modified with reactive functional moieties. The amide bond formation was first employed to dimerize two amino-modified DNA amphiphiles by using alkyl-bisNHS linkers. We found that an efficient dimerization was achieved inside the hydrophobic micellar cores. Alternatively, the reactivity of sulfur atoms in the P-S bonds was exploited as the crosslinking sites in phosphorothioated DNA amphiphiles by using alkyl-bis(iodoacetamide) linkers. We obtained high crosslinking degree, which will be beneficial as a low-cost strategy to crosslink DNA micelles for downstream applications. Preliminary studies to assess reactivity inside DNA cages showed that the crosslinking induces the aggregation of amphiphilic DNA nanostructures. To avoid the addition of external linkers, DNA amphiphiles were functionalized with anthracene units which can undergo photodimerization, and high dimerization efficiency could be rapidly achieved. Future work on these strategies will involve the incorporation of multiple crosslinking sites on DNA amphiphiles, the optimization of crosslinking conditions, and the stability study of crosslinked DNA amphiphiles in biologically relevant environments. Thus, we anticipate that these strategies will be beneficial to the design of amphiphilic DNA materials for their biomedical applications.

We also examined the hydrophobic modification of phosphorothioated DNA by using alkyl-iodoacetamide reagents with the aid of surfactant molecules to increase the conjugation yield of long, hydrophobic alkyl chains to a DNA strand. This provides an alternative low-cost, easily accessible method for site-specific functionalization of DNA strands.

4.5 Experimental Section

4.5.1 Chemicals

The reagents and buffers are as detailed in Section 2.5.1 in Chapter 2 with the following additions. Fmoc-Amino-DMT C3-CED phosphoramidite (NH_2, cat# CLP-1661) and 2-cyanoethyl *N,N*-diisopropylchlorophosphoramidite chloride (cat# RN-1505) were obtained from ChemGenes Corporation. Sulfurizing reagent II was purchased from Glen Research. Sebacic acid bis(*N*-hydroxysuccinimide ester), DDAB, sodium hexafluorophosphate and other chemicals for the synthesis of alkylating reagents and anthracene precursor were purchased from Sigma-Aldrich. 10x PBS buffer (pH 7.4) was purchased from BioShop Canada Inc.

4.5.2 Instrumentation

Instrumentation is as detailed in Section 2.5.2 in Chapter 2 with the following additions. ^{1}H NMR was recorded on 500 MHz AV500 equipped with a 60 position SampleXpress sample changer (Bruker) and 300 MHz Varian Mercury equipped with an SMS-100 sample changer (Agilent). Anthracene photodimerization was performed by using 365-nm Spectroline ENF-240C UV lamp (Spectronics Corporation). High-resolution mass spectra were obtained from Exactive Plus Orbitrap Mass Spectrometer (Thermo Scientific)**.**

4.5.3 Solid-phase synthesis and purification

DNA synthesis and purification are as detailed in Section 2.5.3 in Chapter 2. For phosphorothioate modification, 0.05 M solution of 3-((*N,N*-dimethylaminomethylidene)amino)-3H-1,2,4-dithiazole-5-thione in (6:4) pyridine/acetonitrile was used in the oxidation step. The coupling of Fmoc-Amino-DMT C-3 CED phosphoramidite and anthracene phosphoramidite were performed in a glove box, followed by capping, oxidation and deblocking steps on the synthesizer. For HPLC purification, amino-modified DNA amphiphiles and DNA-anthracene conjugates were run on Hamilton PRP-C18 column by using elution gradient containing two mobile phases (acetonitrile and TEAA).

In addition, we observed that the purification of amino-modified DNA amphiphiles by denaturing PAGE generated the impurities with an additional mass of ~43 Da. This impurity is likely due to the reaction of the amino group with isocyanate, which can potentially form as the gel was heated during the run. The formation of isocyanate and ammonium at high temperature from the hydrolysis of urea is well-known in literature[39-40] and can induce chemical modification of protein during protein analysis which involves the use of urea as the denaturant[41-42]. Therefore, it is necessary to avoid the purification techniques involving urea.

4.5.4 DNA sequences and characterization

The sequences of DNA clips required for cube assembly are listed in Section 2.5.4 in Chapter 2. The sequences of unmodified DNA and DNA amphiphiles are listed in Table 4.3.

Table 4.3 | Sequences of functionalized DNA amphiphiles (X = HE, 6 = HEG, NH_2 = Amino C-3 CED, Ant = anthracene, PS = phosphorothioate linker).

Strand	Sequence (5'→3')
A14	TTTTTCAGTTGACCATATA
NH_2-A14	NH_2-TTTTTCAGTTGACCATATA
NH_2-HE-A14	NH_2-X TTTTTCAGTTGACCATATA
NH_2-HE_{12}-A14	NH_2-XXXXXXXXXXXX TTTTTCAGTTGACCATATA
NH_2-HE_6-A14	NH_2-XXXXXX TTTTTCAGTTGACCATATA
Ant-A14	Ant-TTTTTCAGTTGACCATATA
Ant-HE_{12}-A14	Ant-XXXXXXXXXXXX-TTTTTCAGTTGACCATATA
Ant-HE_{12}-HEG_{12}-A14	Ant-XXXXXXXXXXXX-666666-TTTTTCAGTTGACCATATA
HE_6(PS)-A14	XX-*PS*-XX-*PS*-XX-*PS*-TTTTTCAGTTGACCATATA
A20	GAGCAGTTGACCATATAGGA
A20-1PS	GAGCAGTTGA-*PS*-CCATATAGGA
A20-2PS	GAG-*PS*-CAGTTGACCATATA-*PS*-GGA
A'20	TCCTATATGGTCAACTGCTC

DNA amphiphiles were purified by RP-HPLC. Table 4.4 shows the retention times of all DNA amphiphiles. The strands were further analyzed by LC-ESI-MS in negative ESI mode, which is summarized in Table 4.4.

Table 4.4 | Characterization of functionalized DNA amphiphiles.

Strand	Retention time[a]	Calculated mass[d]	Experimental mass[d]
A14	n/a	5764.99	5765.0000
NH_2-A14	10.330[a]	5918.01	n/a
NH_2-HE-A14	13.142[a]	6182.16	6182.0313
NH_2-HE_6-A14	23.442[a]	7502.90	7502.7344

Strand	Retention time[a]	Calculated mass[d]	Experimental mass[d]
NH_2-HE_{12}-A14	19.907[b]	9087.80	9087.5000
Ant-A14	22.132[c]	6079.06	6079.0938
Ant-HE_{12}-A14	21.471[b]	9248.85	9253.5674
Ant-HE_{12}-HEG_6-A14	21.323[b]	11313.59	11318.8496
HE_6(PS)-A14	26.224[a]	7397.82	7397.7734
A20-1PS	10.062[a]	6203.06	6203.0313
A20-2PS	10.152[a]	6219.04	6218.9688 (75%), 6203.0813 (1 incomplete sulfurization)

[a] Retention time (in minutes) was determined from RP-HPLC with the gradient of 3-50% acetonitrile for 30 minutes
[b] Retention time (in minutes) was determined from RP-HPLC with the gradient of 3-70% acetonitrile for 30 minutes
[c] Retention time (in minutes) was determined from RP-HPLC with the gradient of 3-30% acetonitrile for 30 minutes
[d] mass unit is in g/mole.

4.5.5 Synthesis of small molecules

Synthesis of 2-(9-anthracenylmethoxy)ethanol phosphoramidite:

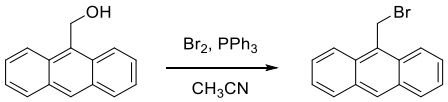

The procedure was adapted from the report by Aathimanikandan *el al*.[43] A solution of PPh_3 (2.6 g, 10 mmol, 1 equiv.) in 20 mL of anhydrous acetonitrile was flushed with argon for 20 minutes, followed by dropwise addition of Br_2 (0.5 mL, 10 mmol, 1 equiv.). Then, 9-anthracenemethaol (2.5 g, 12 mmol, 1.2 equiv.) was added, and the solution was stirred at room temperature for 18 hours and refrigerated for 23 hours. After the mixture was kept in the freezer for additional 30 minutes, it was filtered, washed with 3 mL of cold acetonitrile and recrystallized from $CHCl_3$ to obtain yellow solid as the product (2.7 g, 82% yield)

1H NMR (300 MHz, $CDCl_3$) δ 8.51 (s, 1H), 8.31 (d, 2H), 8.05 (d, 2H), 7.81-7.40 (m, 4H), 5.56 (s, 2H)

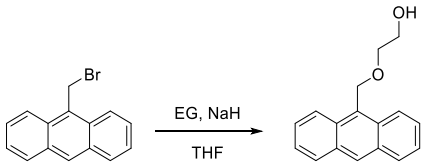

A solution of NaH (60% purity, 0.44 g, 18 mmol, 5 equiv.) in 20 mL of hexane was stirred and flushed with argon for 30 minutes. After decanting hexane, the mixture was cooled in an ice bath, followed by slow addition of ethylene glycol (4.1 mL, 74 mmol, 20 equiv.) under argon flow. The mixture was allowed to warm up to room temperature. Then, 9-bromomethylanthracene (1 g, 3.7 mmol, 1 equiv.) in 10 mL of anhydrous THF was added, and the mixture was stirred at room temperature. After 3 days, the solvent was evaporated. The crude product was added 40 mL of H_2O and extracted with 4x40 mL of Et_2O. The organic phase was combined and dried over anhydrous $MgSO_4$. After evaporating the solvent, orange crystals were obtained as the product (924 mg, 99%).

1H NMR (300 MHz, $CDCl_3$) δ 8.48 (s, 1H), 8.40-8.36 (d, 2H), 8.03 (d, 2H), 7.62-7.40 (m, 4H), 5.55 (s, 2H), 3.85-3.72 (m, 4H)

HRMS EI m/z calculated for $C_{17}H_{16}O_2Na$ $[M+Na]^+$: 252.31, found: 275.1043.

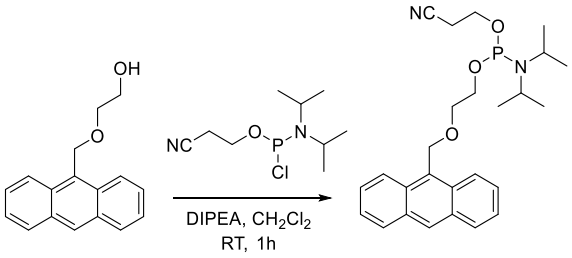

A vial of 2-(9-anthracenylmethoxy)ethanol (5 mg, 0.02 mmol, 1 equiv.) was dried under vacuum for 1 hour, and transferred to the glove box. Then, anhydrous CH_2Cl_2 (200 µL), DIPEA (2.6 µL, 0.02 mmol, 1 equiv.) and 2-cyanoethy-*N,N*-diisopropylchlorophosphoramidite chloride (4.3 µL, 0.02 mmol, 0.9 equiv.) were added. The mixture was stirred at room temperature for 1 hour and used for the coupling with DNA without further purification.

Synthesis of *N,N*'-hexamethylene-bis(iodoacetamide):

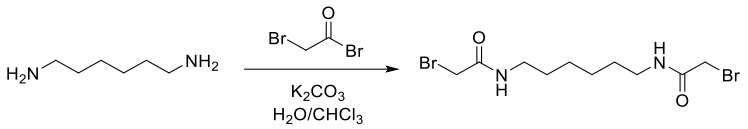

The synthesis of N,N'-hexamethylene-bis(bromoacetamide) was adapted from the report by Hoque *et al*.[23] To a solution of hexamethylenediamine (1.16 g, 10 mmol, 1 equiv.) in 30 mL of $CHCl_3$ was added K_2CO_3 (4.15 g, 30 mmol, 3 equiv.) dissolved in 30 mL of H_2O. The mixture was placed in an ice bath. Bromoacetyl bromide (2.6 mL, 30 mmol, 3 equiv.) was dissolved in 30 mL of CHC_3 and added slowly to the reaction mixture over a period of 40 minutes. The mixture was stirred at room temperature for 18 hours, filtered, and extracted with 2x30 mL of $CHCl_3$. The organic phase was combined, washed with 2x50 mL of H_2O and 50 mL of brine solution, and dried over anhydrous $MgSO_4$. The solvent was evaporated under reduced pressure to obtain white solids as the product (430 mg, 12% yield).

1H NMR (500 MHz, $CDCl_3$) 6.54 (s, 2H), 3.91 (s, 4H), 3.32 (q, 4H), 1.58 (m, 4H), 1.44 – 1.35 (m, 4H)

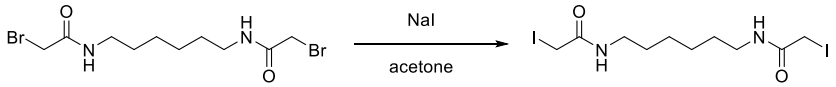

The iodo conversion procedure was adapted from the report by Elmehriki *et al*.[24] To a solution of *N,N'*-hexamethylene-bis(bromoacetamide) (430 mg, 1.2 mmol, 1 equiv.) in 15 mL of acetone was added NaI (1.08 g, 7.2 mmol, 6 equiv.). The mixture was protected from light and stirred at room temperature for 18 hours. After evaporating the solvent, 10 mL of 10% Na_2SO_3 in H_2O was added to the mixture resulting in precipitation, which was collected by filtration to obtain white power as the product (80 mg, 15% yield).

ESI MS EI m/z calculated for $C_{10}H_{18}I_2N_2O_2$ $[M+Na]^+$: 475.07, found: 474.95.

Synthesis of hexyl-2-iodoacetamide:

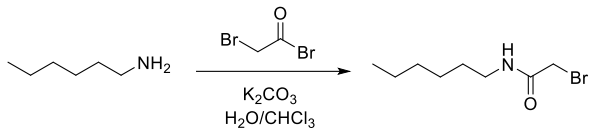

The procedure was adapted from the report by Elmehriki *et al*.[24] To a solution of hexylamine (661 µL, 5 mmol, 1 equiv.) in 15 mL $CHCl_3$ was added K_2CO_3 (2.76 g, 20 mmol, 4 equiv.) dissolved in 15 mL H_2O. The mixture was placed in an ice bath. Bromoacetyl bromide (653 µL, 7.5 mmol, 1.5 equiv.) was dissolved in 15 mL $CHCl_3$, and added slowly to the reaction mixture over a period of 20 minutes. The mixture was stirred at room temperature for 4 hours and washed with 5x25 mL of H_2O and 25 mL of brine solution. The organic phase was dried over anhydrous $MgSO_4$ and evaporated under reduced pressure to obtain white solids as the product (1.11 g, 98% yield).

^{1}H NMR (500 MHz, $CDCl_3$) δ 6.50 (s, 1H), 3.90 (s, 2H), 3.30 (q, 2H), 1.59 – 1.51 (m, 2H), 1.40 – 1.27 (m, 6H), 0.96 – 0.88 (m, 3H).

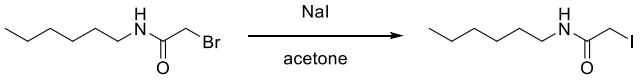

The halogen exchange of hexyl-2-bromoacetamide to hexyl-2-iodoacetamide was performed similarly to the second step in the synthesis of *N,N'*-hexamethylene-bis(iodoacetamide) starting from hexyl-2-bromoacetamide (444 mg, 2 mmol, 1 equiv. in 12.5 mL of acetone) and NaI (900 mg, 6 mmol, 3 equiv.). Yellow solid was obtained as the product (479 mg, 89% yield).

^{1}H NMR (500 MHz, $CDCl_3$) δ 6.21 (s, 1H), 3.71 (s, 2H), 3.27 (q, 2H), 1.58 – 1.49 (m, 2H), 1.40 – 1.24 (m, 6H), 0.94 – 0.87 (m, 3H).

ESI MS m/z calculated for $C_8H_{16}INO$ $[M+Na]^+$: 292.03, found: 292.0169.

Synthesis of dodecyl-2-iodoacetamide:

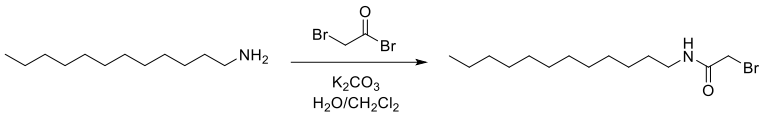

The synthesis of deodecyl-2-bromoacetamide was performed similarly to the synthesis of hexyl-2-bromoacetamide starting from dodecylamine (1.15 mL, 5 mmol, 1 equiv. in 20 mL of CH_2Cl_2), K_2CO_3 (1.02 g, 7.5 mmol, 1.5 equiv. in 20 mL of H_2O) and bromoacetyl bromide (655 µL, 7.5 mmol, 4 equiv. in 15 mL of CH_2Cl_2). The mixture was stirred at room temperature for 24 hours. White solid was obtained as the product (1.56 g, 96% yield).

^{1}H NMR (500 MHz, $CDCl_3$) δ 6.53 (s, 1H), 3.89 (s, 2H), 3.29 (q, 2H), 1.56 (q, 2H), 1.33-1.27 (m, 18H), 0.89 (t, 3H).

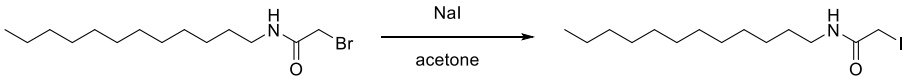

The halogen exchange of dedecyl-2-bromoacetamide to dodecyl-2-iodoacetamide was performed similarly to the second step in the synthesis of *N,N'*-hexamethylene-bis(iodoacetamide) starting from dodecyl-2-bromoacetamide (918 mg, 3 mmol, 1 equiv. in 20 mL acetone) and NaI (1.35 g, 9 mmol, 3 equiv.). White solid as the product (997 mg, 93% yield).

^{1}H NMR (500 MHz, $CDCl_3$) δ 6.17 (s, 1H), 3.72 (s, 2H), 3.32 – 3.24 (q, 2H), 1.55 (q, 2H), 1.38 – 1.26 (m, 18H), 0.90 (t, 3H).

ESI MS m/z calculated for $C_{14}H_{28}INO$ $[M+Na]^+$: 376.12, found: 376.11088.

4.5.6 Dimerization of DNA amphiphiles by amide bond formation

To prepare DNA micelles, 100 µL of 5 µM DNA amphiphiles in 1xTAMg was thermally annealed (95 to 4ºC in 1 hour). Separately, 10 mM of C_{10}-bisNHS in DMSO was prepared. To 10 volumes of the DNA amphiphile was quickly added 1 volume of C_{10}-bisNHS, and the mixture was gently shaken for 16 hours at room temperature. After the reaction, 10 µL of the crude mixture was mixed with 10 µL 8M urea and loaded on denaturing PAGE (15%). The gel was run at 250 V for 30 minutes then 500 V for 1 hour with 1xTBE as the running buffer. The gel was stained with GelRed and imaged.

The conjugation yield refers to the yield of DNA-amphiphile dimers linked via C_{10}-bisamide and was calculated from the band intensity. The crude mixture was also analyzed by RP-HPLC (Figure 4.14a), and the conjugation yield was calculated from the area-under-the-curve ratio between the product peak and the sum of starting material and product peak. The fractions collected from HPLC analysis were then analyzed by denaturing PAGE (Figure 4.14b) and LC-ESI-MS in negative ESI mode (Table 4.5).

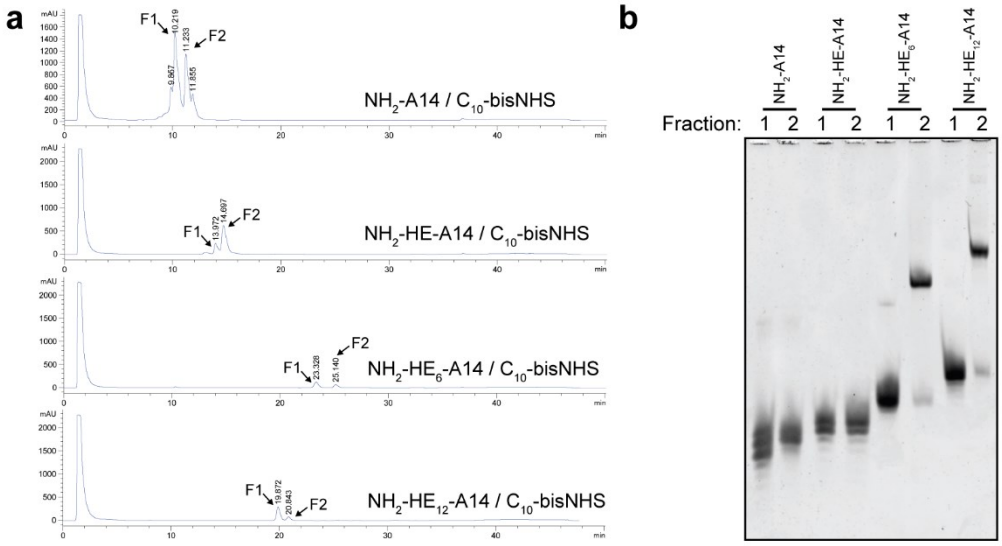

Figure 4.14 | Analysis of the dimerization of amino-modified DNA amphiphiles. a) RP-HPLC was used to isolate the reaction products. The gradient of 3-50% acetonitrile was used for all reactions, except NH_2-HE_{12}-A14/C_{10}-bisNHS where 3-70% acetonitrile was used. b) Denaturing PAGE (15%) shows the purity of individual fractions obtained from RP-HPLC in panel a.

Table 4.5 | Characterization of the dimerization of amino-modified DNA amphiphiles.

Strands	Fraction[a]	Found mass[b]	Interpretation from the mass
NH_2-HE-A14	1	6368.3333	Monomer with C_{10}-bisNHS
		6471.8021	Monomer with C_{10}-bisNHS (tris conjugated)
	2	6367.2500	Monomer with C_{10}-bisNHS
		6471.5000	Monomer with C_{10}-bisNHS (tris conjugated)
NH_2-HE_6-A14	1	7689.8750	Monomer with C_{10}-bisNHS
		7793.0000	Monomer with C_{10}-bisNHS (tris conjugated)
	2	15178.8125	Dimer
		15346.7917	-

Strands	Fraction[a]	Found mass[b]	Interpretation from the mass
NH_2-HE_{12}-A14	1	9091.7078	Unreacted monomer
	2	9091.7531	Unreacted monomer
		18350.3601	Dimer

[a] Fraction in RP-HPLC chromatograms in Figure 4.14.
[b] mass unit is in g/mole.

For amphiphilic DNA nanostructure, cube C_8 (125 nM, 1AA+2AA+3AA+4AA,) and NH_2-HE_6-A14 (1.5 μM) were mixed in 100 μL of 1xTAMg buffer. The sample was heated at 95ºC for 5 minutes, at 80ºC for 3 minutes, cooled to 60ºC (2 min/ºC), and slowly cooled to 4ºC (3 min/ºC). Then, 10 μL of 1 mM C_{10}-bisNHS in DMSO was quickly added to the DNA samples. The mixture was stirred at room temperature for 20 hours. The crosslinked products were analyzed by non-denaturing PAGE, where a 10-μL aliquot of the samples was mixed with 2 μL of glycerol mix (7:1 glycerol/H_2O) and loaded on the gel with 1xTAMg as the running buffer. The gel was run at 250 V for 2.5 hours and stained with GelRed.

4.5.7 Crosslinking of phosphorothioated DNA amphiphiles by *S*-alkylation

To prepare DNA micelles, a solution of 5 μM HE_6(PS)-A14 in 1xTAMg or 1xPBS were thermally annealed. Then, 2.5 mM C_6-2I in DMSO was added to the DNA solution at appropriate equivalents. Additional DMSO was added to bring the volume of total DMSO to 1:10 v/v DMSO/H_2O. The reactions were incubated at 37ºC for 2 days, mixed with an equal volume of 8 M urea and analyzed on denaturing PAGE (15%).

To assemble the cubes decorated with HE_6(PS)-A14, equimolar amounts (1.25 pmole) of all required clips (Cube C_4 = 1AB+2AB+3AB+4AB, C_8 = 1AA+2AA+3AA+4AA, final concentration = 125 nM) and HE_6(PS)-A14 (750 nM for C_4 and 1.5 μM for C_8) were mixed in 10 μL of 1xTAMg buffer. The sample was thermally annealed from 95 to 4ºC in 4 hours. To 9 volumes of DNA samples was added 1 volume of C_6-2I in DMSO at appropriate concentrations. The samples were incubated at 37ºC overnight and analyzed by non-denaturing PAGE (5%).

4.5.8 Photodimerization of anthracene-appended DNA amphiphiles

To prepare DNA micelles, 4 μL of 5 μM anthracene-appended DNA amphiphiles in 1xTAMg buffer was thermally annealed (95 to 4°C in 4 hours). The samples in the plastic PCR tubes were placed in a plastic petri dish. The 365-nm UV lamp was then placed on top of the petri dish with the sample-lamp distance of ~1 cm. Photoirradiation was carried out for 15 minutes, except time-dependent photodimerization experiments. To determine the photodimerization yields, the samples were mixed with 6 μL of H_2O and 10 μL of 8M urea and analyzed by denaturing PAGE (15%). The photodimerization yields were calculated from the band intensity of the dimer band in comparison to the intensity sum of dimer and monomer bands. Alternatively, to examine the assembly in solution, 1.5 μL of 10 μM anthracene-appended DNA amphiphiles was prepared in 1xTAMg buffer and thermally annealed. The samples were mixed with 8.5 μL 1xTAMg and 2 μL glycerol mix, and loaded on non-denaturing AGE (2.5%). The gel was run at 80 V for 2.5 hours with 1xTAMg as the running buffer and stained with GelRed and imaged.

To assemble the cubes decorated with anthracene-appended DNA amphiphiles, the equimolar amounts (1.25 pmole) of all required clips (Cube C_4 = 1AB+2AB+3AB+4AB, C_8 = 1AA+2AA+3AA+4AA, final concentration = 125 nM) and anthracene-appended DNA amphiphiles (750 nM for C_4 and 1.5 μM for C_8) were mixed in 10 μL of 1xTAMg buffer. The sample was thermally annealed from 95 to 4°C in 4 hours. The samples were then irradiated with 365-nm UV source for 15 minutes and analyzed by denaturing PAGE (15%) and non-denaturing AGE (2.5%).

4.5.9 Hydrophobic modification of phosphorothioated DNA by *S*-alkylation

To 0.5 mM solution of phosphorothioated DNA in H_2O was added 100 equivalents of 5 mM DDAB in H_2O (5 equivalents per one nucleotide). The mixtures became cloudy right after vortexing. To collect the DNA/surfactant complex, the mixtures were centrifuged at 21.1 G at room temperature for 20 minutes, and the supernatant was decanted to remove excess DDAB. The white pellets were frozen in liquid N_2 and dried under vacuum by freeze dryer overnight.

To perform the *S*-alkylation, the white pellet (20 nmole with respect to DNA) was dissolved in 50 μL of DMF. The alkylating reagent (25-200 equivalents per one phosphorothioate linker)

was dissolved in 450 µL of DMF and added to the DNA/surfactant mixture to achieve final DNA concentration of 40 µM. The reaction was incubated at room temperature or 37ºC for 1 day. To remove the surfactant, two methods were used: 1) 150 µL of saturated NaCl solution was added, and the mixture was stirred at room temperature for 2-3.5 hours. The solvent was evaporated under reduced pressure to obtain white/yellow solid. Then, 500 µL H_2O was added, and the mixture was centrifuged and filtered to remove precipitates. 2) 500 µL of 5 mM $NaPF_6$ was added, and the mixture was stirred at 37ºC for 2-3.5 hours. The mixture was directly centrifuged and filtered to removed precipitates. In both cases, the filtrate was then analyzed by RP-HPLC and LC-ESI-MS in negative ESI mode (Table 4.6)

Table 4.6 | *S*-alkylation yields of phosphorothioated DNA.

Strand	Retention time[a]	Calculated mass[b]	Experimental mass[b]
A20-1PS/C_6	11.835	6344.18	6344.1250
A20-1PS/C_{12}	16.984	6428.27	6428.3125
A20-2PS/1C_6	12.103	6360.16	6344.1250
A20-2PS/2C_6	13.550	6501.27	6501.1250

[a] Retention time (in minutes) was determined from RP-HPLC with the gradient of 3-50% acetonitrile for 30 minutes
[b] mass unit is in g/mole.

For the hybridization experiment, 50 pmole of each strand was combined in 10 µL of 1xTAMg or 1xPBS and incubated at 37ºC for 40 minutes. The samples were analyzed on non-denaturing PAGE (6%). To study the thermal denaturation, 400 pmole of each strand was combined in 100 µL of 1xTAMg or 1xPBS and thermally annealed from 95ºC to 4ºC for 1 hour. Then, 100 µL of the sample was transferred to a quartz cuvette, and few drops of silicone oil were added on top. The absorbance at 260 nm was monitored in response to a temperature change. The temperature was increased from 25ºC to 95ºC with 1ºC increment per minute. The first derivatives of the normalized melting curves were fitted with Lorentzian distribution function using OriginPro 2015 software. Then, the melting temperature (T_m) was determined from the highest values of the first derivatives and the full width half maximum (FWHM) of the curves which can be used to indicate the degree of cooperativity in DNA binding was also obtained.

4.5.10 Atomic force microscopy

A 5-µL aliquot of samples was deposited on freshly cleaved mica for 5 seconds and washed three times with 50 µL of H_2O. Excess liquid was blown off by the stream of nitrogen for 30 seconds. The sample was then dried under vacuum for at least 20 minutes prior to imaging. The measurement was acquired in ScanAsyst mode under dry condition using ScanAsyst-Air triangular silicon nitride probe (tip radius = 2 nm, k = 0.4 N/m, f_o = 70 kHz; Bruker, Camarillo, CA).

Images were processed by NanoScope Analysis 1.40 Software. The data were treated with flattening to correct tilt, bow and scanner drift. Average particle sizes, heights, and numbers of particles (N) were obtained from Particle Analysis function, and edge lengths of some particles were measured by Section function.

a) NH_2-HE_6-A14 (diameter = 15.5±3.4 nm, height = 0.9±0.3 nm)

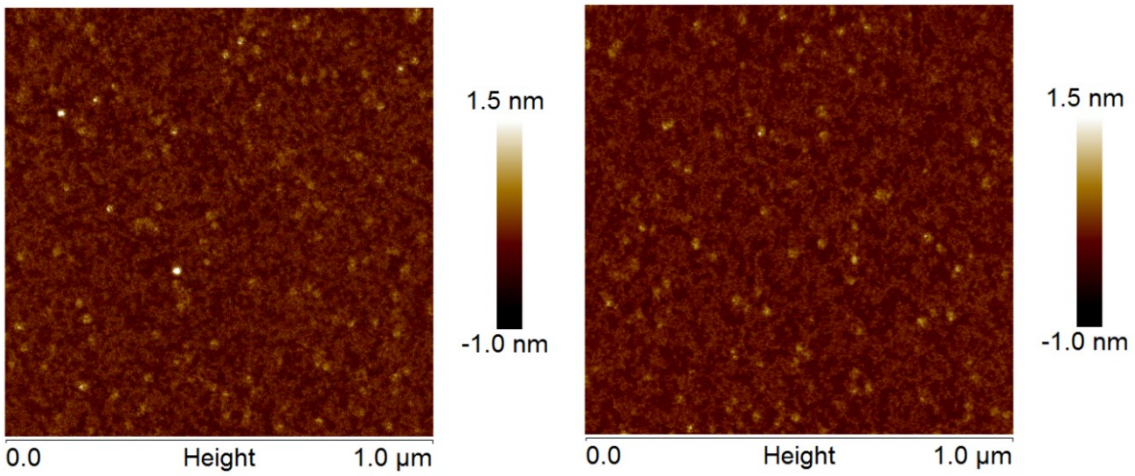

b) NH_2-HE_{12}-A14 (diameter = 26.0±3.4 nm, height = 7.0±1.6 nm)

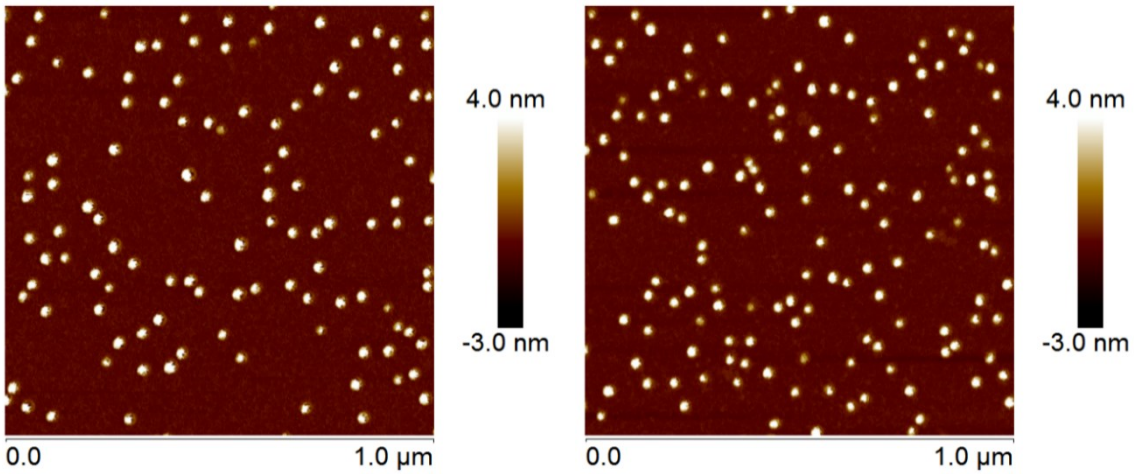

c) NH_2-HE_6-A14 in 1:10 v/v 1xTAMg/DMSO (diameter = 17.1±4.2 nm, height = 1.4±0.5 nm)

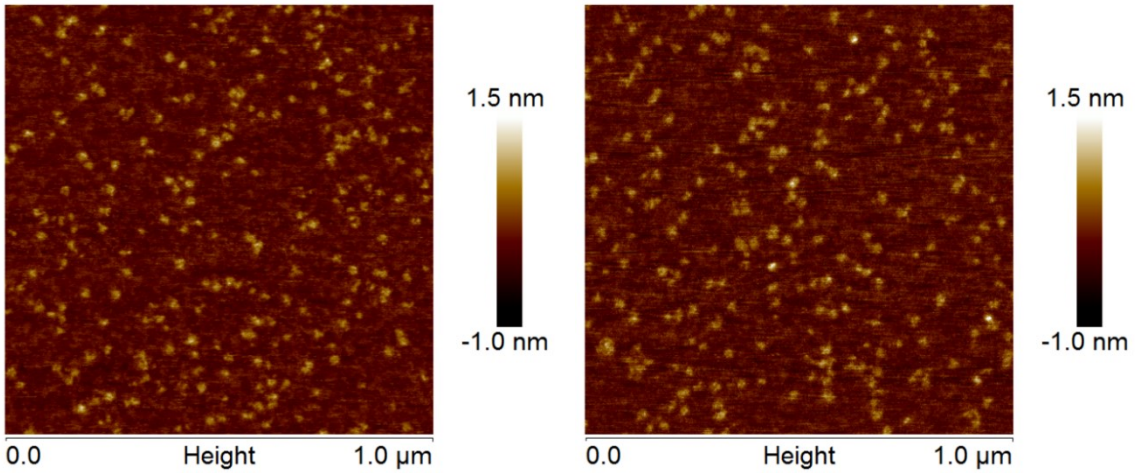

Figure 4.15 | AFM images of amino-modified DNA amphiphiles

a) Ant-HE_{12}-A14

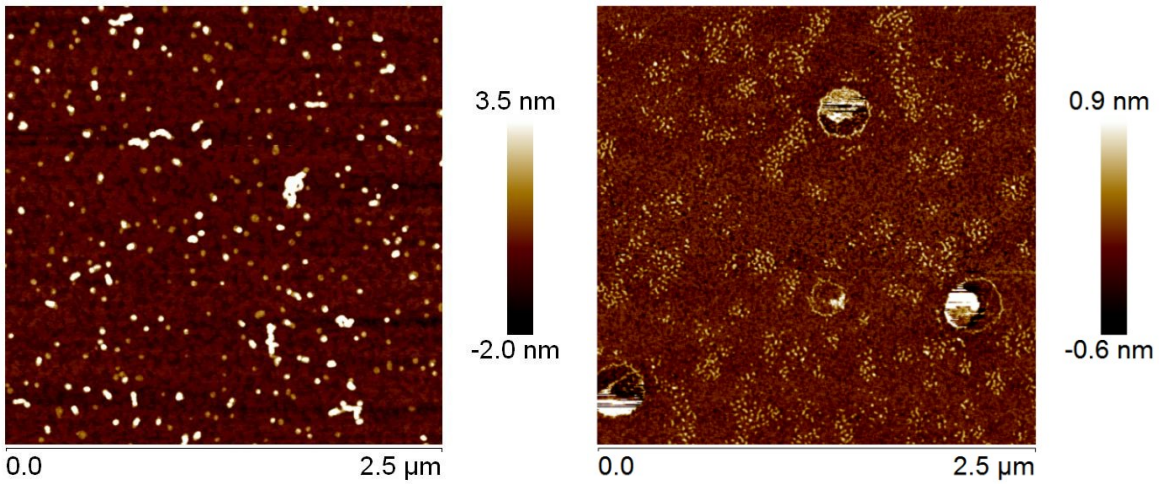

b) Photodimerized C_4/Ant-HE_{12}-A14

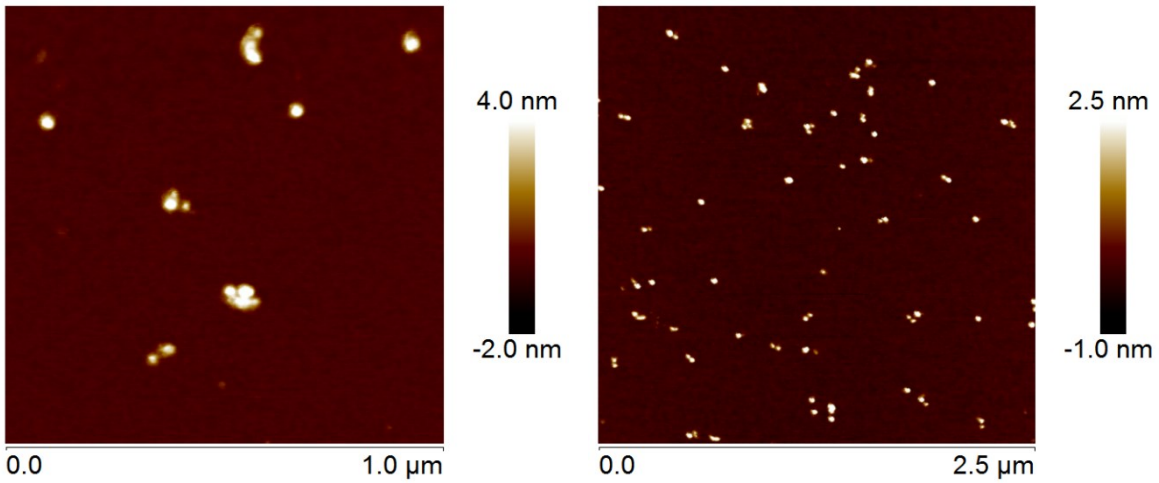

c) Photodimerized C_4/Ant-HE_{12}-HEG_6-A14

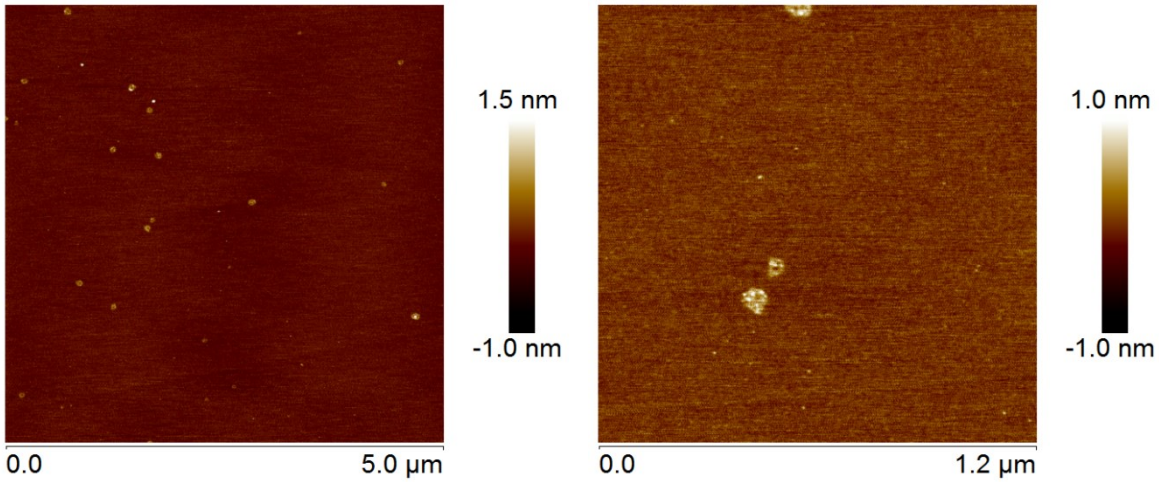

d) Photodimerized C_8/Ant-HE_{12}-A14

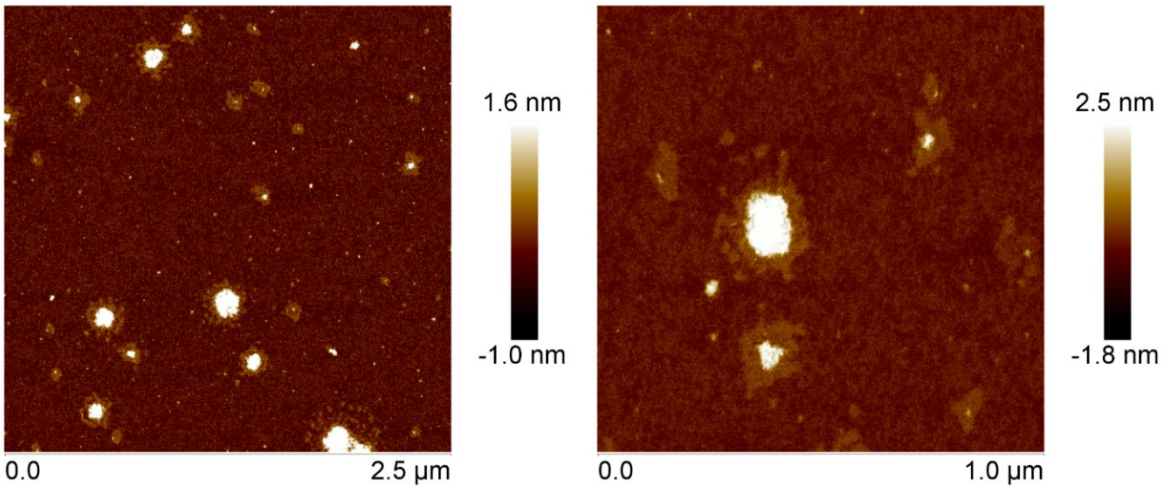

e) Photodimerized C_8/Ant-HE_{12}- HEG_6-A14

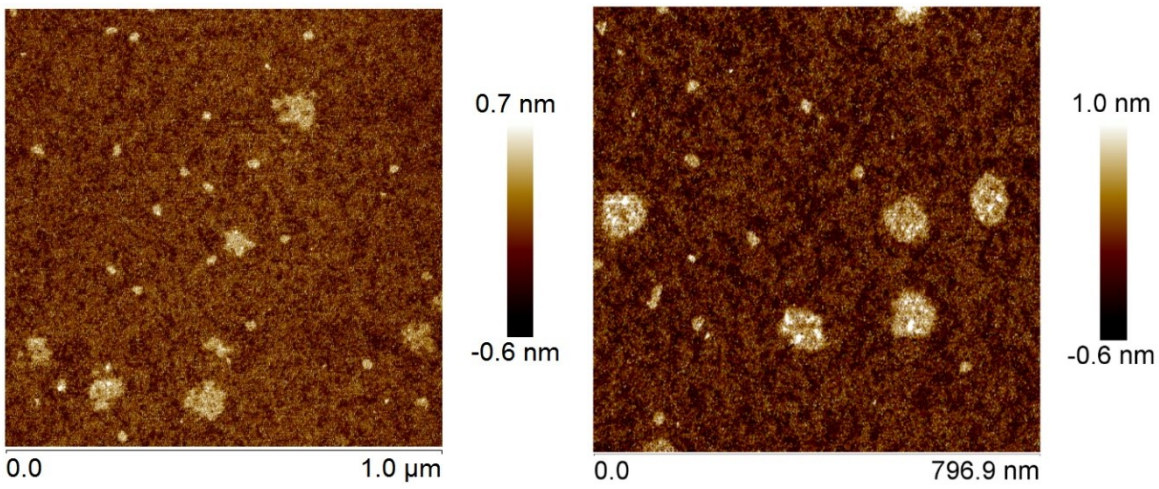

Figure 4.16 | Additional AFM images of photodimerized cube/anthracene constructs.

4.5.11 Transmission electron microscopy

2-5 µL of sample was deposited on the carbon film coated copper grids for one minute. Excess liquid was blotted off with the edge of filter papers. The sample was washed three times with 20 µL H_2O and blotted with filter paper. The sample was dried under vacuum at least 30 minutes prior to the imaging. Average particle sizes and numbers of particles (N) were analyzed by ImageJ software.

a) Ant-HE_{12}-A14

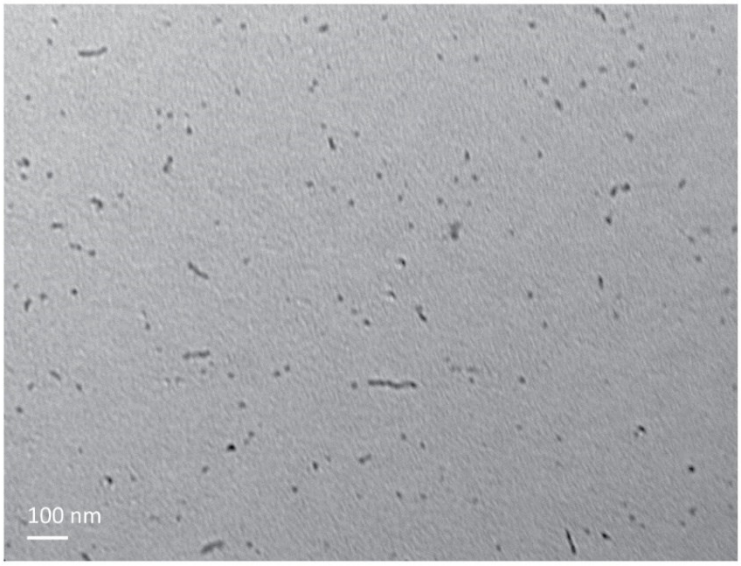

b) Photodimerized C_8/Ant-HE_{12}-A14

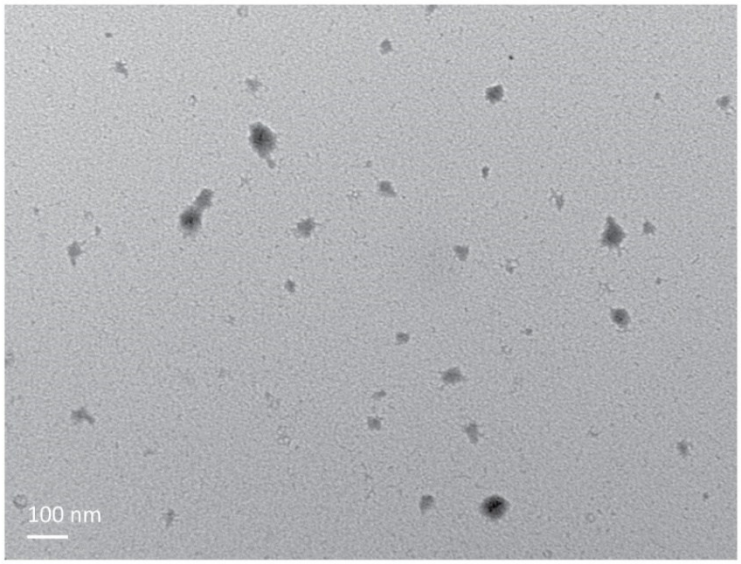

c) Photodimerized C_8/Ant-HE_{12}-HEG6-A14

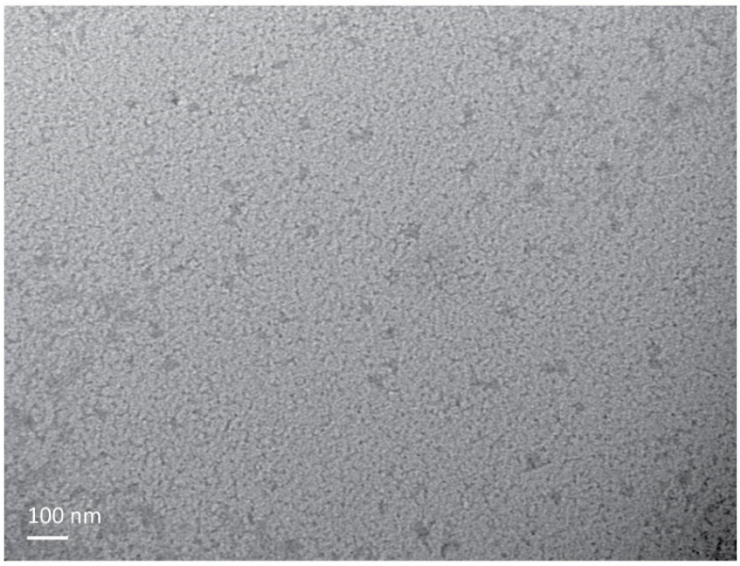

Figure 4.17 | TEM images of photodimerized cube/anthracene constructs.

4.6 References

1. Lombardo, D.; Kiselev, M. A.; Magaz; #xf9; , S.; Calandra, P. *Adv. Cond. Matter Phys.* 2015**,** 2015, 22.
2. Gissot, A.; Camplo, M.; Grinstaff, M. W.; Barthelemy, P. *Org. Biomol. Chem.* 2008**,** 6, 1324-1333.
3. Kwak, M.; Herrmann, A. *Chem. Soc. Rev.* 2011**,** 40, 5745-5755.
4. Raouane, M.; Desmaele, D.; Urbinati, G.; Massaad-Massade, L.; Couvreur, P. *Bioconjugate Chem.* 2012**,** 23, 1091-1104.
5. Howorka, S. *Science* 2016**,** 352, 890-891.
6. Trivedi, R.; Kompella, U. B. *Nanomedicine* 2010**,** 5, 485-505.
7. Talelli, M.; Barz, M.; Rijcken, C. J. F.; Kiessling, F.; Hennink, W. E.; Lammers, T. *Nano Today* 2015**,** 10, 93-117.
8. Wilner, S. E.; Sparks, S. E.; Cowburn, D.; Girvin, M. E.; Levy, M. *J. Am. Chem. Soc.* 2015**,** 137, 2171-2174.
9. Banga, R. J.; Meckes, B.; Narayan, S. P.; Sprangers, A. J.; Nguyen, S. T.; Mirkin, C. A. *J. Am. Chem. Soc.* 2017**,** 139, 4278-4281.
10. Edwardson, T. G.; Carneiro, K. M.; Serpell, C. J.; Sleiman, H. F. *Angew. Chem. Int. Ed.* 2014**,** 53, 4567-4571.
11. Bousmail, D.; Amrein, L.; Fakhoury, J. J.; Fakih, H. H.; Hsu, J. C. C.; Panasci, L.; Sleiman, H. F. *Chem. Sci.* 2017**,** 8, 6218-6229.
12. Anjaneyulu, P. S. R.; Staros, J. V. *Int. J. Pept. Protein Res.* 1987**,** 30, 117-124.
13. Stein, C. A.; Cheng, Y. C. *Science* 1993**,** 261, 1004.
14. Dias, N.; Stein, C. A. *Mol. Cancer. Ther.* 2002**,** 1, 347.
15. Frey, P. A.; Sammons, R. D. *Science* 1985**,** 228, 541-545.

16. Fidanza, J. A.; McLaughlin, L. W. *J. Am. Chem. Soc.* 1989**,** 111, 9117-9119.
17. Fidanza, J. A.; Ozaki, H.; McLaughlin, L. W. *J. Am. Chem. Soc.* 1992**,** 114, 5509-5517.
18. Guzaev, A. P.; Manoharan, M. *Org. Lett.* 2001**,** 3, 3071-3074.
19. Rahman, S. M.; Baba, T.; Kodama, T.; Islam, M. A.; Obika, S. *Biorg. Med. Chem.* 2012**,** 20, 4098-4102.
20. Lee, J. H.; Wernette, D. P.; Yigit, M. V.; Liu, J.; Wang, Z.; Lu, Y. *Angew. Chem. Int. Ed.* 2007**,** 46, 9006-9010.
21. Lee, J. H.; Wong, N. Y.; Tan, L. H.; Wang, Z.; Lu, Y. *J. Am. Chem. Soc.* 2010**,** 132, 8906-8908.
22. Burns, J. R.; Al-Juffali, N.; Janes, S. M.; Howorka, S. *Angew. Chem. Int. Ed.* 2014**,** 53, 12466-12470.
23. Hoque, J.; Konai, M. M.; Gonuguntla, S.; Manjunath, G. B.; Samaddar, S.; Yarlagadda, V.; Haldar, J. *J. Med. Chem.* 2015**,** 58, 5486-5500.
24. Elmehriki, A. A. H.; Milne, M.; Suchý, M.; Bartha, R.; Hudson, R. H. E. *Can. J. Chem.* 2013**,** 91, 211-219.
25. Ihara, T.; Fujii, T.; Mukae, M.; Kitamura, Y.; Jyo, A. *J. Am. Chem. Soc.* 2004**,** 126, 8880-8881.
26. Mukae, M.; Ihara, T.; Tabara, M.; Jyo, A. *Org. Biomol. Chem.* 2009**,** 7, 1349-1354.
27. Mukae, M.; Ihara, T.; Tabara, M.; Arslan, P.; Jyo, A. *Supramol. Chem.* 2009**,** 21, 292-295.
28. Mukae, M.; Tabara, M.; Arslan, P.; Ihara, T.; Jyo, A. *Nucleic Acids Symp. Ser.* 2007, 287-288.
29. Pasternak, K.; Pasternak, A.; Gupta, P.; Veedu, R. N.; Wengel, J. *Biorg. Med. Chem.* 2011**,** 19, 7407-7415.
30. Yu, H.; Alexander, D. T. L.; Aschauer, U.; Haner, R. *Angew. Chem. Int. Ed.* 2017**,** 56, 5040-5044.
31. Manchester, J.; Bassani, D. M.; Duprey, J. L.; Giordano, L.; Vyle, J. S.; Zhao, Z. Y.; Tucker, J. H. *J. Am. Chem. Soc.* 2012**,** 134, 10791-10794.
32. Cooke, L. A.; Frauendorf, C.; Gîlea, M. A.; Holmes, S. C.; Vyle, J. S. *Tetrahedron Lett.* 2006**,** 47, 719-722.
33. Serpell, C. J.; Edwardson, T. G.; Chidchob, P.; Carneiro, K. M.; Sleiman, H. F. *J. Am. Chem. Soc.* 2014**,** 136, 15767-15774.
34. Burns, J. R.; Stulz, E.; Howorka, S. *Nano Lett.* 2013**,** 13, 2351-2356.
35. Liu, K.; Zheng, L.; Liu, Q.; de Vries, J. W.; Gerasimov, J. Y.; Herrmann, A. *J. Am. Chem. Soc.* 2014**,** 136, 14255-14262.
36. Lee, M.-E.; van der Vegt, N. F. A. *J. Am. Chem. Soc.* 2006**,** 128, 4948-4949.
37. Chen, M.; Maetzke, A.; Knak Jensen, S. J.; Gothelf, K. V. *Eur. J. Org. Chem.* 2007**,** 2007, 5826-5833.
38. Chen, M.; Gothelf, K. V. *Org. Biomol. Chem.* 2008**,** 6, 908-911.
39. Marier, J. R.; Rose, D. *Anal. Biochem.* 1964**,** 7, 304-314.
40. Hagel, P.; Gerding, J. J. T.; Fieggen, W.; Bloemendal, H. *Biochimica et Biophysica Acta (BBA) - Protein Structure* 1971**,** 243, 366-373.
41. Stark, G. R.; Stein, W. H.; Moore, S. *J. Biol. Chem.* 1960**,** 235, 3177-3181.
42. Čejka, J.; Vodrážka, Z.; Salák, J. *Biochimica et Biophysica Acta (BBA) - Protein Structure* 1968**,** 154, 589-591.
43. Aathimanikandan, S. V.; Sandanaraj, B. S.; Arges, C. G.; Bardeen, C. J.; Thayumanavan, S. *Org. Lett.* 2005**,** 7, 2809-2812.

| 5 |

Conclusion and future work

5.1 Contributions to Original Knowledge

The central theme of the work described in this thesis is the design and self-assembly of amphiphilic DNA nanostructures, which combine the programmability of DNA with the hydrophobic association driven by the incorporation of small molecules and polymers.

Chapter 2 investigated the interface of sequence-defined polymers and DNA cages regarding the design parameters and the resulting assembly behavior. Both decoration geometry and length of hydrophobic polymers significantly dictate how the polymers interact with one another. The quantized cage assembly was obtained when organizing the polymers on one face of DNA cages, where polymer length defined the number of DNA cages that can be organized around the hydrophobic core. In contrast, the polymer decoration on both faces of DNA cages resulted in well-defined DNA-micelle cages whose hydrophobic core can encapsulate hydrophobic cargos. Interestingly, doughnut-shaped DNA cage-ring structures, where DNA cages were organized into rings, formed when using amphiphilic polymers. It is worth noting that this assembly behavior is a direct consequent of using monodisperse, sequence-defined polymers. This would be challenging to achieve with the classical, polydisperse polymers. In addition, the thermal stability and assembly cooperativity observed in some structures were increased in the presence of hydrophobic interactions. This approach could be further extended for fundamental studies of other supramolecular DNA nanostructures by merely substituting the polymers with functional moieties that can introduce other supramolecular interactions.

Chapter 3 addressed the scaffolding versatility of DNA cubes in organizing multiple cholesterol units to modulate their membrane-binding properties. Structurally, DNA cube is almost twice the dimensions of lipid bilayers, and we observed that the cholesterol orientation on DNA cube dictates its binding mode on the bilayers. Cholesterol decoration on one face of DNA cubes generated lipid-floating nanostructures, while lipid-spanning nanostructures were obtained when distributing cholesterol units on both faces of DNA cubes. This is an exciting design as two binding modes could be achieved with DNA scaffold of a single shape. Cube designs also allowed the systematic investigation of other physical parameters such as the flexibility of cholesterol units tethered on DNA cubes and cholesterol-cholesterol interactions, both of which can dramatically impact lipid-binding characteristics. Furthermore, this cube design resulted in the first ‘wall-less’ and ‘DNA minimal’ synthetic membrane channel.

Chapter 4 presented chemical crosslinking strategies to overcome the instability of amphiphilic DNA nanostructures due to the intrinsic concentration-dependent hydrophobic associations of DNA amphiphiles. The focus was on crosslinking the hydrophobic core of amphiphilic DNA nanostructures by exploiting the confined hydrophobic environments to increase the crosslinking efficiency. First, the chain dimerization was performed by amide bond formation between incorporated amino groups on DNA amphiphiles and alkyl-bis(*N*-hydroxysuccinimidyl ester) linkers. A second method employed the nucleophilicity of sulfur atom on phosphorothioate backbone as a crosslinking site to form covalent bonds with alkyl bis(iodoacetamide) linkers. In the third strategy, anthracene photodimerization provided a linking mechanism in DNA amphiphiles, without the need of external linkers. Overall, this technology will be particularly useful to bring these amphiphilic DNA structures into practical use. Additionally, the site-specific alkylation of phosphorothioated DNA was demonstrated, which will provide an alternative post-synthetic and low-cost method for DNA modification.

In the big picture, several key concepts, which are inspired by the protein-folding process, have been implemented in the work presented herein. DNA-minimal 3D nanostructures were used as scaffolds to position polymers and small molecules to control their association modes, leading to new directed assembly and functions. The use of monodisperse, sequence-defined polymers allowed precise modulation of amphiphilic characters and sequence-dependent self-assembly of the polymers, generating a collection of amphiphilic DNA nanostructures. Furthermore, it was also possible to use hydrophobic interactions as a tool to increase the structural stability and assembly cooperativity of amphiphilic DNA nanostructures. The hydrophobic environments can also serve as a functional site for cargo encapsulation, interactions of DNA with membranes and chemical crosslinking to improve the stability of hydrophobic interactions.

5.2 Suggestions for Future Work

The amphiphilic DNA nanostructures in Chapter 2 are interesting for cellular delivery of hydrophobic drugs or oligonucleotide therapeutics. Their delivery profiles could be modified by the hydrophobicity of the polymers to facilitate their interactions with cell membranes. The loading capacity of hydrophobic guests in these nanostructures could be further improved by using

different monomer architectures. A branched alkyl chain, for example, tends to have a lower chain-packing degree than the linear counterpart, thus potentially increasing loading capacity. In addition, the DNA-micelle cage could be applied as a model to create an artificial enzyme. A variety of functional moieties could be appended to the polymers which can associate inside the confined hydrophobic environment. This provides an opportunity to mimic the catalytic site of natural enzymes if the functional moieties are deliberately positioned inside the hydrophobic core.

It is of note that amphiphilic DNA nanostructures in Chapter 2 use the same polymer sequence for all binding sites. As the DNA cage is highly compatible with anisotropic functionalization, another exciting design parameter is to decorate DNA cages with mixed sequence-defined polymers. In the assembly standpoint, the difference in compositions such as geometrical and amphiphilic mismatches may result in the formation of non-spherical structures due to the change in chain packing and curvature. Additionally, the concept of quantized cage assembly will be an interesting approach to control the aggregation number of molecules or materials of interests. There has been a growing interest in assembling plasmonic nanoclusters whose properties are dependent on geometry and relative position.[1-3] It is envisaged that our approach could be applied to build such constructs, and the hydrophobic micellar core may also function as a hotspot for the detection of hydrophobic molecules by surface-enhanced Raman scattering.

A direct application of DNA cube/cholesterol constructs in Chapter 3 is on membrane interfaces. The ability to control the surface mobility will be beneficial as the lateral diffusion of biomacromolecules is one of the significant parameters to regulate their functions and dynamics on cell membranes.[4] Cube/cholesterol constructs can practically provide handles for the attachment of molecules or materials of interest on the membrane for applications in lipid/cell surface engineering. In addition, their clustering has parallels with membrane protein clustering, and they can potentially be used to probe and influence this effect. More excitingly, the membrane-puncturing nanostructures can be harnessed as synthetic nanopores for membrane transport. It is also viable to deliberately design the pore opening/closing mechanism as the ‘gatekeeper’, which is useful as biophysical tools and drug delivery. Apart from the popular cholesterol modification, other lipid anchors could be decorated on DNA cubes, thus opening an exciting avenue to tune membrane-binding affinity and lipid-phase selectivity of DNA nanostructures.[5-6]

The chemical crosslinking strategies in Chapter 4 provide a method to increase the stability of amphiphilic DNA nanostructures. Although some success in the core-crosslinking in these amphiphilic DNA nanostructures was achieved, there is a need to incorporate multiple reactive units on DNA amphiphile to increase the crosslinking degree. The next steps are to optimize the crosslinking conditions that will generate crosslinked but structurally intact nanostructures and to study whether the crosslinking will effectively prevent the nanostructure from falling apart under dilute environment. For applications in cellular delivery, the linker structures can be modified with acid-labile moieties such that the crosslinked nanostructures remain intact under physiological conditions but degrade after entering the cells. Last but not least, crosslinking DNA-micelle cages can create anisotropic micelles with defined numbers and positions of DNA, which are currently investigated in the Sleiman group.

5.3 List of publications

1. Serpell, C. J.; Edwardson, T. G. W.; Chidchob, P.; Carneiro, K. M. M.; Sleiman, H. F., Precision polymers and 3D DNA nanostructures: Emergent assemblies from new parameter space. *Journal of the American Chemical Society* 2014, 136, 15767-15774.
    - Highlighted in *JACS* Spotlight "complex functionality from DNA boxes and polymer snakes".
2. Chidchob, P.; Edwardson, T. G. W.; Serpell, C. J.; Sleiman, H. F., Synergy of two assembly languages in DNA nanostructures: Self-assembly of sequence-defined polymers on DNA cages. *Journal of the American Chemical Society* 2016, 138, 4416-4425.
    - Chosen as a part of "Hot Materials in a Cool Country" special issue in *Chemistry of Materials* in a celebration of the CSC's 100th anniversary.
3. Chidchob, P.; Sleiman, H. F., Supramolecular Chemistry with DNA. Chapter 2 in Macrocyclic and Supramolecular Chemistry: How Izatt-Christensen Award Winners Shaped the Field, *Wiley*, 2016, 10-37.
4. Trinh, T.*; Chidchob, P.*; Bazzi, H. S.; Sleiman, H. F., DNA micelles as nanoreactors: efficient DNA functionalization with hydrophobic organic molecules. *Chemical Communication* 2016, 52, 10914-10917.

5. Luo, X.; Chidchob. P.; Rahbani, J. F.; Sleiman, H. F., Encapsulation of gold Nanoparticles into DNA minimal cages for 3D-anisotropic functionalization and assembly. *Small* 2017, DOI: 10.1002/smll.201702660
6. Garci, A.; Castor, K. J.; Fakhoury, J.; Do, J.-L.; Di Trani, J.; Chidchob, P.; Stein, R. S.; Mittermaier, A. K.; Friščić, T.; Sleiman, H. F., Efficient and Rapid Mechanochemical Assembly of Platinum(II) Squares for Guanine Quadruplex Targeting. *Journal of the American Chemical Society* 2017, 139, 16913-16922.
7. Rahbani, J. F.; Vengut-Climent, E.; Chidchob, P.; Gidi, Y.; Trinh, T.; Cosa, G.; Sleiman, H. F., DNA Nanotubes with Hydrophobic Environments: Toward New Platforms for Guest Encapsulation and Cellular Delivery. *Advanced Healthcare Materials*, 2017 (accepted).
8. Chidchob, P.; Sleiman, H. F. Recent advances in DNA nanotechnology (to be submitted as an invited review in *Curr. Opin. Chem. Biol.*).
9. Chidchob, P.; Offenbartl-Stiegert, D.; McCarthy, D.; Li, J.; Howorka, S.; Sleiman, H. F., Spatial presentation of cholesterol units on a DNA cube as a determinant of membrane protein-mimicking functions (to be submitted).
10. Rahbani, J. F.; Hsu, J. C. C.; Chidchob, P.; Sleiman, H., F. Single-stranded templates as railroad tracks for hierarchical assembly of DNA origami (to be submitted).

5.4 References

1. Fan, J. A.; He, Y.; Bao, K.; Wu, C.; Bao, J.; Schade, N. B.; Manoharan, V. N.; Shvets, G.; Nordlander, P.; Liu, D. R.; Capasso, F. *Nano Lett.* 2011**,** 11, 4859-4864.
2. Watanabe-Tamaki, R.; Ishikawa, A.; Tanaka, T.; Zako, T.; Maeda, M. *J. Phys. Chem. C* 2012**,** 116, 15028-15033.
3. Lan, X.; Chen, Z.; Liu, B.-J.; Ren, B.; Henzie, J.; Wang, Q. *Small* 2013**,** 9, 2308-2315.
4. Axelrod, D. *J. Membr. Biol.* 1983**,** 75, 1-10.
5. Schade, M.; Knoll, A.; Vogel, A.; Seitz, O.; Liebscher, J.; Huster, D.; Herrmann, A.; Arbuzova, A. *J. Am. Chem. Soc.* 2012**,** 134, 20490-20497.
6. Czogalla, A.; Franquelim, H. G.; Schwille, P. *Biophys. J.* 2016**,** 110, 1698-1707.

| Appendix |

Hierarchical assembly of DNA origami mediated by supramolecular interactions

A.1 Preface

In Chapter 2, the hydrophobically-driven formation of quantized cages was demonstrated by site-specific decoration of hydrophobic polymers on DNA cages. Importantly, this phenomenon is a direct consequence of using monodisperse, structurally well-defined building blocks. The narrow distribution of assembly products will be considered challenging to achieve with polymers synthesized by conventional polymerization methods. In this appendix, we extend the use of sequence-defined hydrophobic polymer-DNA conjugates to guide the assembly of other DNA nanostructures and explore the generality of our supramolecular DNA assembly approach. Here, a rectangular DNA origami structure was chosen due to its versatility and numerous applications. A combination of selected positions on the rectangles was decorated with hydrophobic polymer-DNA conjugates. More specifically, this work aims to examine the interplay of many supramolecular interactions involved in the hierarchical assembly of individual DNA rectangles functionalized with the polymers.

A.2 Introduction

DNA origami is one of the most important assembly approaches in structural DNA nanotechnology. A 7.2-kilobase circular DNA single strand, which is typically derived from the M13 bacteriophage, is folded into an arbitrary shape through the use of hundreds of short DNA single strands, called staple strands.[1] Importantly, the sequences of all staple strands are unique, and each position can be selectively functionalized with desired functional units. This nanoscale patterning capability allows DNA origami to be widely used as a large, addressable scaffold for material templating and organization into a specific pattern. Consequently, the invention of DNA origami has resulted in tremendous impact in many research areas.[2-3]

One of the major limitations of DNA origami is its size limit, where the size of an object that one can create is limited by the scaffold length. This could pose an issue when a large 'working' surface area of DNA origami is required for specific applications. Two main approaches have been demonstrated to overcome this issue. The scaffold size can be tailor-made by molecular biology techniques such as enzyme-based methods and molecular cloning.[4] The longest to-date scaffold (51 kilobases) for DNA origami assembly was prepared from the cloning of λ/M13 hybrid phage.[5]

Another approach toward larger DNA origami is based on the hierarchical assembly. The 2D formation of large DNA arrays could be achieved by selective association of individual DNA origami structures either by sticky-end cohesion mediated by Watson-Crick base-pairing[6-11] or recently by blunt-end stacking[12-15]. Within the design context, the advantages of this approach are sequence-economical design and high versatility.

As an alternative approach to DNA-only assembly, the hierarchical assembly of DNA origami could be facilitated by incorporating supramolecular interactions through attachment of functional molecules on DNA origami. Specifically, the introduction of hydrophobic interactions is still considerably unexplored and, to our knowledge, only two examples have been reported to date. The Simmel group applied an aqueous aggregation behavior of cholesterol units to create two assembly modes, including self-folding and dimerization of DNA rectangles.[16] Similar association modes of DNA rectangles were induced by hydrophobic poly(arylether) dendrons as reported by the Liu group.[17] In both cases, the intermolecular and intramolecular association of the rectangles could be controlled by the number and pattern of hydrophobic units on the rectangles. Hydrophobic interactions can also introduce new functions to DNA nanostructures, thus expanding their application scope. The unfolding of hydrophobically self-folded DNA rectangles, for example, can be triggered by adding surfactants or lipid membranes.[16]

Sequence-controlled polymers are a class of polymers whose monomers are arranged one by one in an ordered fashion, giving rise to precise sequence regulation which can subsequently control physical and chemical properties of the polymers.[18] In Chapter 2, we demonstrated that the decoration of sequence-defined polymer-DNA conjugates on DNA cages could generate a range of unique self-assembled structures such as quantized cage assemblies, DNA-micelle cages, and DNA cage-ring structures. To continue exploring the general applicability of sequence-defined polymers, this appendix examines the self-assembly of a larger rectangular DNA origami decorated with the hydrophobic polymers. As a proof of concept, we investigated the placement of these polymers on DNA rectangles by using three decoration patterns either on the edge or on the top face of the rectangles. This arrangement should in principle induce the edge-to-edge hydrophobically-driven association of DNA rectangles. In addition to DNA base-pairing and hydrophobic interactions, we found that other non-covalent interactions are also involved in directing the rectangle assembly into dimers and aggregates. Interestingly, one attractive outcome

of the interplay between all these supramolecular interactions is the site-specific organization of DNA micelles on the rectangles.

A.3 Results and Discussion

A.3.1 Design of DNA rectangle and polymer-DNA conjugates

A DNA origami rectangle was chosen as a DNA scaffold to position polymer-DNA conjugates and study the self-assembly behavior mediated by hydrophobic interactions of polymer chains. The rectangle has a dimension of 70x100 nm, and it can be assembled from the folding of M13mp18 single-stranded scaffold by using 216 short staple strands (Figure A.1a).[1] As all sequences of staple strands are unique, polymer-DNA conjugates could be in principle organized on 216 different sites on the rectangle with high accuracy (Figure A.1b).

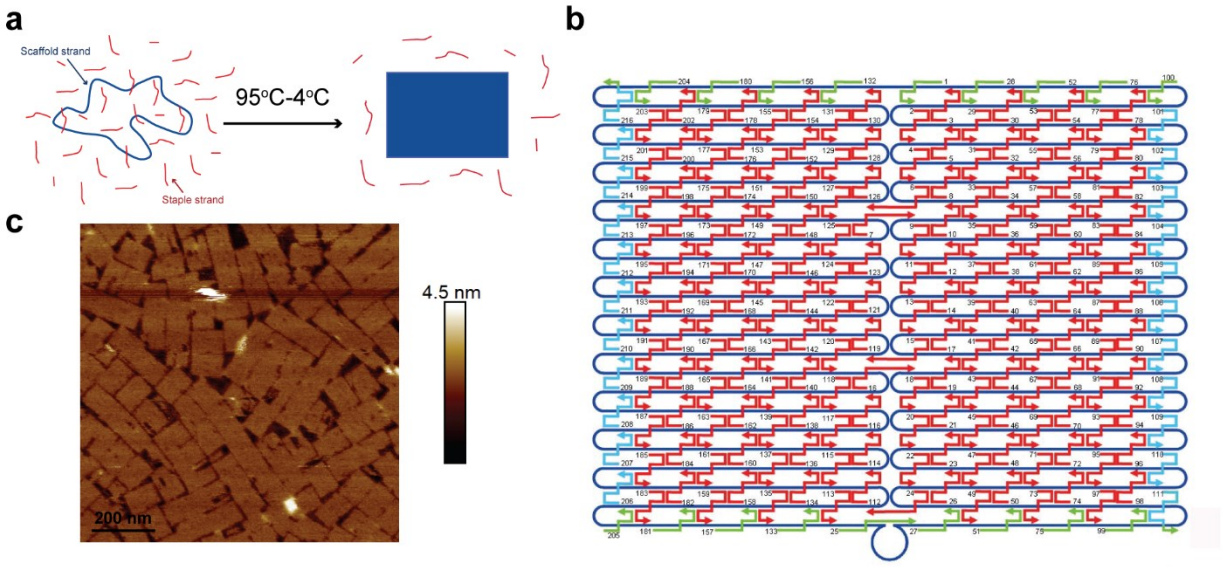

Figure A.1 | Design of DNA rectangle. a) DNA rectangle can be assembled by thermal annealing of the scaffold strand and short staple strands. b) Schematic representation of the rectangle shows the arrangement of staple strands on the scaffold strand. Reproduced with permission from reference 9 (ACS, 2012). c) Liquid AFM image shows the correct assembly of unpurified rectangles on the mica surface. The length scale bar is 200 nm.

Unmodified rectangle (R0) assembly was carried out by mixing all strand components in tris/acetate/magnesium buffer (TAMg) and thermally annealed from 95°C to 20°C in 1.5 hours.

We note that staple strands were added in a large excess (10 equivalents with respect to the scaffold) to ensure the proper folding. Liquid AFM imaging on the mica surface was used to examine R0 assembly in its native state. Figure A.1c shows the formation of rectangles with the correct morphology in high yield.

To incorporate hydrophobic polymers on the rectangles, we designed polymer-DNA conjugates, called HE_n-H20, in which the polymer has a defined number of hexaethylene (HE) repeats separated by phosphodiester linkages. This polymer was attached to a 20-mer DNA strand (H20, Figure A.2a). HE_n-H20 conjugates were prepared by an automated DNA synthesizer and purified by gel electrophoresis and reversed-phase HPLC, yielding a monodisperse, sequence-defined polymer-DNA conjugates.[19]

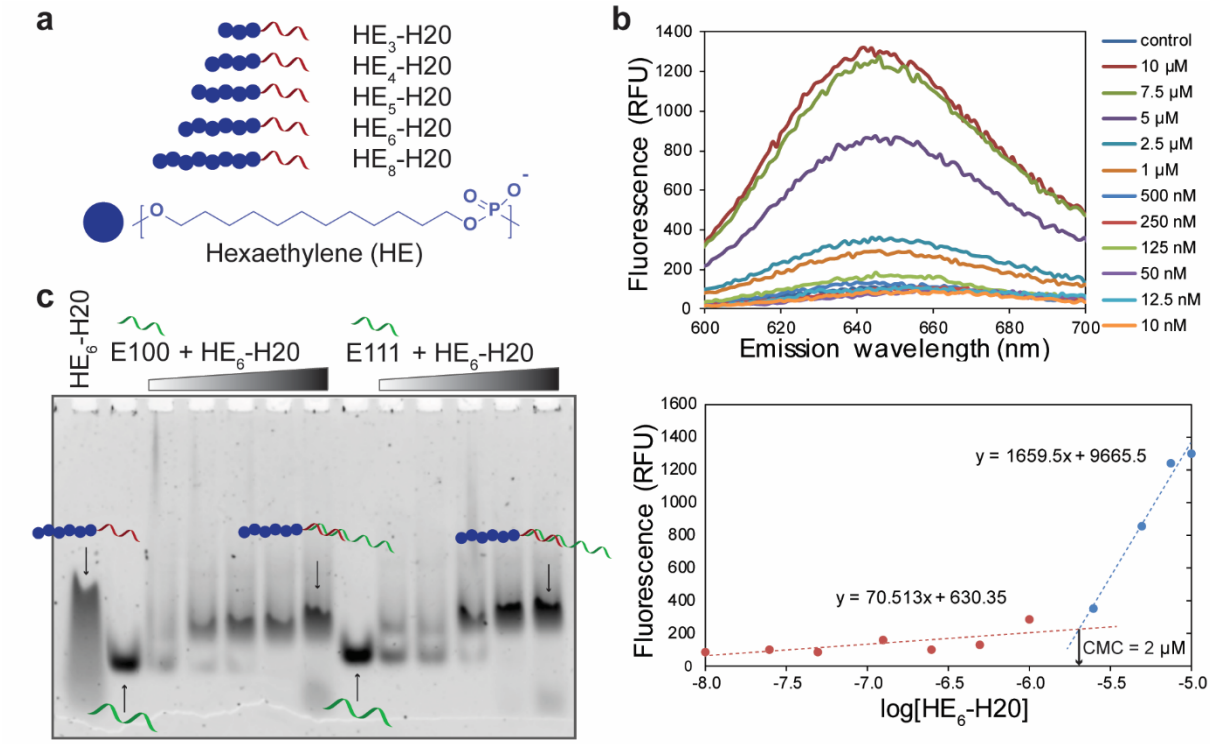

Figure A.2 | Design and characterization of polymer-DNA conjugates. a) HE_n-H20 conjugates contain different numbers of hexaethylene (HE) repeats. b) Determination of critical micelle concentration (CMC) of HE_6-H20 by Nile Red encapsulation. The top panel shows fluorescence spectra of Nile Red in the presence of different HE_6-H20 concentrations. The bottom shows the linear fit plot for CMC determination. The CMC of HE_6-H20 was 2 μM. c) Non-denaturing PAGE (6%) shows the hybridization of HE_6-H20 to its complementary staple strands (E100 and E111). The concentrations of HE_6-H20 were 1, 1.5, 2, 2.5 and 5 equivalents with respect to E100 or E111 (250 nM). The yield of duplex formation increased with HE_6-H20 concentrations.

We first determined the critical micelle concentration (CMC) of one of the polymer-DNA conjugates by fluorescence assay. This value provides an indication of the micelle state of HE_n-H20 at a specific concentration when added to DNA rectangles. Nile Red is a hydrophobic dye that becomes highly emissive in a hydrophobic environment, while it is weakly emissive in aqueous media.[20] In the presence of amphiphilic DNA micelles, Nile Red molecules are likely to be encapsulated inside the hydrophobic core of the micelles, thus leading to an enhanced fluorescence signal. The top panel of Figure A.2b shows the fluorescence spectra of Nile Red added to different HE_6-H20 concentrations. The fluorescence intensity increased with HE_6-H20 concentrations. Also, a slight blue-shift of the peak maximum was observed at higher HE_6-H20 concentrations, indicating increased hydrophobicity of the chemical environment around Nile Red molecules.[20] To determine the CMC value, the average fluorescence intensity at the peak maximum was plotted against HE_6-H20 concentrations as shown in the bottom panel of Figure A.2b. We could see two regimes for the fluorescence signals: non-micelle and micelle. The intersection of the linear fits of the two regimes provided the CMC value of approximately 2 μM for HE_6-H20. Based on our previous data[19], we predict that HE_n-H20 with a higher number of HE repeats will show higher CMC values.

The hybridization between HE_6-H20 and extended staple strands on the rectangle was then studied. Staple strands (E100 and E111; 250 nM) were mixed with increased concentrations of HE_6-H20 (250 nM to 1.25 μM). The strands were incubated at 37ºC for 30 minutes and analyzed by non-denaturing polyacrylamide gel electrophoresis (PAGE). In Figure A.2c, HE_6-H20 micelles showed a smearing band, suggesting disaggregation of HE_6-H20 micelles under our electrophoretic conditions. The extended E100 and E111 strands gave a clear, single band on the gel. Adding low HE_6-H20 concentrations to both E100 and E111 resulted in an additional band of lower electrophoretic mobility, which we assigned as the hybridization products between E100/E111 and HE_6-H20. The bands corresponding to unhybridized E100 and E111 disappeared at 2.5 equivalents of HE_6-H20, suggesting the complete hybridization of E100 and E111. The binding affinity of E100/E111 strand to HE_6-H20 may be lowered by the steric inaccessibility of the DNA strands due to the presence of polymer chains. It is of note that the binding efficiency of E100/E111 to HE_6-H20 could be further enhanced by thermally annealing at a higher temperature. However, when we proceed to the assembly of HE_6-H20 with DNA rectangle, the higher temperature is likely to induce undesired rectangle disassembly.

A.3.2 Decoration of polymer-DNA conjugates on the edge of DNA rectangle

As a proof of concept, we organized polymer-DNA conjugates on the right vertical edge of DNA rectangles to study their hierarchical assembly. In this design, the 3' termini of a selected set of staple strands were extended with 32-mer single-stranded DNA segments, which we named extended 'E' strands. Here, the first 8-mer segment of the 32-mer extension has the same sequence as the 5'-terminal 8-mer segment of the adjacent staple strand (101 in the case of E100, Figure A.3). The second 25-mer segment contains a spacer of five unhybridized thymidines to provide some flexibility and facilitate the binding of polymer-DNA conjugates to the rectangles. The 3'-terminal 20-mer segment is a sticky-end sequence complementary to HE_n-H20 (Figure A.3). This allowed the binding of polymer-DNA conjugates to the specific positions on the rectangle. It is of note that the first 8-mer segment on the 5'-termini of the adjacent staple strands (for example, S101 in the case of E100) was removed. We named this set of strands as shortened 'S' strands.

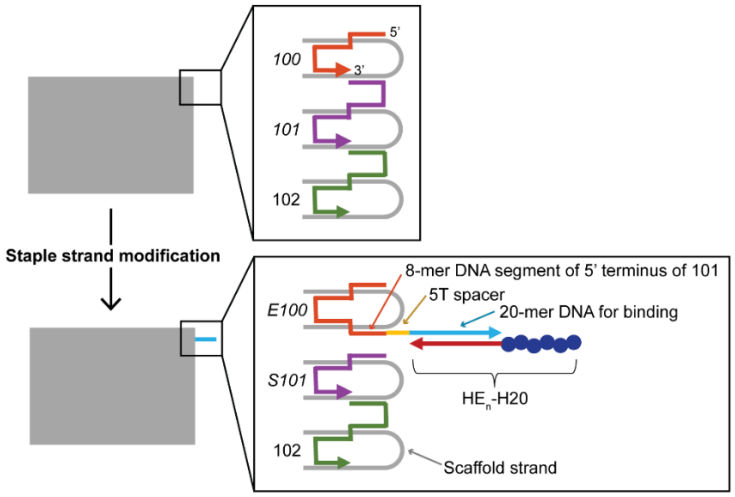

Figure A.3 | Decoration strategy for polymer-DNA conjugates on the edge of DNA rectangle.

We started by organizing only two polymer-DNA conjugates on the top and bottom corners on the right vertical edge of the rectangle, named R2 (Figure A.4a). The rationale of this design was to separate the polymer chains to prevent their self-interactions within the same rectangles, thus making intermolecular interactions of the polymer chains more favorable. We expected the linear dimers as the assembly products.

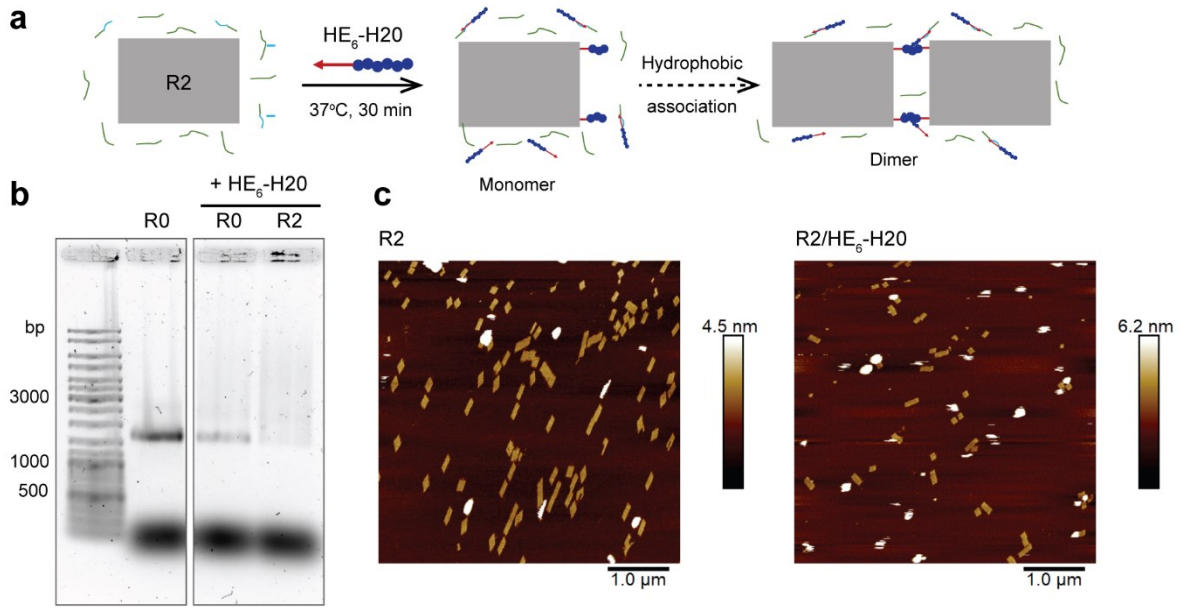

Figure A.4 | Edge functionalization of DNA rectangle with two polymer-DNA conjugates. a) Pre-assembled R2 (1 nM) was incubated with 20 equivalents of HE_6-H20 with respect to R2 at 37°C for 30 minutes. b) Non-denaturing AGE (0.7%) shows that there was the binding of HE_6-HE20 to R2 as indicated by the fainter band of the rectangle monomers. c) Monomers and dimers can be observed in AFM images of both unfunctionalized R2 and R2/HE_6-HE20. The length scale bar is 1 µm.

The assembly was carried out by mixing pre-assembled R2 without removal of excess staple strands and HE_6-H20 at 37°C for 30 minutes, and its assembly product was analyzed by non-denaturing agarose gel electrophoresis (AGE). Figure A.4b shows that adding HE_6-H20 to R2 gave a smeared band. HE_6-H20 was also added to a control rectangle R0 that did not contain any polymer-DNA binding site. The comparison of R2/HE_6-H20 to R0/HE_6-H20 showed that the band of individual rectangles became fainter in the presence of HE_6-H20. The assembly products were further characterized by liquid AFM, revealing a coexistence of monomers and dimers on the mica surface (Figure A.4c). However, similar assembly products were also observed in nonfunctionalized R2. The dimer formation, in this case, was likely to be driven by blunt-end stacking between nonfunctionalized edges of the rectangles.[1] We can conclude that there is the binding of HE_6-H20 to R2 but whether hydrophobic interactions can induce the dimerization of DNA rectangles is still unclear.

To increase the hydrophobicity, we increased the number of polymer-DNA binding sites from two to six on the right vertical edge of the rectangle (R6). We also examined the effect of HE chain lengths from three to six HE repeats. The rectangle R6, which was used without purification, was incubated with HE_n-H20 (n=3-6) at different concentrations at room temperature for 1 hour (Figure A.5a). Figure A.5b shows that the addition of polymer-DNA conjugates to R6 resulted in smeared bands (Lanes 4-9), unlike unfunctionalized R6 that yielded a discrete band on the gel (Lanes 2 and 3). Higher HE_n-H20 concentration seemed to enhance R6 binding as expected, but there was no clear distinction when using HE_n-H20 of different chain lengths. In addition, the screening of other assembly parameters including tile concentration, number of polymer-DNA binding sites and Mg^{2+} concentration were carried out. None of which led to efficient dimer formation.

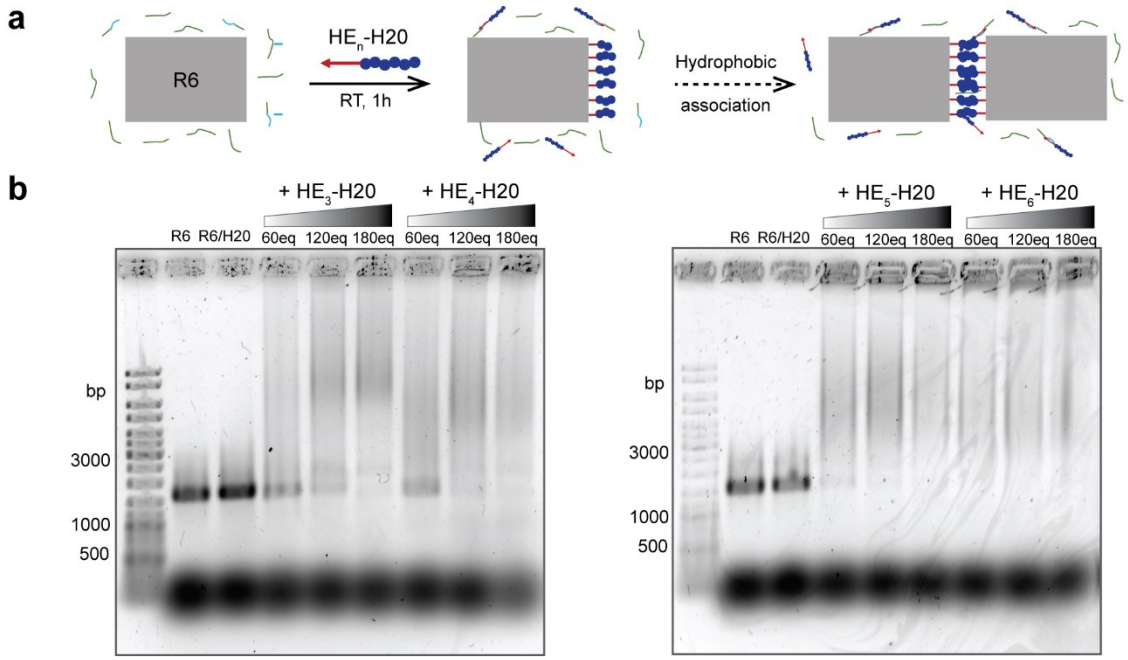

Figure A.5 | Edge functionalization of unpurified DNA rectangle with six polymer-DNA conjugates. a) Unpurified R6 (2 nM) was incubated with HE_n-H20 (n=3-6) at different concentrations at room temperature for 1 hour. B) Non-denaturing AGE (0.7%) shows that the R6 binding efficiency increased with the concentrations of polymer-DNA conjugates. The equivalents of polymer-DNA conjugates were relative to the rectangle concentration.

We note that all previous assembly used unpurified rectangles, and there will be a large amount of unbound staple strands remaining in solution. These excess extended staple strands would compete with the rectangles for polymer-DNA bindings. Although polymer-DNA conjugates were added in excess, this competition can result in low dimerization efficiency. To remove excess staple strands, two purification methods were tested. The filtration method uses the centrifugal filter to separate folded DNA rectangle from unbound staple strands, which could pass through the membrane filter. Another method, called polyethylene glycol (PEG) precipitation, exploits the excellent dispersion of unbound staple strands in PEG solution to isolate folded DNA rectangles, which are not well-dispersed in PEG solution and could be collected by centrifugation.[21] In our hands, we found that cleaner assembly products could be obtained from the filtration method. In Figure A.6b, the rectangle R6 gave a single band without a noticeable amount of staple strands on the gel. The room-temperature incubation of R6 with polymer-DNA conjugates also led to band smearing, which was similar to the previous observation in Figure A.5b. An attempt to increase the binding efficiency by 37^{o}C incubation was unsuccessful.

The assembly products of R6 with polymer-DNA conjugates were further examined by liquid AFM. In Figure A.6c, we observed a small population of dimers for unfunctionalized R6, which was similar to R2 in Figure A.4c. When polymer-DNA conjugates were added to R6, the rectangle clusters became the dominant species on the mica surface. The clusters seemed to extend in both directions of vertical edges of R6. This indicates that cluster formation could be mediated by both hydrophobic interactions between polymer chains and blunt-end stacking between unmodified edges of R6. Beside perfectly-aligned desired dimers, the cluster formation could also be a result of many offset alignments between functionalized edges of R6/HE$_n$-H20 (Figure A.6c). Indeed, we would expect this clustering behavior from a combination of non-directional hydrophobic interactions and the shape effect of large DNA nanostructures, leading to many possible edge-to-edge offset alignments. We also note that, in the rectangle design, hairpin loops composed of four unhybridized thymidines were added to staple strands on the left vertical edge of the rectangles to prevent blunt-end stacking interactions.[1] Still, we did observe some uncontrolled aggregation which is induced by blunt-end stacking. Thus, it is particularly challenging to direct the edge-to-edge assembly of large DNA nanostructures when many uncontrollable parameters are presented.

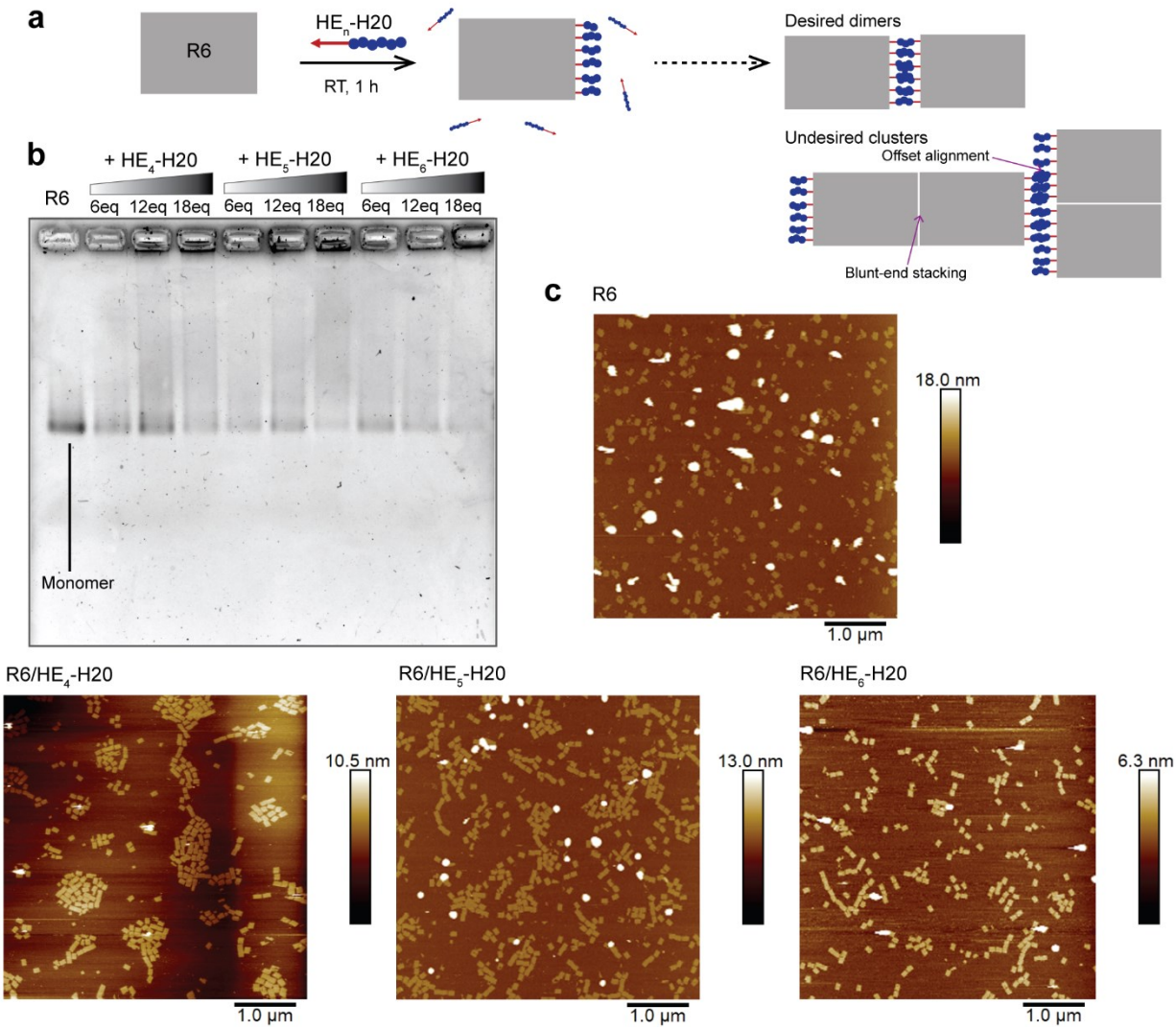

Figure A.6 | Edge functionalization of purified DNA rectangle with six polymer-DNA conjugates. a) Purified R6 (1 nM) was incubated with HE_n-H20 (n=4-6) at different concentrations at room temperature for 1 hour. b) Non-denaturing AGE (0.7%) shows that there was the binding of polymer-DNA conjugates to R6, as indicated by decreased intensity of the monomer bands. The equivalents of polymer-DNA conjugates were relative to the rectangle concentration. c) Cluster formation was predominant in the assembly products of R6/HE_n-H20 as revealed by liquid AFM. The length scale bar is 1 μm.

A.3.3 Decoration of polymer-DNA conjugates on top of DNA rectangle

We designed another decoration pattern on the rectangles to preclude the effect of blunt-end stacking and offset geometrical alignments. In this new design, named R14, two rows of polymer-DNA binding sites were placed on top of the rectangle surface, and each row contains seven binding sites (Figure A.7a). The 20-mer single-stranded DNA segment for the polymer-DNA

binding was extended from the 3'-termini of selected staple strands with three unhybridized thymidines as a spacer in between. The R14 pattern has been shown to favor the dimerization of DNA rectangles into bilayer structures.[16-17] Non-denaturing AGE in Figure A.7b shows that there were two bands for purified R14. The lower band was assigned as R14 monomer, and we suspect that the slower migrating band was R14 dimer, which could possibly form by non-specific interactions between the polymer-DNA binding sites of R14 monomers. We also had frequently observed these non-specific interactions between DNA rectangles when there were multiple binding sites on the rectangles (not parts of this thesis).

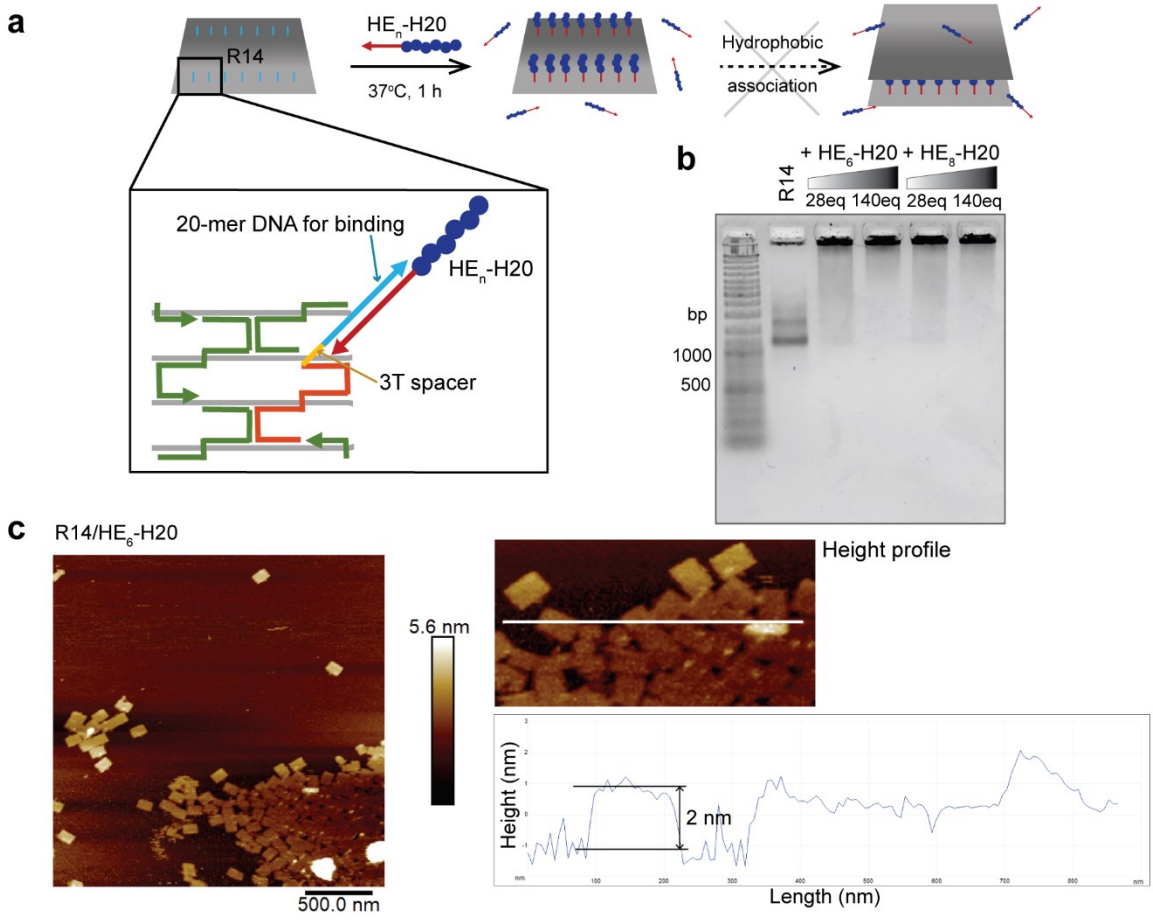

Figure A.7 | Surface functionalization of DNA rectangle with polymer-DNA conjugates. a) Purified R14 (1 nM) was incubated with HE_6-H20 and HE_8-H20 at two concentrations at 37°C for 1 hour. b) Non-denaturing AGE (2%) shows that the binding of polymer-DNA conjugates to R14 resulted in non-penetrating materials. The equivalents of polymer-DNA conjugates were relative to the rectangle concentration. c) AFM image of R14 functionalized with 28 equivalents of HE_6-H20 reveals that monolayer rectangles with the height of 2 nm were the major products.

The addition of HE_6-H20 and HE_8-H20 to purified R14 gave mostly non-penetrating materials and some degree of band smearing (Figure A.7b). We then performed liquid AFM to characterize the assembly products. AFM image of R14 functionalized with 28 nM of HE_6-H20, which was lower than the CMC value of HE_6-H20, in Figure A.7c reveals the presence of mostly monolayer rectangles as indicated by their height (~2 nm). The binding of HE_6-H20 to R14 was not visible, and only a small population of the rectangles contained raised features on their surface. The monomers remained as the major product even at higher HE_6-H20 concentrations (up to 280 nM, still lower than the CMC value of HE_6-H20).

There are two possible scenarios that could contribute to unsuccessful rectangle dimerization in our case. It was suggested by List *et al.* that the electrostatic interactions between mica and DNA could disrupt the hydrophobic interactions deliberately introduced into DNA nanostructures. In their case, this might lead to an undesired opening of the self-folded DNA rectangles functionalized with cholesterol units.[16] Furthermore, the hydrophobicity of our sequence-defined polymers might not be strong enough to overcome electrostatic repulsions involved in bringing together two DNA-dense rectangles. Thus, in the following section, we sought to improve the assembly quality by reducing the strength of electrostatic interactions on the mica surface and increasing the concentration of polymer-DNA conjugates to induce their micelle formation.

A.3.4 Na^+-assisted surface organization of DNA rectangle

Two independent reports demonstrated that NaCl addition on the mica surface during sample deposition and incubation steps could increase the surface mobility of DNA origami, allowing their surface rearrangement into large 2D arrays mediated by blunt-end stacking.[13-14] The mechanism of this surface behavior involves the replacement of Mg^{2+} ions, which provide positively charged bridges between negatively charged mica and DNA, with Na^+ ions. Due to their lower binding affinity to Na^+, DNA nanostructures can diffuse more freely on the mica surface than in the only presence of Mg^{2+} (Figure A.8a).[13] Consequently, this approach could be useful to lower the extent of electrostatic interactions between mica and DNA and possibly aid AFM characterization of our DNA nanostructures.

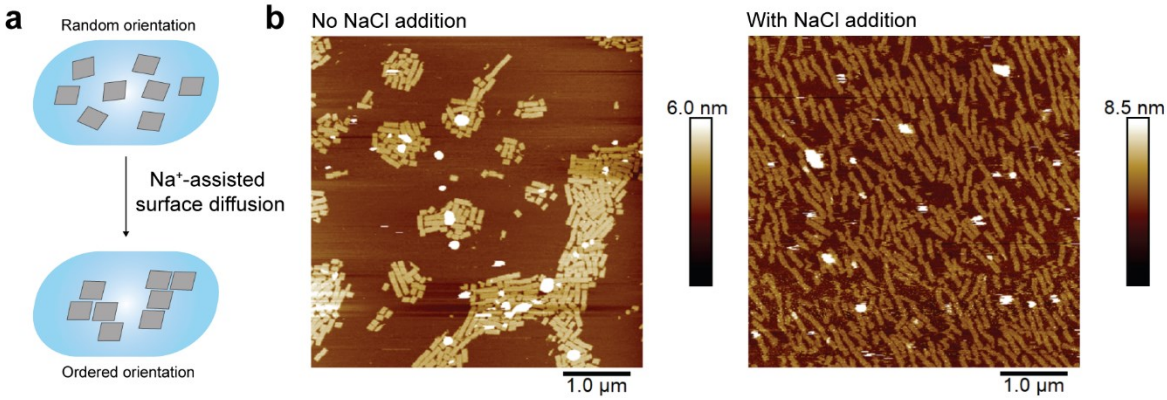

Figure A.8 | Surface ordering of DNA rectangle on mica surface mediated by Na^+. a) Addition of NaCl could increase the mobility and induce the surface organization of DNA nanostructures on the mica surface. b) AFM images show a random aggregation of DNA rectangles on the mica surface. A 3.5-hour incubation with NaCl (200 mM) resulted in higher rectangle organization on the surface. The rectangle concentration was 1 nM in both cases. The length scale bar is 1 μm.

We first optimized the surface diffusion protocol by following the guideline reported by Aghebat Rafat *et al.*[14] Briefly, the solution of R0 supplemented with NaCl was deposited and incubated on the mica surface, followed by AFM imaging in liquid mode. The effect of experimental conditions, such as DNA concentration, NaCl concentration and incubation time, on the surface ordering of R0 was examined. The high surface-ordering degree was achieved with relatively high R0 concentration (1 nM) and long deposition time (up to 3.5 hours) as shown in Figure A.8b (right image). Without NaCl addition, R0 aggregates with poor geometric alignment were obtained (Figure A.8b, left image). With the increased degree of surface organization, we also sought to employ the surface diffusion as another tool to achieve the hierarchical assembly of DNA rectangles, where 2D edge-to-edge ordering is guided by shape complementarity, and 3D dimerization is driven by hydrophobic associations of polymer-DNA conjugates.

With the optimized surface-diffusion protocol, DNA rectangles functionalized with HE_8-H20 were characterized on the mica surface in the presence of NaCl. We note that HE_8-H20 was used instead of HE_6-H20 to increase the hydrophobicity of the polymer chains. The assembly was carried out by incubating 2 nM of purified rectangles with 10 μM of HE_8-H20 at 37°C for 1 hour. HE_8-H20 at this concentration could form micelles in solution. The samples were mixed with an equal volume of the buffer supplemented with 400 mM NaCl and deposited on mica for 2.5-4.5 hours. Preliminary AFM images in Figure A.9 reveal the coexistence of DNA rectangles and

spherical micelles on the mica surface for both R14/HE_8-H20 and R_6/HE_8/H20. Interestingly, there were multiple raised spherical features on the rectangles (on top of the surface for R14 and on the vertical edge of R6). The pattern of these spheres was similar to the binding sites on the rectangles. In the case of R14/HE_8-H20 (Figure A.9a), the height measurement indicated that the rectangles were monolayers, suggesting that the dimerization of R14 does not happen. Although some linear dimers were observed in R6/HE_8-HE20 (Figure A.9b), it was unclear whether the dimerization is driven mainly by hydrophobic associations of HE_8 chains because it is difficult to prevent blunt-end stacking from occurring completely. In addition, we observed a lower density of the rectangles functionalized with HE_8-H20 on the mica surface as compared to R0 even though the same rectangle concentration was used. The possible explanation is that these hydrophobic nanostructures could have a lesser binding affinity to the mica surface due to their higher hydrophobicity when compared to unmodified DNA nanostructures.

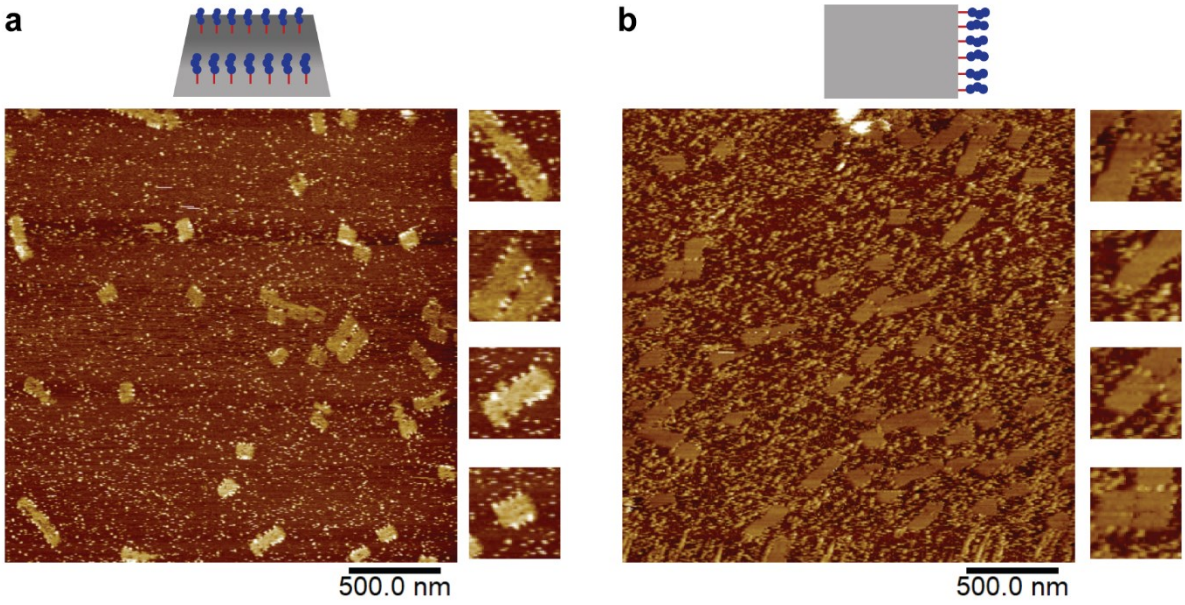

Figure A.9 | Micelle templating on DNA rectangle. AFM images of a) R14/HE_8-H20 and R6/HE_8-H20 in the presence of NaCl (200 mM) show that there were small spheres along polymer-DNA binding sites on the rectangles. HE_8-H20 was added in large excess (5,000 equivalents) with respect to the rectangle concentration (final concentration for surface deposition was 1 nM). The length scale bar is 500 nm.

We believe that the small spheres on the rectangles are HE_8-H20 micelles that formed and immobilized on the rectangles through the hybridization with extended linking strands. Thus, the initial goal to achieve rectangle dimerization by hydrophobic associations of polymer-DNA is not successful. The possible explanation is that the polymer-DNA binding sites on the rectangles are likely to be saturated by DNA micelles, thus potentially blocking the dimerization process. A dense DNA shell of the micelles could also lead to a significant electrostatic repulsion that can further prevent the rectangle dimerization. This issue can be resolved by optimizing the concentration of polymer-DNA conjugates.

Nevertheless, these rectangles may serve as templates for organizing polymer-DNA micelles. We note that the purification of the functionalized rectangles will be challenging due to low recovery of the samples from the filtration and the strong adhesion tendency of the micelles to the membrane filters. The future improvement on this strategy is to optimize the purification process to remove unbound micelles to allow the analysis of binding efficiency (i.e., how many binding sites are occupied by the micelles). Surface diffusion of functionalized rectangles could be further optimized to obtain their long-range organization on the mica surface.

A.4 Conclusions

We have demonstrated the possible use of sequence-defined hydrophobic polymers as a tool to incorporate hydrophobic interactions in the hierarchical assembly of DNA origami. This was designed by decorating the polymer chains on one vertical edge of DNA rectangles. We observed the rectangle clustering when the number of polymer chains per rectangle increased. This cluster formation was mediated by a combination of hydrophobic association of polymer chains and blunt-end stacking between unmodified vertical edge of the rectangles. In the second design to preclude these effects, we decorated the top face of the rectangles with the polymer chains. The dimerization to create bilayer rectangles was not successfully achieved, possibly due to electrostatic repulsions between the rectangles that overcome the hydrophobic interactions introduced by the polymers.

This observation suggest that the polymer-DNA conjugates do not display strong enough hydrophobic interactions to compete with other supramolecular interactions at play in DNA origami. Instead, blunt-end stacking and electrostatic interactions seem to dominate the assembly

landscape of DNA origami. As such, incorporating hydrophobic interactions to direct the hierarchical assembly of large, DNA-dense nanostructures is a challenging task, and more directional, stronger supramolecular interactions will be required to achieve better assembly control. Yet, this work provides an exciting method to organize DNA micelles site-specifically on DNA origami. To our knowledge, there is only one method to template hydrophobic micelles on DNA origami without inducing origami aggregation.[22] Thus, we anticipate that our method could be useful as an alternative method to create a platform for reaction cascades and multidrug encapsulation on DNA origami.

The future direction of this work is to increase the strength and directionality of supramolecular interactions that will facilitate hierarchical assembly of DNA rectangles with improved ordering degree. One of the possible ways is to apply DNA base-pairing to guide the assembly direction of hydrophobic interactions by extending the polymer chain-end with a unique, short DNA segment that can hybridize to its complementary strand on another DNA amphiphiles on another position on the rectangle. Nevertheless, the introduction of hydrophobic interactions in DNA origami is still considerably unexplored. Yet, many potential applications particularly in membrane interfaces can already be perceived from the reported examples.[16-17]

A.5 Experimental Section

A.5.1 Chemicals

The reagents and buffers are as detailed in Section 2.5.1 in Chapter 2 with the following additions. Single-stranded M13mp18 scaffold (100 nM) was purchased from Guild BioSciences. Staple strands with Bio-RP purification were obtained and used without further purification from Bioneer, Inc.

A.5.2 Instrumentation

Instrumentation is as detailed in Section 2.5.2 in Chapter 2.

A.5.3 Solid-phase synthesis and purification

DNA synthesis and purification are as detailed in Section 2.5.3 in Chapter 2.

A.5.4 Sequences and characterization of polymer-DNA conjugates

The sequences of unmodified DNA and polymer-DNA conjugates are listed in Table A.1.

Table A.1 | Sequences of polymer-DNA conjugates (X = HE).

Strand	Sequence (5'→3')
H20	GTCGCTCTCTCAAGTAGAAT
HE_3-H20	XXX GTCGCTCTCTCAAGTAGAAT
HE_4-H20	XXXX GTCGCTCTCTCAAGTAGAAT
HE_5-H20	XXXXX GTCGCTCTCTCAAGTAGAAT
HE_6-H20	XXXXXX GTCGCTCTCTCAAGTAGAAT
HE_8-H20	XXXXXXXX GTCGCTCTCTCAAGTAGAAT

The purity of polymer-DNA conjugates was evaluated by denaturing PAGE (Figure A.10).

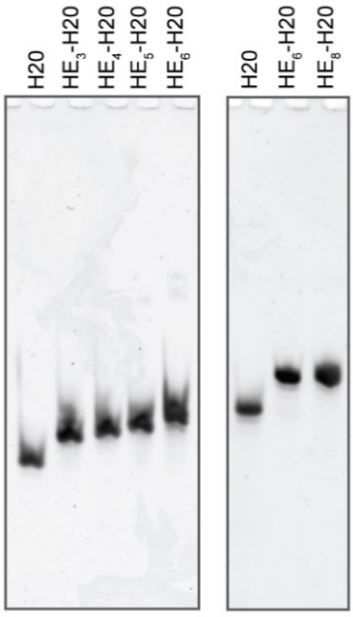

Figure A.10 | Purity of polymer-DNA conjugates. Denaturing PAGE (15%) shows the good purity of polymer-DNA conjugates, as indicated by their single band on the gels.

Table A.2 shows the retention times of some polymer-DNA conjugates on RP-HPLC. The DNA conjugates were further analyzed by LC-ESI-MS in negative ESI mode, which is summarized in Table A.2

Table A.2 | Characterization of polymer-DNA conjugates.

Strand	Retention time[a]	Calculated mass[b]	Experimental mass[b]
HE_4-H20	22.052	7145.65	n/a
HE_6-H20	23.720	7673.94	7673.8672
HE_8-H20	24.922	8202.24	8202.2500

[a] Retention time (in minutes) was determined from RP-HPLC with the gradient of 3-50% acetonitrile for 30 minutes.
[b] mass unit is in g/mole.

A.5.5 Determination of critical micelle concentration

Nile Red fluorescence assay was used to determine the CMC of HE_6-H20, following the protocol reported by Edwardson *et al*.[23] HE_6-H20 at various concentrations (50 nM to 10 μM) was prepared in 100 μL of 1xTAMg and thermally annealed from 95ºC to 4ºC. In a separate vial, Nile Red was dissolved in acetone at a concentration of 100 μM. To HE_6-H20 solution was added 2.5 μL of Nile Red solution to obtain the final Nile Red concentration of 2.5 μM. The mixtures were incubated at room temperature with the protection from light for 3 hours. To measure the fluorescence signals, the samples were transferred to a 96-well plate, and the fluorescence spectra of Nile Red were acquired by the BioTek Synergy well-plate fluorometer. The excitation wavelength was 535 nm with a slit width of 9 nm, and the fluorescence emission was monitored from 560 to 750 nm.

A.5.6 Design of DNA rectangle

Strand components of DNA rectangle:

Staple strands 1-216 were used in the assembly of all rectangle designs. The sequences of staple strands are listed in Section A.5.8. The modifications of staple strands required for DNA rectangles with polymer-DNA binding sites are listed in Table A.3. The modified strands were

used in places of unmodified strands of the same number for the assembly of functionalized rectangles.

Table A.3 | Staple strands for DNA rectangles containing polymer-DNA binding sites.

Rectangle	Staple strand modifications
R2	E100, E111
	S101
R6	E100, E102, E104, E106, E108, E110
	S101, S103, S105, S107, S109, S111
R14	E5, E23, E32, E48, E56, E72, E114, E128, E136, E152, E160, E176, E184, E200

Rectangle assembly and purification:

The rectangle assembly was adapted from the protocol reported by Rothemund.[1] The rectangles were assembled in one-pot annealing at 5 nM of M13mp18 scaffold and 50 nM of individual staple strands in 1xTAMg buffer. The mixtures were then heated to and held at 95ºC for 5 minutes and slowly annealed to 20ºC with a gradient of 1ºC per minute. Non-denaturing AGE assay was used to characterize the assembly products by mixing the samples with 6X loading dye. The gel (0.7-1.5%) was run at 80-85 V for 2-2.5 hours using 1xTAMg as the running buffer and stained with GelRed.

Two purification methods were used to remove excess staple strands (Figure A.11).

1) Filtration by using 100 kDa Amicon centrifugal filters (Millipore). The 500 µL of sample was loaded in the filter and centrifuged at 6500 rpm at 4ºC for 5 minutes. Then, 400 µL of 1xTAMg was added, and the sample was centrifuged at 5000 rpm at 4ºC for 5 minutes. This washing step was repeated two more times. Approximately 50-100 µL of sample was recovered, which can be stored at 4ºC up to a week before use. We found that this method gave clean, purified products but the recovery yield was usually low.

2) PEG precipitation.[21] To 50 µL of 20 µM of the samples was added 50 µL of 1xTAMg supplemented with 15% PEG (8 kDa). The mixtures were centrifuged at 13.4 krpm for 30 minutes at 4ºC, and the supernatant was carefully removed by pipetting. Then, 100 µL of 1xTAMg supplemented with 7.5% PEG (8 kDa) was added, and the samples were centrifuged at 13.4 krpm for 30 minutes. This second step was repeated two more times, followed by an addition of 50 µL of 1xTAMg to redisperse the purified samples. More concentrated purified samples can be obtained, but residual PEG was remaining in the solution.

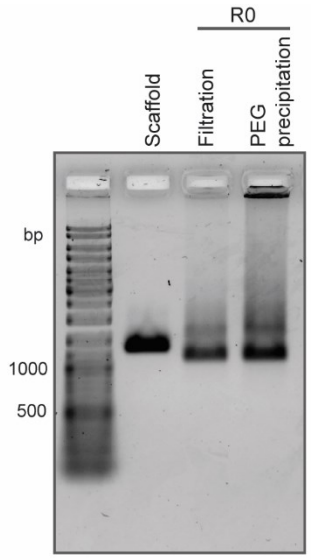

Figure A.11 | Purification of DNA rectangles. Two purification methods to remove excess staple strands were tested. Non-denaturing AGE (1.5%) shows that both could efficiently remove excess staple strands but cleaner purified products were obtained from the filtration method.

It has been observed that DNA origami tends to non-specifically adsorb on the membrane filters, leading to the significant loss of DNA origami during the purification process.[24] To determine the accurate concentration of purified DNA rectangles, the absorbance at 260 nm was measured. The extinction coefficient of different rectangle designs can be approximated by equation (1), adapted from the report by Hung *et al*.[25]

$$\varepsilon = 6700\text{ds} + 10000\text{ss} \quad (1)$$

where ds is the number of double-stranded bases and ss is the number of single-stranded bases. The rectangle concentrations were then calculated by Beer-Lambert's law ($A_{260\text{ nm}} = \varepsilon bc$, b=1cm).

Assembly of DNA rectangles with polymer-DNA conjugates:

For polymer-DNA conjugates, DNA rectangles (1-2 nM) were mixed with stoichiometric concentrations of HE_n-H20 and incubated at room temperature or 37°C for 30 minutes to 1 hour. The assembly products were examined by non-denaturing AGE and AFM imaging.

A.5.7 Atomic force microscopy

To prepare an AFM sample, 2.5 μL of samples (1-5 nM with respect to the rectangle concentration) was deposited on freshly cleaved mica for 5 minutes. The mica was mounted on AFM, followed by the injection of 40-100 μL of 1xTAMg to the fluid cell before imaging. The measurement was acquired in ScanAsyst Fluid mode using ScanAsyst-Fluid triangular silicon nitride probe (tip radius = 20 nm, k = 0.7 N/m, f_o = 150 kHz; Bruker, Camarillo, CA) and ScanAsyst-Fluid+ triangular silicon nitride probe (tip radius = 2 nm, k = 0.7 N/m, f_o = 150 kHz; Bruker, Camarillo, CA).

Images were processed by NanoScope Analysis 1.50 Software. Raw data were treated with flattening function to correct tilt, bow and scanner drift.

a) R6

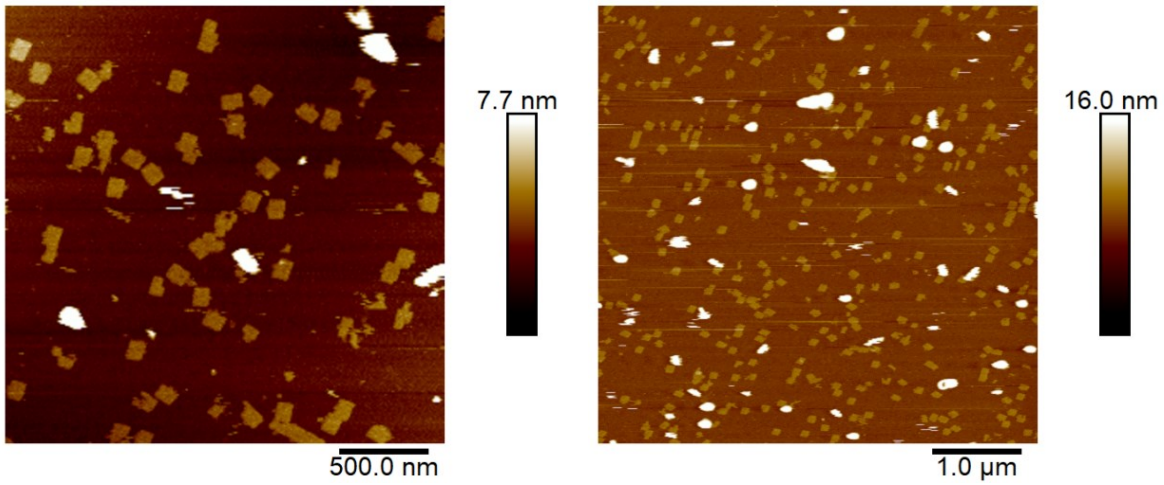

b) R6/HE_4-H20

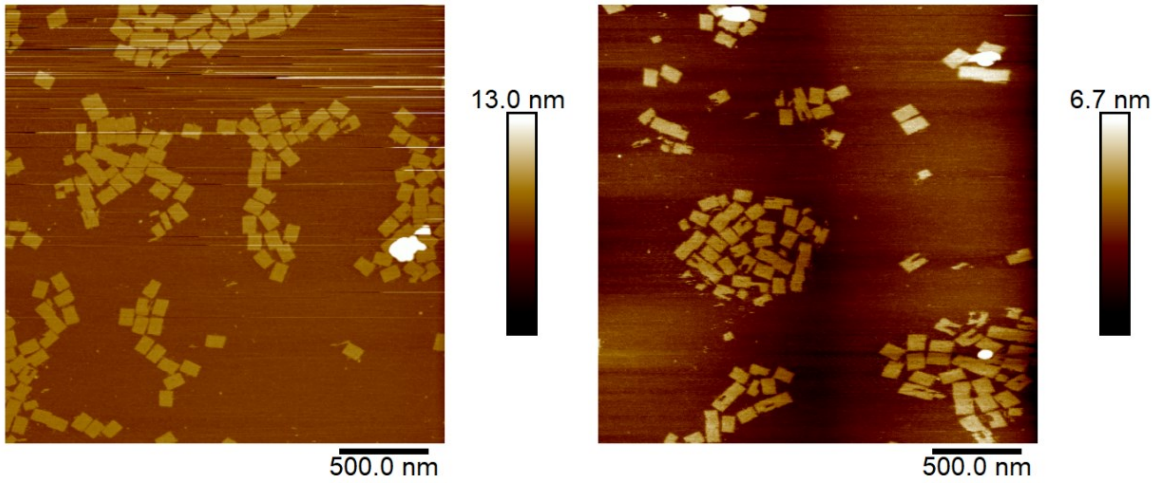

c) R6/HE_5-H20

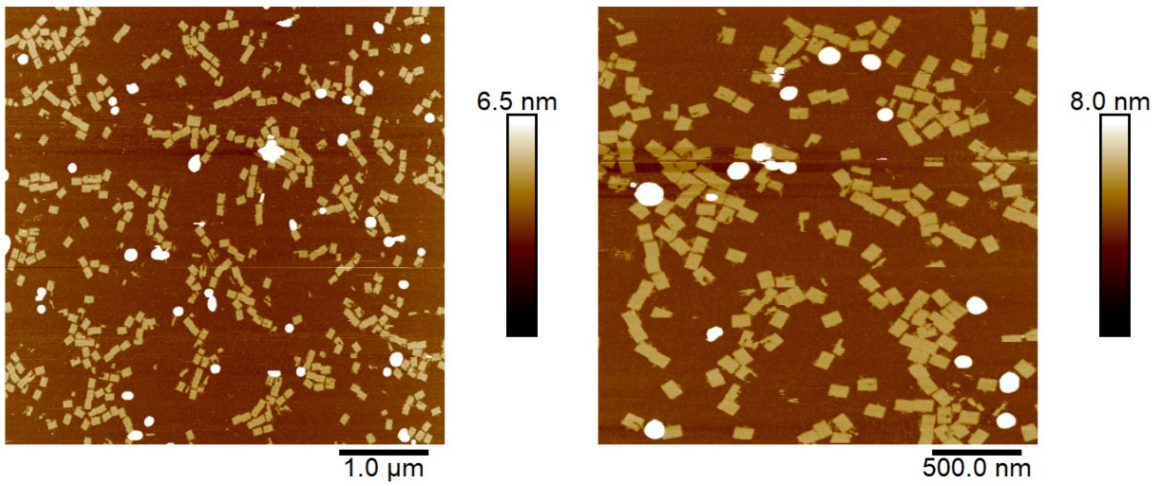

d) R6/HE_6-H20

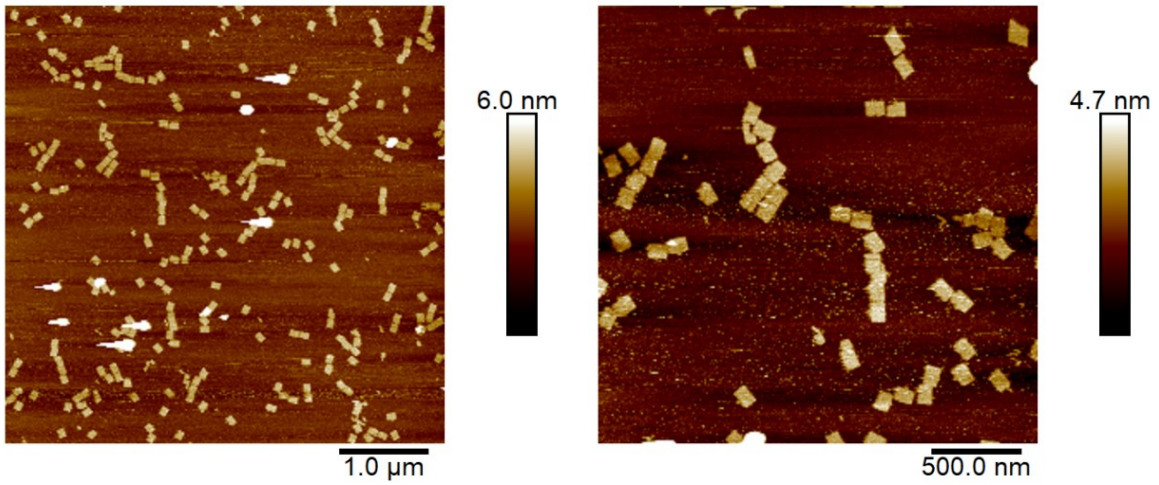

e) R14 with 28 equivalents of HE_6-H20

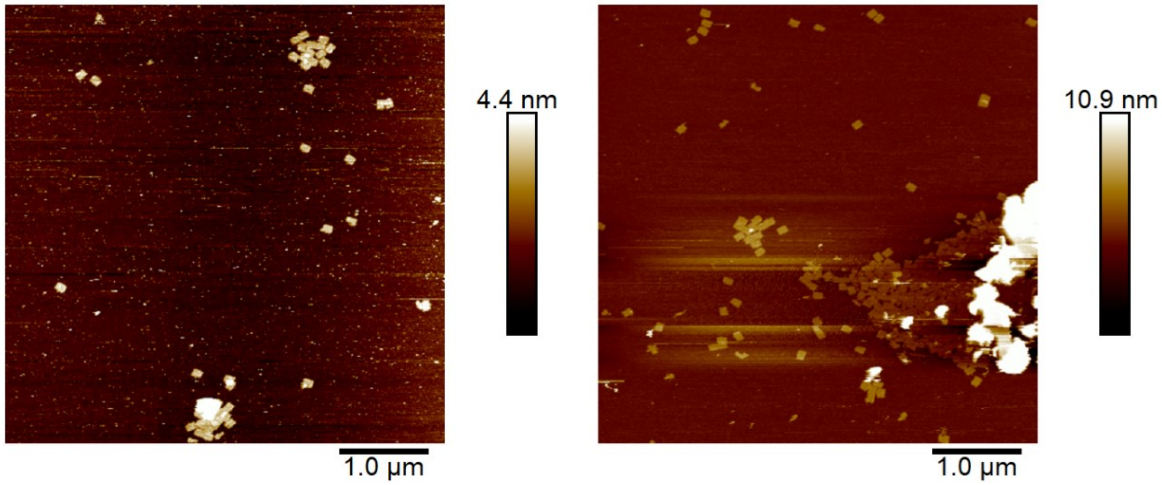

f) R14 with 28 equivalents of HE_8-H20

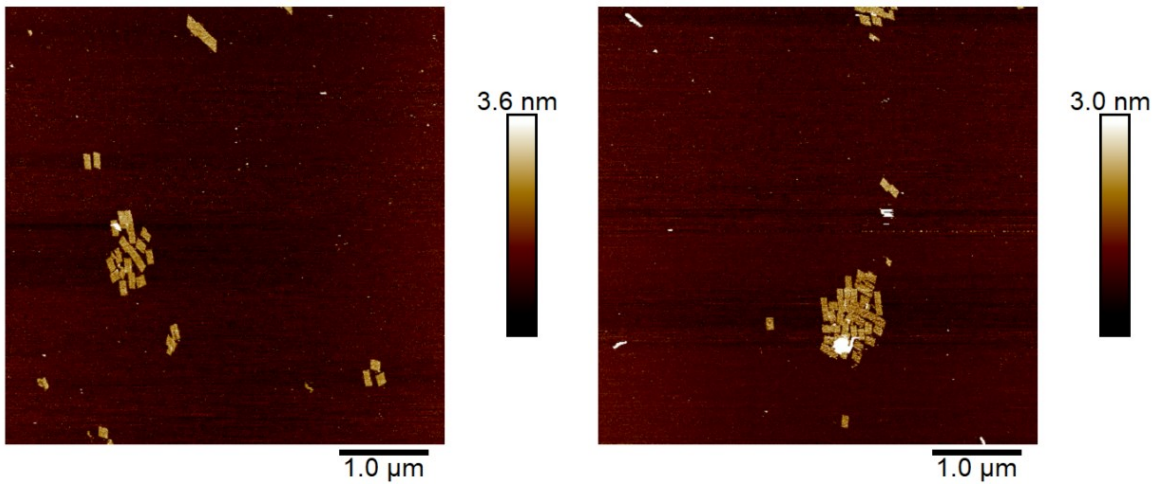

Figure A.12 | AFM images of DNA rectangles decorated with polymer-DNA conjugates.

The Na^+-assisted surface diffusion was performed by mixing 20 µL of 2 nM rectangles with 20 µL of 1xTAMg supplemented with 400 mM NaCl and depositing 40 µL of the mixtures on freshly cleaved mica. To reduce buffer evaporation, the mica was kept in a sealed petri dish containing a small cup of water inside. After incubating at room temperature for 1-4 hours, the mica was mounted on AFM, followed by the injection of 60 µL of 1xTAMg supplemented with 200 mM NaCl to the fluid cell before imaging.

a) R0 after 1-hour incubation with NaCl addition

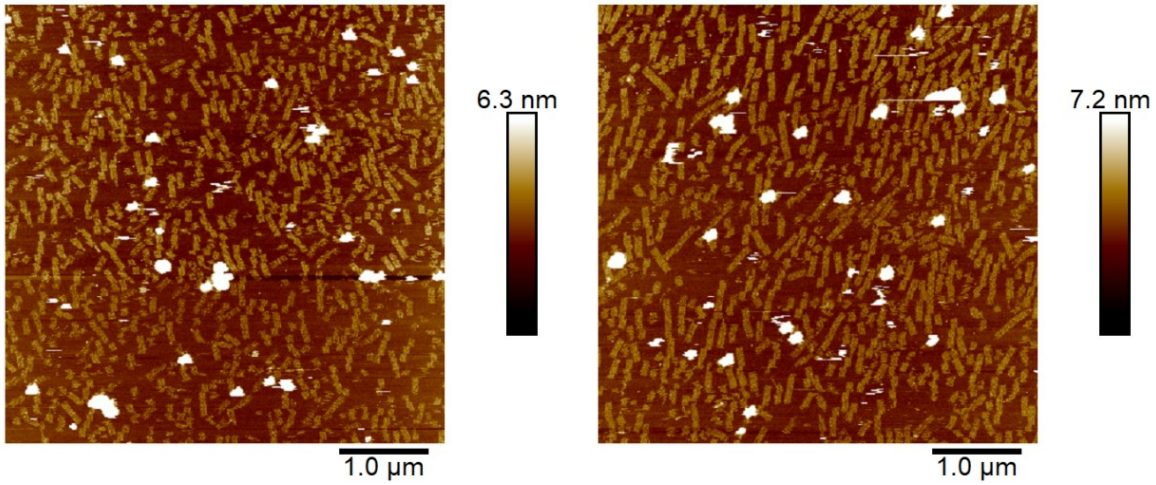

b) R0 after 3.5-hour incubation with NaCl addition

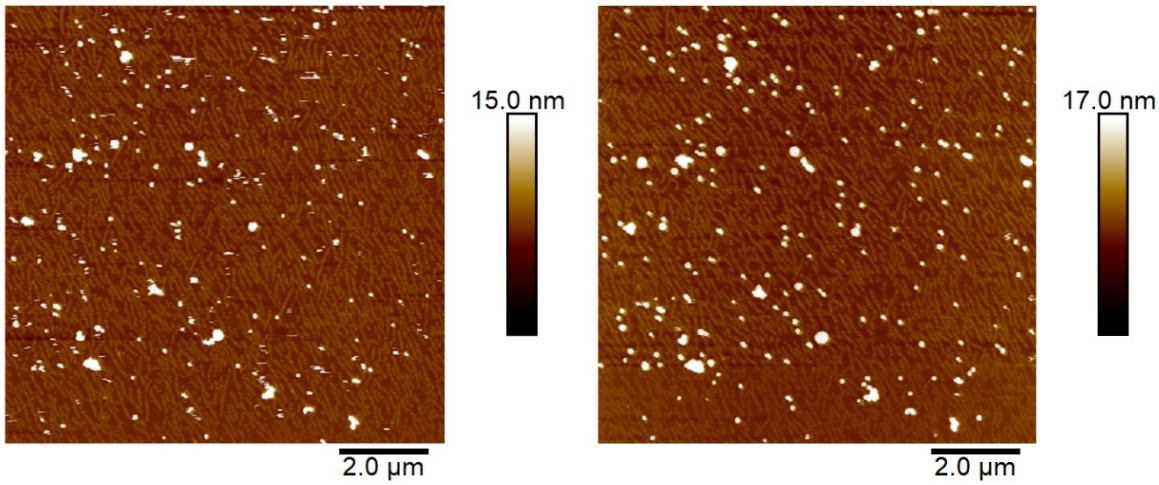

c) R0 after 3.5-hour incubation with no NaCl addition

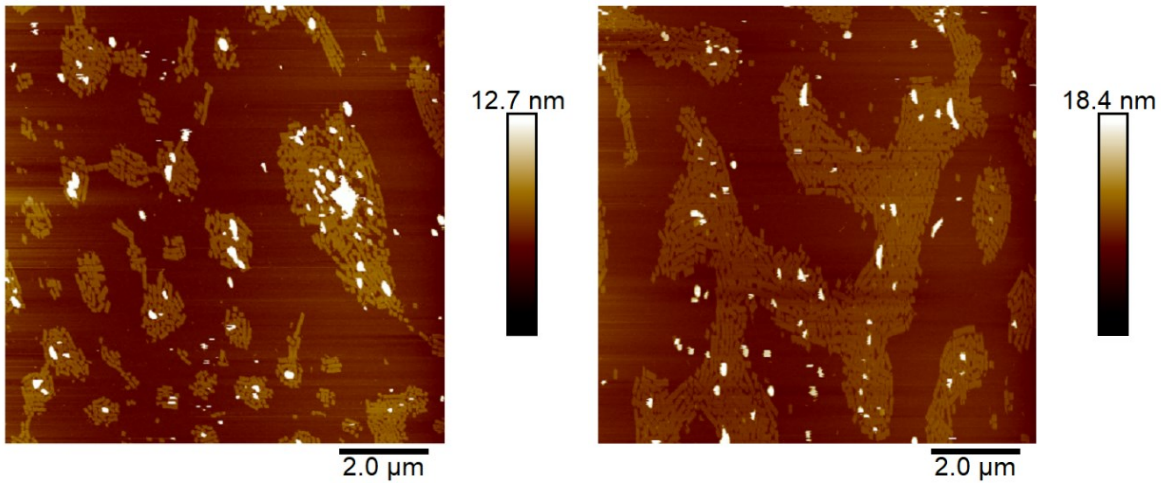

d) Purified R0 after 4-hour incubation with NaCl addition

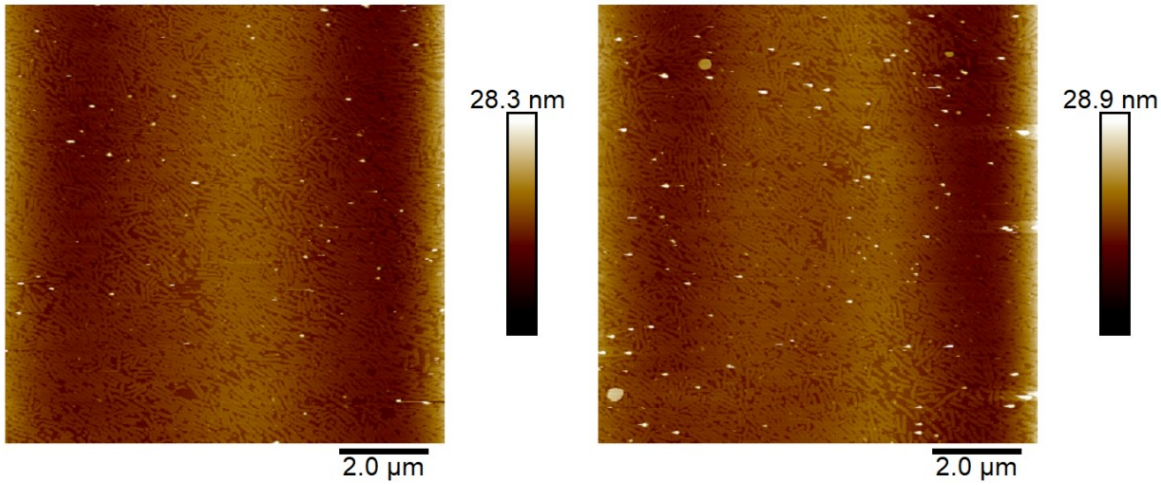

e) R14/HE_8-H20 after 4.5-hour incubation with NaCl addition

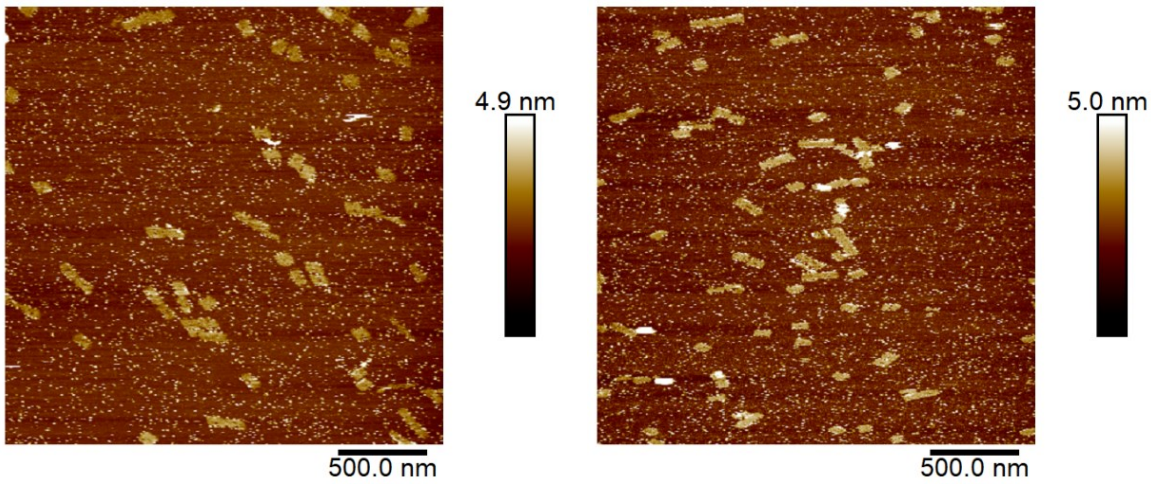

f) R6/HE$_8$-H20 after 2.5-hour incubation with NaCl addition

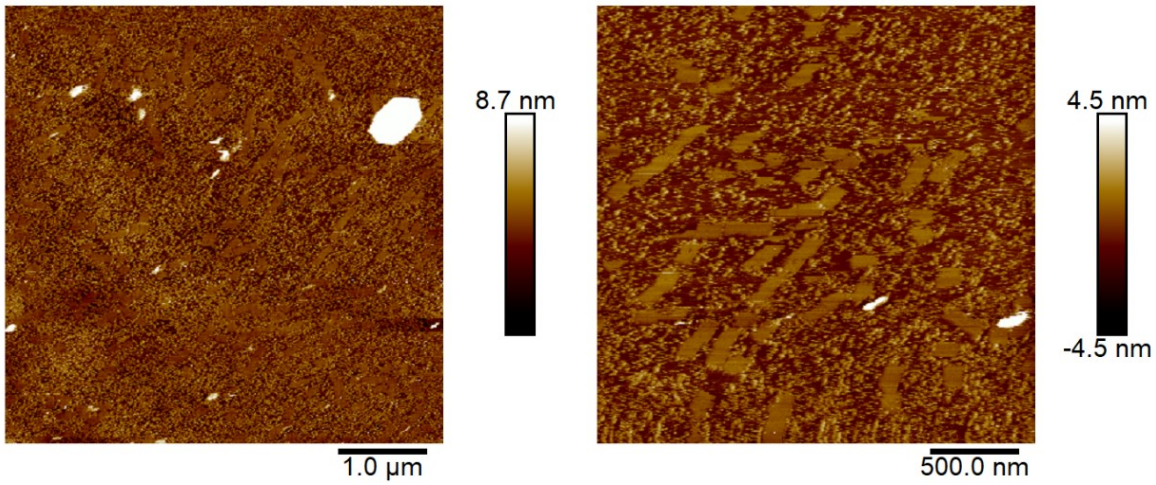

Figure A.13 | AFM images of DNA rectangles on mica incubated with NaCl.

A.5.8 Sequences of staple strands

Unmodified staple strands:

1	CAAGCCCAATAGGAACCCATGTACAAACAGTT	24	ACGAACCAAAACATCGCCATTAAATGGTGGTT
2	AATGCCCCGTAACAGTGCCCGTATCTCCCTCA	25	GAACGTGGCGAGAAAGGAAGGGAACAAACTAT
3	TGCCTTGACTGCCTATTTCGGAACAGGGATAG	26	TAGCCCTACCAGCAGAAGATAAAAACATTTGA
4	GAGCCGCCCCACCACCGGAACCGCGACGGAAA	27	CGGCCTTGCTGGTAATATCCAGAACGAACTGA
5	AACCAGAGACCCTCAGAACCGCCAGGGGTCAG	28	CTCAGAGCCACCACCCTCATTTTCCTATTATT
6	TTATTCATAGGGAAGGTAAATATTCATTCAGT	29	CTGAAACAGGTAATAAGTTTTAACCCCTCAGA
7	CATAACCCGAGGCATAGTAAGAGCTTTTTAAG	30	AGTGTACTTGAAAGTATTAAGAGGCCGCCACC
8	ATTGAGGGTAAAGGTGAATTATCAATCACCGG	31	GCCACCACTCTTTTCATAATCAAACCGTCACC
9	AAAAGTAATATCTTACCGAAGCCCTTCCAGAG	32	GTTTGCCACCTCAGAGCCGCCACCGATACAGG
10	GCAATAGCGCAGATAGCCGAACAATTCAACCG	33	GACTTGAGAGACAAAAGGGCGACAAGTTACCA
11	CCTAATTTACGCTAACGAGCGTCTAATCAATA	34	AGCGCCAACCATTTGGGAATTAGATTATTAGC
12	TCTTACCAGCCAGTTACAAAATAAATGAAATA	35	GAAGGAAAATAAGAGCAAGAAACAACAGCCAT
13	ATCGGCTGCGAGCATGTAGAAACCTATCATAT	36	GCCCAATACCGAGGAAACGCAATAGGTTTACC
14	CTAATTTATCTTTCCTTATCATTCATCCTGAA	37	ATTATTTAACCCAGCTACAATTTTCAAGAACG
15	GCGTTATAGAAAAAGCCTGTTTAGAAGGCCGG	38	TATTTTGCTCCCAATCCAAATAAGTGAGTTAA
16	GCTCATTTTCGCATTAAATTTTTGAGCTTAGA	39	GGTATTAAGAACAAGAAAAATAATTAAAGCCA
17	AATTACTACAAATTCTTACCAGTAATCCCATC	40	TAAGTCCTACCAAGTACCGCACTCTTAGTTGC
18	TTAAGACGTTGAAAACATAGCGATAACAGTAC	41	ACGCTCAAAATAAGAATAAACACCGTGAATTT
19	TAGAATCCCTGAGAAGAGTCAATAGGAATCAT	42	AGGCGTTACAGTAGGGCTTAATTGACAATAGA
20	CTTTTACACAGATGAATATACAGTAAACAATT	43	ATCAAAATCGTCGCTATTAATTAACGGATTCG
21	TTTAACGTTCGGGAGAAACAATAATTTTCCCT	44	CTGTAAATCATAGGTCTGAGAGACGATAAATA
22	CGACAACTAAGTATTAGACTTTACAATACCGA	45	CCTGATTGAAAGAAATTGCGTAGACCCGAACG
23	GGATTTAGCGTATTAAATCCTTTGTTTTCAGG	46	ACAGAAATCTTTGAATACCAAGTTCCTTGCTT

47	TTATTAATGCCGTCAATAGATAATCAGAGGTG
48	AGATTAGATTTAAAAGTTTGAGTACACGTAAA
49	AGGCGGTCATTAGTCTTTAATGCGCAATATTA
50	GAATGGCTAGTATTAACACCGCCTCAACTAAT
51	CCGCCAGCCATTGCAACAGGAAAAATATTTTT
52	CCCTCAGAACCGCCACCCTCAGAACTGAGACT
53	CCTCAAGAATACATGGCTTTTGATAGAACCAC
54	TAAGCGTCGAAGGATTAGGATTAGTACCGCCA
55	CACCAGAGTTCGGTCATAGCCCCCGCCAGCAA
56	TCGGCATTCCGCCGCCAGCATTGACGTTCCAG
57	AATCACCAAATAGAAAATTCATATATAACGGA
58	TCACAATCGTAGCACCATTACCATCGTTTTCA
59	ATACCCAAGATAACCCACAAGAATAAACGATT
60	ATCAGAGAAAGAACTGGCATGATTTTATTTTG
61	TTTTGTTTAAGCCTTAAATCAAGAATCGAGAA
62	AGGTTTTGAACGTCAAAAATGAAAGCGCTAAT
63	CAAGCAAGACGCGCCTGTTTATCAAGAATCGC
64	AATGCAGACCGTTTTTATTTTCATCTTGCGGG
65	CATATTTAGAAATACCGACCGTGTTACCTTTT
66	AATGGTTTACAACGCCAACATGTAGTTCAGCT
67	TAACCTCCATATGTGAGTGAATAAACAAAATC
68	AAATCAATGGCTTAGGTTGGGTTACTAAATTT
69	GCGCAGAGATATCAAAATTATTTGACATTATC
70	AACCTACCGCGAATTATTCATTTCCAGTACAT
71	ATTTTGCGTCTTTAGGAGCACTAAGCAACAGT
72	CTAAAATAGAACAAAGAAACCACCAGGGTTAG
73	GCCACGCTATACGTGGCACAGACAACGCTCAT
74	GCGTAAGAGAGAGCCAGCAGCAAAAAGGTTAT
75	GGAAATACCTACATTTTGACGCTCACCTGAAA
76	TATCACCGTACTCAGGAGGTTTAGCGGGGTTT
77	TGCTCAGTCAGTCTCTGAATTTACCAGGAGGT
78	GGAAAGCGACCAGGCGGATAAGTGAATAGGTG
79	TGAGGCAGGCGTCAGACTGTAGCGTAGCAAGG
80	TGCCTTTAGTCAGACGATTGGCCTGCCAGAAT
81	CCGGAAACACACCACGGAATAAGTAAGACTCC
82	ACGCAAAGGTCACCAATGAAACCAATCAAGTT
83	TTATTACGGTCAGAGGGTAATTGAATAGCAGC
84	TGAACAAACAGTATGTTAGCAAACTAAAAGAA
85	CTTTACAGTTAGCGAACCTCCCGACGTAGGAA
86	GAGGCGTTAGAGAATAACATAAAAGAACACCC
87	TCATTACCCGACAATAAACAACATATTTAGGC
88	CCAGACGAGCGCCCAATAGCAAGCAAGAACGC
89	AGAGGCATAATTTCATCTTCTGACTATAACTA
90	TTTTAGTTTTTCGAGCCAGTAATAAATTCTGT
91	TATGTAAACCTTTTTTAATGGAAAAATTACCT
92	TTGAATTATGCTGATGCAAATCCACAAATATA
93	GAGCAAAAACTTCTGAATAATGGAAGAAGGAG
94	TGGATTATGAAGATGATGAAACAAAATTTCAT
95	CGGAATTATTGAAAGGAATTGAGGTGAAAAAT
96	ATCAACAGTCATCATATTCCTGATTGATTGTT
97	CTAAAGCAAGATAGAACCCTTCTGAATCGTCT
98	GCCAACAGTCACCTTGCTGAACCTGTTGGCAA
99	GAAATGGATTATTTACATTGGCAGACATTCTG
100	TTTTTATAAGTATAGCCCGGCCGTCGAG
101	AGGGTTGATTTTATAAATCCTCATTAAATGATATTC
102	ACAAACAATTTTAATCAGTAGCGACAGATCGATAGC
103	AGCACCGTTTTTTAAAGGTGGCAACATAGTAGAAAA
104	TACATACATTTTGACGGGAGAATTAACTACAGGGAA
105	GCGCATTATTTTGCTTATCCGGTATTCTAAATCAGA
106	TATAGAAGTTTTCGACAAAAGGTAAAGTAGAGAATA
107	TAAAGTACTTTTCGCGAGAAAACTTTTTATCGCAAG
108	ACAAAGAATTTTATTAATTACATTTAACACATCAAG
109	AAAACAAATTTTTTCATCAATATAATCCTATCAGAT
110	GATGGCAATTTTAATCAATATCTGGTCACAAATATC
111	AAACCCTCTTTTACCAGTAATAAAAGGGATTCACCAGTCACACGTTTT
112	CCGAAATCCGAAAATCCTGTTTGAAGCCGGAA
113	CCAGCAGGGGCAAAATCCCTTATAAAGCCGGC
114	GCATAAAGTTCCACACAACATACGAAGCGCCA
115	GCTCACAATGTAAAGCCTGGGGTGGGTTTGCC
116	TTCGCCATTGCCGGAAACCAGGCATTAAATCA
117	GCTTCTGGTCAGGCTGCGCAACTGTGTTATCC
118	GTTAAAATTTTAACCAATAGGAACCCGGCACC
119	AGACAGTCATTCAAAAGGGTGAGAAGCTATAT
120	AGGTAAAGAAATCACCATCAATATAATATTTT
121	TTTCATTTGGTCAATAACCTGTTTATATCGCG
122	TCGCAAATGGGGCGCGAGCTGAAATAATGTGT
123	TTTTAATTGCCCGAAAGACTTCAAAACACTAT
124	AAGAGGAACGAGCTTCAAAGCGAAGATACATT
125	GGAATTACTCGTTTACCAGACGACAAAAGATT
126	GAATAAGGACGTAACAAAGCTGCTCTAAAACA
127	CCAAATCACTTGCCCTGACGAGAACGCCAAAA
128	CTCATCTTGAGGCAAAAGAATACAGTGAATTT
129	AAACGAAATGACCCCCAGCGATTATTCATTAC
130	CTTAAACATCAGCTTGCTTTCGAGCGTAACAC
131	TCGGTTTAGCTTGATACCGATAGTCCAACCTA
132	TGAGTTTCGTCACCAGTACAAACTTAATTGTA
133	CCCCGATTTAGAGCTTGACGGGGAAATCAAAA
134	GAATAGCCGCAAGCGGTCCACGCTCCTAATGA

135 GAGTTGCACGAGATAGGGTTGAGTAAGGGAGC

136 GTGAGCTAGTTTCCTGTGTGAAATTTGGGAAG

137 TCATAGCTACTCACATTAATTGCGCCCTGAGA

138 GGCGATCGCACTCCAGCCAGCTTTGCCATCAA

139 GAAGATCGGTGCGGGCCTCTTCGCAATCATGG

140 AAATAATTTTAAATTGTAAACGTTGATATTCA

141 GCAAATATCGCGTCTGGCCTTCCTGGCCTCAG

142 ACCGTTCTAAATGCAATGCCTGAGAGGTGGCA

143 TATATTTTAGCTGATAAATTAATGTTGTATAA

144 TCAATTCTTTTAGTTTGACCATTACCAGACCG

145 CGAGTAGAACTAATAGTAGTAGCAAACCCTCA

146 GAAGCAAAAAAGCGGATTGCATCAGATAAAAA

147 TCAGAAGCCTCCAACAGGTCAGGATCTGCGAA

148 CCAAAATATAATGCAGATACATAAACACCAGA

149 CATTCAACGCGAGAGGCTTTTGCATATTATAG

150 ACGAGTAGTGACAAGAACCGGATATACCAAGC

151 AGTAATCTTAAATTGGGCTTGAGAGAATACCA

152 GCGAAACATGCCACTACGAAGGCATGCGCCGA

153 ATACGTAAAAGTACAACGGAGATTTCATCAAG

154 CAATGACACTCCAAAAGGAGCCTTACAACGCC

155 AAAAAAGGACAACCATCGCCCACGCGGGTAAA

156 TGTAGCATTCCACAGACAGCCCTCATCTCCAA

157 GTAAAGCACTAAATCGGAACCCTAGTTGTTCC

158 AGTTTGGAGCCCTTCACCGCCTGGTTGCGCTC

159 AGCTGATTACAAGAGTCCACTATTGAGGTGCC

160 ACTGCCCGCCGAGCTCGAATTCGTTATTACGC

161 CCCGGGTACTTTCCAGTCGGGAAACGGGCAAC

162 CAGCTGGCGGACGACGACAGTATCGTAGCCAG

163 GTTTGAGGGAAAGGGGGATGTGCTAGAGGATC

164 CTTTCATCCCCAAAAACAGGAAGACCGGAGAG

165 AGAAAAGCAACATTAAATGTGAGCATCTGCCA

166 GGTAGCTAGGATAAAAATTTTTAGTTAACATC

167 CAACGCAATTTTTGAGAGATCTACTGATAATC

168 CAATAAATACAGTTGATTCCCAATTTAGAGAG

169 TCCATATACATACAGGCAAGGCAACTTTATTT

170 TACCTTTAAGGTCTTTACCCTGACAAAGAAGT

171 CAAAAATCATTGCTCCTTTTGATAAGTTTCAT

172 TTTGCCAGATCAGTTGAGATTTAGTGGTTTAA

173 AAAGATTCAGGGGGTAATAGTAAACCATAAAT

174 TTTCAACTATAGGCTGGCTGACCTTGTATCAT

175 CCAGGCGCTTAATCATTGTGAATTACAGGTAG

176 CGCCTGATGGAAGTTTCCATTAAACATAACCG

177 TTTCATGAAAATTGTGTCGAAATCTGTACAGA

178 ATATATTCTTTTTTCACGTTGAAAATAGTTAG

179 AATAATAAGGTCGCTGAGGCTTGCAAAGACTT

180 CGTAACGATCTAAAGTTTTGTCGTGAATTGCG

181 ACCCAAATCAAGTTTTTTGGGGTCAAAGAACG

182 TGGACTCCCTTTTCACCAGTGAGACCTGTCGT

183 TGGTTTTTAACGTCAAAGGGCGAAGAACCATC

184 GCCAGCTGCCTGCAGGTCGACTCTGCAAGGCG

185 CTTGCATGCATTAATGAATCGGCCCGCCAGGG

186 ATTAAGTTCGCATCGTAACCGTGCGAGTAACA

187 TAGATGGGGGGTAACGCCAGGGTTGTGCCAAG

188 ACCCGTCGTCATATGTACCCCGGTAAAGGCTA

189 CATGTCAAGATTCTCCGTGGGAACCGTTGGTG

190 TCAGGTCACTTTTGCGGGAGAAGCAGAATTAG

191 CTGTAATATTGCCTGAGAGTCTGGAAAACTAG

192 CAAAATTAAAGTACGGTGTCTGGAAGAGGTCA

193 TGCAACTAAGCAATAAAGCCTCAGTTATGACC

194 TTTTTGCGCAGAAAACGAGAATGAATGTTTAG

195 AAACAGTTGATGGCTTAGAGCTTATTTAAATA

196 ACTGGATAACGGAACAACATTATTACCTTATG

197 ACGAACTAGCGTCCAATACTGCGGAATGCTTT

198 CGATTTTAGAGGACAGATGAACGGCGCGACCT

199 CTTTGAAAAGAACTGGCTCATTATTTAATAAA

200 GCTCCATGAGAGGCTTTGAGGACTAGGGAGTT

201 ACGGCTACTTACTTAGCCGGAACGCTGACCAA

202 AAAGGCCGAAAGGAACAACTAAAGCTTTCCAG

203 GAGAATAGCTTTTGCGGGATCGTCGGGTAGCA

204 ACGTTAGTAAATGAATTTTCTGTAAGCGGAGT

205 TTTTCGATGGCCCACTACGTAAACCGTC

206 TATCAGGGTTTTCGGTTTGCGTATTGGGAACGCGCG

207 GGGAGAGGTTTTTGTAAAACGACGGCCATTCCCAGT

208 CACGACGTTTTTGTAATGGGATAGGTCAAAACGGCG

209 GATTGACCTTTTGATGAACGGTAATCGTAGCAAACA

210 AGAGAATCTTTTGGTTGTACCAAAAACAAGCATAAA

211 GCTAAATCTTTTCTGTAGCTCAACATGTATTGCTGA

212 ATATAATGTTTTCATTGAATCCCCCTCAAATCGTCA

213 TAAATATTTTTTGGAAGAAAAATCTACGACCAGTCA

214 GGACGTTGTTTTTCATAAGGGAACCGAAAGGCGCAG

215 ACGGTCAATTTTGACAGCATCGGAACGAACCCTCAG

216 CAGCGAAATTTTAACTTTCAACAGTTTCTGGGATTTTGCTAAACTTTT

Modified staple strands:

E100	TTTTTATAAGTATAGCCCGGCCGTCGAGAGGGTTGATTTTTATTCTACTTGAGAGAGCGAC
E102	ACAAACAATTTTAATCAGTAGCGACAGATCGATAGCAGCACCGTTTTTTATTCTACTTGAGAGAGCGAC
E104	TACATACATTTTGACGGGAGAATTAACTACAGGGAAGCGCATTATTTTTATTCTACTTGAGAGAGCGAC
E106	TATAGAAGTTTTCGACAAAAGGTAAAGTAGAGAATATAAAGTACTTTTTATTCTACTTGAGAGAGCGAC
E108	ACAAAGAATTTTATTAATTACATTTAACACATCAAGAAAACAAATTTTTATTCTACTTGAGAGAGCGAC
E110	GATGGCAATTTTAATCAATATCTGGTCACAAATATCAAACCCTCTTTTTATTCTACTTGAGAGAGCGAC
E111	AAACCCTCTTTTACCAGTAATAAAAGGGATTCACCAGTCACACGTTTTTATTCTACTTGAGAGAGCGAC

C101	ATAAATCCTCATTAAATGATATTC
C103	TAAAGGTGGCAACATAGTAGAAAA
C105	GCTTATCCGGTATTCTAAATCAGA
C107	CGCGAGAAAACTTTTTATCGCAAG
C109	TTCATCAATATAATCCTATCAGAT
C111	ACCAGTAATAAAAGGGATTCACCAGTCACACG

E5	AACCAGAGACCCTCAGAACCGCCAGGGGTCAGTTTATTCTACTTGAGAGAGCGAC
E23	GGATTTAGCGTATTAAATCCTTTGTTTTCAGGTTTATTCTACTTGAGAGAGCGAC
E32	GTTTGCCACCTCAGAGCCGCCACCGATACAGGTTTATTCTACTTGAGAGAGCGAC
E48	AGATTAGATTTAAAAGTTTGAGTACACGTAAATTTATTCTACTTGAGAGAGCGAC
E56	TCGGCATTCCGCCGCCAGCATTGACGTTCCAGTTTATTCTACTTGAGAGAGCGAC
E72	CTAAAATAGAACAAAGAAACCACCAGGGTTAGTTTATTCTACTTGAGAGAGCGAC
E114	GCATAAAGTTCCACACAACATACGAAGCGCCATTTATTCTACTTGAGAGAGCGAC
E128	CTCATCTTGAGGCAAAAGAATACAGTGAATTTTTTATTCTACTTGAGAGAGCGAC
E136	GTGAGCTAGTTTCCTGTGTGAAATTTGGGAAGTTTATTCTACTTGAGAGAGCGAC
E152	GCGAAACATGCCACTACGAAGGCATGCGCCGATTTATTCTACTTGAGAGAGCGAC
E160	ACTGCCCGCCGAGCTCGAATTCGTTATTACGCTTTATTCTACTTGAGAGAGCGAC
E176	CGCCTGATGGAAGTTTCCATTAAACATAACCGTTTATTCTACTTGAGAGAGCGAC
E184	GCCAGCTGCCTGCAGGTCGACTCTGCAAGGCGTTTATTCTACTTGAGAGAGCGAC
E200	GCTCCATGAGAGGCTTTGAGGACTAGGGAGTTTTTATTCTACTTGAGAGAGCGAC

A.6 References

1. Rothemund, P. W. *Nature* 2006**,** 440, 297-302.
2. Hong, F.; Zhang, F.; Liu, Y.; Yan, H. *Chem. Rev.* 2017.
3. Wang, P.; Meyer, T. A.; Pan, V.; Dutta, P. K.; Ke, Y. *Chem* 2017**,** 2, 359-382.
4. Chandrasekaran, A. R.; Pushpanathan, M.; Halvorsen, K. *Mater. Lett.* 2016**,** 170, 221-224.
5. Marchi, A. N.; Saaem, I.; Vogen, B. N.; Brown, S.; LaBean, T. H. *Nano Lett.* 2014**,** 14, 5740-5747.

6. Li, Z.; Liu, M.; Wang, L.; Nangreave, J.; Yan, H.; Liu, Y. *J. Am. Chem. Soc.* 2010**,** 132, 13545-13552.
7. Liu, W.; Zhong, H.; Wang, R.; Seeman, N. C. *Angew. Chem. Int. Ed.* 2011**,** 50, 264-267.
8. Zhao, Z.; Liu, Y.; Yan, H. *Nano Lett.* 2011**,** 11, 2997-3002.
9. Fu, Y.; Zeng, D.; Chao, J.; Jin, Y.; Zhang, Z.; Liu, H.; Li, D.; Ma, H.; Huang, Q.; Gothelf, K. V.; Fan, C. *J. Am. Chem. Soc.* 2013**,** 135, 696-702.
10. Kocabey, S.; Kempter, S.; List, J.; Xing, Y.; Bae, W.; Schiffels, D.; Shih, W. M.; Simmel, F. C.; Liedl, T. *ACS Nano* 2015**,** 9, 3530-3539.
11. Wang, P.; Gaitanaros, S.; Lee, S.; Bathe, M.; Shih, W. M.; Ke, Y. *J. Am. Chem. Soc.* 2016**,** 138, 7733-7740.
12. Woo, S.; Rothemund, P. W. *Nat. Chem.* 2011**,** 3, 620-627.
13. Woo, S.; Rothemund, P. W. *Nat. Commun.* 2014**,** 5, 4889.
14. Aghebat Rafat, A.; Pirzer, T.; Scheible, M. B.; Kostina, A.; Simmel, F. C. *Angew. Chem. Int. Ed.* 2014**,** 53, 7665-7668.
15. Suzuki, Y.; Endo, M.; Sugiyama, H. *Nat. Commun.* 2015**,** 6, 8052.
16. List, J.; Weber, M.; Simmel, F. C. *Angew. Chem. Int. Ed.* 2014**,** 53, 4236-4239.
17. Zhou, C.; Wang, D.; Dong, Y.; Xin, L.; Sun, Y.; Yang, Z.; Liu, D. *Small* 2015**,** 11, 1161-1164.
18. Lutz, J. F.; Ouchi, M.; Liu, D. R.; Sawamoto, M. *Science* 2013**,** 341, 1238149.
19. Edwardson, T. G.; Carneiro, K. M.; Serpell, C. J.; Sleiman, H. F. *Angew. Chem. Int. Ed.* 2014**,** 53, 4567-4571.
20. Greenspan, P.; Fowler, S. D. *J. Lipid Res.* 1985**,** 26, 781-789.
21. Stahl, E.; Martin, T. G.; Praetorius, F.; Dietz, H. *Angew. Chem. Int. Ed.* 2014**,** 53, 12735-12740.
22. Zhou, C.; Zhang, Y.; Dong, Y.; Wu, F.; Wang, D.; Xin, L.; Liu, D. *Adv. Mater.* 2016**,** 28, 9819-9823.
23. Edwardson, T. G.; Carneiro, K. M.; McLaughlin, C. K.; Serpell, C. J.; Sleiman, H. F. *Nat. Chem.* 2013**,** 5, 868-875.
24. Shaw, A.; Benson, E.; Hogberg, B. *ACS Nano* 2015**,** 9, 4968-4975.
25. Hung, A. M.; Micheel, C. M.; Bozano, L. D.; Osterbur, L. W.; Wallraff, G. M.; Cha, J. N. *Nat. Nanotechnol.* 2010**,** 5, 121-126.